https://ntrs.nasa.gov/search.jsp?R=19680020235 2020-03-12T09:47:53+00:00Z

Frank D. Rowan 192

Final Report:

FEASIBILITY STUDY FOR A SCANNING CELESTIAL ATTITUDE DETERMINATION SYSTEM (SCADS) ON THE IMP SPACECRAFT

Contract No. NAS5-9439

Control Data Project No. 9573

RD 2005

10 June 1967

GPO PRICE $ _____

CFSTI PRICE(S) $ _____

Hard copy (HC) 3.00

Microfiche (MF) .65

ff 653 July 65

Prepared by:

D. F. Nickel
C. B. Grosch
H. R. Paetznick
R. W. Peterson
B. D. Vannelli

Prepared for:

National Aeronautics and Space Administration
Goddard Space Flight Center
Greenbelt, Maryland

Aerospace Research Department
Research Division
CONTROL DATA CORPORATION
8100 34th Avenue South
Minneapolis, Minnesota 55440

N68-29707 (ACCESSION NUMBER) 24 (PAGES) CR-95508 (NASA CR OR TMX OR AD NUMBER) 1 (THRU) 1 (CODE) 21 (CATEGORY)

FACILITY FORM 602

RECEIVED NASA STI FACILITY INPUT BRANCH AUG 1968

Final Report:

FEASIBILITY STUDY FOR A SCANNING CELESTIAL ATTITUDE DETERMINATION SYSTEM (SCADS) ON THE IMP SPACECRAFT

Contract No. NAS5-9439

Control Data Project No. 9573

RD 2005

10 June 1967

Prepared by:

D. F. Nickel
C. B. Grosch
H. R. Paetznick
R. W. Peterson
B. D. Vannelli

Prepared for:

National Aeronautics and Space Administration
Goddard Space Flight Center
Greenbelt, Maryland

Aerospace Research Department
Research Division
CONTROL DATA CORPORATION
8100 34th Avenue South
Minneapolis, Minnesota 55440

FOREWORD

This report was prepared by Control Data Corporation, Research Division, under National Aeronautics and Space Administration, Goddard Space Flight Center, Contract No. NAS5-9439.

The Control Data Project Engineer and principal investigator was Donald F. Nickel. Other areas of technical responsibility were assigned as follows: C. B. Grosch, error analysis and star availability search; H. R. Paetznick, mathematical analysis; R. W. Peterson, sun shield design and particle radiation study; B. D. Vannelli, star identification procedures. The above named personnel were also contributing authors of this report.

Control Data Corporation would particularly like to acknowledge the technical guidance of the National Aeronautics and Space Administration Technical Project Officer, Irving B. Lowen, Goddard Space Flight Center.

ABSTRACT

This report describes the feasibility of using an electro-optical celestial scanning sensor on board the IMP spacecraft for determination of the spacecraft attitude by utilizing star measurements. The sensor basically consists of a wide-angle lens with a slit positioned on the focal surface, a photomultiplier detector positioned behind the slit aperture and star signal processing electronics. The sensor, which consists of no moving parts, rotates with the spin stabilized vehicle. After automatic identification of the stars detected, the vehicle attitude is determined by computer solution of the system constraint equations.

The study effort was largely devoted to the areas of optical design, electrical design, mechanical design, signal detection analysis, system error analysis, and star identification. A recommended system design is determined.

TABLE OF CONTENTS

TABLE OF CONTENTS (concluded)

LIST OF FIGURES

LIST OF FIGURES (continued)

LIST OF FIGURES (continued)

LIST OF FIGURES (concluded)

LIST OF TABLES

SECTION I

GENERAL DESCRIPTION

It is the purpose of this section to briefly describe the attitude determination problem for the Interplanetary Monitoring Platform (IMP) spacecraft, the method of solution using a SCADS sensor, and the instrumentation required to acquire data for the solution.

A. Purpose of Study

The purpose of this study is to perform a system design analysis to establish the feasibility of using the Scanning Celestial Attitude Determination System (SCADS) aboard the IMP spacecraft to provide data at a ground receiving station to compute the following spacecraft performance characteristics:

(a) three axis attitude to within an accuracy of 0.1 degree RMS per axis,

(b) spin period accurate to within .03 percent.

The perigee of the IMP vehicle orbit is given as an altitude of 10^4 nautical miles above the earth's surface and the apogee is given as 10^5 nautical miles from the earth's center.

The study basically consists of these major topics:

(1) system design analysis,

(2) mathematical analysis and star identification,

(3) error analysis.

A detailed discussion of each topic is covered in the body of the report.

B. Overall Summary of Study

The general conclusion of this study is that attitude determination for the IMP vehicle by employment of a SCADS sensor is indeed feasible. Measurement of both the three axis attitude to within 0.1 degree RMS per axis and the spin period accurate to .03 per cent can be readily achieved with the sensor.

Some of the gross characteristics of the SCADS-IMP sensor and system are summarized below.

Preferred Cant Angle = 25° = Γ
Optical Field of View = 20° = FOV
Photomultiplier = EMR541N
Single Radial Slit
Rotational Slit Width = 6 arc minutes
Limiting Required Detectable Magnitude = $4^{m}.0$
Optical Aperture Diameter ($\Gamma = 25^{\circ}$, FOV = 20°)
2.65 inches for $2 \leq T < 7$ seconds
1.51 inches for $7 \leq T$ seconds

Size (excluding sun shield with no on-board transit time encoding)

30.5 $(\text{inch})^3$ for $2 \leq T < 7$ seconds (scan period)

20.2 $(\text{inch})^3$ for $7 \leq T$ seconds

Size (excluding sun shield with on-board transit time encoding)

34.5 $(\text{inch})^3$ for $2 \leq T < 7$ seconds

24.2 $(\text{inch})^3$ for $7 \leq T$ seconds

Weight (with no on-board transit time encoding)

4.63 pounds for $2 \leq T < 7$ seconds (scan period)

2.83 pounds for $7 \leq T$ seconds

Weight (with on-board transit time encoding)

4.96 pounds for $2 \leq T < 7$ seconds

3.16 pounds for $7 \leq T$ seconds

Sun Shade Dimensions

11 inch diameter x 4.9 inch height for $2 \leq T < 7$ seconds

6.2 inch diameter x 2.8 inch height for $7 \leq T$ seconds

Power

.86 watt (includes analog filters and power supply and assumes transit time encoding is done at the ground station)

1.4 watts (includes logic for on-board encoding of transit times)

C. Basic Description of Operation

The basic problem of attitude determination with a SCADS sensor is finding the orientation of the IMP space vehicle coordinate system with respect to the celestial coordinate system by optical sighting of stars as the sensor scans the celestial sphere. The star sightings are made through a slit fixed in the vehicle coordinate system which establishes the stars to lie along a great circle on the celestial sphere. This slit is uniformly rotated by the spinning of the IMP vehicle about its axis, and at each instant a star brighter than a fixed threshold appears in the slit, a measurement of the star transit time is taken. A number (greater than or equal to the number of unknown orientation parameters) of such measurements then establishes a system of equations which may be solved for the required vehicle orientation. The solution to the system of equations requires the location (right ascension and declination) of the detected stars on the celestial sphere. This means that the transit time measurements must be used to first identify the stars before a solution can be obtained. Crude star intensity measurements are also of great assistance in star identification. Star identification essentially consists of matching angular separations between transited stars (obtained from the transit time measurements) and the approximate relative star intensities with the angular separations and magnitudes obtained from a star catalog.

The basic SCADS instrument consists of a sun shield, a lens, a single transparent slit in the lens focal plane radial to the spin axis, a photomultiplier, and signal processing electronics. The SCADS-IMP sensor is illustrated in Figure 1. The entire system is fixed within the IMP spacecraft and rotates along with the vehicle about the vehicle spin axis. The instrument is designed to detect when stars brighter than $4^{m}.0$ magnitude cross the slit. Filtering of the star signals is provided in the signal processing electronics. The signal processing electronics may also encode into a binary data word the star transit time, although the encoding could be done at the ground station from the filtered analog signal transmitted

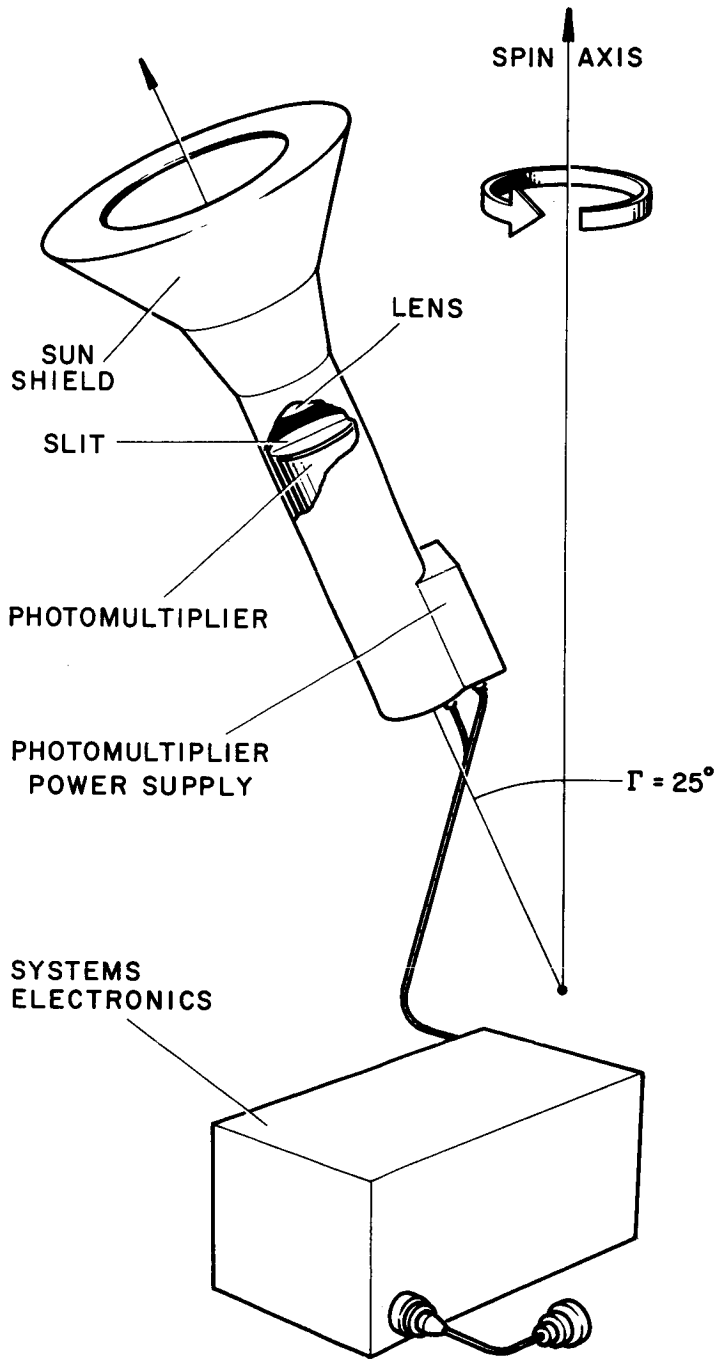

Figure 1: SCADS-IMP Sensor

via telemetry to the ground station. The star signal electronics can also crudely measure and encode the star pulse amplitudes which give relative star intensity information. The transit time measurements along with the crude star magnitude measurements are then used to perform star identification and the computation of the attitude.

The complexity of the attitude determination problem depends upon the alignment accuracy of the sensor with respect to the IMP coordinate system. For the SCADS-IMP system of equations, there will be no less than seven but no more than nine unknowns.

SECTION II

ORBITAL PARAMETERS FOR IMP VEHICLE

The primary purpose of the IMP satellite is to investigate energetic particle radiations, plasmas, and magnetic fields in space. To accomplish this task, a highly eccentric orbit as pictured in Figure 2 is required.

The distance between the earth's center and apogee is 10^5 nm, while the altitude at perigee is 10^4 nm. These distances together with a mean Earth radius of 3438 nm imply:

$a = 5.67 \times 10^4$ nm (length of semi-major axis),

$e = 0.763$ (eccentricity),

$T = 94.2$ hours (orbital period).

We are also given that the orbital inclination is 33 degrees, the satellite is spin-stabilized with a spin rate of from 5 to 30 revolutions per minute, and the spin axis is roughly perpendicular to a line joining the satellite and sun. Other parameters are dependent on the time of launch and, hence, cannot be specified at the present time.

In Figure 3 we plot the half-angle subtended by the earth at the satellite as a function of the satellite's position. It is important to consider this angle, for it determines the extent of the region over which stars cannot be viewed and Earth reflected radiation may be received. From this figure we see that this angle varies from 17 degrees at perigee to 2 degrees at apogee.

Figure 4 is a projection of the orbit, Earth blocking, sun, and effective field of view on the celestial sphere. The instantaneous Earth blocking is centered about the satellite's nadir, and represents a region on the celestial sphere over which stars cannot be viewed. As shown in this figure, the spin axis is perpendicular to the sun's direction. However, the possible angles this axis makes with the ecliptic are not specified.

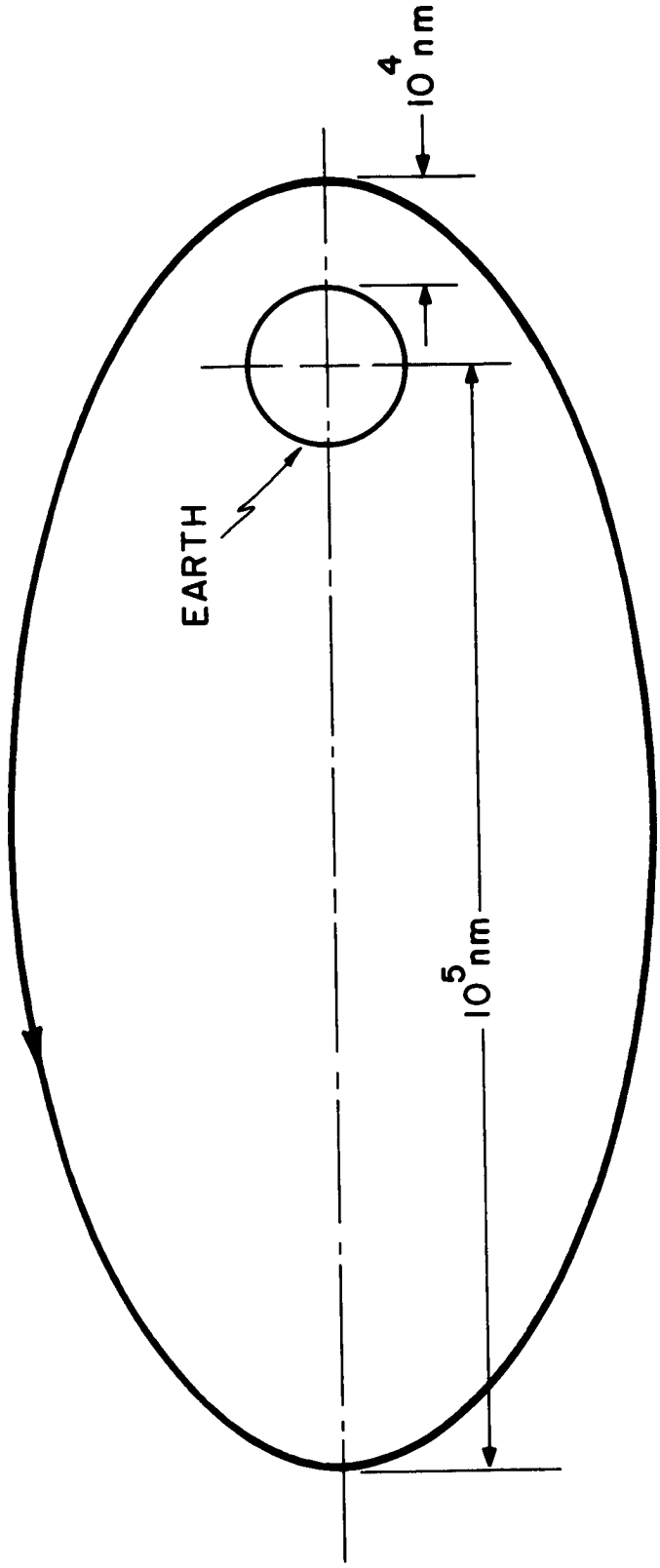

Figure 2: Orbit of IMP Spacecraft

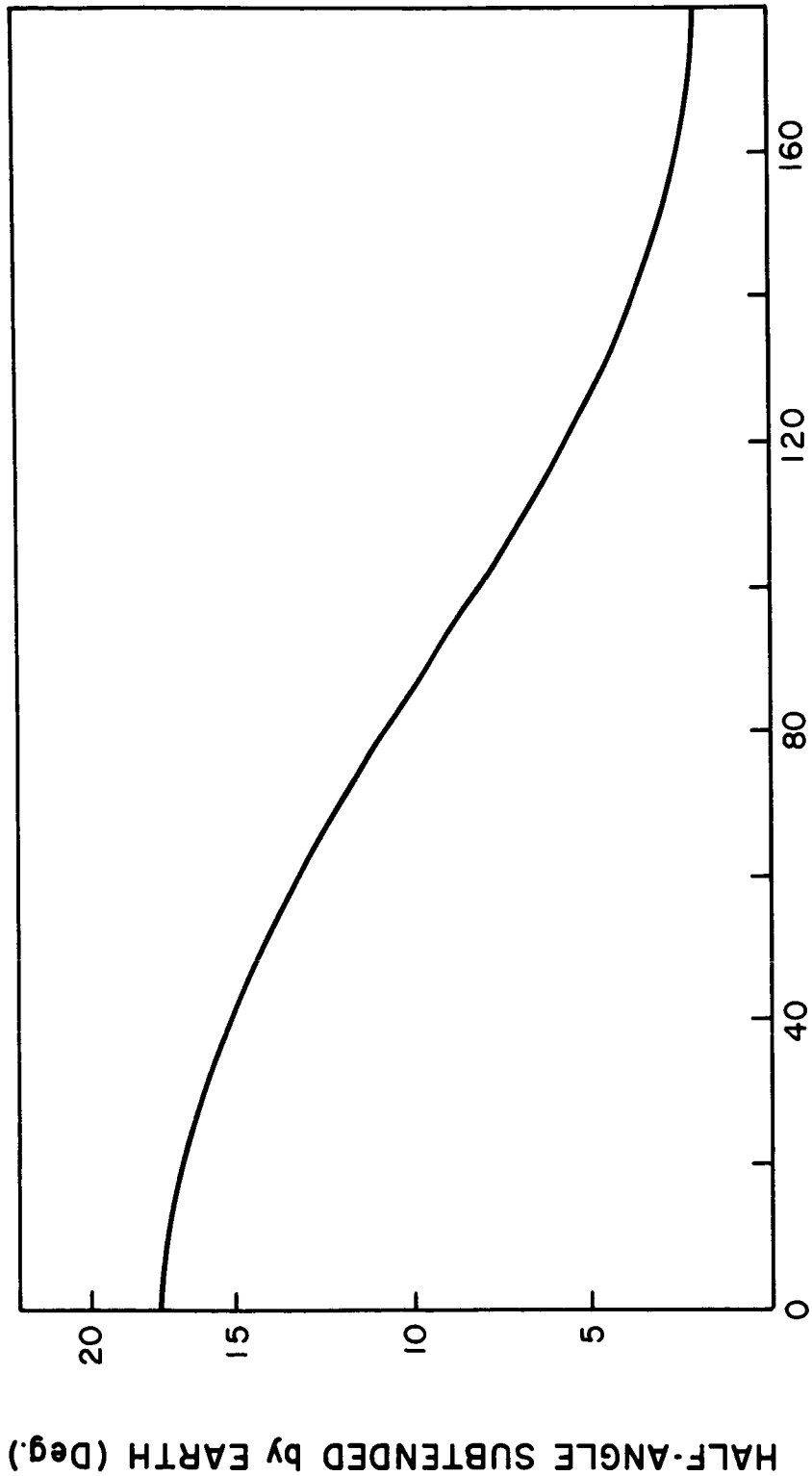

Figure 3: Extent of Earth Blocking as a Function of Orbital Position

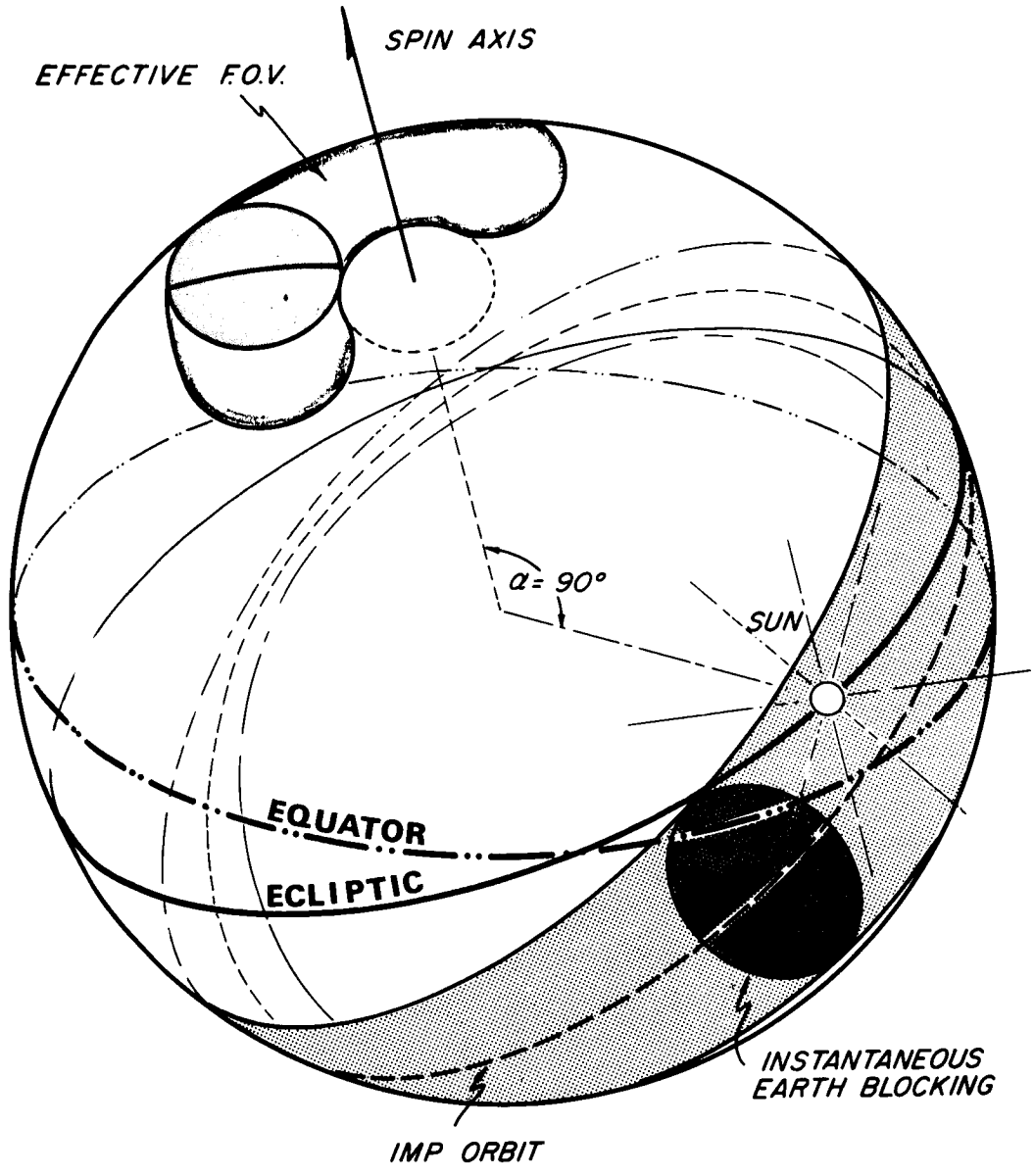

Figure 4: Earth Blocking, Sun, and FOV Projected on Celestial Sphere

The field of view is canted with respect to the spin axis, and one slit is shown in Figure 4. Note that the sun will not directly enter the field of view, but nevertheless, it may cause difficulties during that part of the scan period which places the slit nearest the sun. These difficulties will be a result of scattering of sunlight onto the lens. It is difficult to calculate the effect of sun scattering, but it is felt that the effective field of view will be reduced so that the star transits can be measured over only about one-half the scan period. This effect is also pictured in Figure 4.

PRECEDING PAGE BLANK NOT FILMED.

SECTION III

SYSTEM DESIGN ANALYSIS

A. Determination of Optical Axis Cant Angle with Respect to Vehicle Spin Axis

The spin axis of the IMP vehicle is nominally fixed at 90 degrees to the spacecraft-sun vector and may be inclined with any arbitrary angle to the plane of the ecliptic. The optical axis is free to be inclined at a cant angle, Γ, with respect to the spin axis where Γ is restricted to 25 degrees or less. The problem then arises of determining the best angle for canting the optical axis with respect to the spin axis. This requires choosing some criteria which describe the optimum cant angle.

In selecting the best cant angle criteria, two factors must be considered. The first factor involves the field of view. In particular, the field of view required to scan a given area on the celestial sphere decreases as the cant angle increases. The second factor involves the problem of shielding the optical system from locally reflected radiation from the sun or from the sun-illuminated earth. The latter factor is important even if the sun or the earth are not in the optical system field of view.

To illustrate the above statement, consider Figure 5, where the cant angle $\Gamma = 0$ and the spin axis is inclined by an angle β to the radiation from the sun. A simple cone is used as a sun shield and nominally β is 90 degrees. For $\beta \geq 90^{\circ}$, no inner portion of the sun shield is illuminated, hence the optical system sees only the stellar background radiation. However, for $\beta < 90^{\circ}$, an inner portion of the sun shield is illuminated by direct sunlight and radiation is scattered into the optical system. Hence, the optical system now sees radiation in addition to that contributed by the stellar background. The locally reflected sun radiation is not negligible and depends upon factors such as the incidence angle, β, the field of view, the absorptivity and reflectivity of the inner cone surface, the number of multiple reflections within the cone before entering the lens, and the slit area.

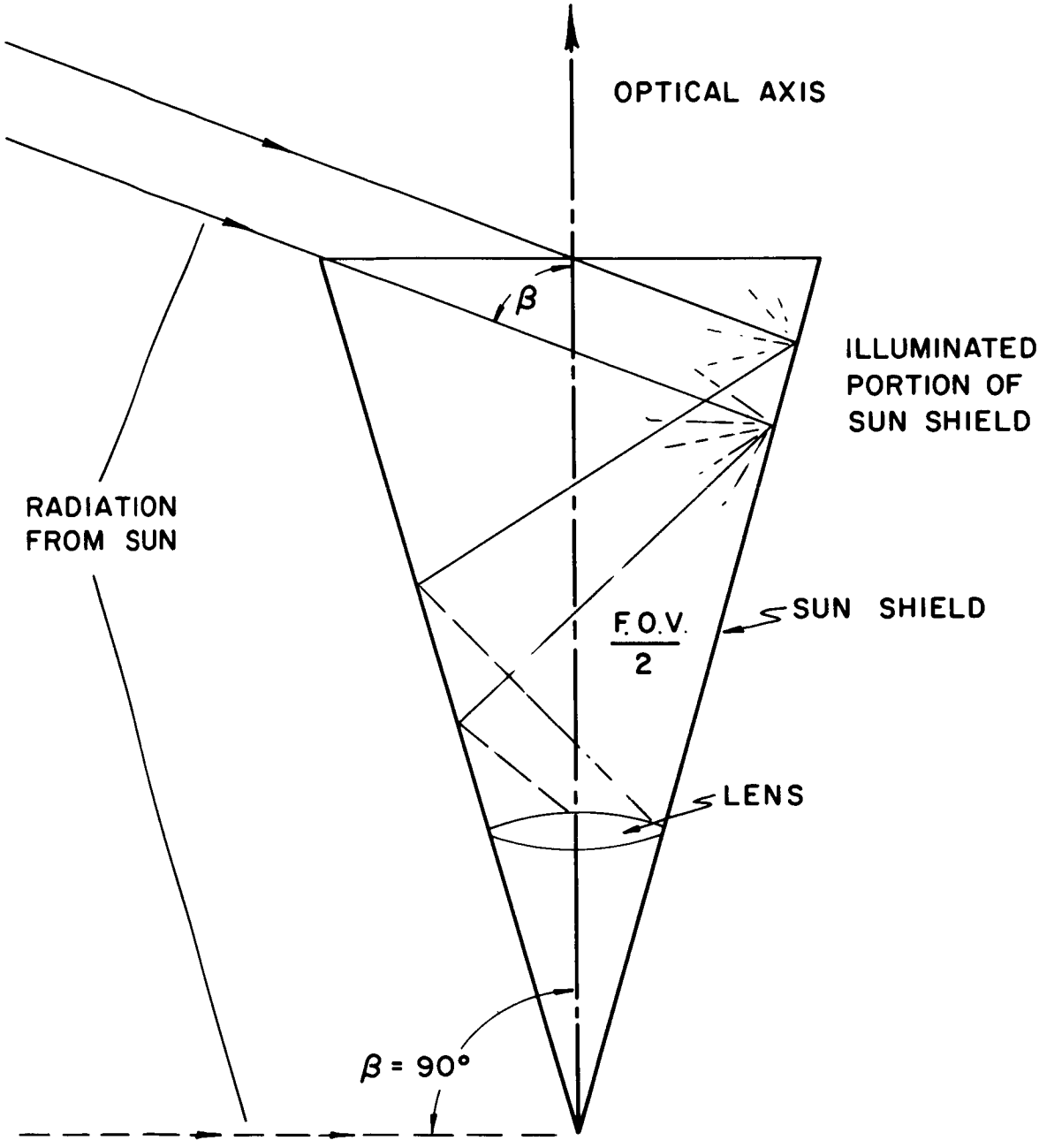

Figure 5: Scattered Sun Radiation from Illuminated Portion of Sun Shield

The intensity of the locally reflected sun radiation may be crudely estimated by considering the sun as a star of magnitude - $26^m.2$ and comparing it to a + $3^m.0$ or + $4^m.0$ magnitude star which must be detected for determining attitude. Therefore, the sun intensity is 10^{12} times that of a + $4^m.0$ magnitude star, hence the attenuation of sunlight by the shield inner surfaces, optics, and sensor must be at least 10^{-12}. The attenuation per surface reflection is no better than 10^{-3}. More detailed analysis shows that an accurate prediction of star detectability is not possible for $\beta < 90^o$. In fact, detection of even bright stars may be difficult when β becomes small.

The Earth reflected sun radiation is about 40 percent of the direct sun radiation, so this radiation, though extended, is of the same order of magnitude as the sun. It is therefore concluded that star detectability cannot be accurately predicted when either the sun or earth's limb is closer than 90 degrees to the optical axis. So with the spin axis-optical axis of Figure 5 at a nominal 90 degrees to the sun, a movement of the axis by only a few degrees closer to the sun will degrade sensor operation for the entire scan period. Hence, a cant angle $\Gamma = 0$ is not acceptable.

Figure 6 shows the optical axis canted by an angle Γ with respect to the spin axis. As the vehicle rotates about its spin axis, the locus of the optical axis is a cone concentric to the spin axis. With the spin axis a nominal 90 degrees to the spacecraft-sun vector, locally reflected sun radiation can enter the optical system for 180 degrees of each scan period provided the earth's limb is always greater than 90 degrees from the spin axis. During the remaining 180 degrees of the scan period, star detectability can be accurately predicted based on the stellar background radiation.

As the spacecraft moves in its orbit with its spin axis 90 degrees to the sun line and inclined at some angle, ψ, to the plane of the ecliptic, the earth's limb will not always be greater than 90 degrees to the optical axis for the entire scan period. Therefore, the best cant angle may be

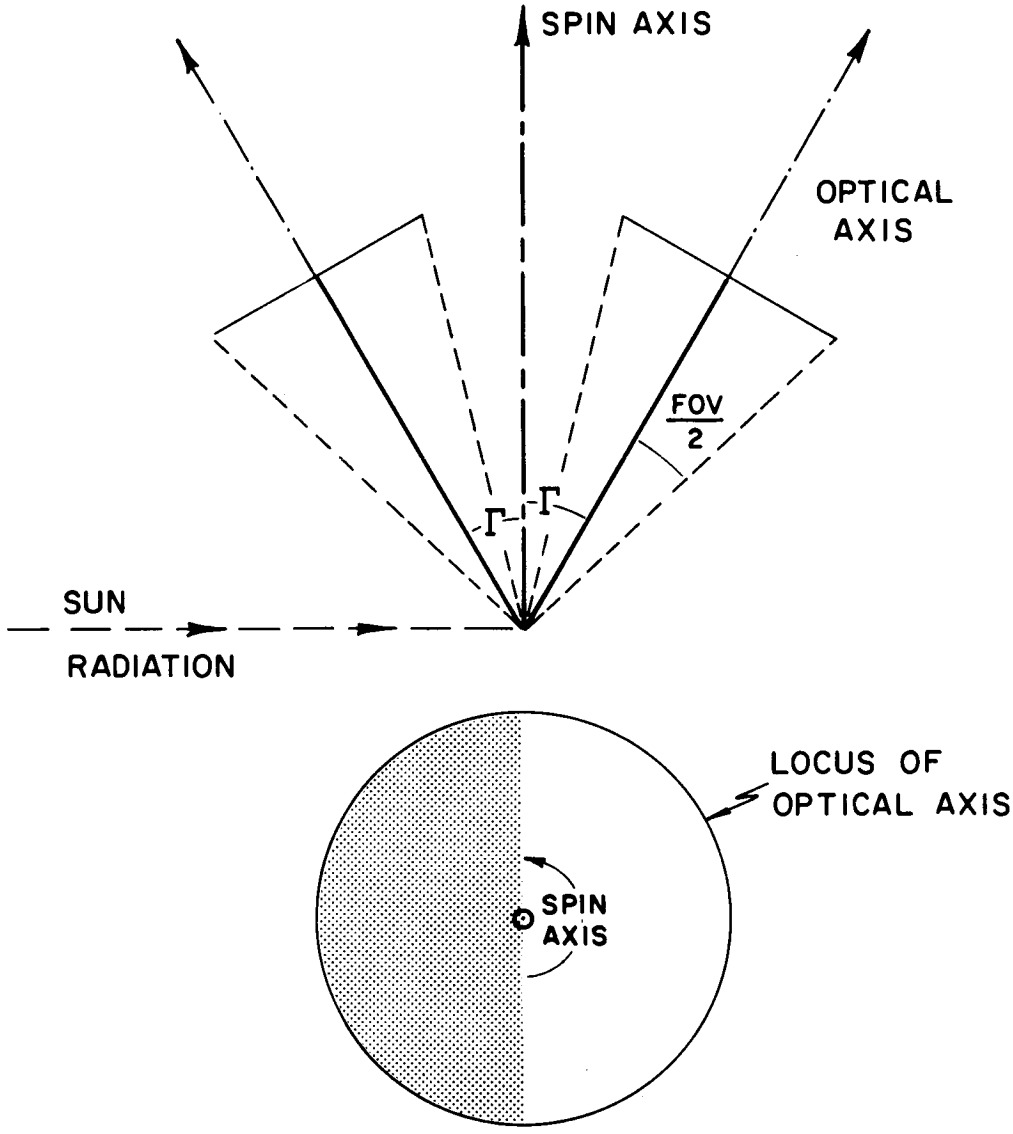

Figure 6: Locus of Optical Axis Canted at an Angle Γ with Respect to the Spin Axis

selected by using as a criteria the amount of time the earth's limb is greater than 90 degrees to the optical axis for a one year interval. For a given vehicle orbit and spin axis inclination, the amount of time the spin axis is greater than 90 degrees to the optical axis may be numerically evaluated. A computer program has been written to perform this computation. The basic concept of this program will be described in the following paragraphs.

For this program the spin axis of the IMP vehicle was constrained to be perpendicular to the spacecraft-sun vector, but inclined at some fixed angle, ψ, with respect to the plane of the ecliptic. The program numerically evaluates the amount of time during a year the earth's limb is greater than 90 degrees from the optical axis for a fixed cant angle. By comparing these times for different cant angles, the best cant angle may be selected.

In order to perform the computations, the program is logically divided into three parts. First, the program computes azimuth angles of the available scan period relative to North based upon the restriction that the sun must be at least 90 degrees to the optical axis. Secondly, the program computes the azimuth angles of the available scan period relative to North based upon the restriction that the limb of the earth is greater than 90 degrees from the optical axis. Finally, the program determines the overall available fraction of the scan period in which both the sun and earth's limb are greater than 90 degrees from the optical axis. This is accomplished by determining the regions of overlap for the azimuth angles relative to North.

Before further proceeding with the computer program, it is necessary to consider the relative proximity of the sun, earth, and spacecraft on the celestial sphere. This requires vector analysis of the geometry relating the three bodies. In particular, it is necessary to determine the unit vector of the spin axis, $\overline{S}_s$, and the unit vector from the earth's center to the spacecraft, $\overline{S}_{EC}$, from which the angle between the spin axis and the earth-satellite line may be determined as,

$$\beta_1 = \cos^{-1}\left\{\bar{S}_{EC} \cdot \bar{S}_s\right\} \quad .$$

Also, it is necessary to know the angle, ϕ_e, subtended by the earth from the spacecraft. These angles vary as a function of time and are essentially periodic for a one year interval for a fixed spacecraft orbit.

Figure 7 shows the geometry of the spin axis inclined at an angle, ψ, with the plane of the ecliptic. The angle from the First Point of Aries to the sun in the plane of the ecliptic is measured by ρ. Other angles shown in Figure 7 are defined as,

α = right ascension of the sun,

δ = declination of the sun,

$\theta = 23.5^{\circ}$ = inclination of the plane of the ecliptic with the celestial equator.

Rotation of the $(\bar{i}_1, \bar{j}_1, \bar{k}_1)$ coordinate system of Figure 7 through an angle θ about the $\bar{i}_1$ axis results in

$$\begin{pmatrix} \bar{i}_2 \\ \bar{j}_2 \\ \bar{k}_2 \end{pmatrix} = \begin{pmatrix} 1 & 0 & 0 \\ 0 & \cos\theta & \sin\theta \\ 0 & -\sin\theta & \cos\theta \end{pmatrix} \begin{pmatrix} \bar{i}_1 \\ \bar{j}_1 \\ \bar{k}_1 \end{pmatrix} \qquad (1)$$

Next, a rotation of the $(\bar{i}_2, \bar{j}_2, \bar{k}_2)$ coordinate system about the $\bar{k}_2$ axis through an angle ρ results in

$$\begin{pmatrix} \bar{i}_3 \\ \bar{j}_3 \\ \bar{k}_3 \end{pmatrix} = \begin{pmatrix} \cos\rho & \sin\rho & 0 \\ -\sin\rho & \cos\rho & 0 \\ 0 & 0 & 1 \end{pmatrix} \begin{pmatrix} \bar{i}_2 \\ \bar{j}_2 \\ \bar{k}_2 \end{pmatrix} \qquad (2)$$

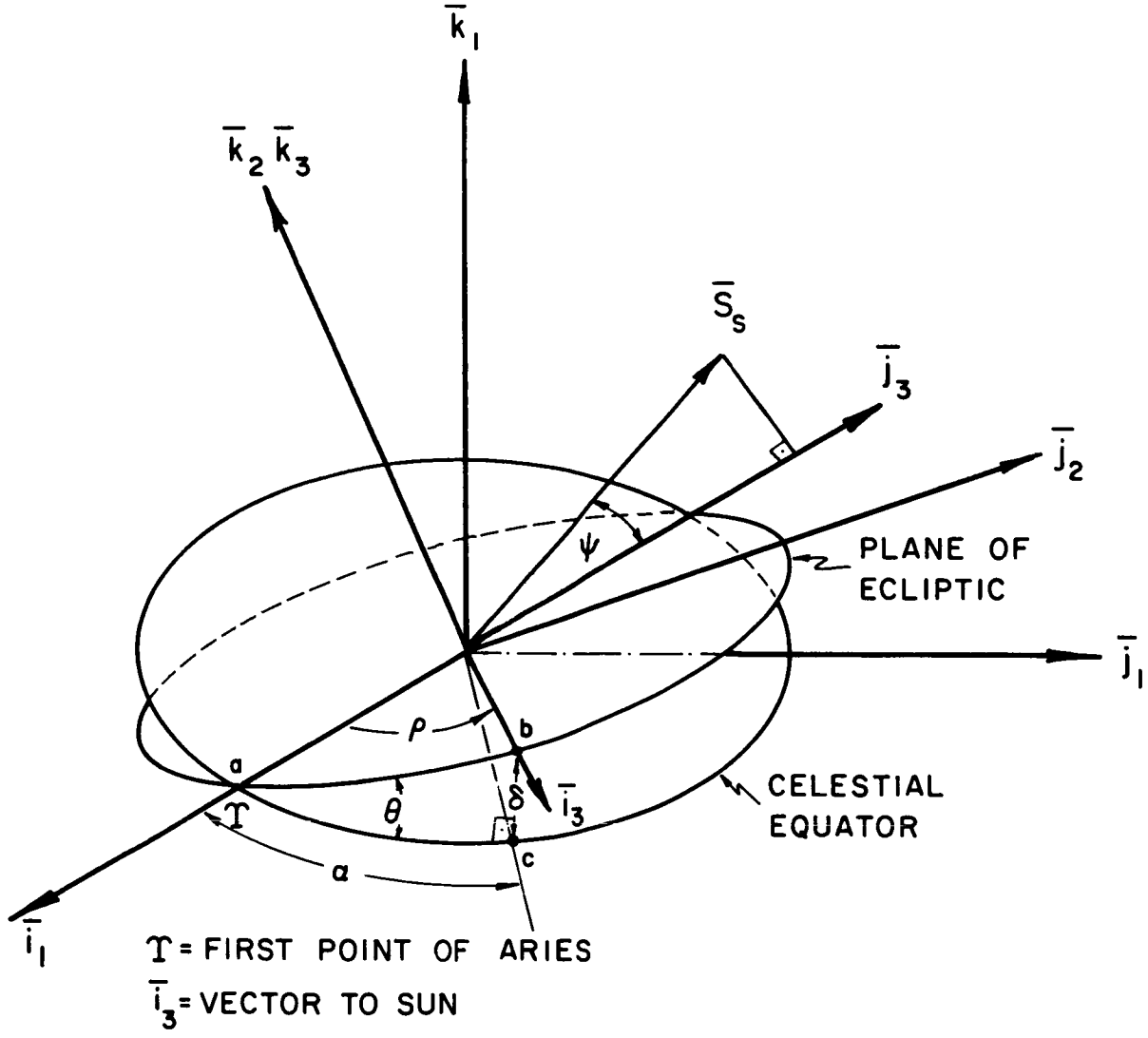

Figure 7: Vector Geometry of Spin Axis at an Angle ψ with the Plane of the Ecliptic

The direction of the spin axis is described by

$$\bar{S}_s = (0, \cos\psi, \sin\psi) \begin{pmatrix} \bar{i}_3 \\ \bar{j}_3 \\ \bar{k}_3 \end{pmatrix} \tag{3}$$

Note that the spin axis was chosen to have no component in the direction of the $\bar{i}_3$ axis, which points toward the sun (Figure 7), since the spin axis for the IMP vehicle is specified as perpendicular to the sun line. By combining Equations (1), (2), and (3), $\bar{S}_s$ becomes

$$\bar{S}_s = (0, \cos\psi, \sin\psi) \begin{pmatrix} \cos\rho & \sin\rho & 0 \\ -\sin\rho & \cos\rho & 0 \\ 0 & 0 & 1 \end{pmatrix} \begin{pmatrix} \bar{i}_2 \\ \bar{j}_2 \\ \bar{k}_2 \end{pmatrix} \tag{4}$$

Since abc in Figure 7 is a right spherical triangle, $\cos\rho = \cos\alpha \cos\delta$ and $\sin\delta = \sin\rho \sin\theta$.

Figure 8 shows the orbital plane inclined at an angle I with the plane of the celestial equator. The angles shown in Figure 8 are defined as

Ω = argument of the ascending node (longitude),

ω = argument of perigee,

I = inclination of the orbital plane to the plane of the celestial equator,

f = angle of the true anomaly for an eliptical orbit.

Rotation of the $(\bar{i}_1, \bar{j}_1, \bar{k}_1)$ coordinate system of Figure 8 through an angle Ω about the $\bar{k}_1$ axis results in,

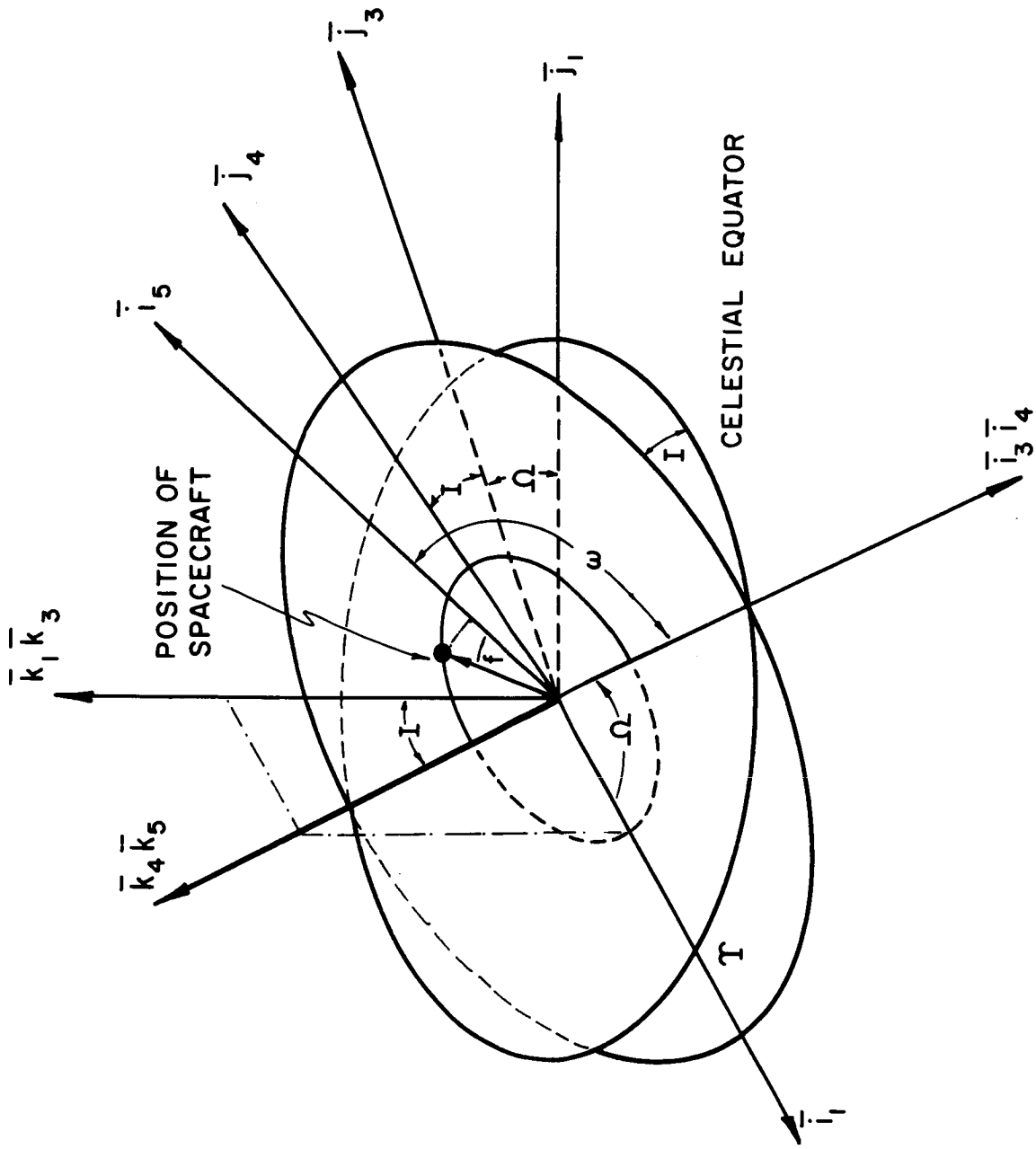

Figure 8: Geometry of Orbital Plane Inclined at an Angle I with the Plane of the Celestial Equator

$$\begin{pmatrix} \bar{i}_3 \\ \bar{j}_3 \\ \bar{k}_3 \end{pmatrix} = \underbrace{\begin{pmatrix} \cos\Omega & \sin\Omega & 0 \\ -\sin\Omega & \cos\Omega & 0 \\ 0 & 0 & 1 \end{pmatrix}}_{E} \begin{pmatrix} \bar{i}_1 \\ \bar{j}_1 \\ \bar{k}_1 \end{pmatrix} \tag{5}$$

Rotation of the $(\bar{i}_3, \bar{j}_3, \bar{k}_3)$ coordinate system through an angle I about the $\bar{i}_3$ axis yields,

$$\begin{pmatrix} \bar{i}_4 \\ \bar{j}_4 \\ \bar{k}_4 \end{pmatrix} = \underbrace{\begin{pmatrix} 1 & 0 & 0 \\ 0 & \cos I & \sin I \\ 0 & -\sin I & \cos I \end{pmatrix}}_{F} \begin{pmatrix} \bar{i}_3 \\ \bar{j}_3 \\ \bar{k}_3 \end{pmatrix} \tag{6}$$

Rotation of the $(\bar{i}_4, \bar{j}_4, \bar{k}_4)$ system through an angle ω about the $\bar{k}_4$ axis gives a result similar to Equation (5),

$$\begin{pmatrix} \bar{i}_5 \\ \bar{j}_5 \\ \bar{k}_5 \end{pmatrix} = \underbrace{\begin{pmatrix} \cos\omega & \sin\omega & 0 \\ -\sin\omega & \cos\omega & 0 \\ 0 & 0 & 1 \end{pmatrix}}_{G} \begin{pmatrix} \bar{i}_4 \\ \bar{j}_4 \\ \bar{k}_4 \end{pmatrix} \tag{7}$$

The $(\bar{i}_5 - \bar{j}_5)$ plane contains the plane of the orbit. The position of the spacecraft is given by the unit vector,

$$\bar{S}_{EC} = (\cos f, \quad \sin f, \quad 0) \begin{pmatrix} \bar{i}_5 \\ \bar{j}_5 \\ \bar{k}_5 \end{pmatrix}$$

$$= (\cos f, \quad \sin f, \quad 0)(G)(F)(E) \begin{pmatrix} \bar{i}_1 \\ \bar{j}_1 \\ \bar{k}_1 \end{pmatrix} \tag{8}$$

$\bar{S}_{EC}$ is a unit vector from the center of the earth to the spacecraft. Since angle f is a function of time, the orientation of the vector $\bar{S}_{EC}$ is also a function of time.

Figure 9 shows the geometry for elliptical orbit motion. The relationships for Figure 9 have been derived[1] and can be summarized as follows:

$$M = \sqrt{\frac{\mu}{a^3}}\, t$$

where μ = earth gravitational constant

$$= 39.8 \times 10^4 \frac{(\text{km})^3}{(\text{sec})^2}$$

$$E - \frac{c}{a} \sin E = M$$

$$D_{EC} = a\left(1 - \frac{c}{a} \cos E\right)$$

$$\tan \frac{f}{2} = \sqrt{\frac{1 + c/a}{1 - c/a}} \tan \frac{E}{2}$$

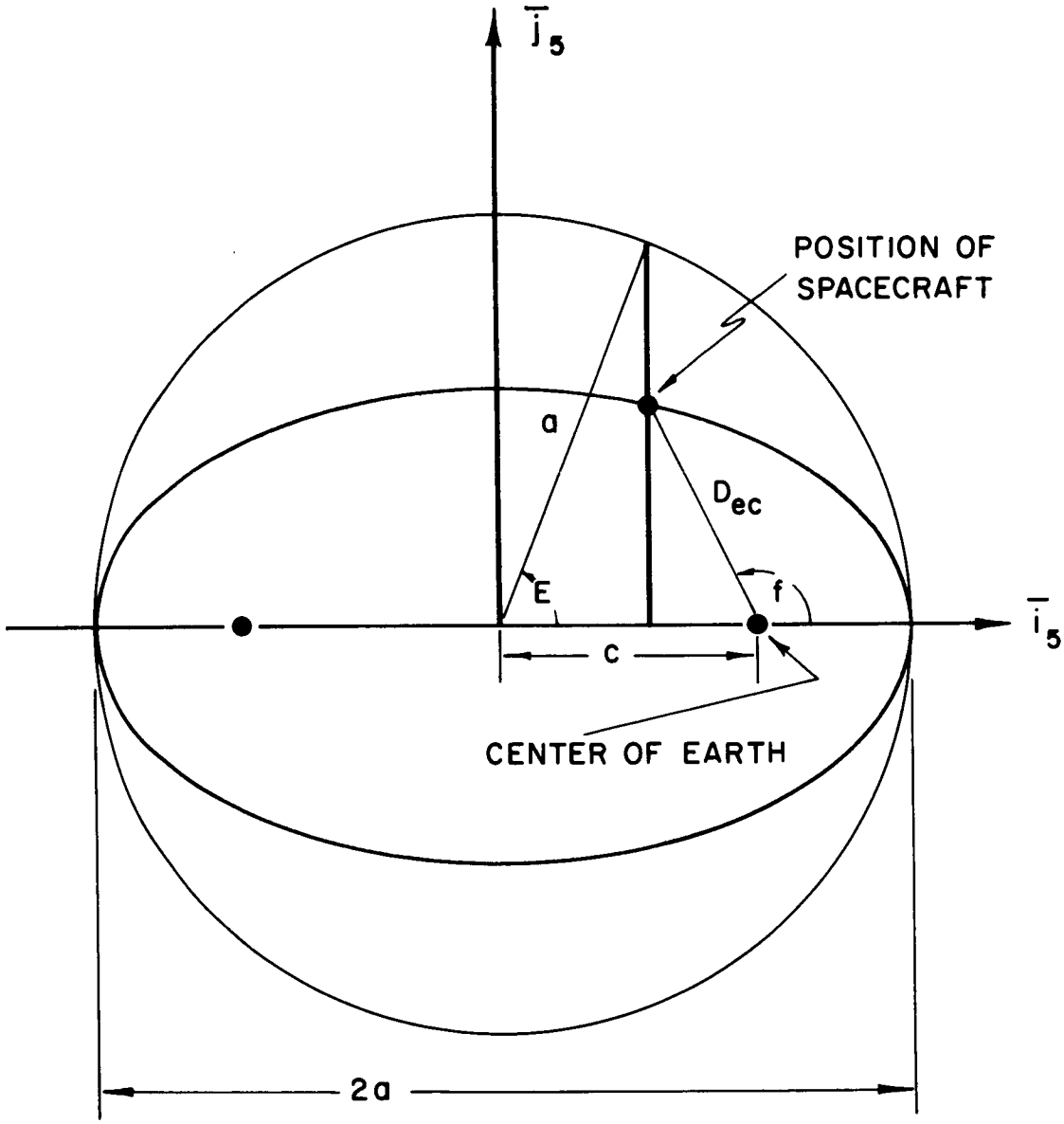

Figure 9: Orbital Anomalies for Elliptic Motion

At $t = 0$, $M = 0$, and $E = 0$ so $\bar{S}_{EC}$ coincides with $\bar{i}_5$.

Figure 10 shows the vector geometry for the sun position. The sun's position with respect to the celestial sphere is given by an ephemeris which specifies the right ascension, α, and declination, δ. From Figure 10 the unit vector from the center of the earth to the sun is given by

$$\bar{S}_u = \cos \delta_s \cos \alpha_s \bar{i}_1 + \cos \delta_s \sin \alpha_s \bar{j}_1 + \sin \delta_s \bar{k}_1 \qquad (9)$$

Figure 11 shows the angle of parallax subtended by the earth from the spacecraft. Figure 12 shows the nominal orbital dimensions for the IMP vehicle.

Now that the positions of the sun, earth, and spacecraft have been described, it is possible to continue the development of the computer program to compute the amount of time per year that the sun and the earth's limb are greater than 90 degrees from the optical axis. The sun will be considered first.

The sun's position on the celestial sphere is given in the ephemeris by its right ascension, α_s, and declination, δ_s. So any axis pointing on the celestial sphere within 90 degrees of $(\alpha_s + 180^\circ, -\delta_s)$ is always greater than or equal to 90 degrees to a vector pointed at the sun. Hence, whenever the optical axis points within 90 degrees of $(\alpha_s + 180^\circ, -\delta_s)$, no portion of the sun shield inner cone is illuminated and locally reflected sun radiation is nonexistant. Figure 13 shows the points where the North Pole and the spin axis intersect the celestial sphere and $(\alpha_s + 180^\circ, -\delta_s)$ denotes the opposite phase position of the sun on the celestial sphere. The angle, A_1, represents the azimuth angle from North to the great circle arc through the sun and the spacecraft which are separated by 90 degrees. It can be shown that A_1 can be determined from,[2]

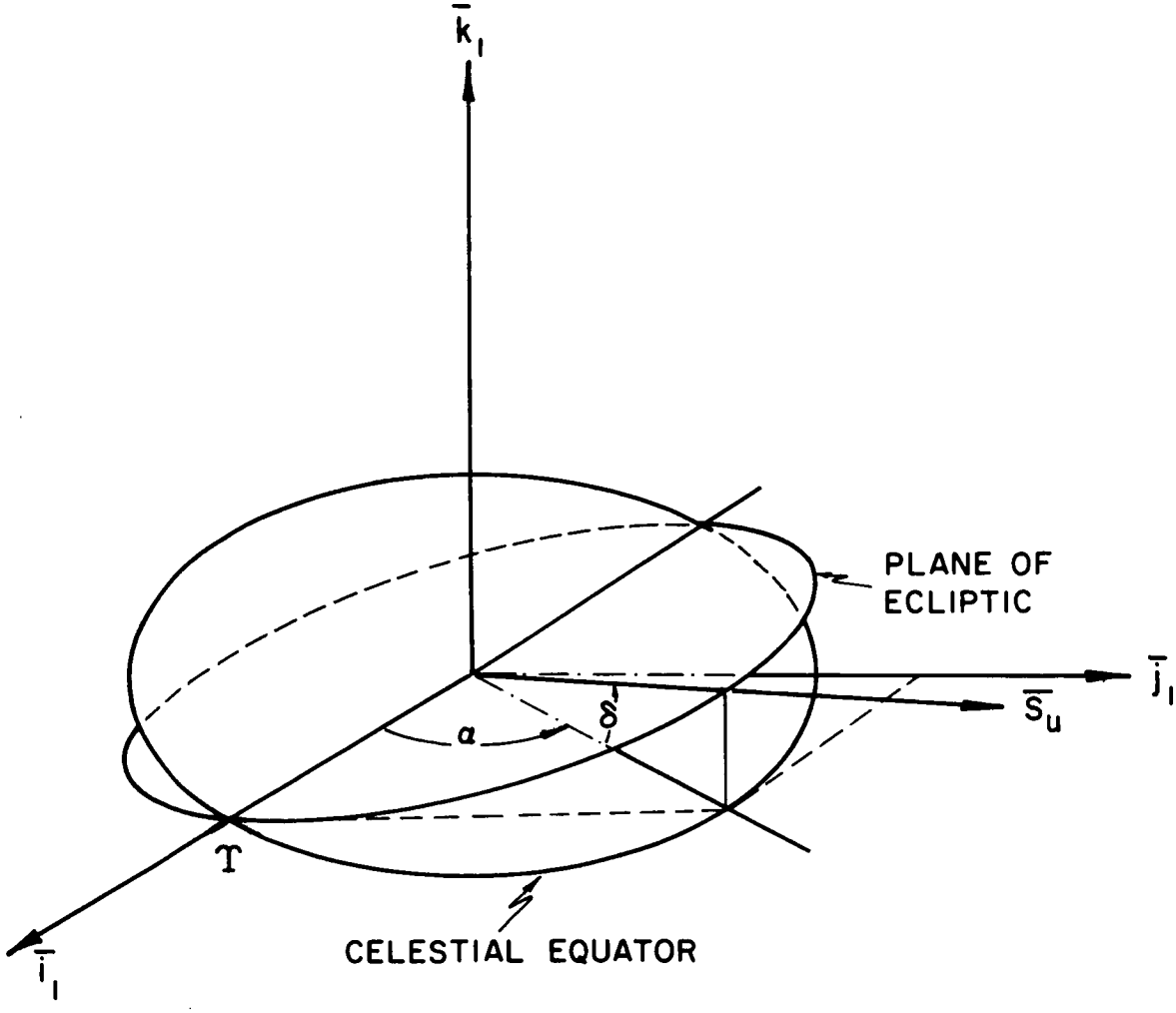

Figure 10: Vector Geometry for Sun Position

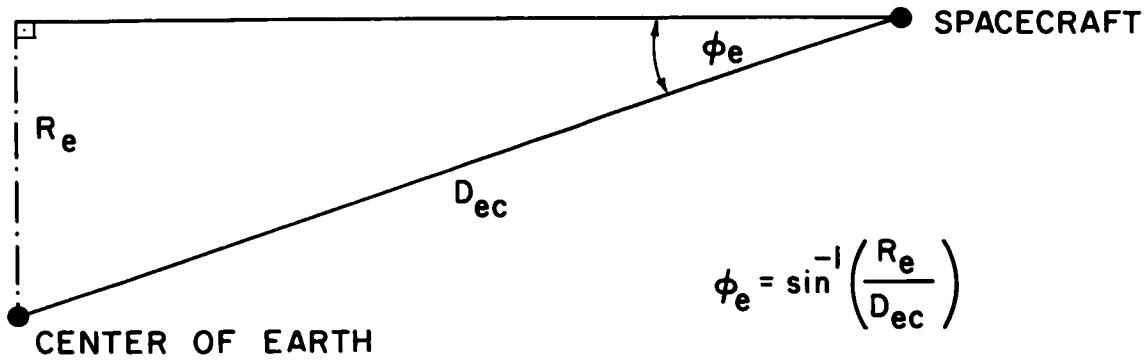

Figure 11: Angle of Parallax for Spacecraft and Earth, ϕ_e

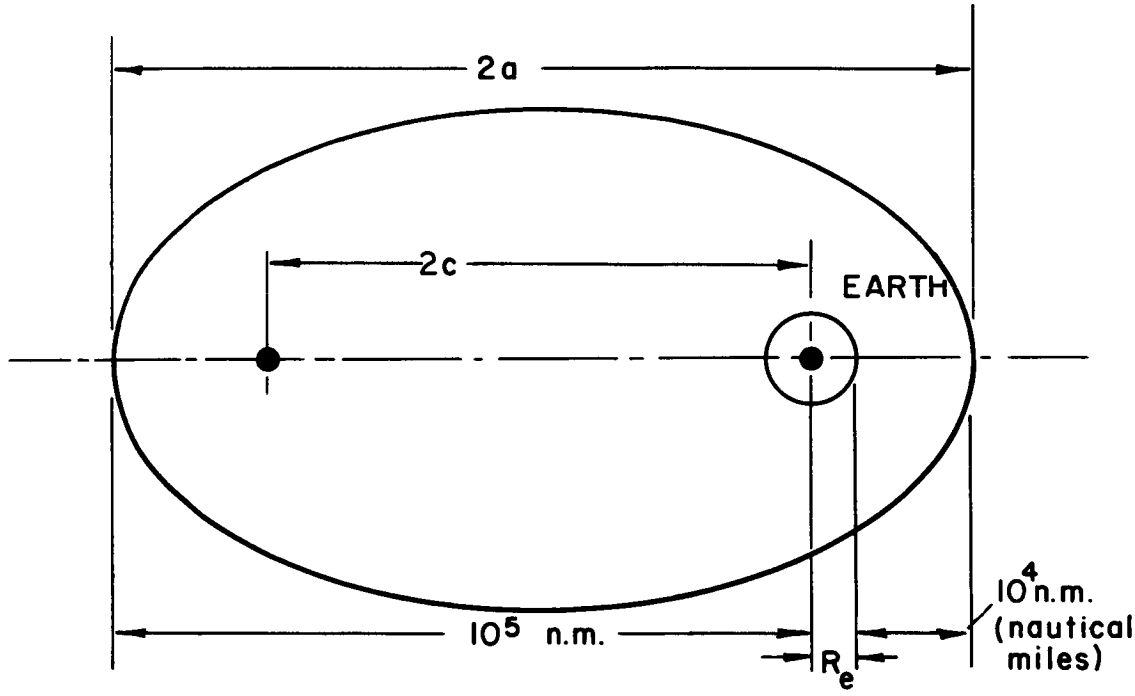

Figure 12: Dimensions of Eliptical Orbit for IMP

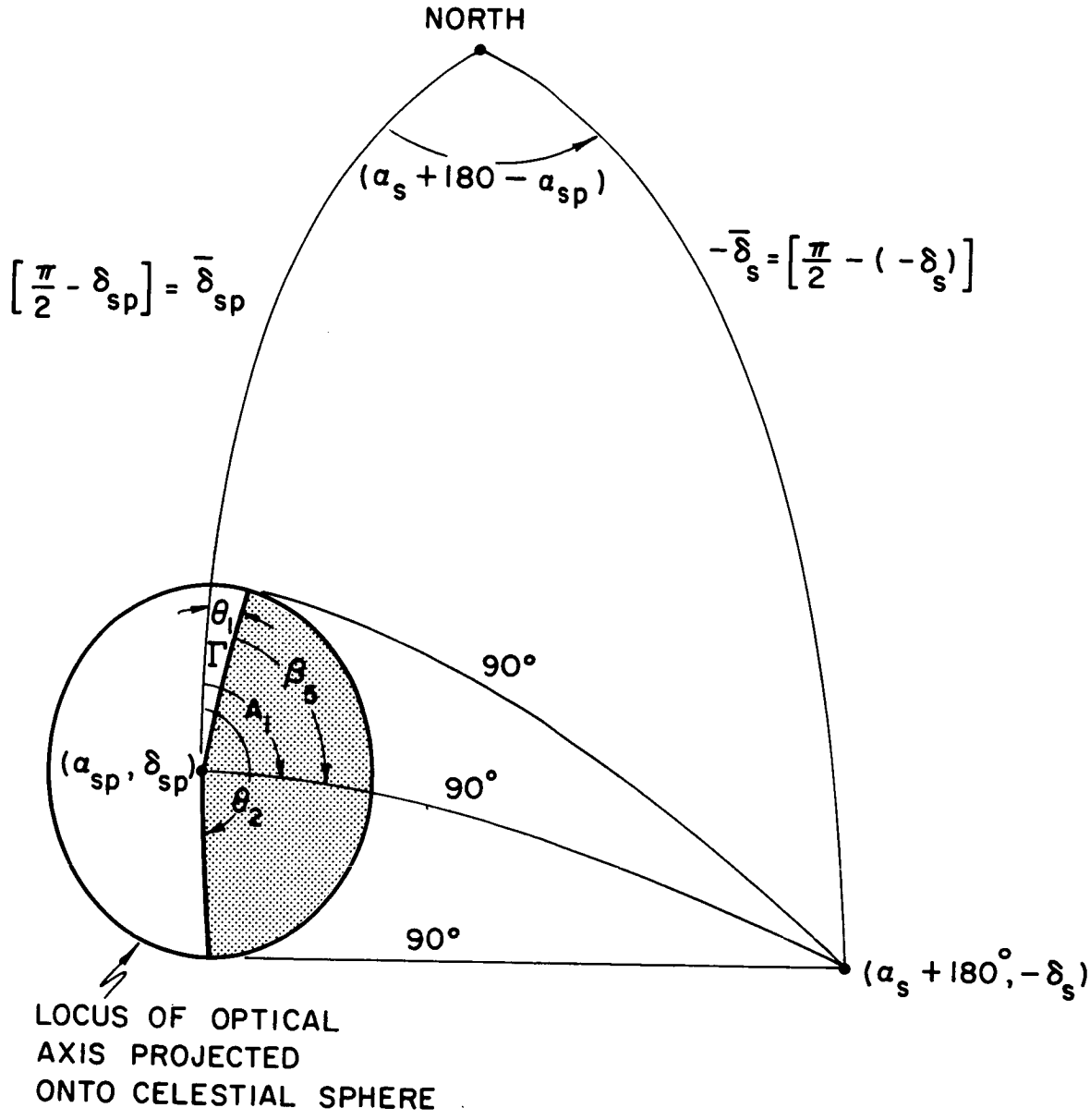

Figure 13: Region on Celestial Sphere for Which the Optical Axis is 90° or More From the Sun

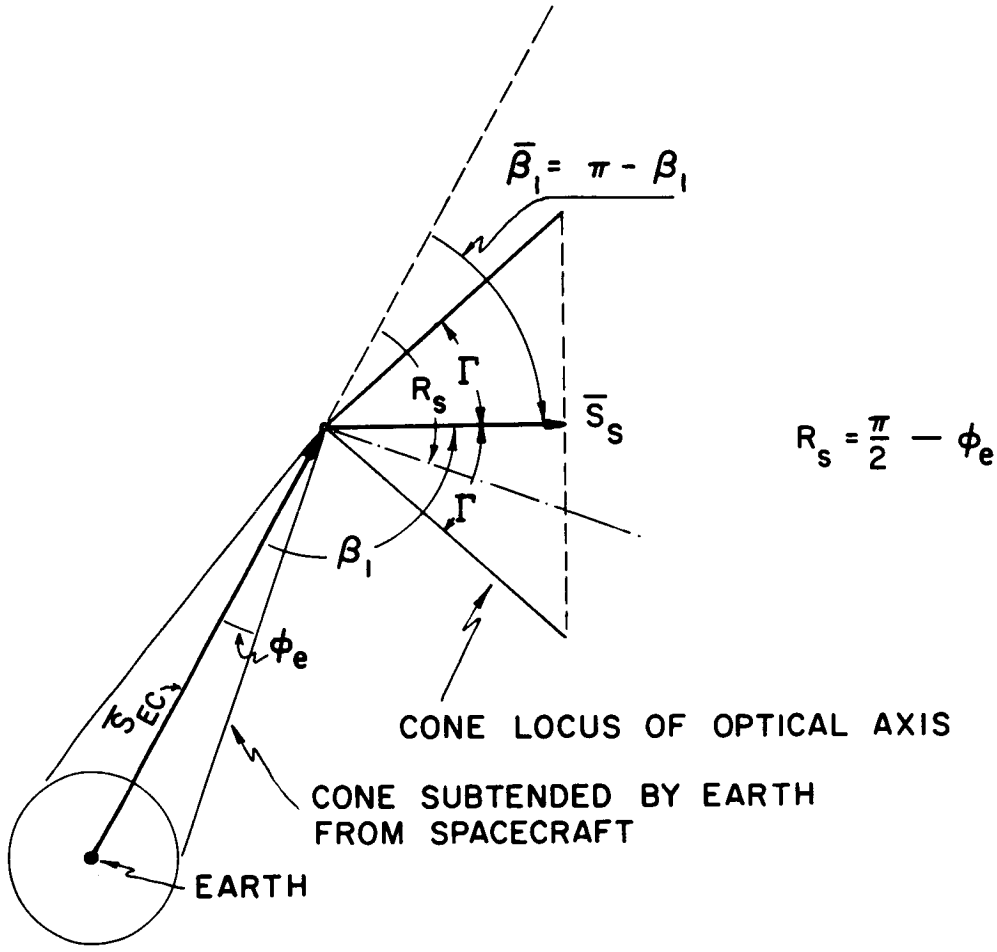

Figure 14: Vector Geometry Relating Spacecraft, Spin Axis, Optical Axis, and Earth

$$\tan A_1 = \frac{\sin(\alpha_s + 180 - \alpha_{sp}) \cos(-\delta_s)}{\sin(-\delta_s) \cos(\delta_{sp}) - \cos(-\delta_s) \sin(\delta_{sp}) \cos(\alpha_s + 180 - \alpha_{sp})}$$

where

α_s = right ascension of the sun,
δ_s = declination of the sun,
α_{sp} = right ascension of the spin axis,
δ_{sp} = declination of the spin axis.

Also, angle β_5 can be expressed as

$$\beta_5 = \cos^{-1}\left\{\frac{\cos 90 - \cos \Gamma \cos 90^o}{\sin \Gamma \sin 90^o}\right\} = 90^o.$$

So, the azimuth angles measured from North at $(\alpha_{sp}, \delta_{sp})$ which denote the boundaries of the scan region such that the optical axis is greater than or equal to 90 degrees from the sun are given by,

$$\theta_1 = A_1 - \beta_5$$

$$\theta_2 = A_1 + \beta_5.$$

The shaded region in Figure 13 represents the portion of the scan region for which the optical axis is greater than or equal to 90 degrees from the sun-spacecraft vector.

Similarly, Figure 14 illustrates the vector geometry relating the spacecraft spin axis, optical axis, and earth. Whenever the optical axis is interior to a cone whose axis is $\overline{S}_{EC}$ and whose half-vertex angle is $R_s = \pi/2 - \phi_e$, then the optical axis is greater than 90 degrees from the earth's limb. The shaded region in Figure 15 shows the portion of the scan region projected on the celestial sphere where the optical axis is 90 degrees or more from the earth's limb. From Figure 15 it can be shown that

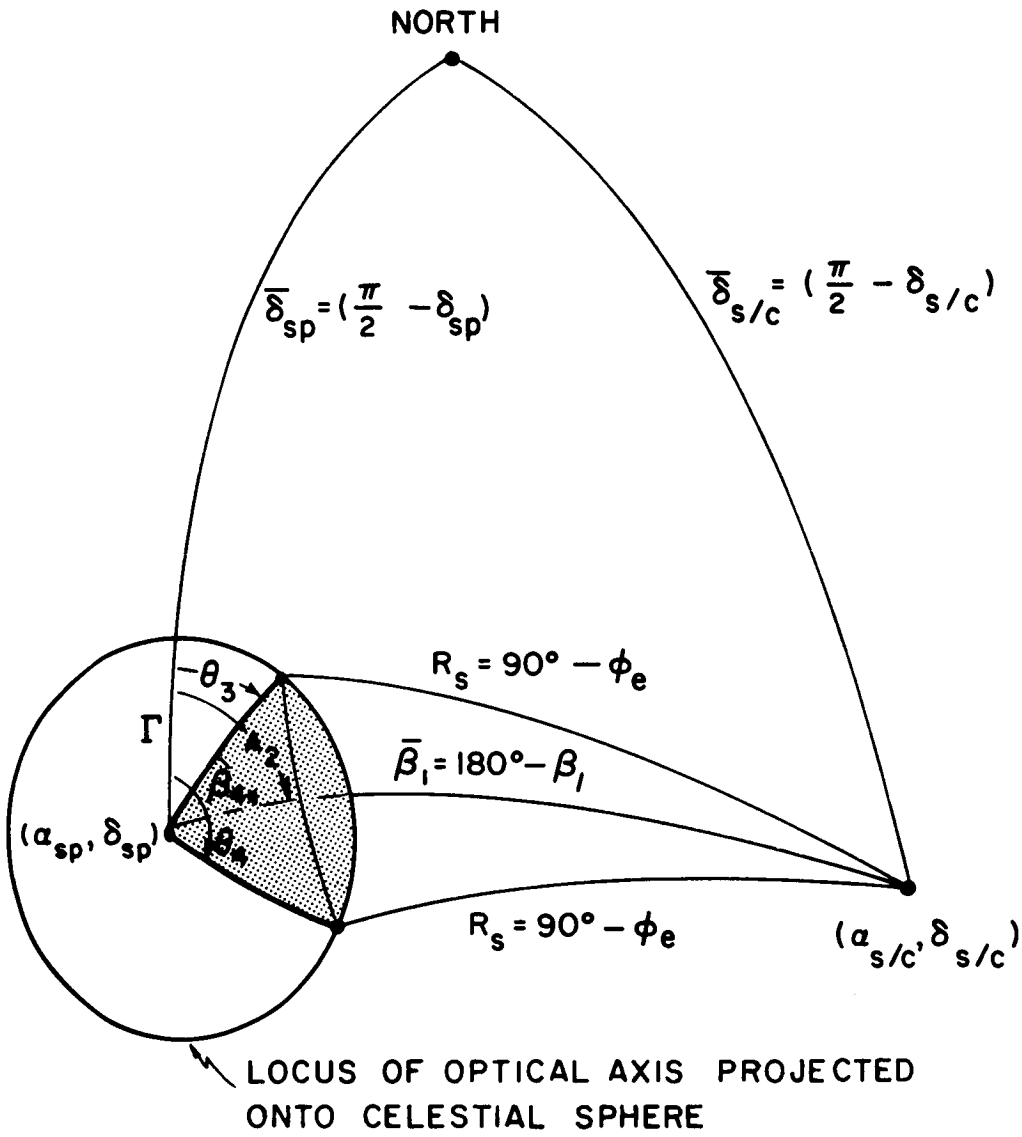

Figure 15: Region on Celestial Sphere for Which the Optical Axis is 90° or More from Earth's Limb

$$\tan A_2 = \frac{\sin(\alpha_{sc} - \alpha_{sp}) \cos \delta_{sc}}{\sin \delta_{sc} \cos \delta_{sp} - \cos \delta_{sc} \sin \delta_{sp} \cos(\alpha_{sc} - \alpha_{sp})}$$

and

$$\cos \beta_4 = \frac{\cos R_s - \cos \Gamma \cos \bar{\beta}_1}{\sin \Gamma \sin \bar{\beta}_1}$$

Hence, the azimuth angles measured from North at $(\alpha_{sp}, \delta_{sp})$ which denote the boundaries of the scan region such that the optical axis is 90 degrees or more from the earth's limb are given by,

$$\theta_3 = A_2 - \beta_4$$

$$\theta_4 = A_2 + \beta_4.$$

The intersection of the acceptable region determined by the sun restriction with the acceptable region determined by the earth restriction determines the acceptable region. The acceptable region may be readily determined by ordering of the azimuth angles θ_1, θ_2, θ_3, and θ_4 from North reference. This is illustrated in Figure 16 on the celestial sphere where the region from θ_1 to θ_2 defines the acceptable region based on the sun restriction and the region from θ_3 to θ_4 defines the acceptable region based on the earth restriction. Hence, for the figure shown, θ_1 to θ_4 denotes the scan region in which <u>both</u> the sun <u>and</u> the earth's limb are 90 degrees or more from the optical axis.

All the important steps have now been described to compute the amount of time the earth's limb is greater than 90 degrees to the optical axis for a one year interval. The sun ephemeris for 1967 was used as a program input and calculations were made at each four hour interval. The IMP orbital period was determined as approximately 96 hours. The program for the nominal

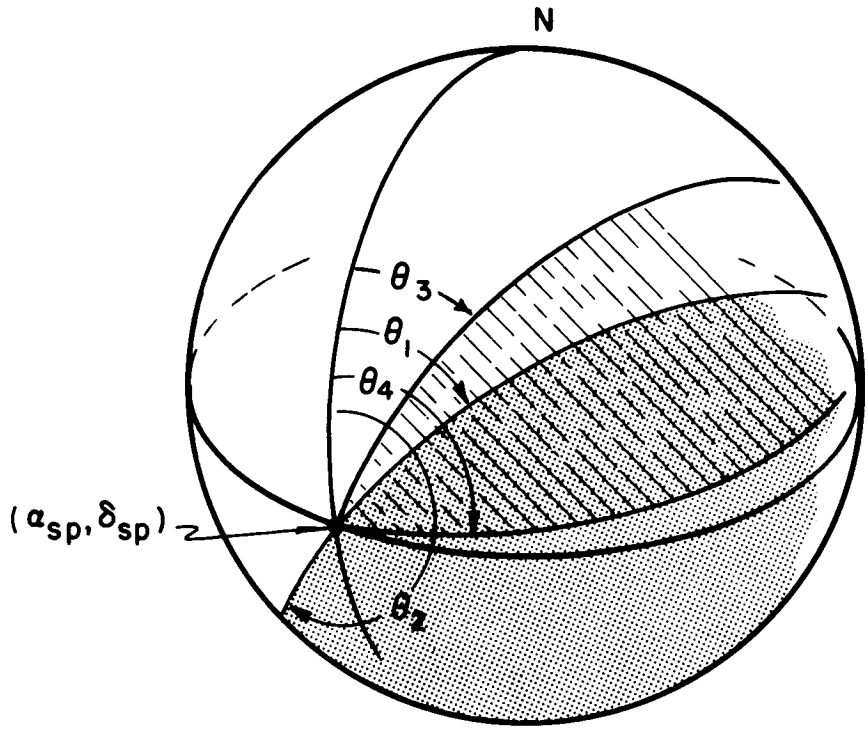

Figure 16: Overlapping Region of Scan in Which Optical Axis is 90° or More from Satellite-Sun Vector and Earth's Limb

IMP orbit (ascending node longitude = $\Omega = 197^{\circ}$, and perigee argument = $\omega = 133^{\circ}$) was run for the two cant angles,

$$\Gamma = 16^{\circ}$$

$$\Gamma = 25^{\circ}.$$

In both cases the spin axis was inclined by $\psi = 0^{\circ}$ to the ecliptic plane. Both runs required a total of one hour computing time on the 160-G. The results showed that for $\Gamma = 16^{\circ}$, both the sun and earth's limb are 90 degrees or more from the optical axis for 24.74 percent of the year while for $\Gamma = 25^{\circ}$, the percentage is 24.92 percent. It should be noted that because of the sun restriction, only one-half of each scan period is ever acceptable, so the maximum expected percentage is 50 percent if the proximity of the earth is not considered. Since the difference in percentages is small for these two cant angles, it was concluded that the percentage of acceptable scanning time was essentially independent of the cant angle.

Figure 17 shows a plot of the acceptable portion of the scan period versus time for an orbital period with the spin axis inclined at an angle $\psi = 0^{\circ}$ with respect to the ecliptic plane. This plot represents the worst condition and shows that one-half of the scan period is available for approximately four hours of each orbit. During the remainder of the orbit, either the sun or the earth's limb is closer than 90 degrees to the optical axis. Figure 18 shows a similar plot which represents the best condition. For this case, one-half the scan period is available for approximately 76 hours of each orbit.

Similarly, Figures 19 and 20 show best condition and worst condition plots, respectively, for a spin axis inclined at $\psi = 45^{\circ}$ with respect to the ecliptic plane.

Because the acceptable scanning time is virtually independent of the

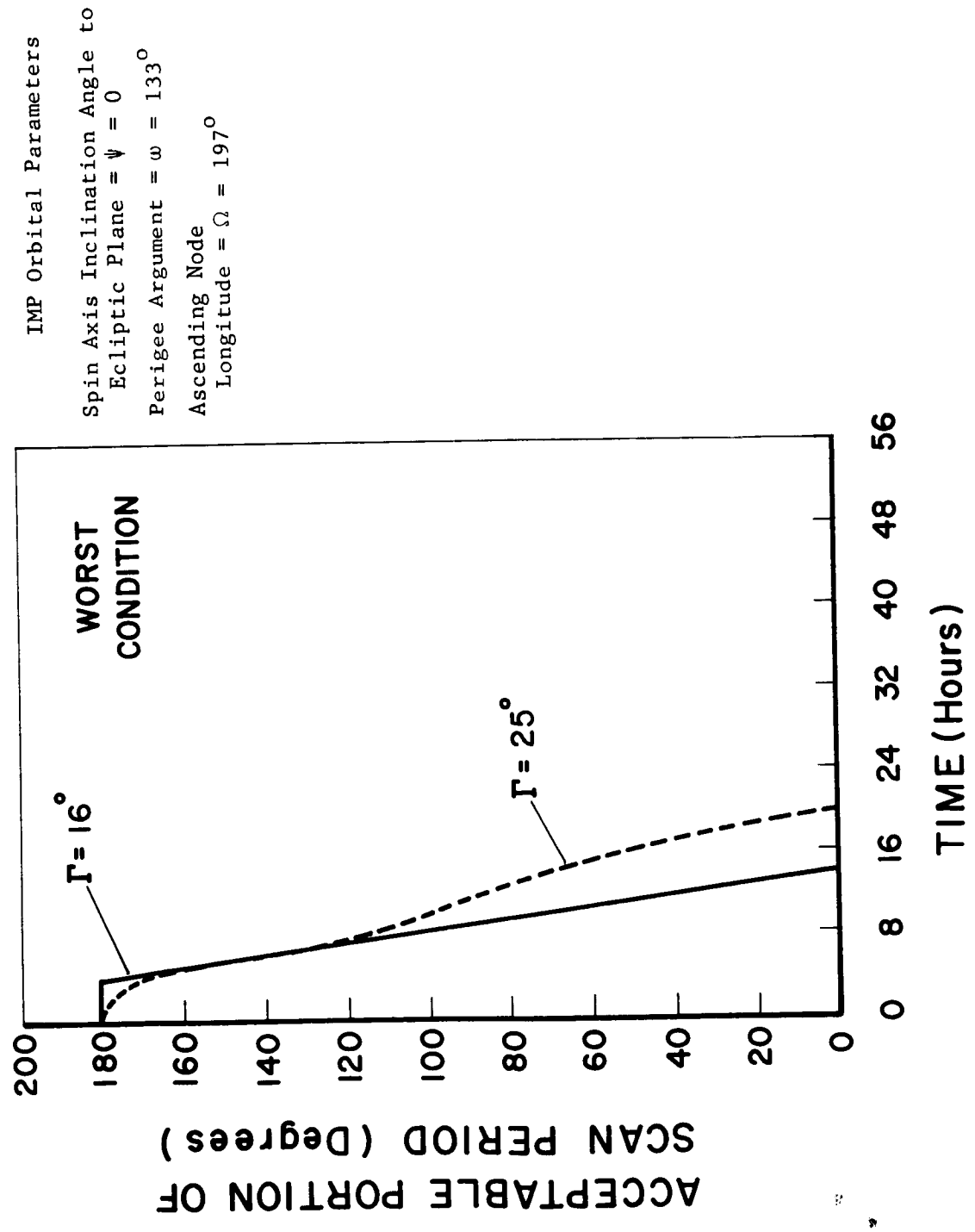

Figure 17: Acceptable Portion of Scan Period Versus Time for One Orbit

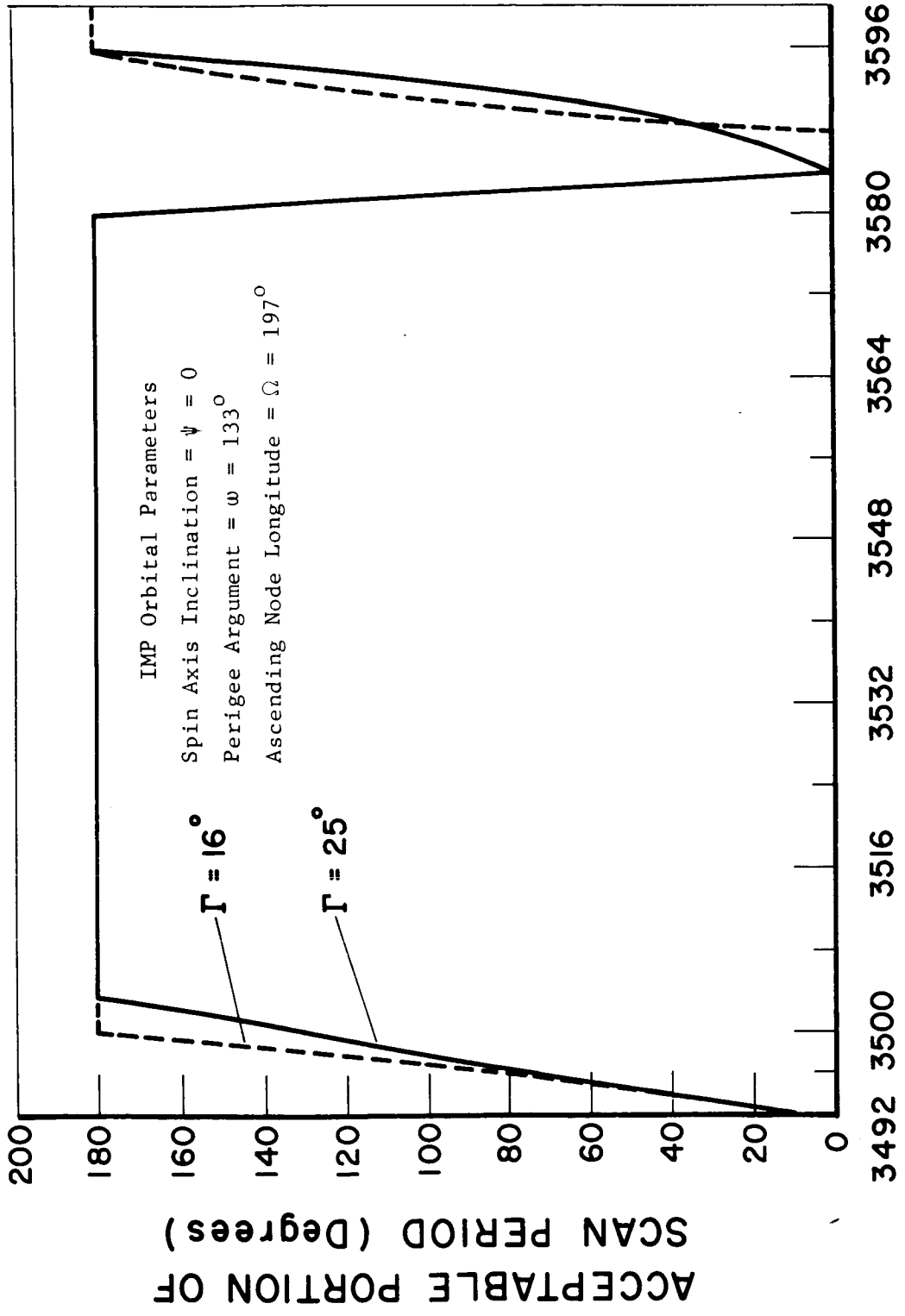

Figure 18: Acceptable Portion of Scan Period Versus Time for One Orbit

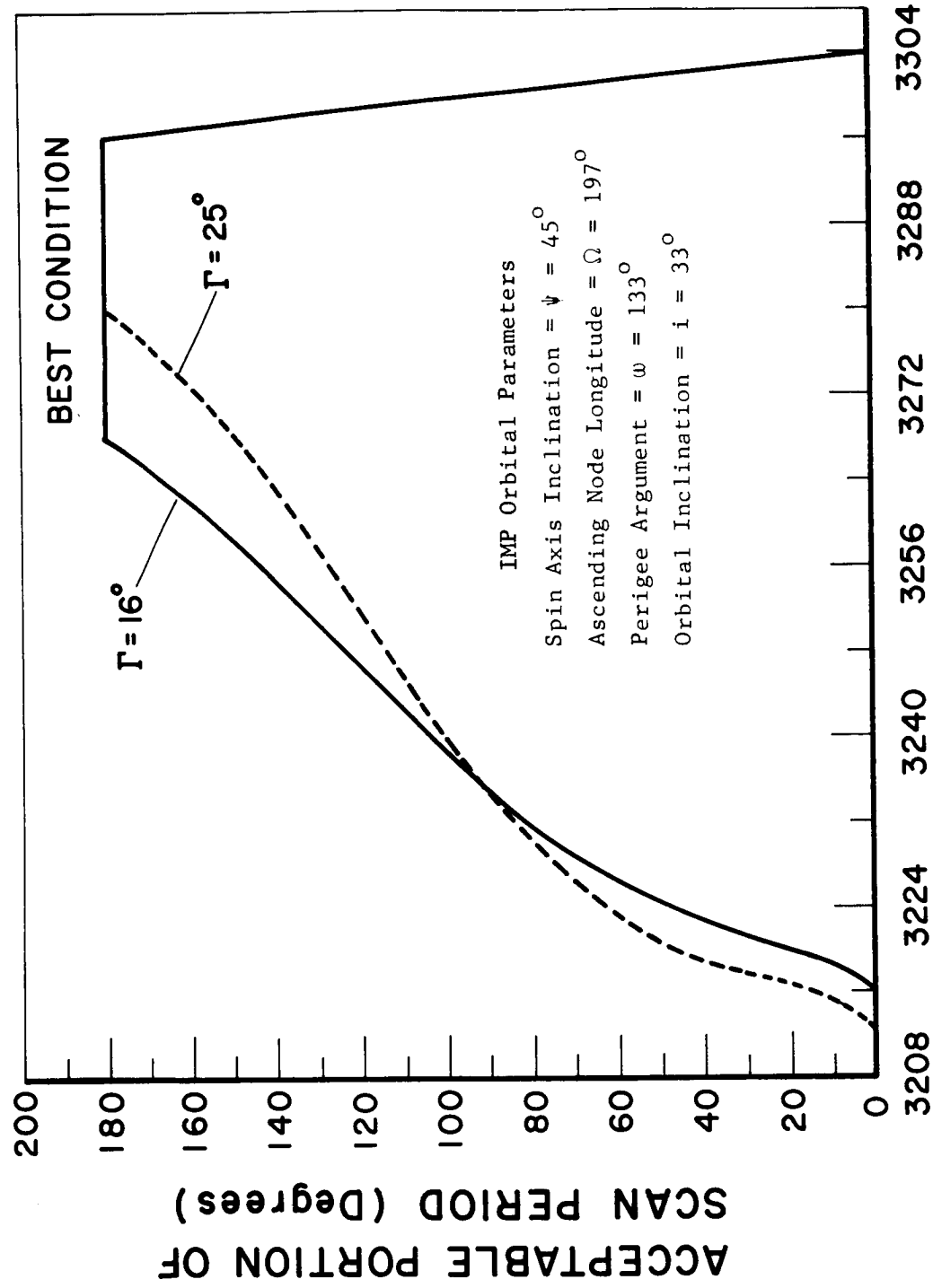

Figure 19: Acceptable Portion of Scan Period Versus Time for One Orbit

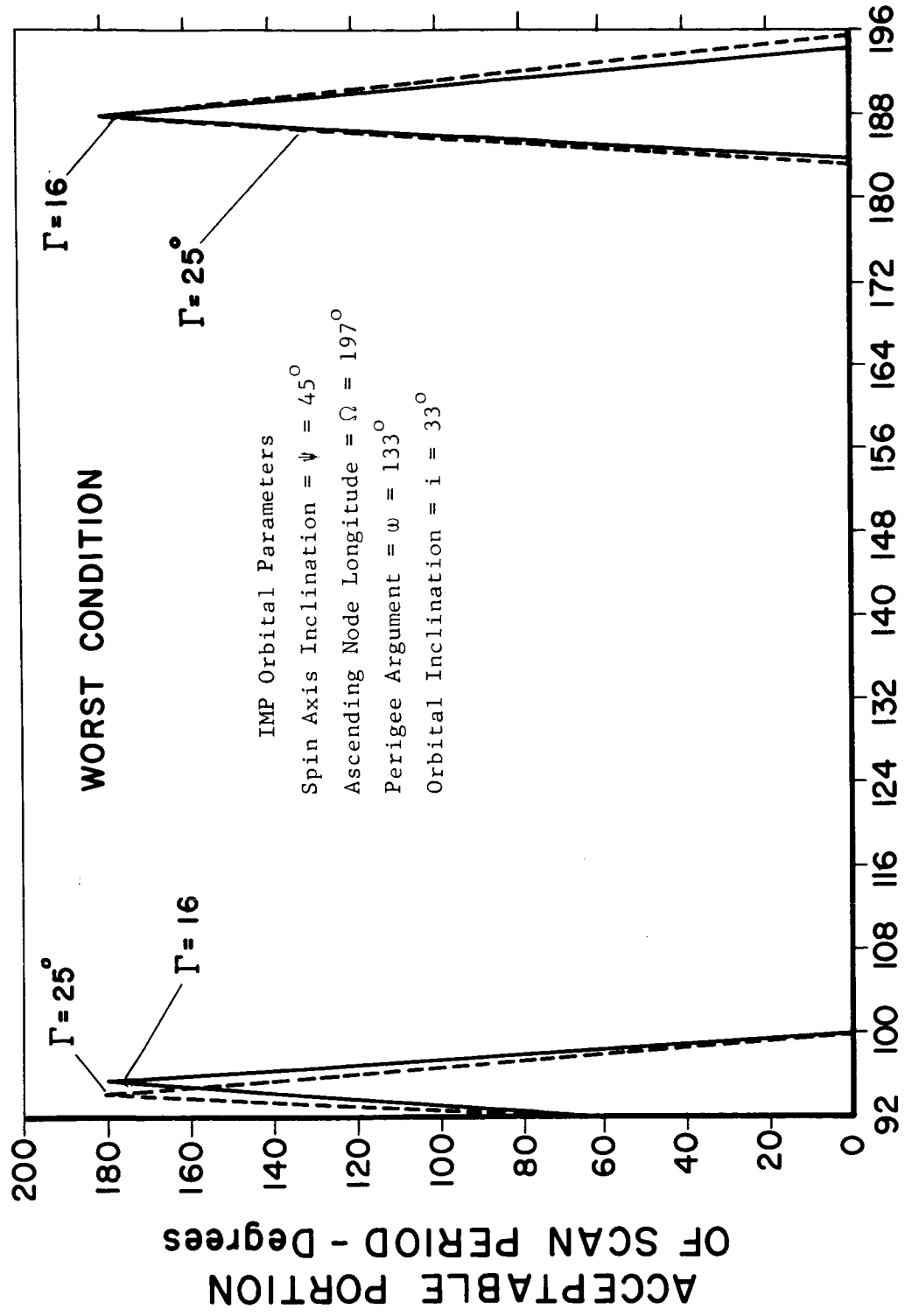

Figure 20: Acceptable Portion of Scan Period Versus Time for One Orbit

cant angle, then the cant angle should be as large as possible so that the required optical field of view is a minimum. Since the cant angle is restricted to be 25 degrees or less, then the preferred cant angle must be determined as 25 degrees.

The analysis of this section may be extended to determine the frequency with which the earth and moon may appear in the field of view. This is of interest since the high voltage to the photomultiplier must be turned OFF whenever the earth or moon enters the field of view in order to prevent cathode degradation. The proximity of the earth or moon to the field of view can be, respectively, determined from the angle, θ_{SE}, between the vehicle spin axis and the earth's limb and the angle, θ_{SM}, between the spin axis and the moon's limb.

Figure 21 shows the angle, θ_{SE}, from the spin axis to a line tangent to the earth. From the dot product of two unit vectors,

$$\theta_{SE} = \cos^{-1}\left\{-\bar{S}_s \cdot \bar{S}_{EC}\right\} - \sin^{-1}\left(\frac{R_e}{D_{ec}}\right) .$$

The unit vector from the center of the earth to the moon is given by

$$\bar{S}_m = \cos\delta_m \cos\alpha_m \bar{i}_1 + \sin\alpha_m \cos\delta_m \bar{j}_1 + \sin\delta_m \bar{k}_1 .$$

Similarly, the angle from the spacecraft spin axis to a line tangent to the moon is

$$\theta_{sm} = \cos^{-1}\left\{\frac{\bar{S}_s \cdot \bar{S}_{cm}}{|\bar{S}_{cm}|}\right\} - \underbrace{\sin^{-1}\left(\frac{R_m}{D_{cm}}\right)}_{\phi_m}$$

$$D_{em} = \frac{R_e}{\sin \phi_m}$$

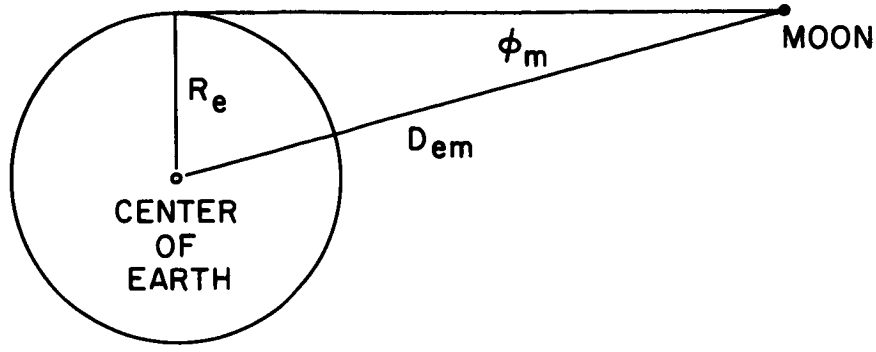

(a)

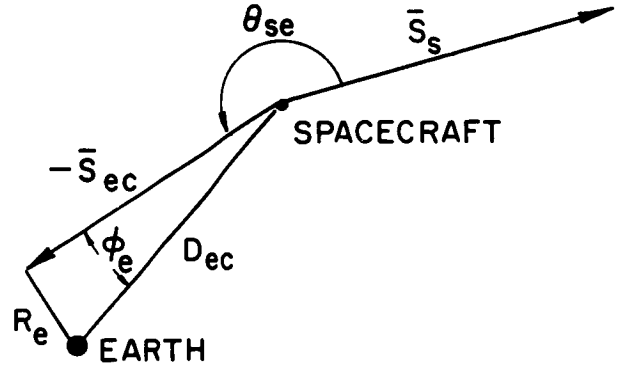

(b)

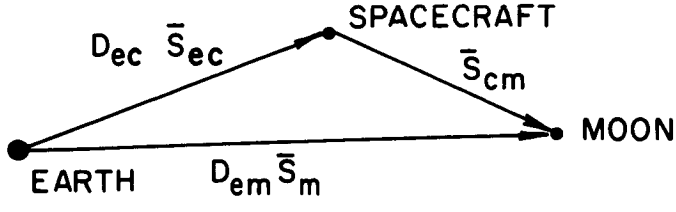

(c)

$$\bar{S}_{cm} = D_{em}\bar{S}_m - D_{ec}\ \bar{S}_{ec}$$

Figure 21 : (a) Angle of Parallax for Earth and Moon, ϕ_m
(b) Angle from Spin Axis to Line Tangent to Earth, θ_{SE}
(c) Vector from Spacecraft to Moon, $\bar{S}_{cm}$

where $\bar{S}_s$ is a unit vector in direction of spin axis

$$\bar{S}_{cm} = D_{em}\,\bar{S}_m - D_{ec}\,\bar{S}_{EC}$$

R_m = radius of the moon

$D_{cm} = |\bar{S}_{cm}|$ = distance from spacecraft to the moon.

Figure 21 shows $D_{em} = R_e/\sin \phi_m$ = distance from Earth to moon where

R_e = radius of Earth

ϕ_m = angle of parallax between between the earth and moon given in the ephemeris.

Usually ϕ_m is small and may be neglected.

A computer program has been written to evaluate θ_{sm} and θ_{SE}. Portions of these results have been plotted for the 1967 ephemeris and several values of the angle ψ.

Figure 22 shows a plot of the region about the minimum angular separaration from the spin axis to the moon and Figure 23 shows a similar plot for the angle from the spin axis to the edge of the earth. For both cases the IMP spin axis is assumed inclined 90° to the ecliptic plane and perpendicular to the sun line. Also, the orbit ascending node longitude $= \Omega = 197^\circ$, argument of perigee = 133° and the orbital plane is inclined 33° to the equatorial plane.

Figure 22 shows that the moon never gets into the field of view for a spin axis inclined 90° to the ecliptic. However, Figure 23 shows the earth does get into the field of view during part of each scan period for approximately 12 hours of the 96 hour orbit.

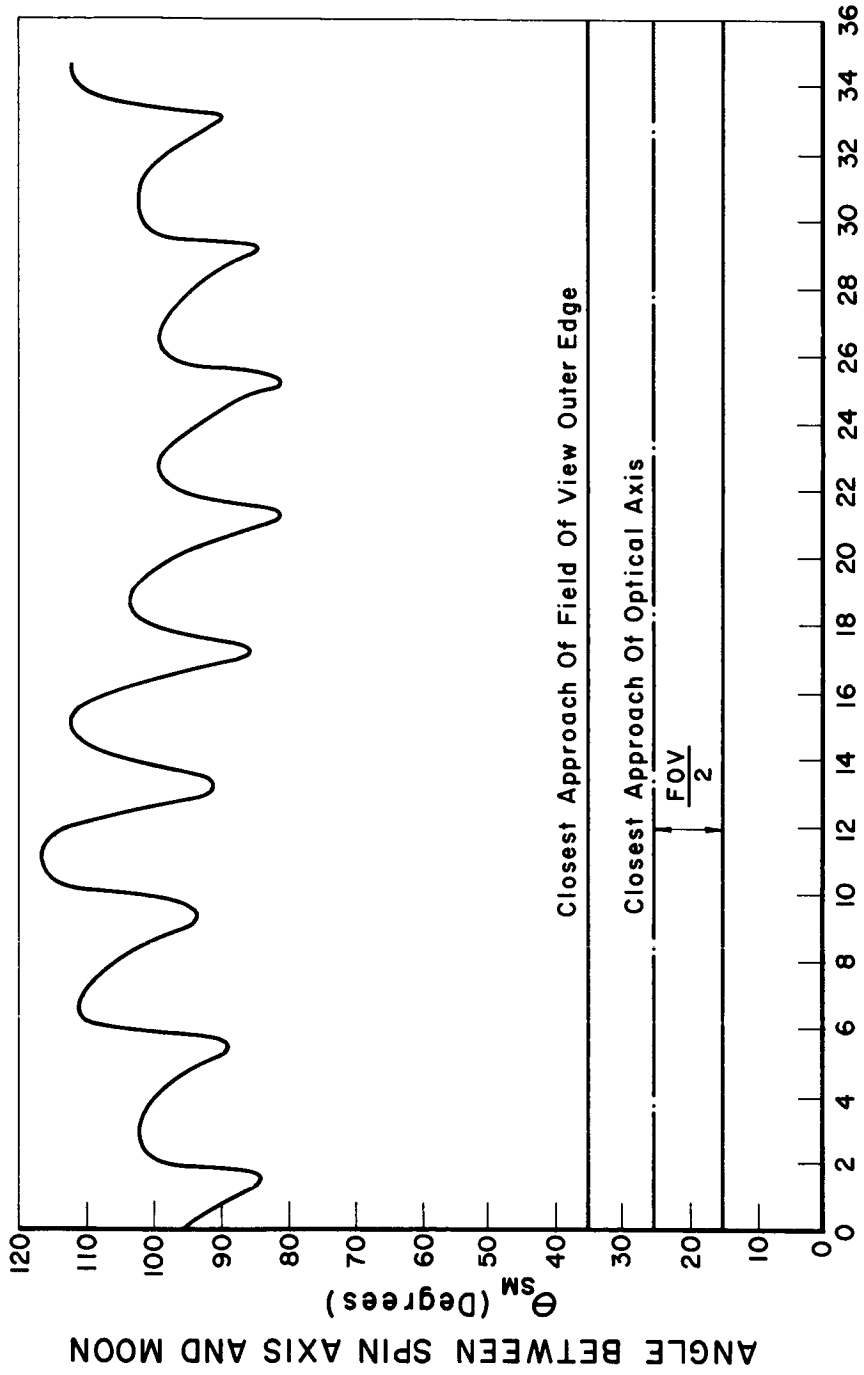

Figure 22: Angle Between the Spin Axis and the Moon for Longitude of the Ascending Node = 197°; Inclination of the Spin Axis to the Ecliptic = 90°; Argument of Perigee = 133°; Orbital Inclination = 33°

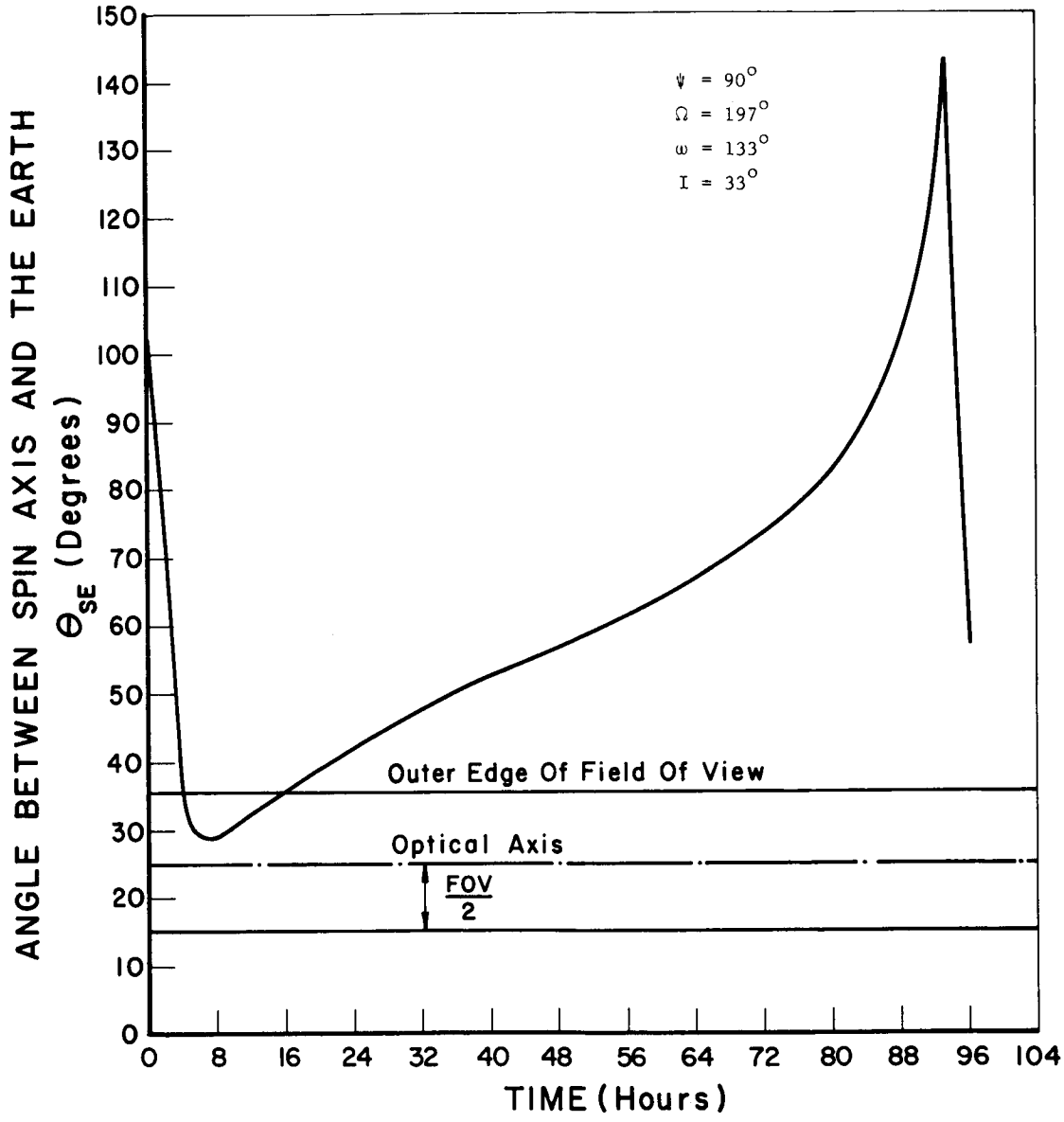

Figure 23: Angle Between the Spin Axis and the Earth for Ascending Node Longitude = 197°; Spin Axis Inclination = 90°; Argument of Perigee = 133°; Orbital Inclination = 33°

θ_{sm} and θ_{SE} are plotted in Figures 24 and 25, respectively, for the same orbital parameters as above except $\Omega = 0^{o}$. Figure 24 shows that the moon will be within the field of view during part of each scan period for approximately eight days out of each 28 days. Figure 25 shows the earth appears in the field of view for approximately four hours of each 96 hour orbit.

Figures 26 and 27 show plots of θ_{sm} and θ_{SE}, respectively, for the same parameter as Figures 24 and 25, except the spin axis is inclined $\psi = 90^{o}$ to the ecliptic plane. In either case, neither the moon nor the earth gets into the field of view.

By comparing Figures 22 through 27, it can be concluded that the SCADS system prefers the IMP spin axis be inclined 90^{o} to the ecliptic plane.

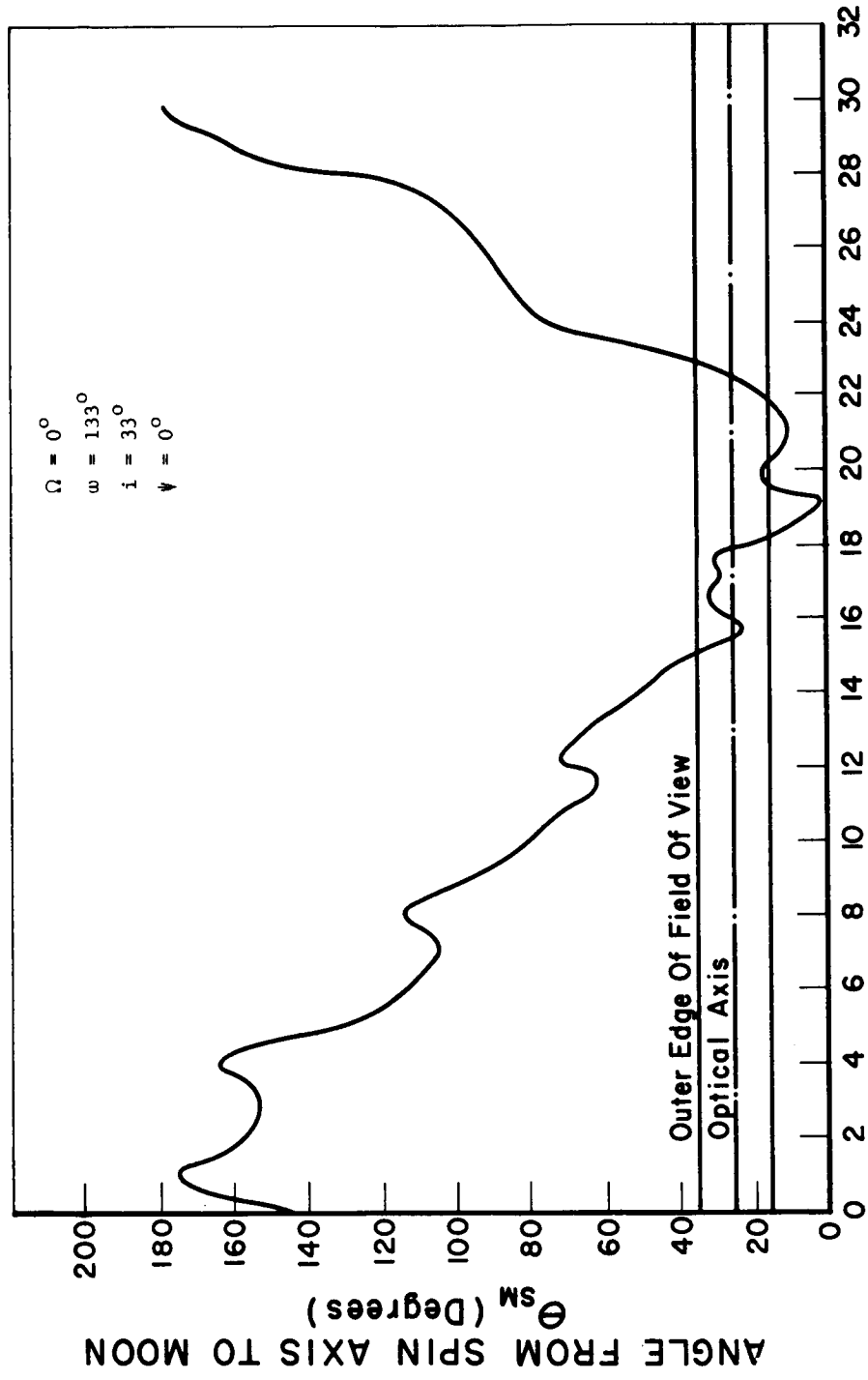

Figure 24: Angle Between Spin Axis and the Moon for Ascending Node Longitude = 0^{o}; Spin Axis Inclination = 0^{o}; Argument of Perigee = 133^{o}; Orbital Inclination = 33^{o}

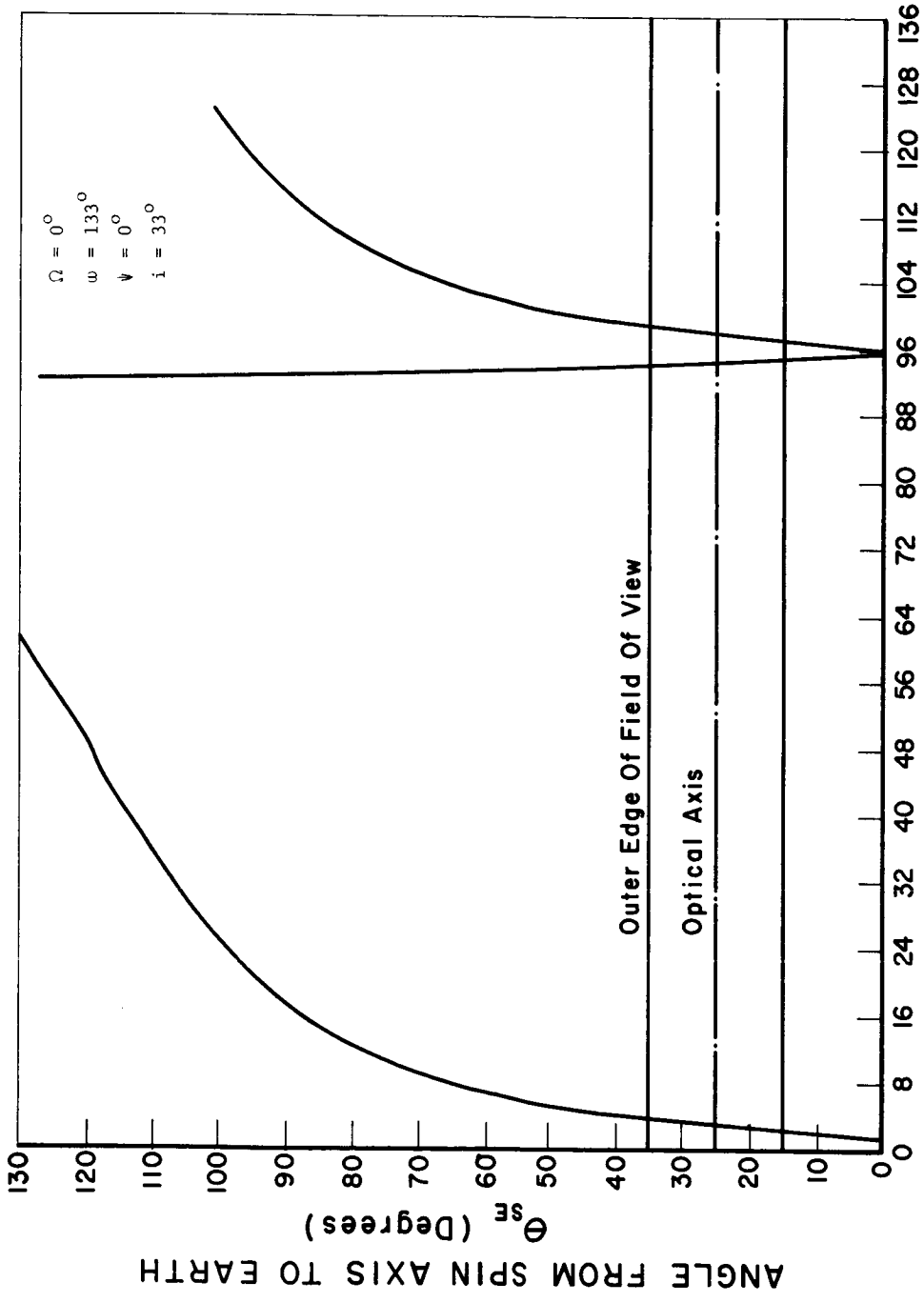

Figure 25: Angle from Spin Axis to Earth for Ascending Node Longitude = 0°; Spin Axis Inclination = 0°; Argument of Perigee = 133°; Orbital Inclination = 33°

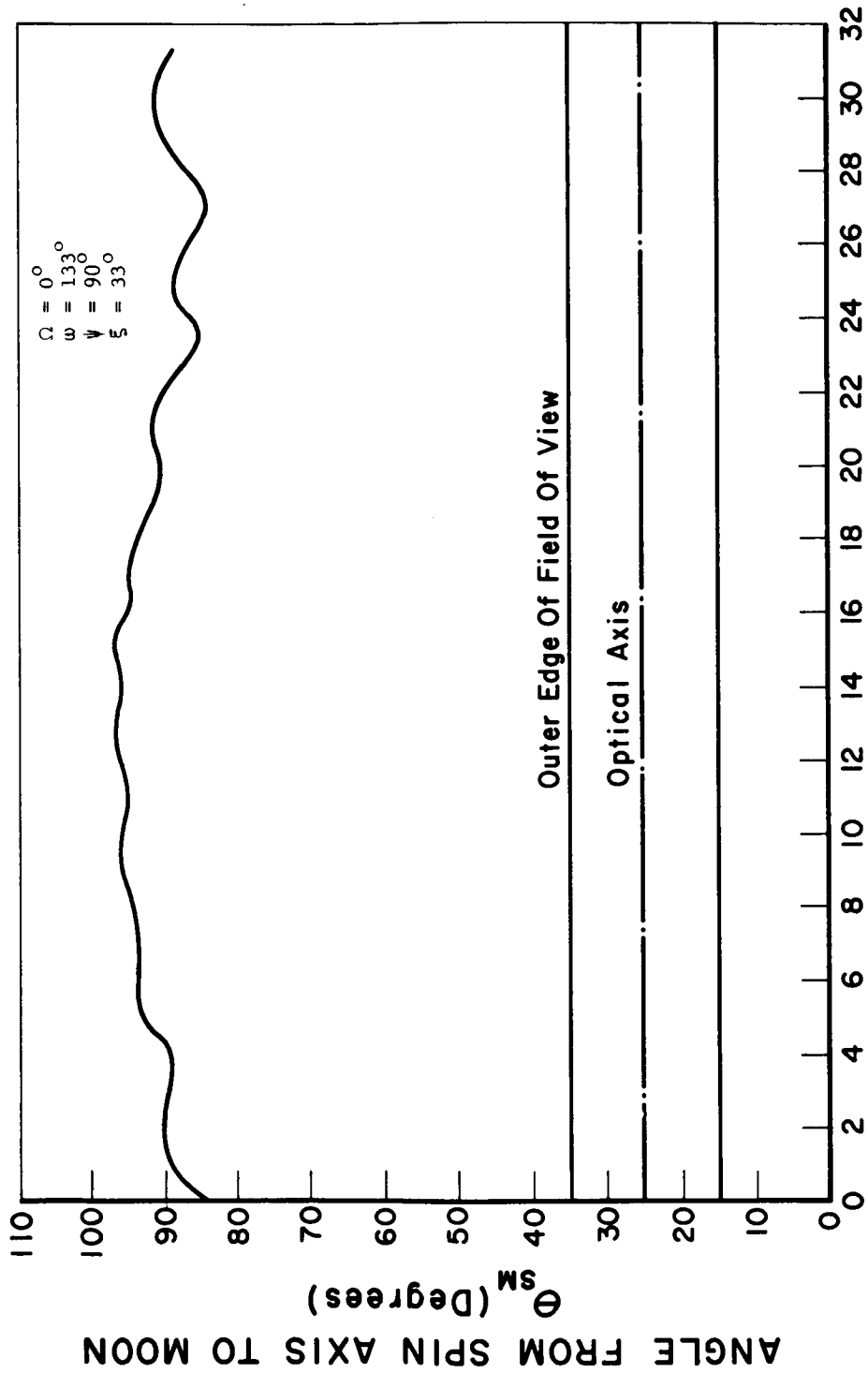

Figure 26: Angle from Spin Axis to Moon for Ascending Node Longitude = 0^{o}; Spin Axis Inclination = 90^{o}; Argument of Perigee = 133^{o}; Orbital Inclination = 33^{o}

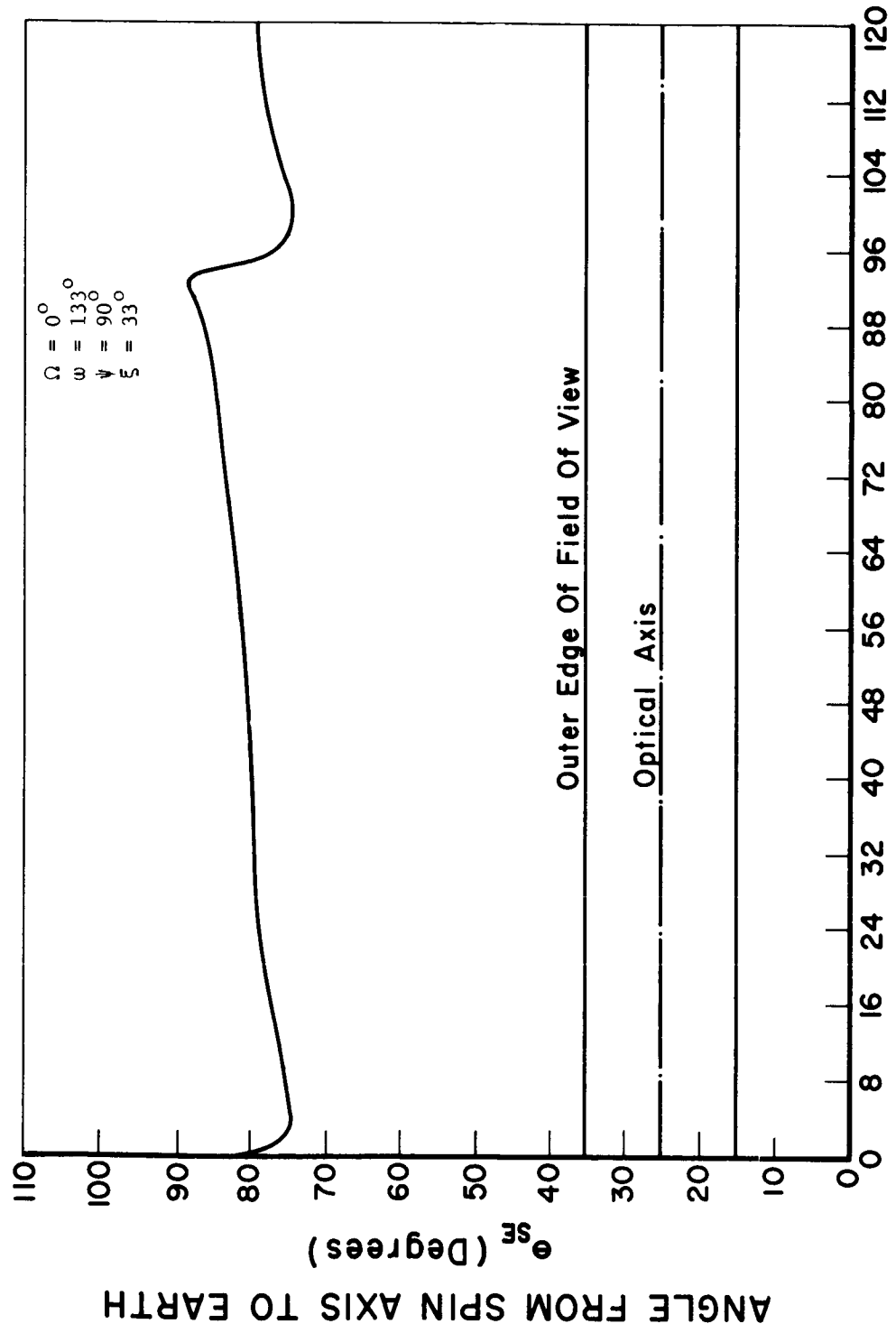

Figure 27 : Angle from Spin Axis to Earth for Ascending Node Longitude = 0^{o}; Spin Axis Inclination = 90^{o}

B. Star Availability Search and Determination of Field of View

In Section III-A, the preferred cant angle was determined to be $\Gamma = 25^{\circ}$. For a given cant angle, it is possible to determine the required optical field of view to detect a given number of stars per scan brighter than a fixed magnitude. This section will determine the field of view required to detect three stars brighter than magnitude $4^{m}.0$.

Detection of stars no dimmer than visual magnitude $4^{m}.0$ limits the number of possible stars in the celestial sphere which must be considered for star identification. There are only 437 stars in the celestial sphere that are visual magnitude $4^{m}.0$ or brighter.

The number of stars required in the field of view to determine the spacecraft attitude with a SCADS sensor depends upon the number of scanning slits. A single radial slit has been selected for the IMP sensor (slit configuration and reticle design is discussed in Section III-F). Hence, three stars brighter than visual magnitude $4^{m}.0$ must be detected per scan period to determine attitude.

Since the ascending node longitude of the IMP orbit can be any angle between 0 and 360° and the spin axis inclination to the ecliptic plane can be any angle between 0 and 90°, any point on the celestial sphere is a potential pointing direction for the spin axis. Hence, the instantaneous area enclosed by the optical system field of view projected on the celestial sphere can potentially be centered about any point on the sphere. For the IMP sensor, the area enclosed on the celestial sphere by the field of view must be sufficiently large to enclose with high probability three stars brighter than magnitude $4^{m}.0$. A computer program has been written to determine the required area enclosed on the celestial sphere in order to include three stars brighter than magnitude m with a given probability.

The computer program positioned the optical axis at 2580 uniformly

spaced points on the celestial sphere. This was achieved by incrementing the declination of the zenith in steps of 4° from -88° to $+88^{\circ}$ declination. The number of right ascensions was determined by

$$N = [90 \cos \delta], \text{ for } -88^{\circ} \leq \delta \leq 88^{\circ}$$

where $[x]$ = greatest integer $\leq x$.

As special cases, the optical axis was centered at $\delta = +90^{\circ}$ and $\delta = -90^{\circ}$.

The program was initialized with the reading in of the star data (right ascension, declination, and magnitude) cards, which were sorted from brightest to dimmest. The star data was obtained from the 789 stars brighter than +4.5 magnitude listed in Atlas Coeli. Then, a declination was fixed, and the right ascension values were computed and fixed.

The zenith angles of all 789 stars were then computed using the relationship,

$$\cos z_i = \sin \tilde{\delta} \sin \delta_i + \cos \tilde{\delta} \cos \delta_i \cos(\tilde{\alpha} - \alpha_i)$$

where

z_i = zenith angle of the i^{th} star
α_i = right ascension of the i^{th} star
δ_i = declination of the i^{th} star
$\tilde{\delta}$ = declination of zenith
$\tilde{\alpha}$ = the right ascension of the zenith.

Next, a magnitude limit was set. The zenith angles of all stars brighter than this limit were ordered from smallest to largest. The first, second, third, and fourth smallest angles then corresponded to one-half the required field of view to see one, two, three, or four stars in the field

of view. The magnitude limit was then lowered in steps of +.5 and the sort repeated. This was done for nine magnitude limits from 0 to +4.0 in steps of .5. Then the right ascension was stepped, and the above procedure repeated.

After all calculations were completed and tabulated, the results were plotted as shown in Figure 28. Figure 28 shows that three or more stars of magnitude +4.0 or brighter were always within a 44° field of view for each of the 2580 pointing directions. Here the field of view was taken to be the entire field with no central dead zone, and the optical axis was coincident with the spin axis. Hence, the area scanned on the celestial sphere by the field of view is given by

$$S_A = 2\pi(1 - \cos 22^{\circ}) \text{ steradians}$$

In order to insure that three or more stars brighter than magnitude +4.0 are scanned by a field of view whose optical axis is canted at an angle Γ with respect to the spin axis, the area scanned by the canted field of view must be equivalent to S_A. However, for IMP only one-half of each scan period can be reliably utilized since locally reflected sun radiation interferes with star detectability whenever the optical axis is less than 90° to the sun-satellite vector. Therefore, the required canted field of view can be derived as

$$\pi[\cos(\Gamma - FOV/2) - \cos(\Gamma + FOV/2] = 2\pi(1 - \cos 22^{\circ})$$

which may be rewritten as

$$\sin \frac{FOV}{2} = \frac{.0728}{\sin \Gamma} \tag{10}$$

So for the recommended cant angle of $\Gamma = 25^{\circ}$, the required field of view is 20 degrees. For $\Gamma = 16^{\circ}$, the field of view equals 30.6 degrees. From

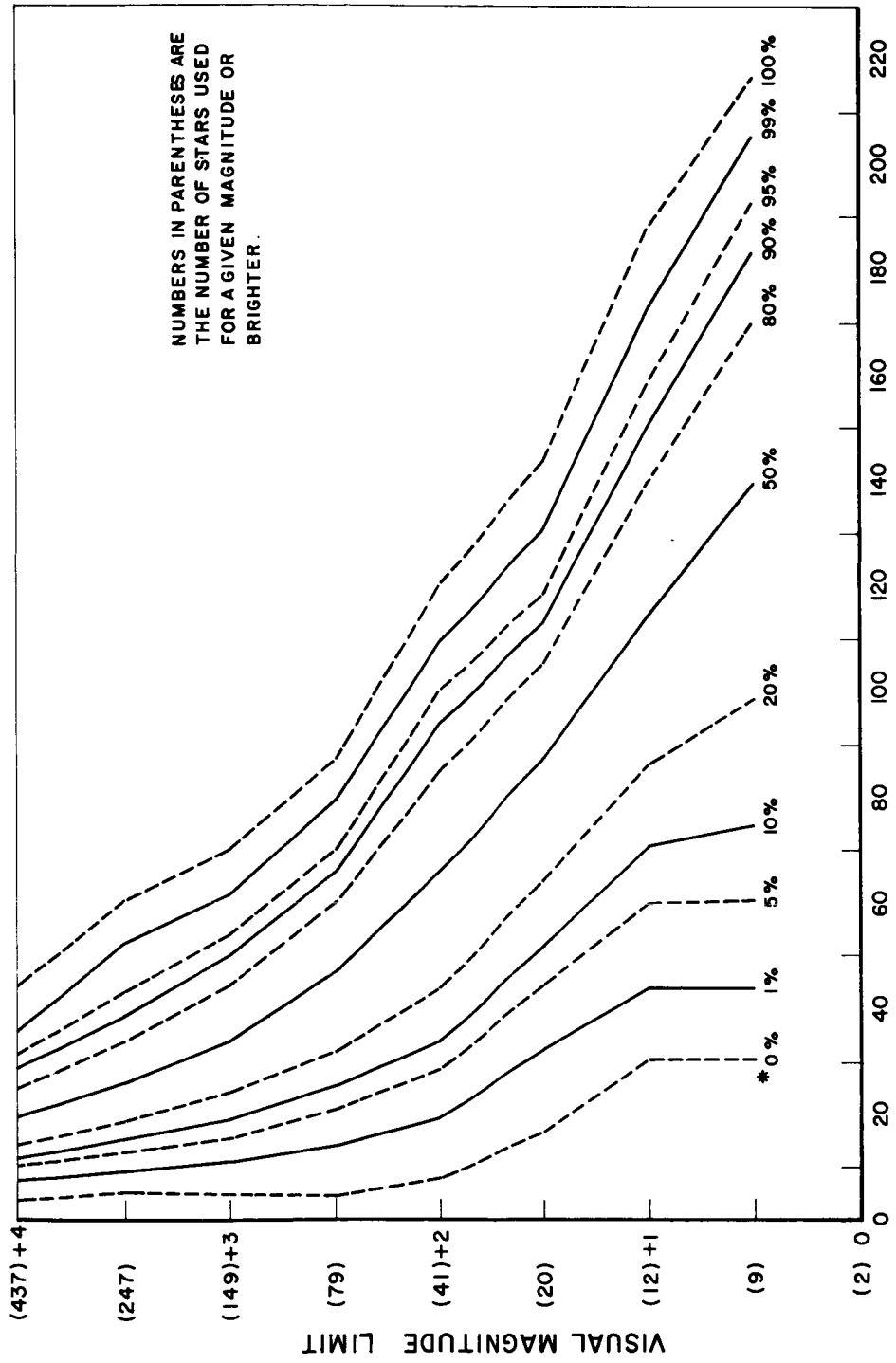

Figure 28: The Field of View Required for a Given Magnitude Limit as a Function of Percentage for Three Stars in the Field of View

Equation (10), the smallest permissible cant angle occurs when FOV/2 = Γ. This occurs for FOV/2 = Γ = 15.1°.

At this point we have tentatively arrived at the following recommendations concerning the field of view:

(1) Γ = 25°, where Γ is the cant angle, i.e. the angle between the spin axis and the optical axis,

(2) the field of view is 20 degrees,

(3) only stars in a 180 degree azimuthal sector may be reliably detected.

The above choice of parameters are summarized in Figure 29. In this figure a single radial slit is shown as per the recommendations of Section III-F.

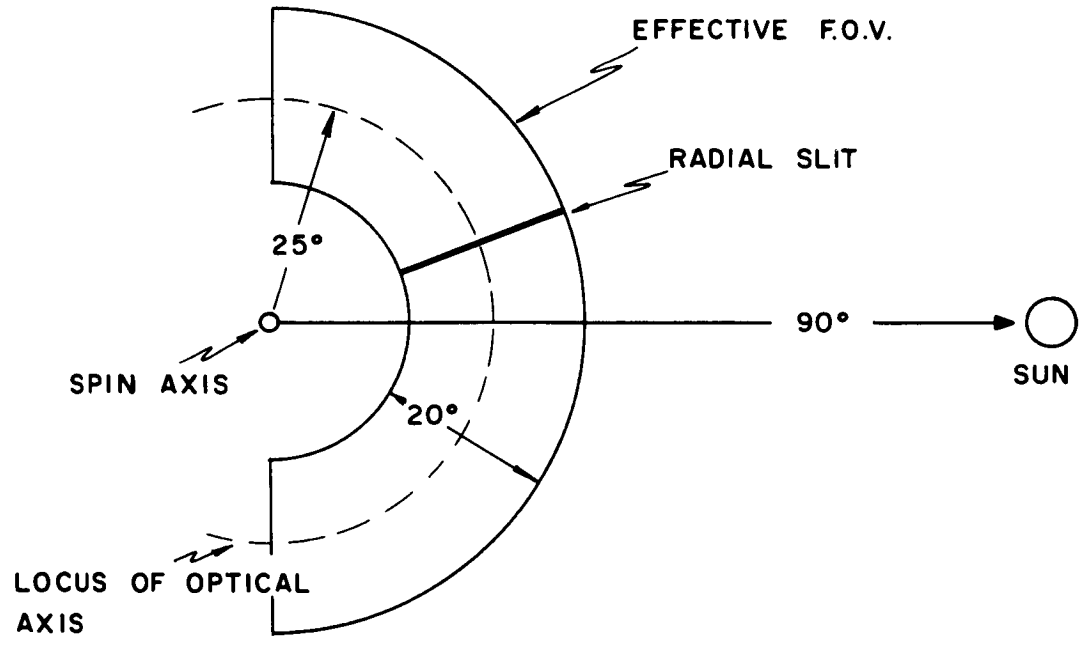

Figure 29: Recommended Field of View

Since the geometric shape of the recommended field of view differs from the circular shape used in the previous star search, the star availability program was rerun. For this program, the sun's longitude was chosen from 0° to 350° in steps of 10°, and the angle between the spin axis and ecliptic was chosen from -90° to 90°.

As a result of this search it was found that a limiting visual magnitude of 3.8 was sufficient to include four or more stars in the effective field for 99.8 percent of the spin axis directions.

Finally, in Figure 30 we plot the probability of having n stars whose visual magnitude is 3.8 or less in the field of view as a function of n.

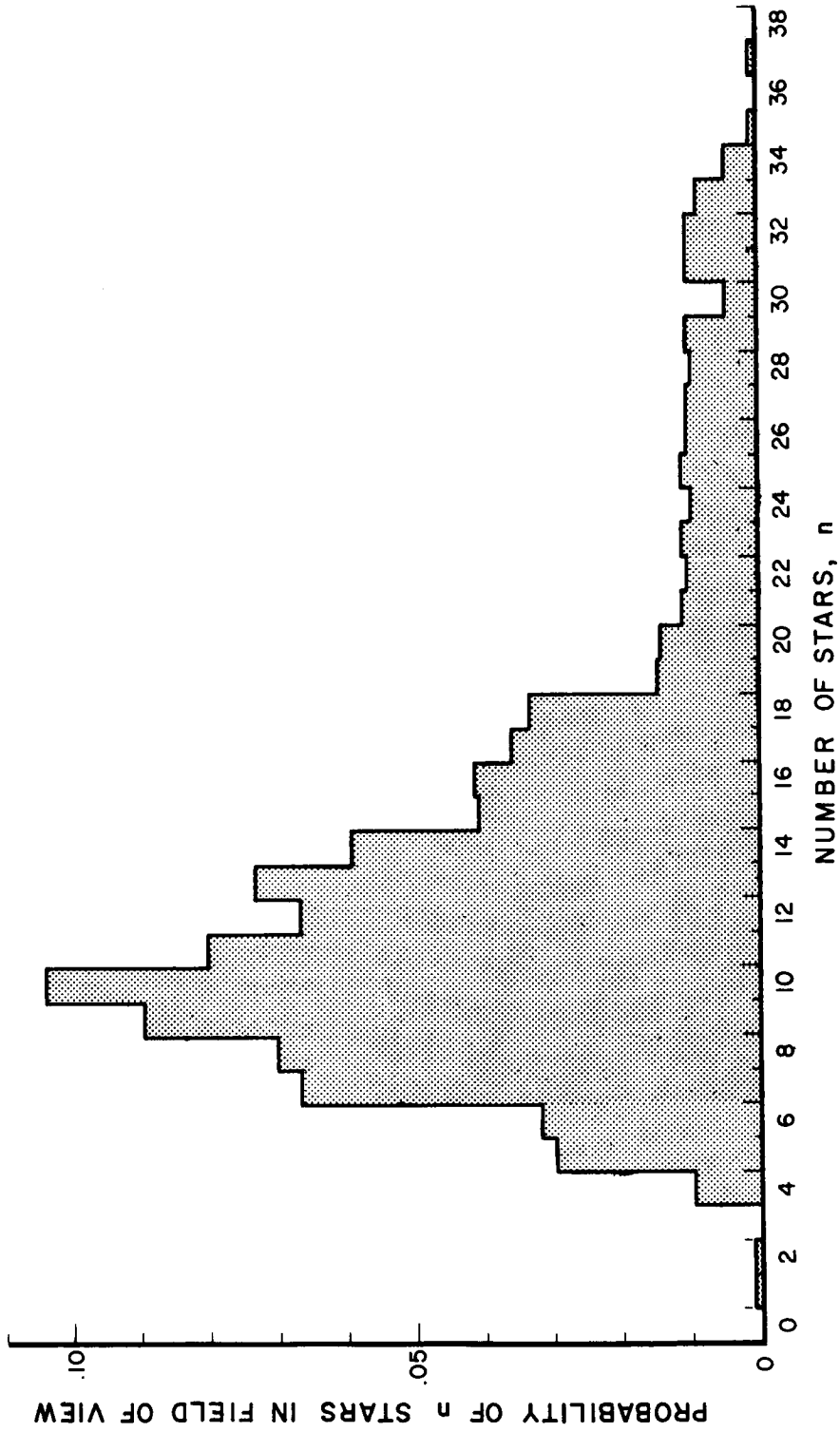

Figure 30: Probability of n Stars with Visual Magnitude 3.8 or Brighter Being in Field of View

C. Selection of Photomultiplier

In order to achieve adequate signal-to-noise ratios with a minimum aperture optical system for the detection of star signals with the IMP sensor, it is required that the photodetector for IMP be a photomultiplier. Previous investigations have shown that current solid state detectors are inadequate or at best marginal for a SCADS-type sensor rotating at relatively short scan periods. One of the principal reasons for the superiority of photomultipliers is the relatively noise-free gain achieved by the electron multiplication provided by the secondary emissions of the photomultiplier dynode chain.[3] The dynode gain provides adequate gain to raise the signal levels well above the level of the thermal Johnson noise of the photodetector load resistor.

Extensive investigation has been performed in the applicability of photomultiplier tubes for SCADS systems. The results of these investigations have shown that venetian blind tubes are optimum for several reasons; in particular, the rugged tube structure, the large photocathode area, and the high multiplier gain are some of its outstanding characteristics. Venetian blind photomultipliers have been utilized in two previous SCADS-type experimental systems. For a Breadboard Design of a SCADS System (NAS5-9661), a venetian blind tube designated as the EMR-543A (manufactured by Electro-Mechanical Research, Inc.) was employed. For the ATS Self-Contained Navigation System Experiment, the venetian blind photomultiplier employed was an EMR-541E. Both tubes were ruggedized and capable of withstanding the environment of space vehicle launching. Since both tube types supplied by EMR performed satisfactorily, this feasibility study will primarily consider EMR photomultipliers.

The cathode type employed in the photomultiplier is particularly important in SCADS sensor applications. It is desirable that the cathode exhibit high quantum efficiency and a low dark emission rate. EMR has given letter designations to indicate different cathode types. For example, the EMR-543A has a cathode designated as an "A" cathode, and its response

conforms closely to an S-4 response with a typical peak quantum efficiency of 14 percent and a cathode dark current of $.274 \times 10^{-15}$ ampere per square centimeter of cathode area at $+20^{o}C$. Similarly, the EMR-541E has an "E" cathode which conforms closely to a S-20 response with a typical peak quantum efficiency of 25 percent and a cathode dark current of $.407 \times 10^{-16}$ amperes per square centimeter at $+20^{o}C$. The "E" cathode has a broad range of spectral response plus its peak sensitivity corresponds closely with the spectral energy distribution of blue stars. More recently EMR has announced the "N" type cathode which has a higher quantum efficiency than the "A" type but somewhat less efficient than the "E" type. The "N" cathode response conforms closely to the S-11 response. Typical peak quantum efficiency of the "N" cathode is 21.5 percent, however its dark current is $.51 \times 10^{-17}$ amperes per square centimeter at $+20^{o}C$. Hence, its dark current characteristic is much superior to either the "A" or "E" cathodes. In addition, the "N" cathode can withstand a much higher temperature ($+150^{o}C$) than either the "A" ($+75^{o}C$) or "E" ($+85^{o}C$) cathodes. The high temperature characteristic is particularly attractive since cathode heating will likely occur whenever the sensor sees earth reflected sun radiation which, as shown in Section III-A, occurs during portions of each orbit for small spin axis inclination angles with respect to the ecliptic plane.

Because of its desirable characteristics of relatively high quantum efficiency, low dark current and tolerance to high temperatures, the EMR type "N" cathode is recommended for the SCADS-IMP sensor. The type "N" cathode is currently available in two ruggedized EMR photomultipliers, the EMR-541N and the EMR-543N. The active cathode diameter of the EMR-541N is 25 millimeters and the active cathode diameter of the EMR-543N is 43 millimeters. Both of these photomultipliers will be given further consideration for application in the SCADS-IMP sensor.

Data sheets for both the EMR-541N and EMR-543N photomultipliers are shown in Appendix A.

D. Sensitivity of Photomultiplier to Star Radiation

For a given photomultiplier it is possible to determine the response of the tube to star radiation. To calculate signal currents at the photomultiplier output, it is necessary to know the absolute spectral energy distribution (ASED) for the star spectral class which contains the greatest percentage of stars. It has been shown that star spectral class A contains the greatest percentage of the 100 brightest stars.[4] Code (1960)[5] has published data from which the ASED of Vega (spectral class A_o) can be calculated.

Code gives the monochromatic magnitudes of Vega as a function of wave number (inverse of wavelength). These magnitudes can be converted to monochromatic magnitudes as a function of wavelength by using the transformation[6]

$$m(\lambda) = M(1/\lambda) + 5 \log_{10} \left[\frac{\bar{\lambda}}{\lambda_o}\right] .$$

In this case λ_o = .556 micron. The monochromatic intensity of Vega at wavelength λ relative to the intensity at λ_o can be obtained from the expression

$$\frac{f(\lambda)}{f(\lambda_o)} = 10^{-.4\,[m(\lambda) - m(\lambda_o)]}$$

where $m(\lambda_o) = 0.0$ at λ_o = .556 micron. The relative spectral energy distribution (RSED) for Vega can be obtained by plotting $f(\lambda)/f(\lambda_o)$ versus λ. By determining f(.556), the absolute spectral energy distribution of Vega can be obtained. Based on measurements, Code has adopted a monochromatic flux value of 3.8×10^{-12} watts per square centimeter micron at .556 micron from a star of visual magnitude V = 0.0. Figure 31 shows a plot of the absolute spectral energy distribution for Vega.

The absolute spectral energy distribution for Vega is modified by the spectral response of the photomultiplier cathode, resulting in an effective

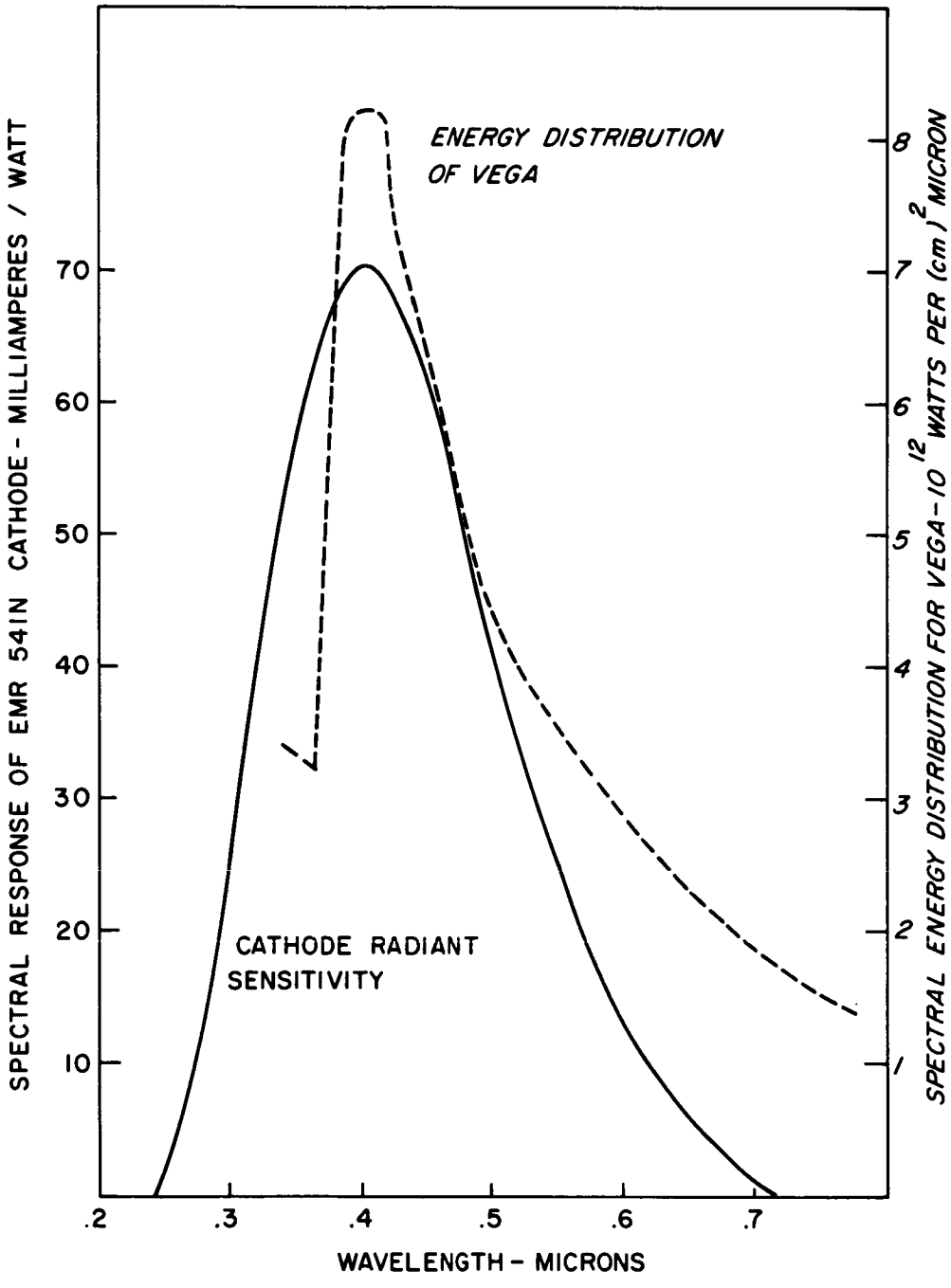

Figure 31: Cathode Radiant Sensitivity Spectral Energy Distribution of Vega

spectral energy distribution for Vega as shown in Figure 32. The spectral response of the EMR-541N cathode is shown in Figure 31. Numerical integration of the effective spectral energy distribution in Figure 32 yields a cathode current of 7.92×10^{-14} amperes per square centimeter of optical aperture. The visual magnitude of Vega is +0.04. The cathode current for a Vega type star of visual magnitude m can be obtained by scaling the cathode current by the factor $10^{-.4(m-.04)} = 1.04 \times 10^{-.4m}$. So a star of magnitude m causes a cathode current of $8.25 \times 10^{-14} \times 10^{-.4m}$ ampere per square centimeter for 100 percent optical efficiency.

Similar calculations have been made for the "E" and "A" cathodes. The results of these calculations are stated as follows for a $0^m.0$ visual magnitude type A star and 100 percent optical efficiency:

"E" cathode sensitivity = 10.3×10^{-14} amperes per square centimeter
"A" cathode sensitivity = 5.49×10^{-14} amperes per square centimeter.

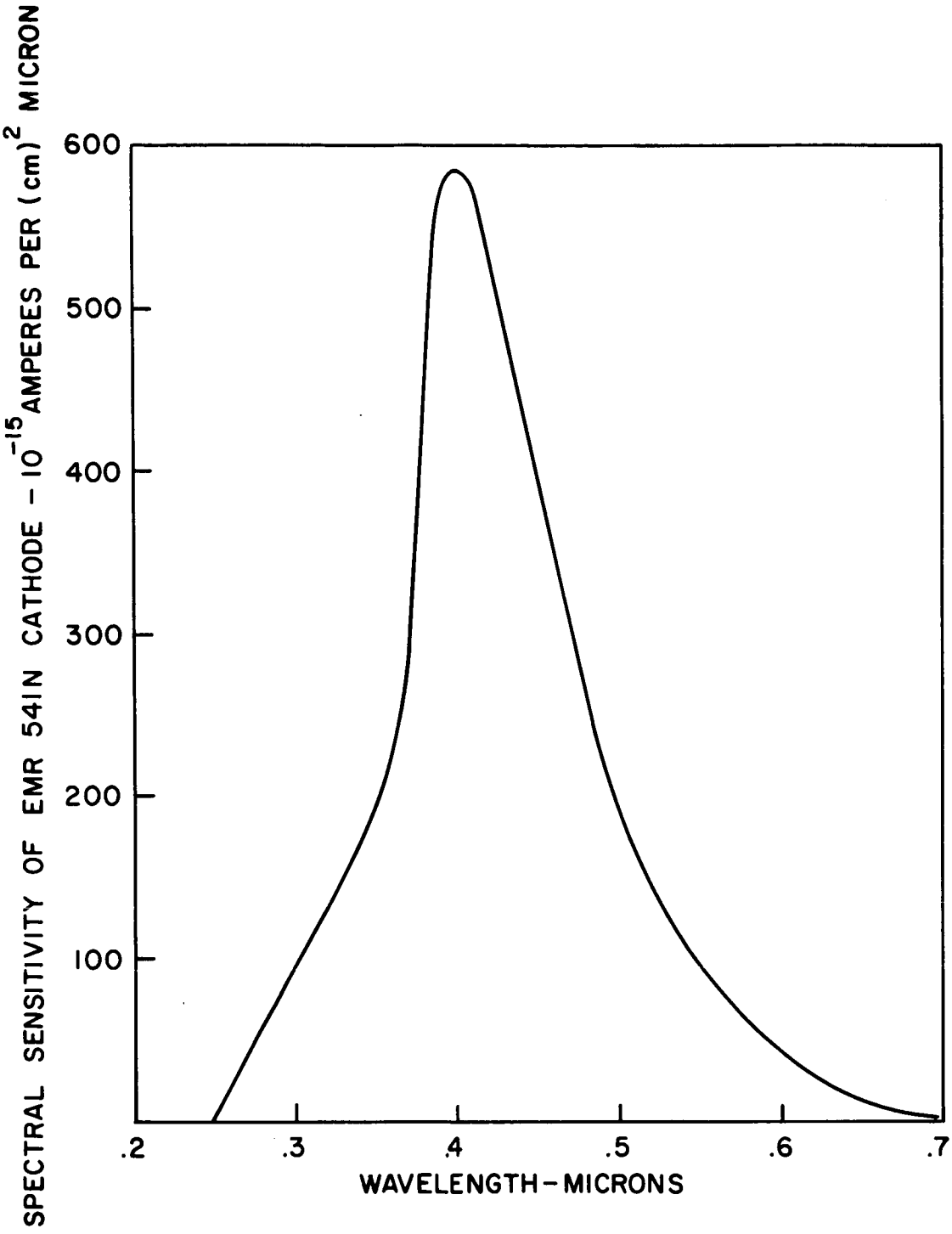

Figure 32: Effective Spectral Energy Distribution for Vega and EMR-541N Cathode

E. Determination of Optical Aperture Required to Detect a Given Magnitude Star for a Fixed False Detection Rate and Detection Probability

For the SCADS-IMP sensor, star signal detection will be achieved by threshold detection of the filtered analog signal. In this section, determination of the threshold level for a permissible false detection rate will be based on results derived by S. O. Rice[7] The required optical aperture diameter will be determined to detect a given magnitude star with a fixed detection probability.

Rice has shown that a noise signal at the output of a low pass filter having an amplitude probability density function which is normal will pass through the threshold value I_T with a positive slope an average number of times per second equal to

$$(1.155)\, e^{-\frac{1}{2}\left(\frac{I_T - I_{BD}}{I_{RMS}}\right)^2} f_b \qquad (11)$$

where

I_T = threshold value of current
I_{BD} = average value of noise current
I_{RMS} = RMS value of noise current
f_b = noise equivalent bandwidth of low pass filter in cycles per second.

It will be shown in Section III-G-3 that the noise equivalent bandwidth for a two pole linear phase shift versus frequency filter has been determined to be

$$f_b = \frac{6205.15}{\widehat{SW} \cdot T} \text{ cycles per second} \qquad (12)$$

where

$\widehat{SW}$ = slit width in arc minutes projected onto the celestial sphere,
T = scan period in seconds.

Hence, the average number of threshold crossings per scan period, N_f, equals

$$N_f = \frac{7166.95}{\widehat{SW}} e^{-\frac{1}{2}\left(\frac{I_T - I_{BD}}{I_{RMS}}\right)^2} \tag{13}$$

So

$$\frac{I_T - I_{BD}}{I_{RMS}} = \left[2 \ell n \frac{7166.95}{N_f \cdot \widehat{SW}}\right]^{\frac{1}{2}} \tag{14}$$

The values of I_T, I_{BD}, and I_{RMS} are taken as current values at the output of the photocathode. The value of I_{RMS} is obtained from the shot noise equation with an additional factor included to account for photomultiplier noise. The current levels at the photomultiplier output can be obtained by multiplying all three values by a noise-free constant equal to the gain of the dynode chain. So at the cathode, the RMS noise equals

$$I_{RMS} = 1.3\left[2e\, I_{BD}\, \Delta f\right] \tag{15}$$

where the factor of 1.3 is included to account for noise introduced by the photomultiplier dynode chain.[3] In Section III-G-3 it will be shown that the noise equivalent bandwidth for the two pole filter may be expressed as

$$\Delta f = f_b = \frac{.2873}{T_s} \text{ cycles per second} \tag{16}$$

where T_s = time required for the center of the star image blur circle to cross the slit.

Next, the following quantities may be introduced,

$$n_T = \frac{I_T\, T_s}{e} \tag{17}$$

$$n_{BD} = \frac{I_{BD}\, T_s}{e}$$

where n denotes the average effective number of equally weighted photocathode emissions occurring during a transit interval, T_s. After substitution of Equations (15), (16), and (17), Equation (14) may be rewritten as

$$n_T = (1.3936)\left[n_{BD}\,\ell n\,\frac{7166.95}{N_f \cdot \widehat{SW}}\right]^{\frac{1}{2}} + n_{BD} \tag{18}$$

The limiting detectable star magnitude can be determined by considering the value of I required in order to exceed the detection threshold I_T a specified fraction of the time referred to as the detection probability. Consequently, the detection level must be

$$I_T \leq I_{BD} + I - k\,I_{RMS} \tag{19}$$

where

I = the peak value of the star signal at the filter output,

I_{RMS} = the RMS output noise generated by the average peak signal level at the input to the low pass filter, and

k = constant determined by the required detection probability.

In Section III-G-3 it will be shown that the peak value of the star signal at the output of a two pole linear phase filter is

$$I = .597\,I_s \tag{20}$$

where I_s = the average photocathode current produced by 100 percent of the star radiation striking the photocathode. Equation (20) assumes that 80 percent of the star radiation passes the slit when the blur circle is centered in the slit. The RMS noise current in Equation (19) is given by

$$I_{RMS} = 1.3\left[2e(.8\,I_s + I_{BD})\,f_b\right]^{\frac{1}{2}} \tag{21}$$

Substitution of Equations (16), (17), and (18) into Equation (19) yields

$$(n_T - n_{BD} - .597\ n_s)^2 = \left\{-k(1.3)\left[(.5746)(.8\ n_s + n_{BD})\right]^{\frac{1}{2}}\right\}^2 \tag{22}$$

Equation (22) can be written as a quadratic in n_s

$$(.597\ n_s)^2 - n_s\left[1.194(n_T - n_{BD}) + (1.3\ k)^2\ (.5746)(.8)\right]$$

$$+ (n_T - n_{BD})^2 - (1.3\ k)^2\ (.5746)\ n_{BD} = 0 \tag{23}$$

From a table of the error function, k = 1.66 for a detection probability of 0.95. So Equation (23) becomes

$$(.3564)\ n_s^2 - n_s\left[1.194(n_T - n_{BD}) + 2.141\right] + (n_T - n_{BD})^2 - 2.676\ n_{BD} = 0 \tag{24}$$

The limiting detectable star magnitude, m, can now be obtained by equating

$$I_s = \frac{n_s\ e}{T_s} = \epsilon_o\ S_K\ 10^{-.4m}\ \frac{\pi}{4}\ D^2 \tag{25}$$

where

ϵ_o = efficiency of the optical system,

S_K = sensitivity of the cathode to a zero magnitude star per unit area of optical aperture,

D = diameter of the optical aperture.

So

$$m = 2.5\ \log_{10}\left[\frac{\pi}{4}\ D^2\left(\frac{T_s}{n_s \cdot e}\right)\ \epsilon_o\ S_K\right] \tag{26}$$

The limiting detectable magnitude can be determined if the following quantities are known or assumed:

(a) S_K = photocathode sensitivity,
(b) θ_2 = angle between the field of view outer edge and the spin axis,
(c) θ_1 = angle between the field of view inner edge and the spin axis,
(d) SW = angular width of slit radial to the spin axis as projected onto the celestial sphere,
(e) N_S = number of radial slits
(f) N_B = equivalent stellar background,
(g) D = optical aperture diameter,
(h) ϵ_o = efficiency of optical system,
(i) I_D = dark current of the photocathode,
(j) N_f = an average number of false star detections per scan period,
(k) T = scan period.

Items (a) through (i) are required to determine

$$I_{BD} = I_B + I_D$$

where I_B = cathode current generated by stellar background radiation striking the photocathode. The stellar background radiation, N_B, is commonly expressed in terms of tenth magnitude stars per square degree of slit area projected onto the celestial sphere. The total slit area projected onto the celestial sphere is

$$S_A = N_S \frac{\widehat{SW}}{60} (\cos \theta_1 - \cos \theta_2) \frac{180}{\pi} (\text{degree})^2$$

where $\widehat{SW}$ is expressed in arc minutes.

With S_K expressed in terms of amperes per square centimeter and D in centimeters, I_B, can be determined by

$$I_B = \epsilon_o \cdot N_B \cdot S_A \cdot S_K \, 10^{-4} \, \frac{\pi}{4} D^2$$

As an example, assume that

(a) $S_K = 8.25 \times 10^{-14}$ amperes per square centimeter (EMR Type N cathode)
(b) $\theta_2 = 31.3$ degrees
(c) $\theta_1 = 0.7$ degree
(d) $\widehat{SW} = 1$ arc minute
(e) $N_S = 1$
(f) $N_B = 325$ tenth magnitude stars per square degree
(g) $D = 7.62$ centimeters (3 inches)
(h) $\epsilon_o = .5$
(i) $I_D = 3.2 \times 10^{-15}$ ampere (EMR-541N at $+83^{\circ}C$)
(j) $N_f = 1/5$
(k) $T = 2$ seconds.

So

$$S_A = .13885 \text{ (degree)}^2, \quad n_{BD} = \frac{(I_B + I_D)}{e} \frac{\widehat{SW}\, T}{21.6 \times 10^3} = 6.75$$

$$n_T - n_{BD} = 1.3936 \left[(6.75) \ln (7167 \times 5)\right]^{\frac{1}{2}} = 11.7$$

The value of n_s is determined as 35.8, so m = 3.72.

Based on the results of this section, a computer program has been written to determine the diameter of the optical aperture required to detect a $+4^m.0$ magnitude star for the following conditions:

(a) $S_K = 8.25 \times 10^{-14}$ amperes per square centimeter (EMR Type N cathode)
(b) cant angle $\Gamma = 25$ degrees
(c) field of view = 20 degrees
(d) $N_S = 1$
(e) $N_B = 325$ tenth magnitude stars per square degree

(f) $\epsilon_o = .5$

(g) $I_D = 3.2 \times 10^{-15}$ ampere (EMR-541N at $+83^oC$)

(h) $N_f = 1/5$

(i) detection probability = $P_d = 0.95$

(j) scan periods, T = 2, 7, and 12 seconds

(k) slit widths, $\widehat{SW}$ = 1, 3, 6, 12, 24, 36, and 48 minutes of arc.

The results of these computations are summarized in Table I where the tabulated entries represent the values of the optical aperture diameter expressed in inches. As can be seen, the required aperture diameter decreases as the slit width increases. However, as will be shown by the error analysis in Section V, the system accuracy decreases as the slit width increases. The result of the error analysis shows that the maximum allowable slit width is six arc minutes in order to achieve the required system accuracy of 0.1 degree. Hence, for a two second scan period, the required optical aperture is 2.648 inches. For scan periods of 7 seconds and 12 seconds, the required optical apertures are, respectively, 1.51 inches and 1.21 inches.

Tabulated in Table II are the average effective number of equally weighted photocathode emissions occurring during a transit interval, T_s, where

(a) n_s represents the number of emissions from a fourth magnitude star,

(b) n_T represents the threshold number of emissions,

(c) n_{BD} represents the sum of the dark current and background emissions.

The numbers in parentheses represent the peak signal to RMS noise which is calculated from an equation which is derived in Section III-G-3.

The calculations required for Tables I and II were repeated for a cant angle $\Gamma = 16^o$ and the corresponding field of view equal to 30.6 degrees. The results of these calculations are tabulated in Tables III and IV.

TABLE I

DIAMETER REQUIRED TO DETECT FOURTH MAGNITUDE STAR
Inches

$\Gamma = 25^{o}$

FOV = 20^{o}

Slit Width	Spin Period		
$\widehat{\text{min.}}$	2 seconds	7 seconds	12 seconds
1	3.657	2.175	1.778
3	2.936	1.703	1.377
6	2.648	1.506	1.205
12	2.445	1.365	1.079
24	2.297	1.262	.987
36	2.226	1.215	.945
48	2.180	1.185	.919

TABLE II

AVERAGE EFFECTIVE NUMBER OF EQUALLY WEIGHTED PHOTOCATHODE EMISSIONS OCCURRING DURING TRANSIT INTERVAL FOR +4.^{m}0 MAGNITUDE STAR, THRESHOLD LEVEL, AND DARK CURRENT PLUS BACKGROUND

$\Gamma = 25^{o}$

$FOV = 20^{o}$

Slit Width		Spin Period	
$\widehat{min.}$	2 seconds	7 seconds	12 seconds
n_S	40.6	50.3	57.6
1 n_T	22.9 (3.81)	33.4 (4.08)	42.6 (4.24)
n_{BD}	9.21	15.6	21.6
n_S	78.6	92.6	104
3 n_T	78.0 (4.52)	105.5 (4.68)	130 (4.79)
n_{BD}	48.3	69.8	89.7
n_S	127.9	145	159
6 n_T	200 (4.88)	253.6 (4.97)	304 (5.02)
n_{BD}	150	196	240
n_S	218	238	255
12 n_T	583.8 (5.10)	691 (5.14)	791 (5.17)
n_{BD}	496	595	688
n_S	385	407	427
24 n_T	1874 (5.18)	2089 (5.20)	2296 (5.21)
n_{BD}	1718	1924	2122
n_S	542	565	586
36 n_T	3823 (5.17)	4148 (5.17)	4463 (5.18)
n_{BD}	3603	3919	4225
n_S	694	717	739
48 n_T	6400 (5.14)	6836 (5.14)	7260 (5.15)
n_{BD}	6120	6546	6961

$$\frac{S_{peak}}{N_{RMS}} = \frac{.597\ n_S}{1.3[(.5746)(.8\ n_S + n_{BD})]^{\frac{1}{2}}} = \frac{.60582\ n_S}{(.8\ n_S + n_{BD})^{\frac{1}{2}}}$$

TABLE III

DIAMETER REQUIRED TO DETECT FOURTH MAGNITUDE STAR
Inches

$\Gamma = 16^{o}$

FOV = 30.6^{o}

Slit Width	Spin Period		
$\widehat{\text{min.}}$	2 seconds	7 seconds	12 seconds
1	3.65	2.173	1.776
3	2.928	1.7	1.375
6	2.64	1.503	1.203
12	2.437	1.361	1.076
24	2.288	1.258	.984
36	2.217	1.210	.942
48	2.172	1.180	.915

TABLE IV

AVERAGE EFFECTIVE NUMBER OF EQUALLY WEIGHTED PHOTOCATHODE EMISSIONS OCCURRING DURING TRANSIT INTERVAL FOR $+4^{m}.0$ MAGNITUDE STAR, THRESHOLD LEVEL, AND DARK CURRENT PLUS BACKGROUND

$\Gamma = 16^{\circ}$

$FOV = 30.6^{\circ}$

Slit Width		Spin Period	
$\widehat{min.}$	2 seconds	7 seconds	12 seconds
n_S	40.5	50.2	57.5
1 n_T	22.7 (3.81)	33.3 (4.08)	42.3 (4.24)
n_{BD}	9.1	15.5	21.4
n_S	78.2	92.3	103
3 n_T	77.2 (4.51)	104.7 (4.67)	129.4 (4.76)
n_{BD}	47.7	69.2	89.1
n_S	127.1	144.2	158
6 n_T	198.1 (4.87)	251.6 (4.97)	300 (5.02)
n_{BD}	148.1	194	237
n_S	216.6	236	254
12 n_T	576.4 (5.10)	683.2 (5.13)	783 (5.18)
n_{BD}	489.2	587.6	680
n_S	382.1	404	424
24 n_T	1847 (5.18)	2063 (5.19)	2268 (5.21)
n_{BD}	1692	1899	2095
n_S	538	561	583
36 n_T	3765 (5.17)	4091 (5.18)	4404 (5.19)
n_{BD}	3547	3863	4168
n_S	688	712	734
48 n_T	6303 (5.14)	6738 (5.15)	7160 (5.15)
n_{BD}	6025	6450	6863

$$\frac{S_{peak}}{N_{RMS}} = \frac{.597\, n_S}{1.3[(.5746)(.8\, n_S + n_{BD})]^{\frac{1}{2}}} = \frac{.60582\, n_S}{(.8\, n_S + n_{BD})^{\frac{1}{2}}}$$

If a detection threshold is determined with the intent to detect stars of a given magnitude with a given false detection rate and detection probability, fainter stars will be detected with a smaller probability. These fainter stars will randomly appear and disappear over a period of successive scans.

The detection probabilities for stars fainter than $4^m.0$ magnitude may be easily determined. If n_s is the average number of effective photoelectrons per scan period from a $4^m.0$ magnitude star, then

$$n_{sm} = n_s \, 10^{.4(4-m)}$$

is the average effective number of photoelectrons from a star of magnitude m for the same scan period and optical aperture. Now Equation (22) may be solved for k

$$k = \frac{-(n_T - n_{BD} - .597\, n_{sm})}{1.3[(.5746)(.8\, n_{sm} + n_{BD})]^{\frac{1}{2}}}$$

Finally, the detection probability for the star of magnitude m is given by

$$P_d = \int_{-\infty}^{k} \frac{1}{\sqrt{2\pi}} e^{-\frac{1}{2}x^2} \, dx \, .$$

Figures 33, 34, and 35 show the faint star detection probabilities for FOV = 20°, $\Gamma = 25^\circ$, and respective scan periods of 2, 7, and 12 seconds. Note that a detection probability less than .05 occurs for stars fainter than $5^m.1$ magnitude.

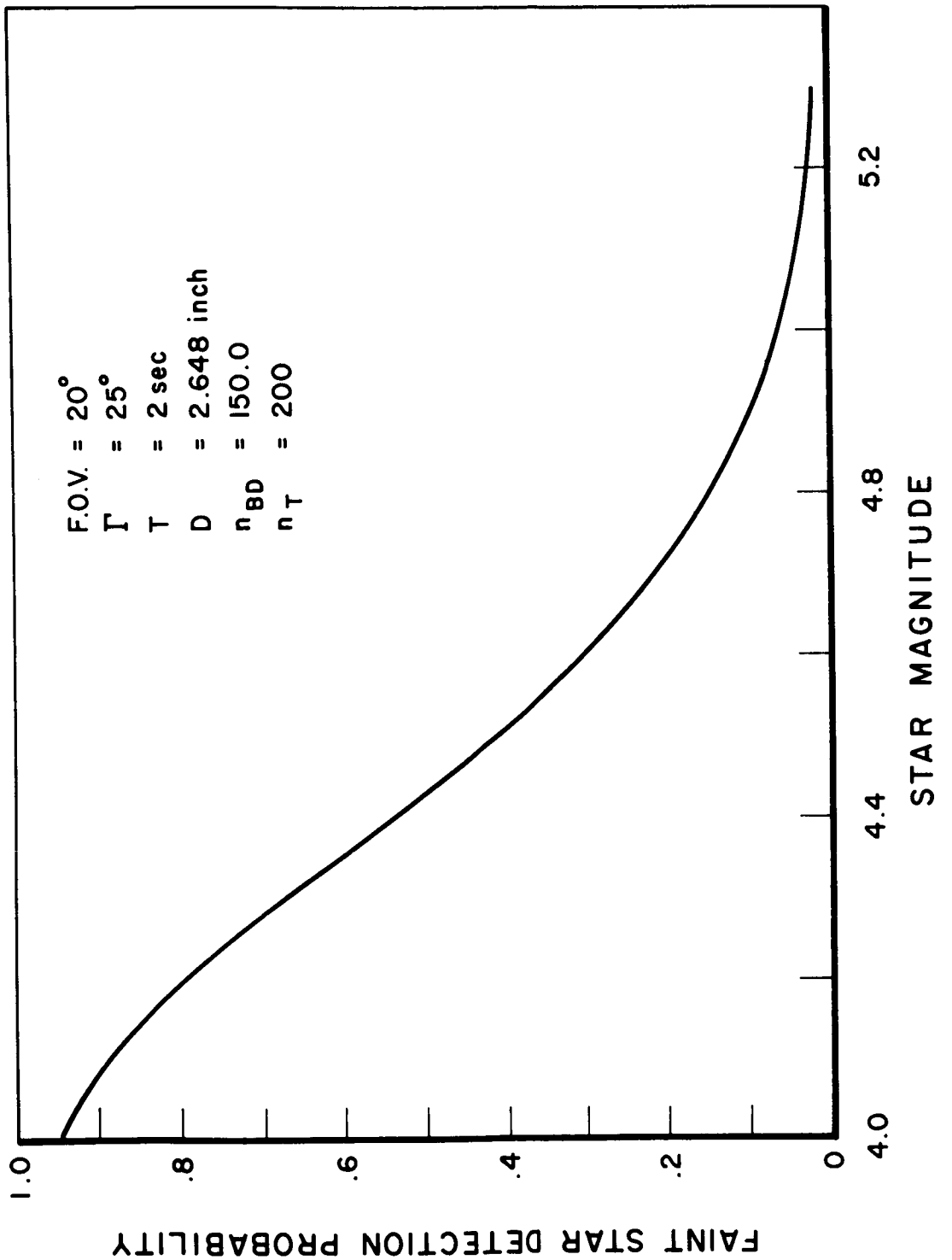

Figure 33: Faint Star Detection Probability for 6 Arc Minute Slit Width and 2 Second Scan Period

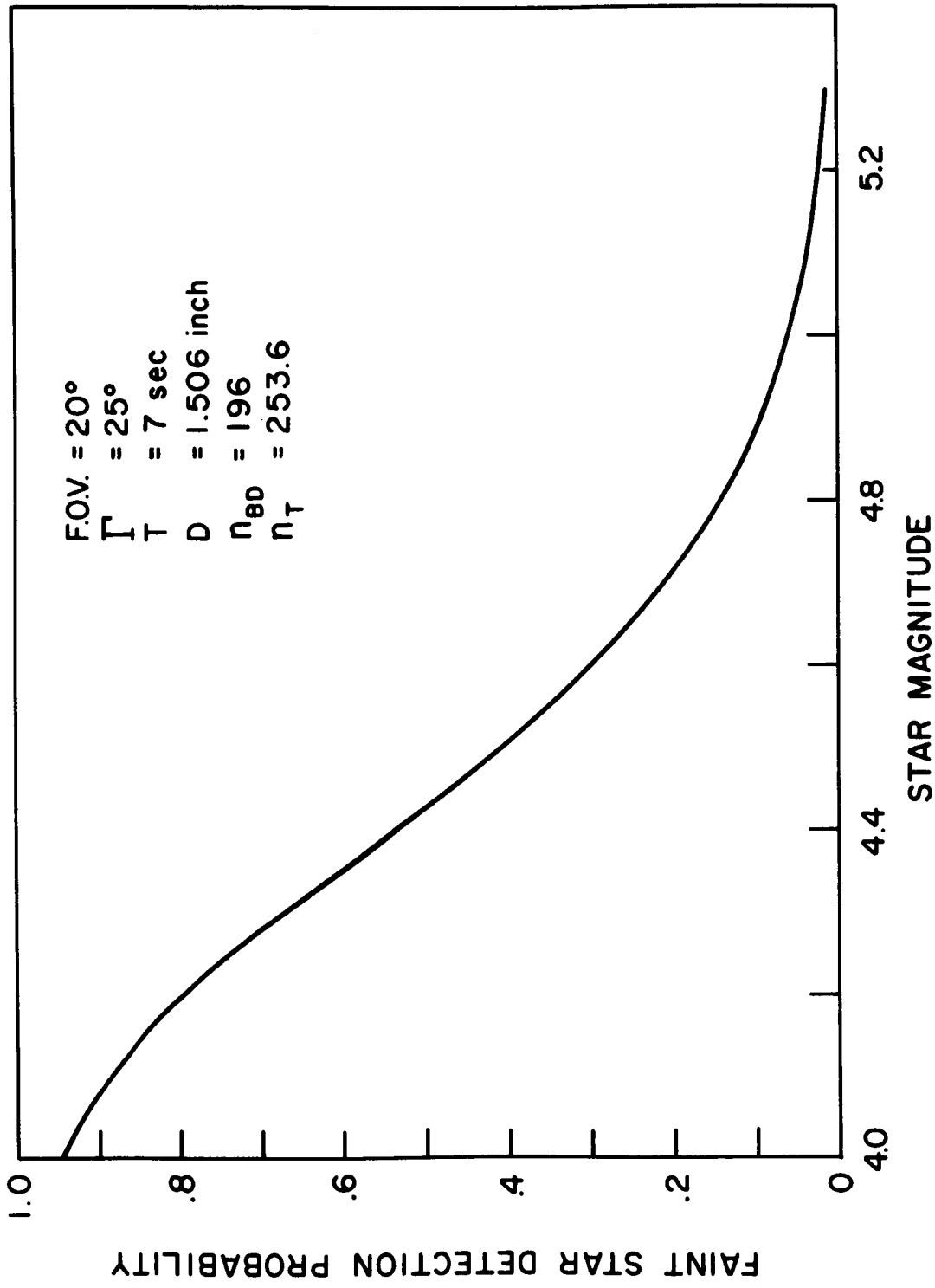

Figure 34: Faint Star Detection Probability for 6 Arc Minute Slit Width and 7 Second Scan Period

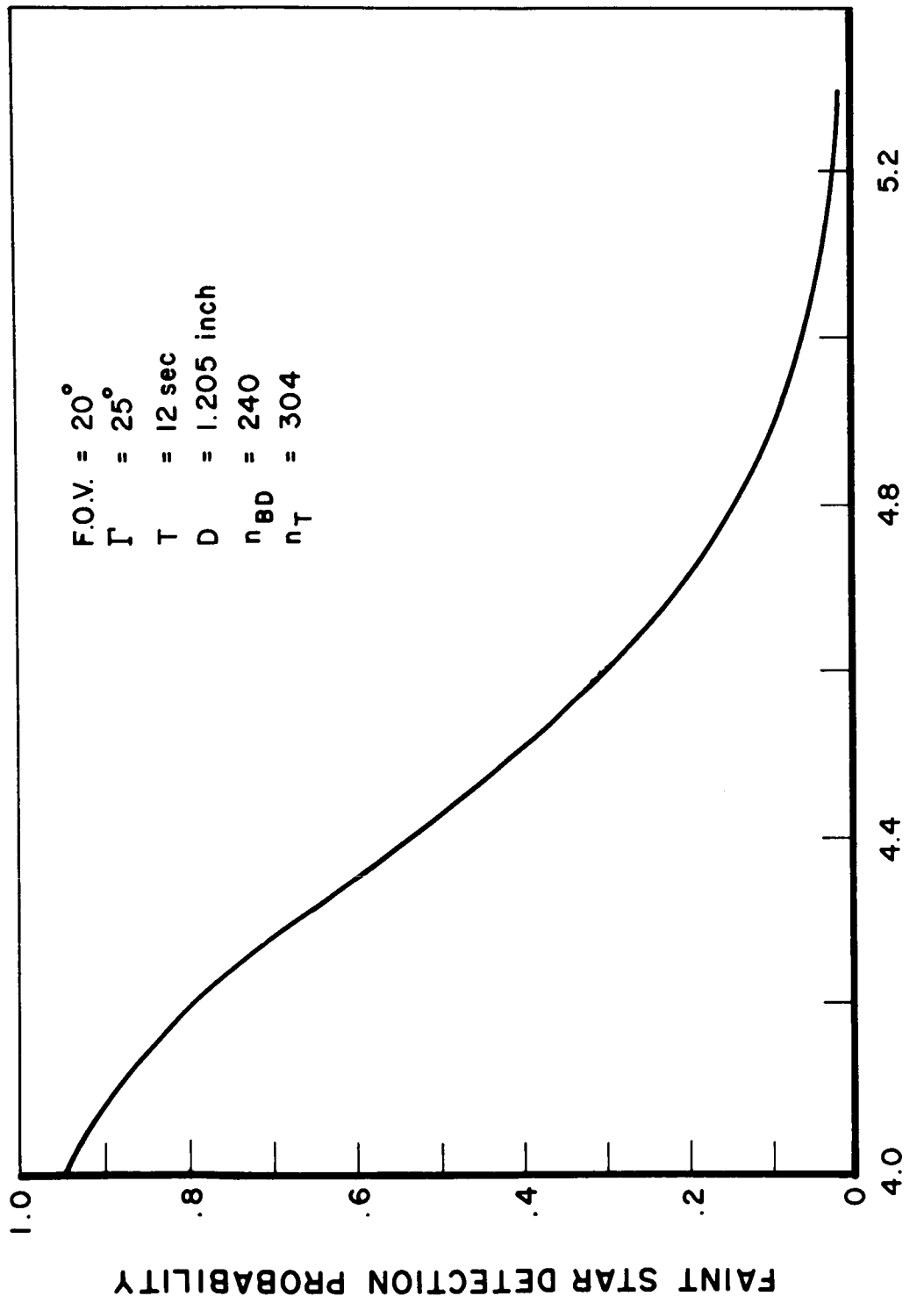

Figure 35: Faint Star Detection Probability for 6 Arc Minute Slit Width and 12 Second Scan Period

F. Optical Design

1. Lens Design

This section will further analyze the optical system required by the SCADS-IMP sensor. The required field of view and optical aperture have already been determined. The next step will be to determine the limit of the ratio f/no = focal length per diameter. Then the blur circle characteristics of several specific lenses will be analyzed with the aid of an automated ray tracing program.

The required f/no of the lens may be determined from the relation

$$f/n \leqq \frac{d}{2\ D \tan \frac{FOV}{2}}$$

where

d = diameter of the star field image in the focal plane,

D = diameter of the optical aperture.

Since field condensing lenses and fiber optics will not be employed as a part of the optical system, the diameter of the star field image must be no larger than the active cathode diameter of the photomultiplier. When the photomultiplier cathode lies in the focal plane, the active cathode diameter must $\geqq$ the star field image diameter, d. Two type N EMR photomultipliers have been selected for application to the SCADS-IMP sensor. These two tubes designated as the EMR-541N and EMR-543N have active cathode diameters of 25 millimeters and 43 millimeters, respectively. The limiting ratios of the f/no have been determined for each tube and for scan periods of 2, 7, and 12 seconds. These f/no values are summarized in Table V for cant angle $\Gamma = 25^{\circ}$ and FOV = 20°. Similarly, Table VI summarizes the limits on the permissible f/no for $\Gamma = 16^{\circ}$ and FOV = 30.6°.

Once the field of view, optical aperture diameter and f/n ratio have been determined, lens analysis may be further extended to include the resolution characteristics. A basic requirement for the detailed analysis of any

TABLE V

LIMITING LENS f/no RATIOS FOR THE EMR-541N AND EMR-543N PHOTOMULTIPLIERS WITH $\Gamma = 25^{\circ}$ AND FOV = 20°

Scan Period-Seconds	$2 \leq T < 7$	$7 \leq T < 12$	$T \geq 12$
Lens Diameter-Inches	D = 2.648	D = 1.506	D = 1.205
EMR-541N	$f/n \leq 1.05$	$f/n \leq 1.854$	$f/n \leq 2.317$
EMR-543N	$f/n \leq 1.78$	$f/n \leq 3.13$	$f/n \leq 3.92$

TABLE VI

LIMITING LENS f/no RATIOS FOR THE EMR-541N AND EMR-543N PHOTOMULTIPLIERS WITH $\Gamma = 16^{\circ}$ AND FOV = 30.6°

Scan Period-Seconds	$2 \leq T < 7$	$7 \leq T < 12$	$T \geq 12$
Lens Diameter-Inches	D = 2.64	D = 1.503	D = 1.203
EMR-541N	$f/n \leq .68$	$f/n \leq 1.197$	$f/n \leq 1.495$
EMR-543N	$f/n \leq 1.172$	$f/n \leq 2.059$	$f/n \leq 2.572$

sensor lens, which must image infinite distance point sources, is the capability of tracing the passage of large bundles of parallel light rays through the system to the focal plane. A computer ray tracing program has been written which can handle such conditions as arbitrary off-axis angles of incidence, multiple element lenses, differing light wavelengths, and lens vignetting (off-axis transmission efficiency). In particular, the required program inputs can be listed as:

(a) field of view,
(b) aperture diameter,
(c) thickness of each element along the optical axis,
(d) separations between elements,
(e) refractive index of each element,
(f) incident light wavelength,
(g) off-axis angle of incident light.

Among the principal outputs of this program is a set of blur spot diagrams for bundles of parallel rays which completely fill the lens aperture. These spot diagrams cover a range of incidence angles from 0 degrees (along the optical axis) out to the edge of the angular field of view. Another output of this program is the lens focal length.

In general, no standard off-the-shelf lens will meet the specific requirements of Tables V or VI . However, there are various multi-element lens designs available which can be tailored to satisfy the field of view, aperture, and f/no requirements. Most of the high quality lens designs have registered patents and are described in detail in the patent description. After an extensive survey of existing lens patents, it was concluded that the lens of the SCADS-IMP sensor could be satisfactorily tailored from U.S. Patent No. 2,846,923. This patent describes the Super-Farron f/0.87 lens which has a 30 degree field of view, 40 millimeter focal plane, and 77 millimeter focal length. Figure 36 shows a cross section drawing of the Super-Farron lens elements. Since the Super-Farron lens

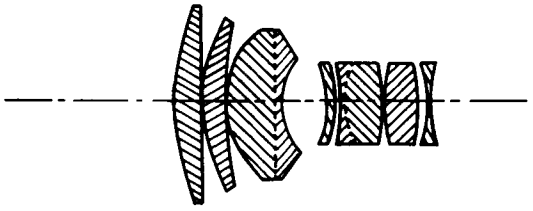

Figure 36: Cross-Sectional Drawing of Super-Farron Lens Elements

characteristics do not match exactly the requirements of Table V , it is necessary to scale the lens to fit the requirements.

In order to visualize the concept of scaling a lens, consider the thick lens element with refractive index μ shown in Figure 37. The focal length of this lens element may be expressed as[8]

$$\frac{1}{F} = (\mu - 1)\left[\frac{1}{R_1} - \frac{1}{R_2} + \frac{t(\mu - 1)}{R_1 R_2 \mu}\right]$$

where R_1 and R_2 are the radii of curvature, and t = thickness of the lens element. Now each radii and the thickness may be multiplied by a constant k which results in a new focal length, 1/kF.

Similarly, each lens element in a multi-element lens may be scaled resulting in a new overall lens focal length. Consequently, the dimensions of the Super-Farron lens elements may be scaled to meet the focal length requirements from Table V.

Using the scaled dimensions of the lens elements as inputs to the computer ray tracing program, blur spot diagrams were obtained for angles of incidence of 0°, 2.5°, 5°, 7.5°, and 10°. Figures 38 to 42 illustrate the blur spot diagrams for the required lens in Table V having a 2.648 inch

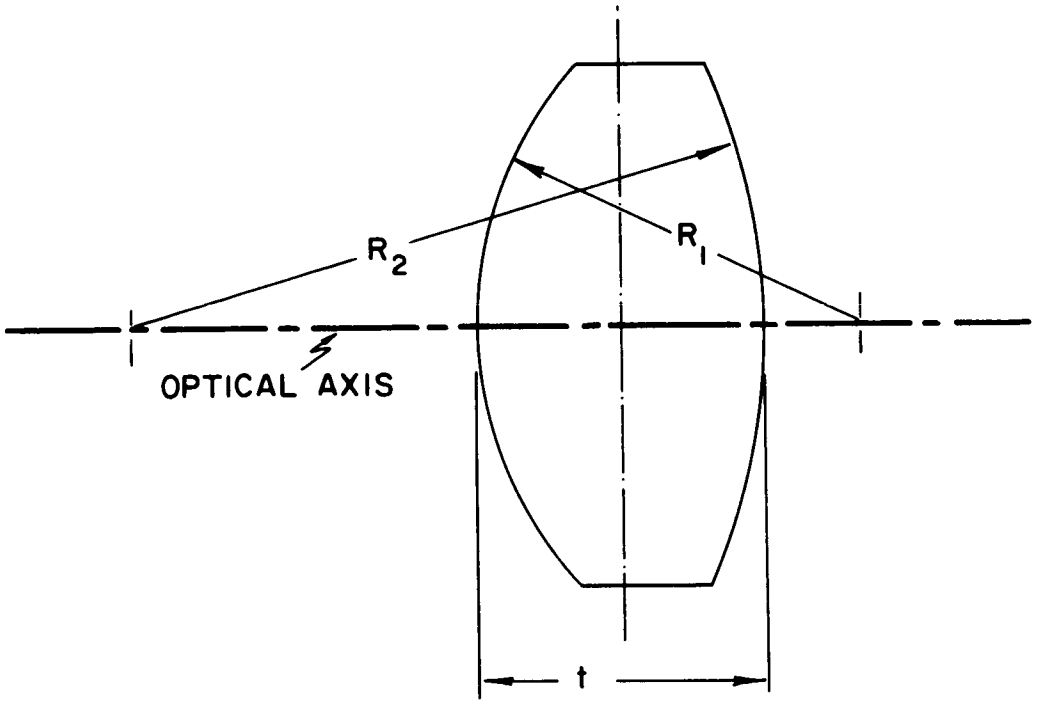

Figure 37 : Dimensions of Single Lens Element

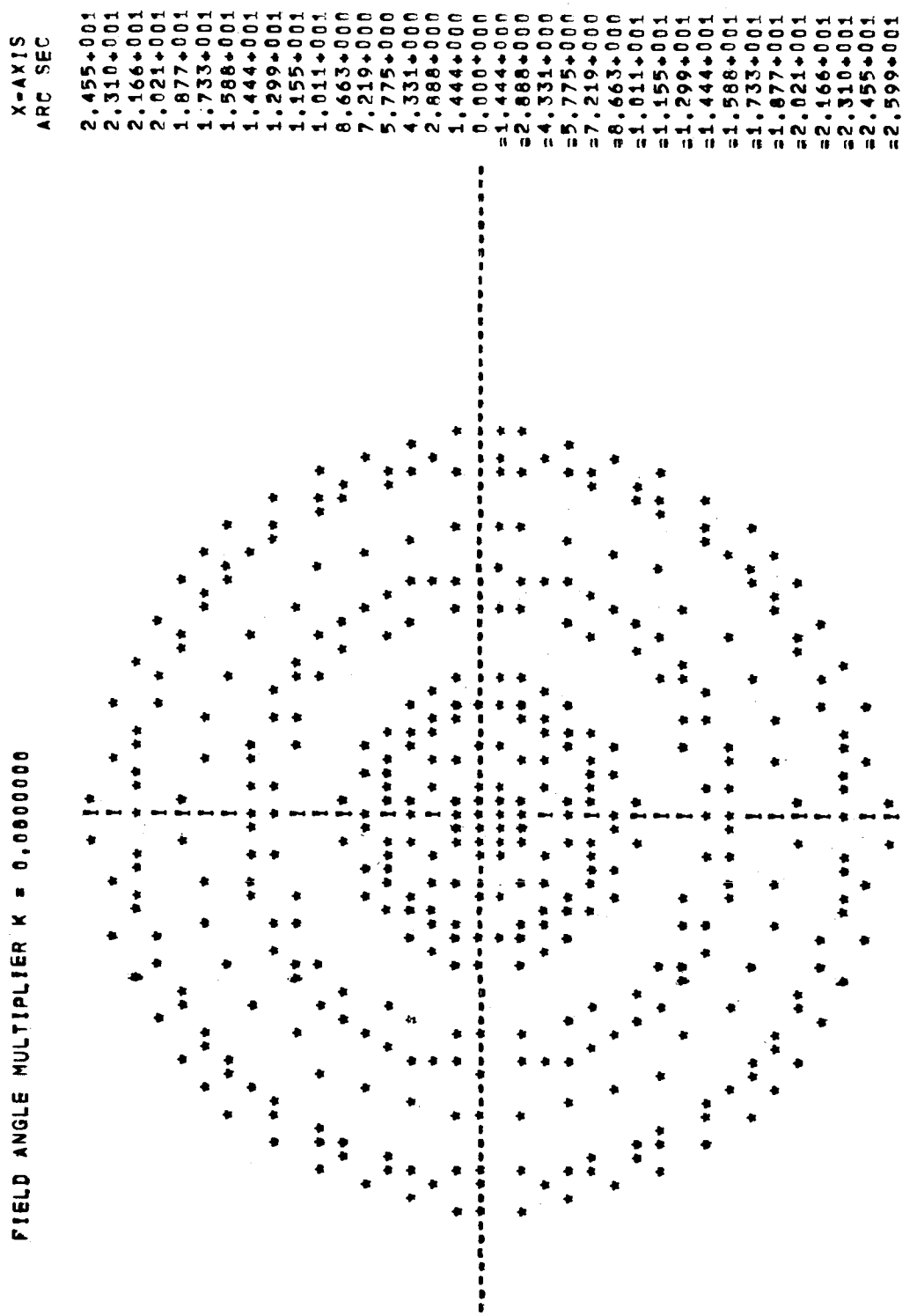

Figure 38: Spot Diagram for Scaled Super-Farron Lens; Field of View = 20^{o}; f/1.05; Incidence Angle = 0^{o}

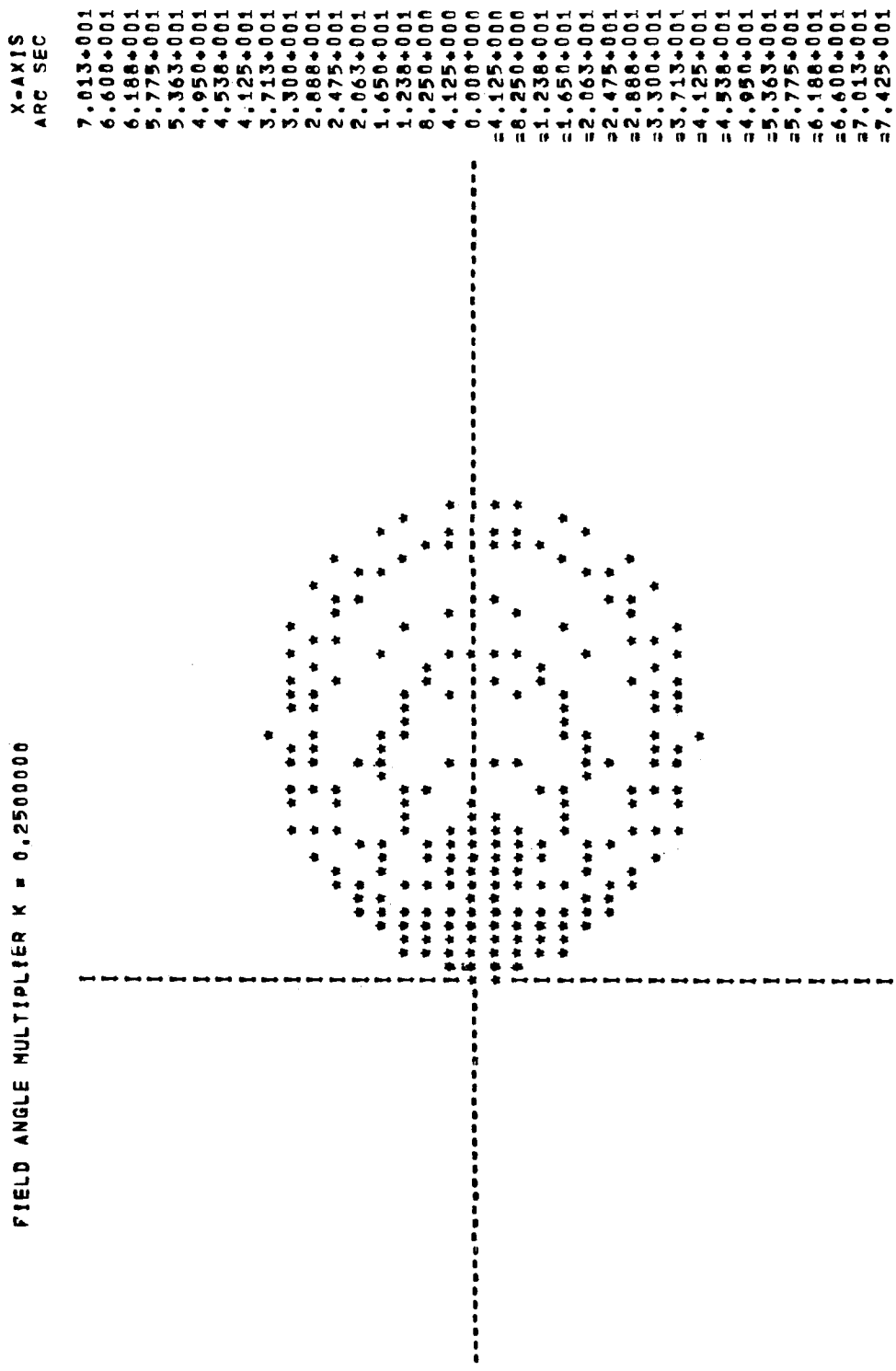

Figure 39: Spot Diagram for Scaled Super-Farron Lens; Field of View = 20^{o}; f/1.05; Incidence Angle = 2.5^{o}

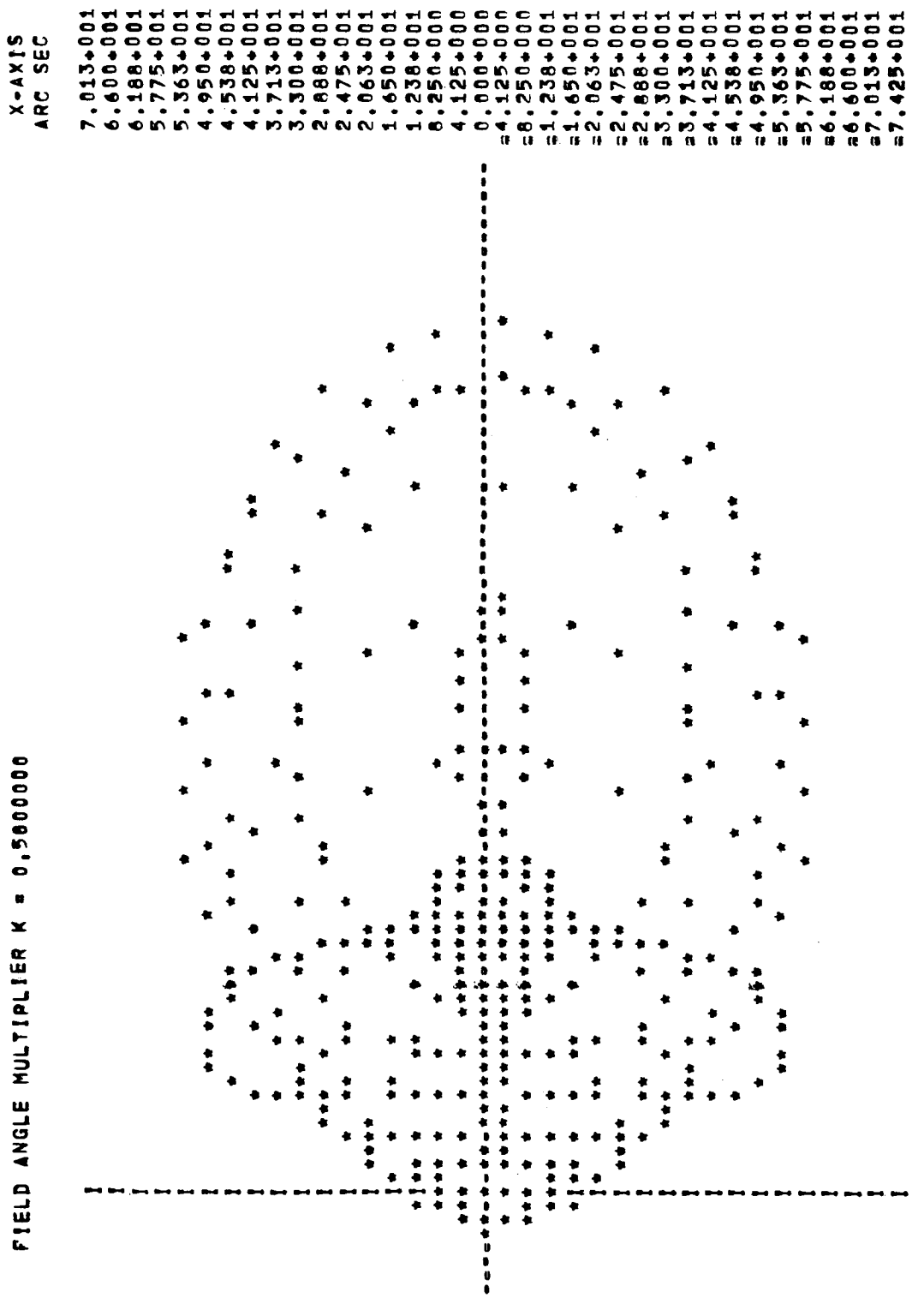

Figure 40: Spot Diagram for Scaled Super-Farron Lens; Field of View = 20^{o}; f/1.05; Incidence Angle = 5^{o}

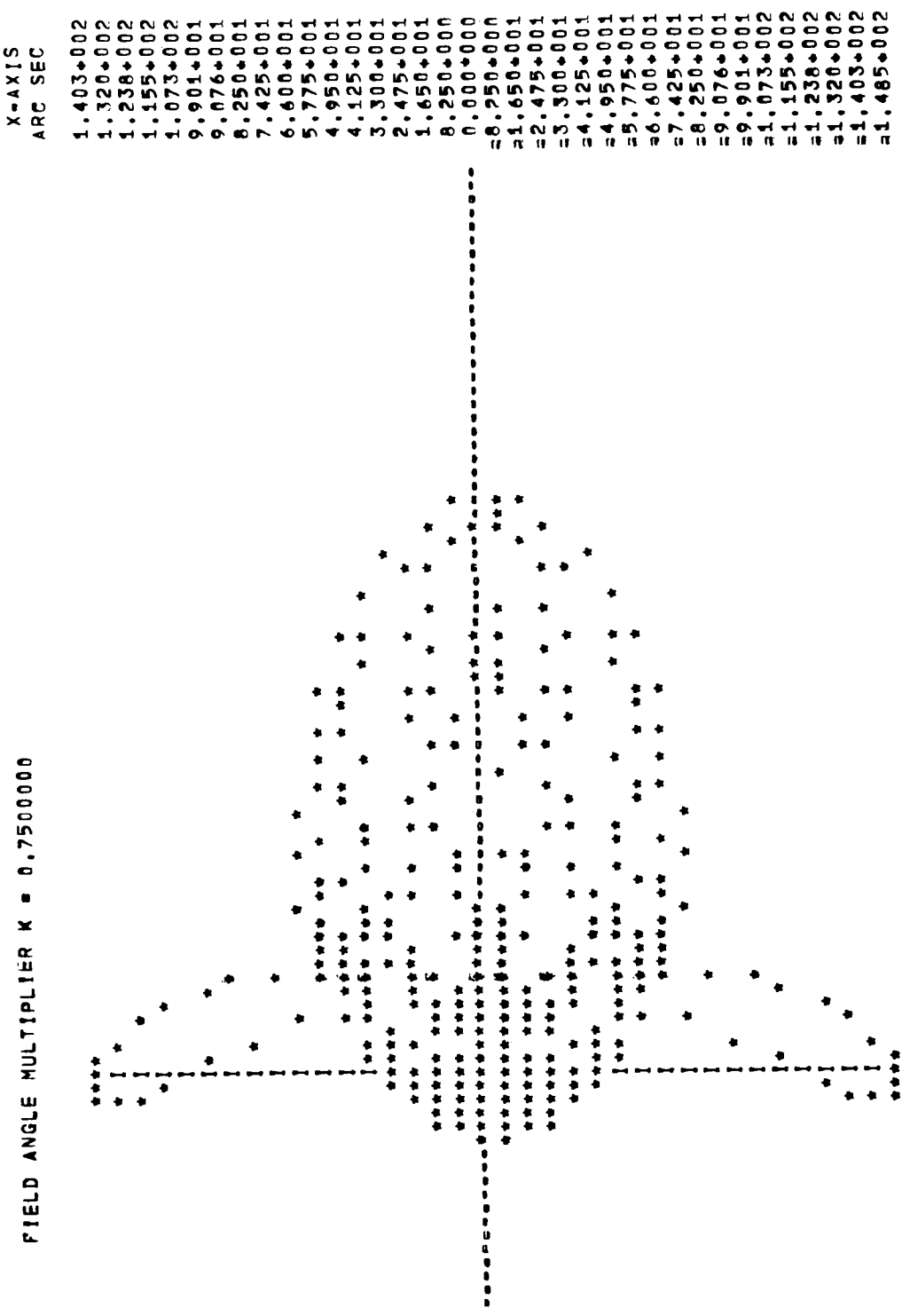

Figure 41: Spot Diagram for Scaled Super-Farron Lens; Field of View = 20^{o}; f/1.05; Incidence Angle = 7.5^{o}

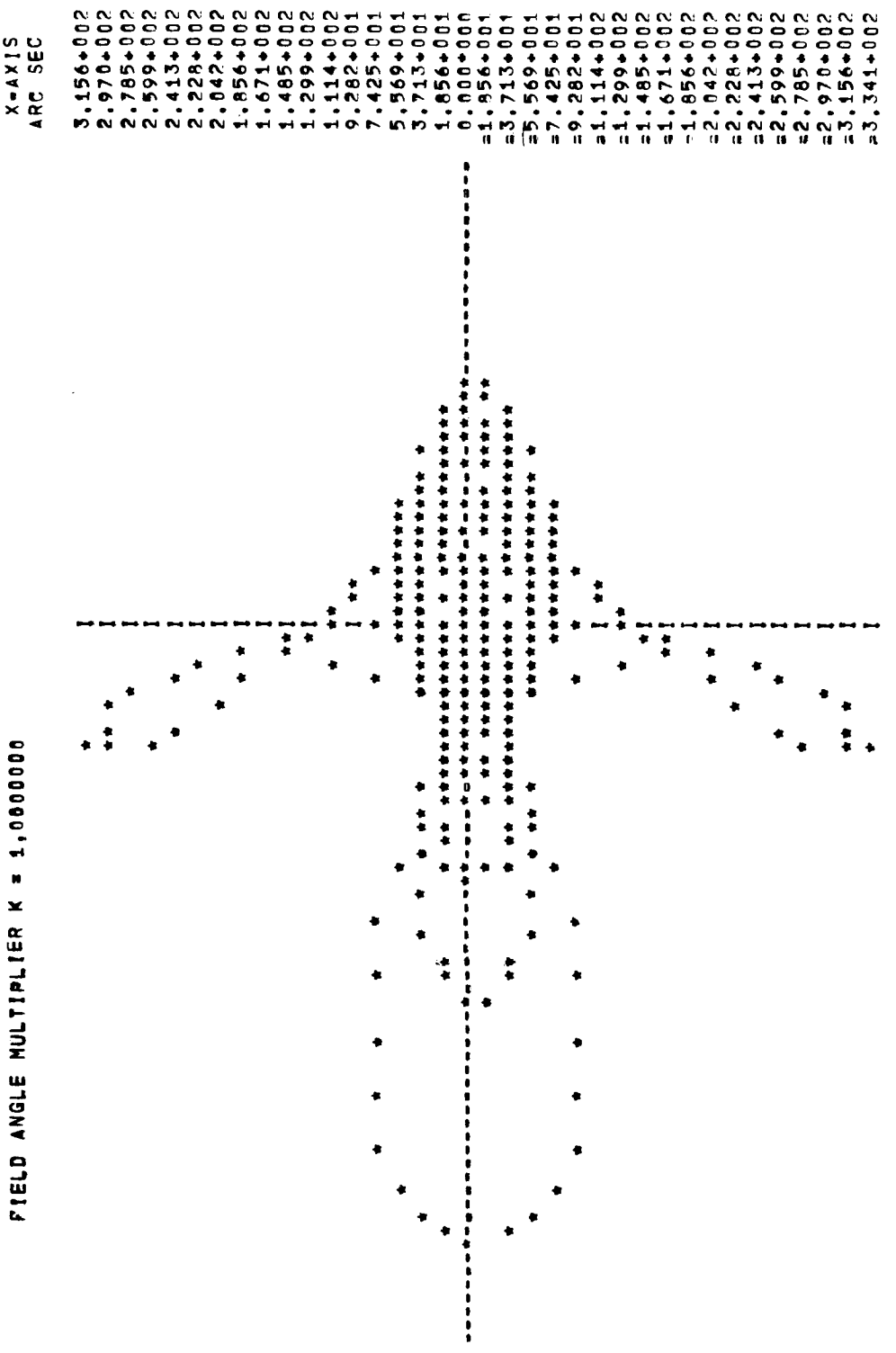

Figure 42: Spot Diagram for Scaled Super-Farron Lens; Field of View = 20°; f/1.05; Incidence Angle = 10°

diameter and f/n = 1.05. The angle subtended by the dimensions of the spot diagram from the nodal point of the lens is given at the right hand side of the spot. The angle which subtends a large percentage of the spot diagram must match the angular dimension of the slit radial to the spin axis as projected on the celestial sphere.

Figure 43 shows the relationship between the optical angle, $\widehat{BC}$, subtended by a slit radial to the spin axis and the rotational slit width, $\widehat{SW}$, projected on the celestial sphere. The relationship is given by

$$\widehat{BC} = \widehat{SW} \sin \gamma.$$

So for the f/1.05 lens in Table V , the angle $\widehat{BC}$ = 93.2 arc seconds at $\gamma = \Gamma - FOV/2 = 15^{o}$ and $\widehat{BC}$ = 206.5 arc seconds at $\gamma = \Gamma + FOV/2 = 35^{o}$. Note that the angle subtended by the entire spot diagram is contained within the angle $\widehat{BC}$ all along the slit except when γ approaches 15 degrees. However, it is estimated that approximately 70 percent or more of the spot diagram energy is included within the angle $\widehat{BC}$ = 93 arc seconds at γ = 15 degrees. Therefore, it is concluded that the scaled Super-Farron lens design with f/n = 1.05 is adequate for a scan period range of $2 \leq T < 7$ seconds when Γ = 25 degrees and field of view = 20 degrees.

Note that it is proper to speak of a blur "circle" only for axial incidence. For the other angles of incidence, the spot shape varies quite radically. Note also that the slit axis will correspond to the horizontal (radial) axis of the blur spot diagrams. Thus, the symmetrical spreading of the blur spot about this axis will yield a symmetrical signal and hence will not degrade the achievable azimuth accuracy of the system.

Additional spot diagrams are given for the remaining cases in Table V. Figures 44 through 48 illustrate the blur spot diagrams for the f/1.854 lens in Table V , while Figures 49 through 53 illustrate the blur spot diagrams for the f/2.317 lens in Table V.

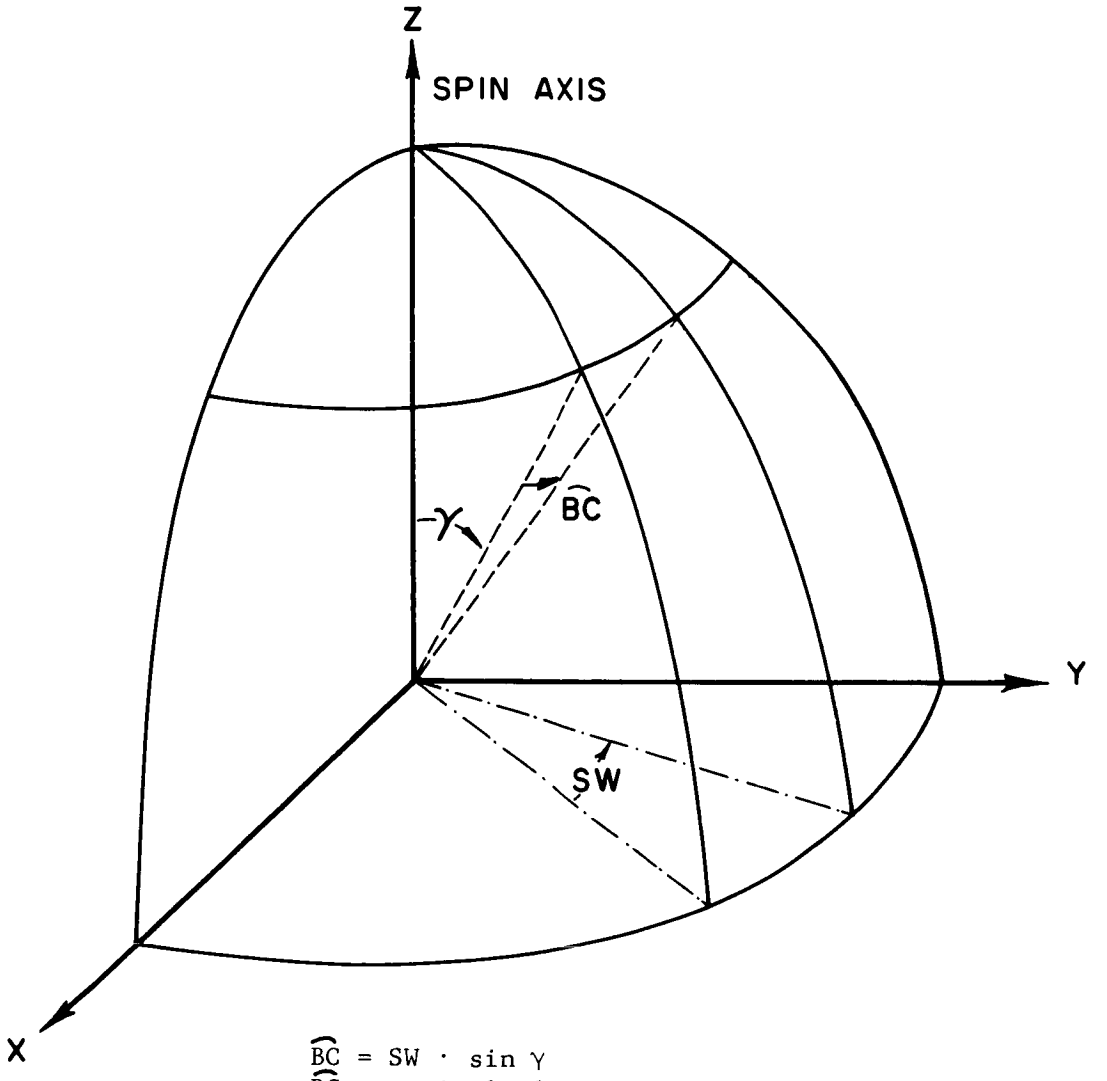

$\widehat{BC} = SW \cdot \sin \gamma$
$\widehat{BC}$ = optical slit width
SW = rotational slit width

Figure 43: Relation Between Optical Slit Width and Rotational Slit Width

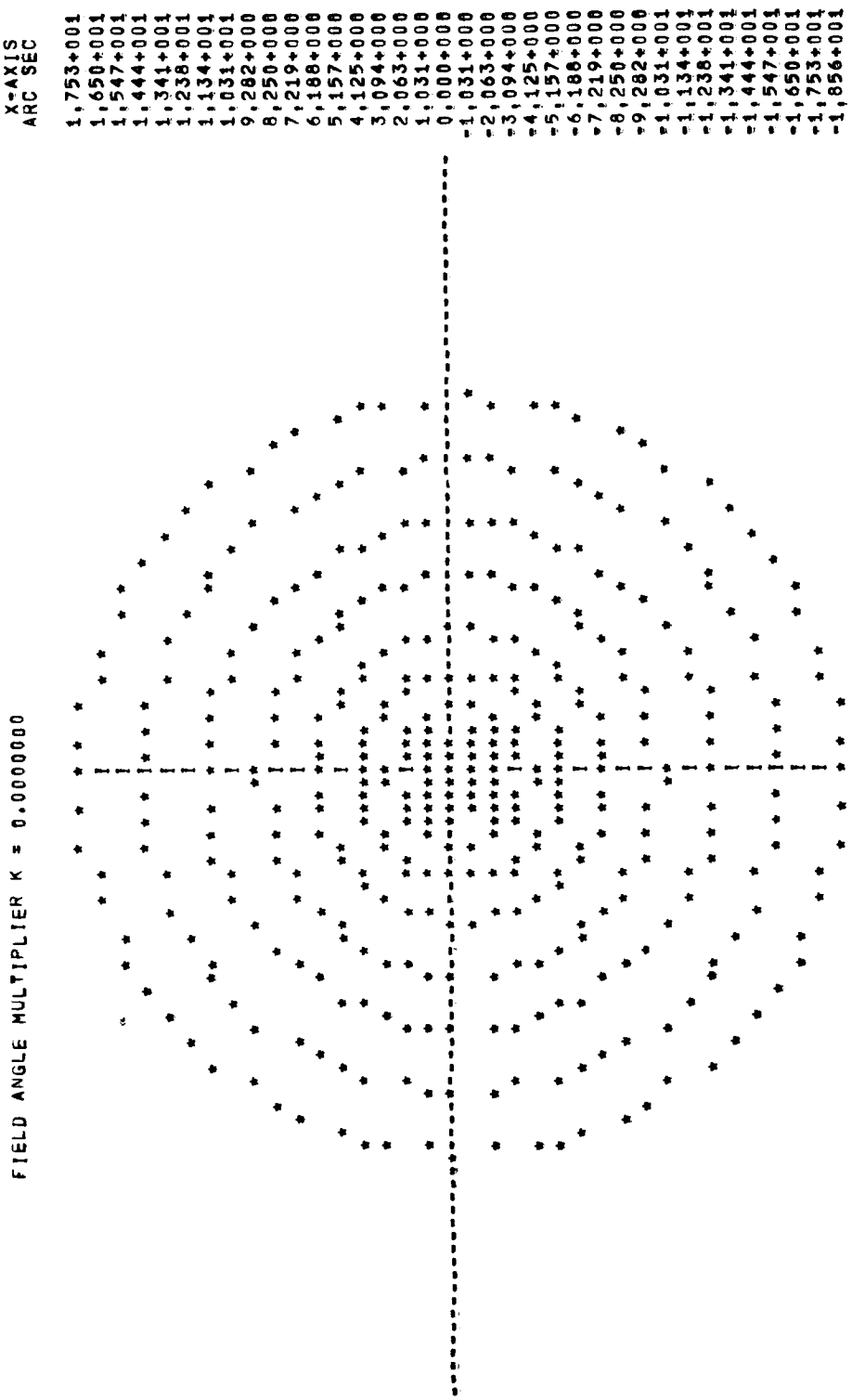

Figure 44: Spot Diagram for Scaled Super-Farron Lens; Field of View = 20^{o}; f/1.854, Incidence Angle = 0^{o}

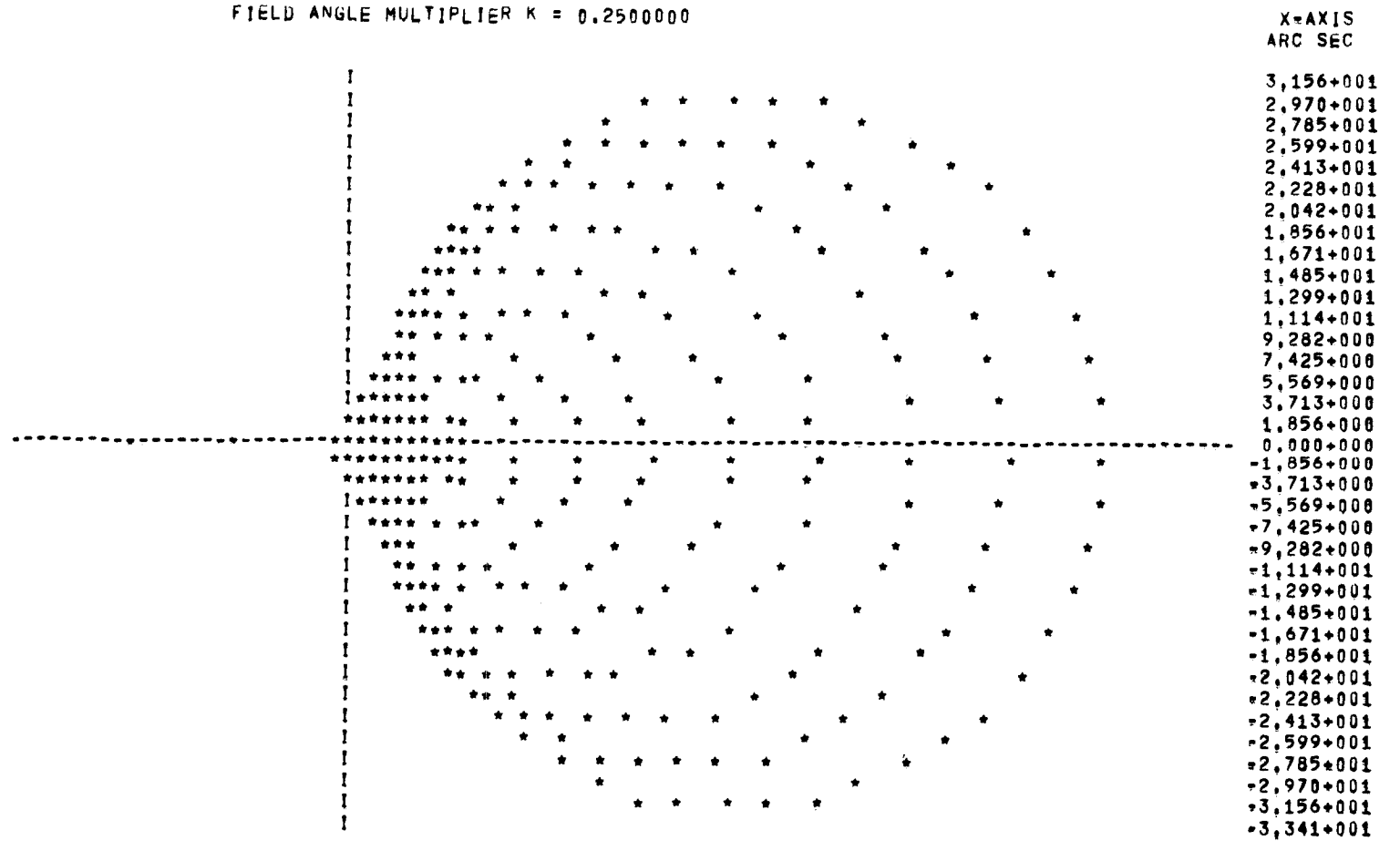

Figure 45: Spot Diagram for Scaled Super-Farron Lens; Field of View = 20^{o}; f/1.854; Incidence Angle = 2.5^{o}

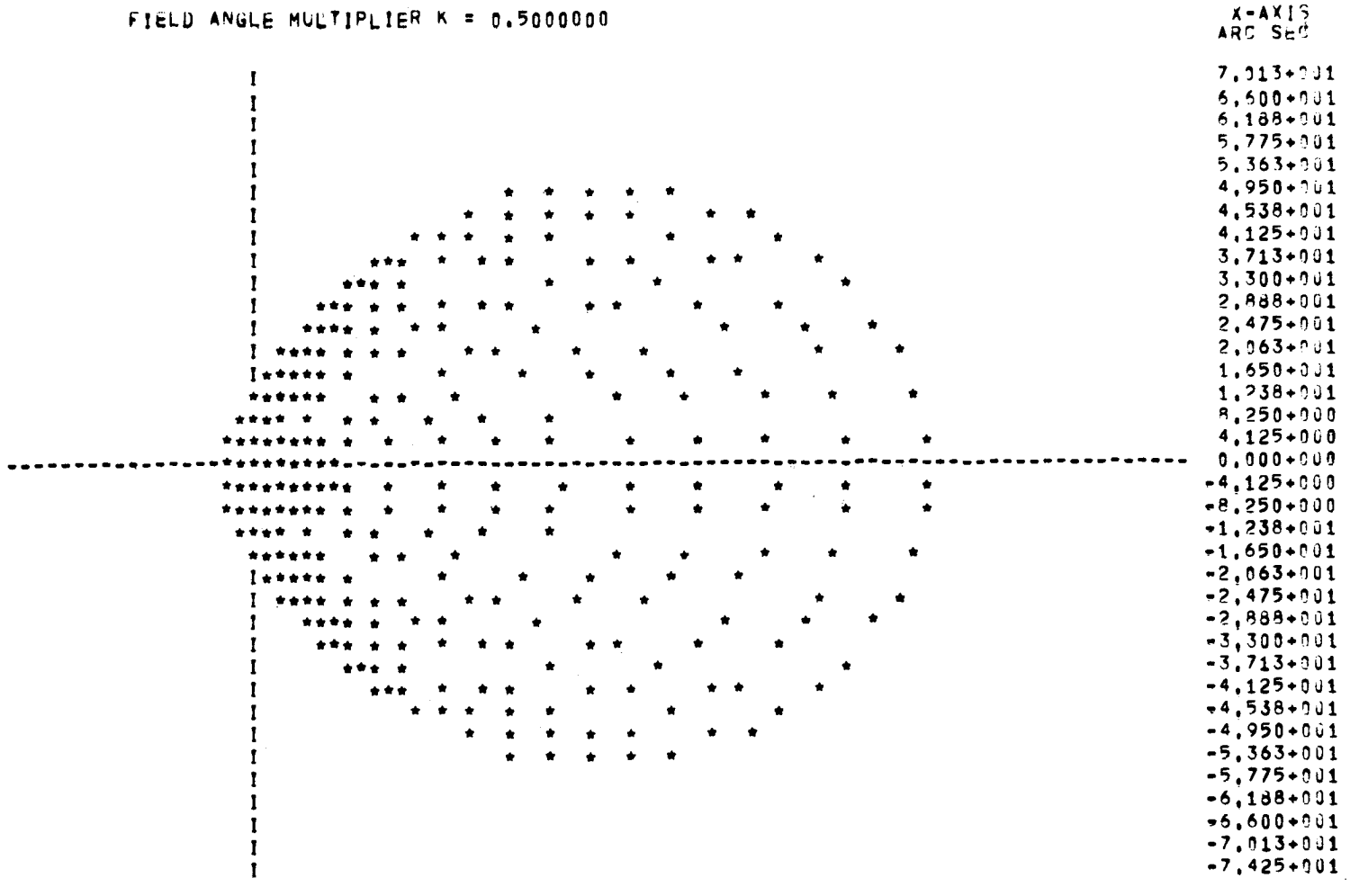

Figure 46: Spot Diagram for Scaled Super-Farron Lens; Field of View = 20^{o}; f/1.854; Incidence Angle = 5^{o}

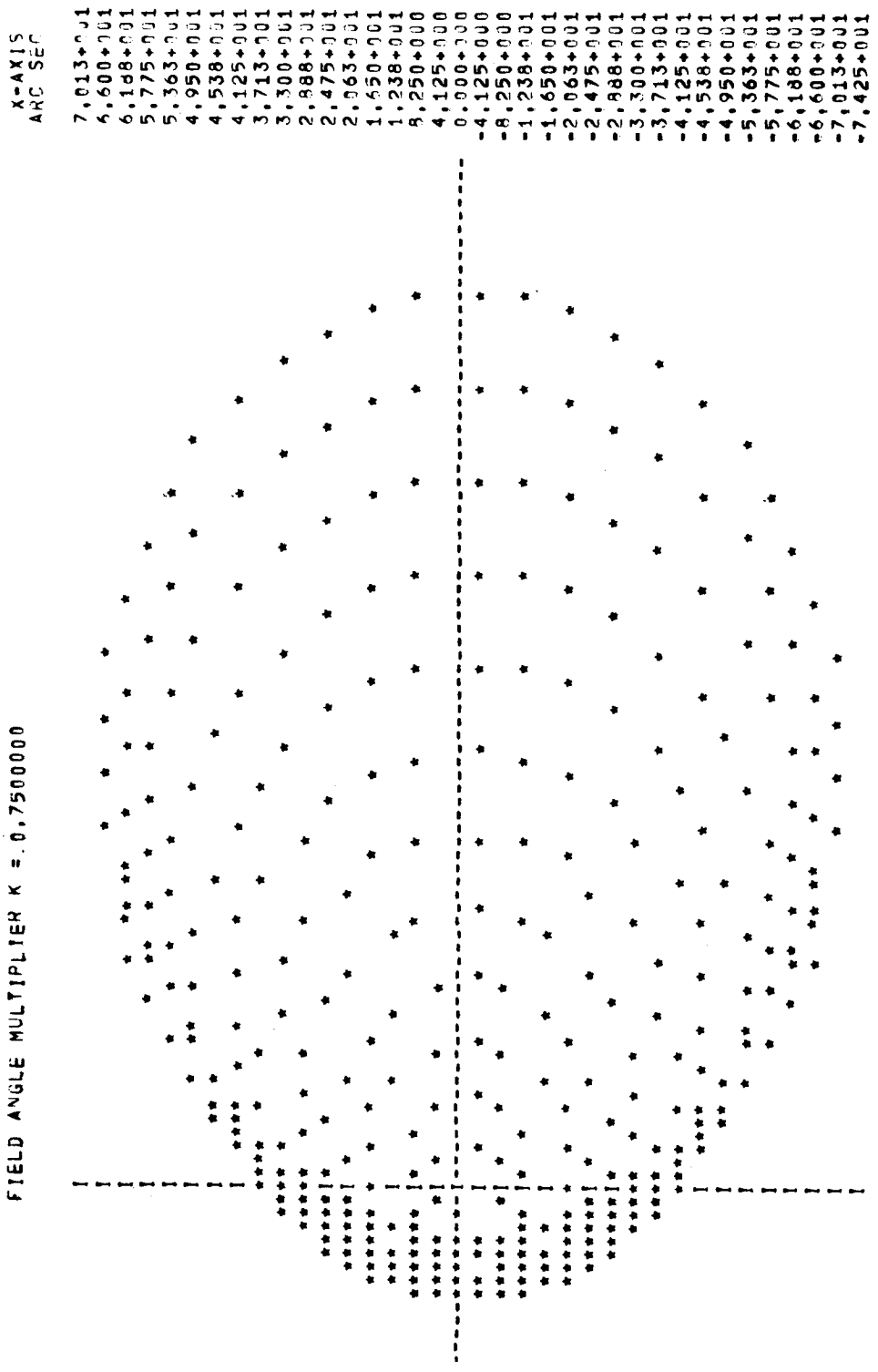

Figure 47: Spot Diagram for Scaled Super-Farron Lens; Field of View = 20^{o}; f/1.854; Incidence Angle = 7.5^{o}

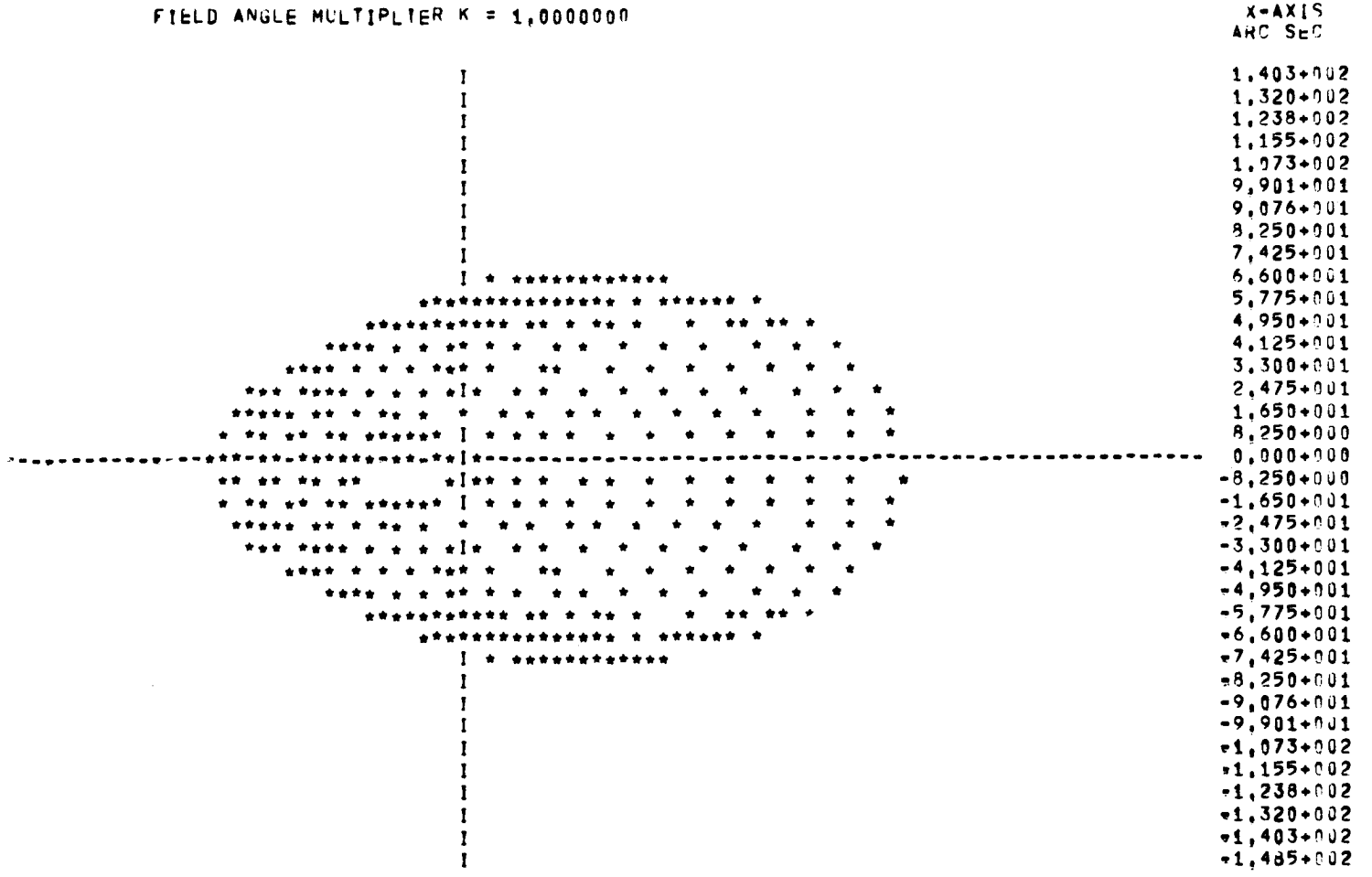

Figure 48: Spot Diagram for Scaled Super-Farron Lens, Field of View = 20^{o}; f/1.854; Incidence Angle = 10^{o}

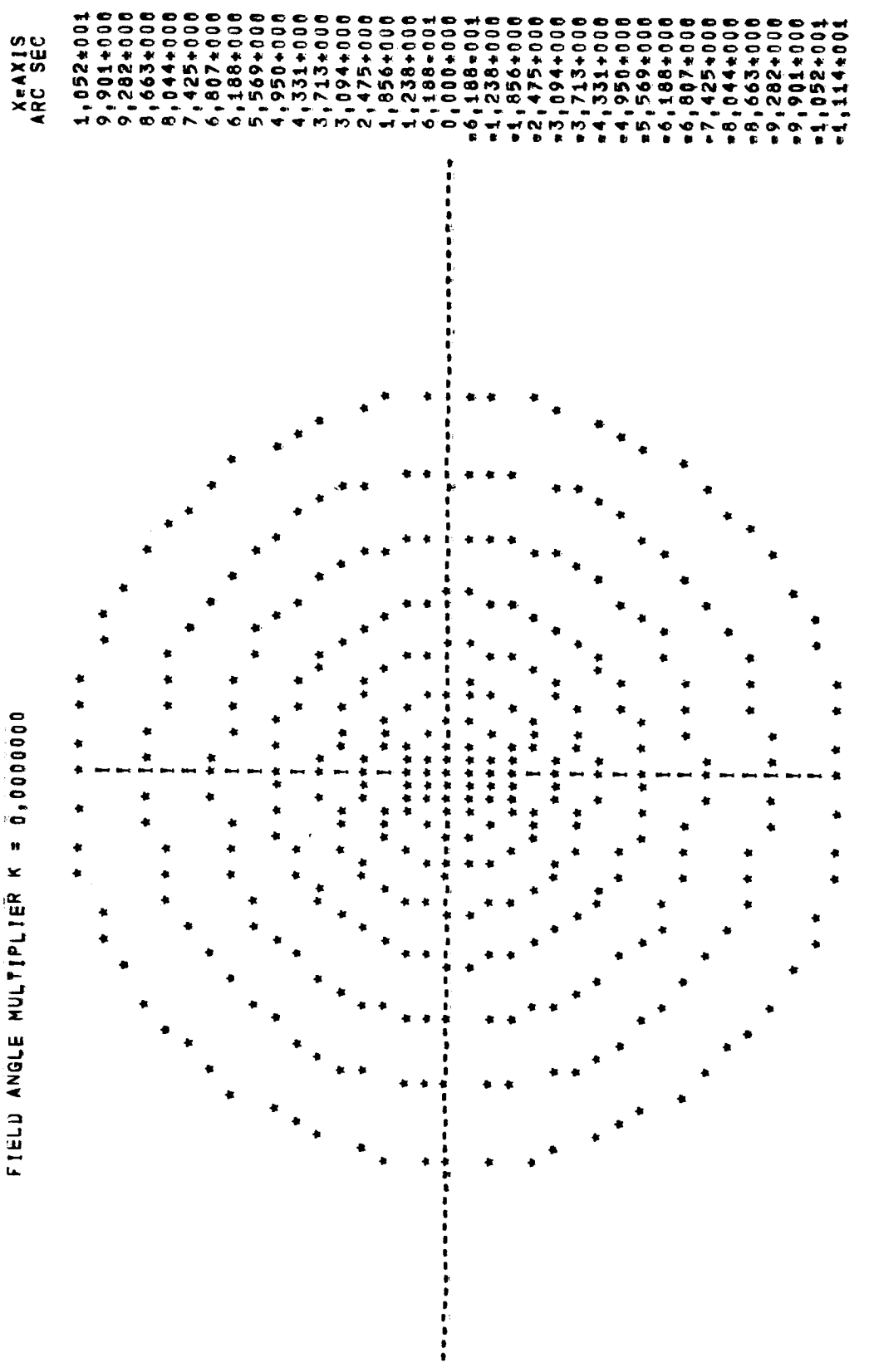

Figure 49: Spot Diagram for Scaled Super-Farron Lens; Field of View = 20^{o}; f/2.317; Incidence Angle = 0^{o}

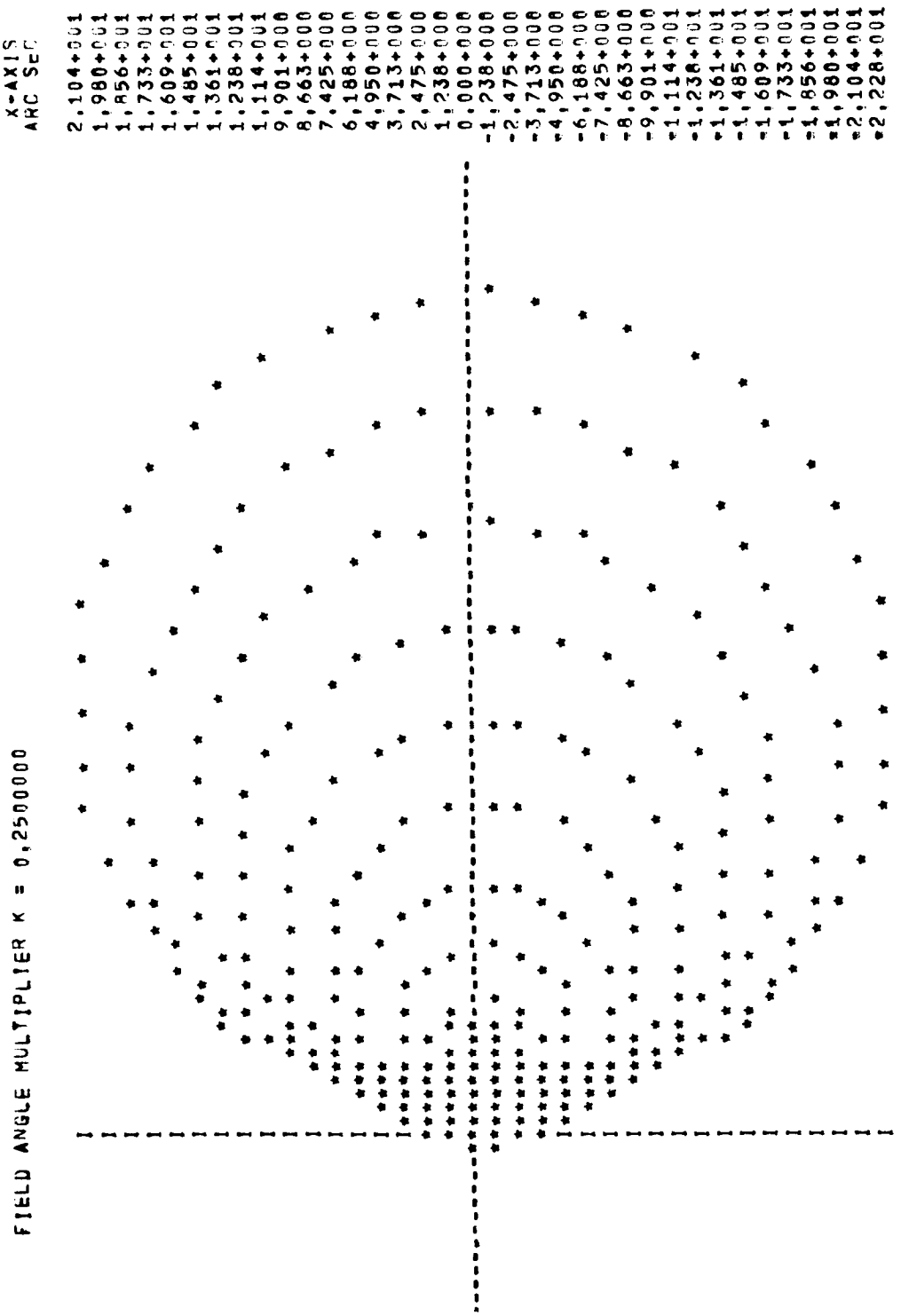

Figure 50: Spot Diagram for Scaled Super-Farron Lens; Field of View = 20^{o}; f/2.317; Incidence Angle = 2.5^{o}

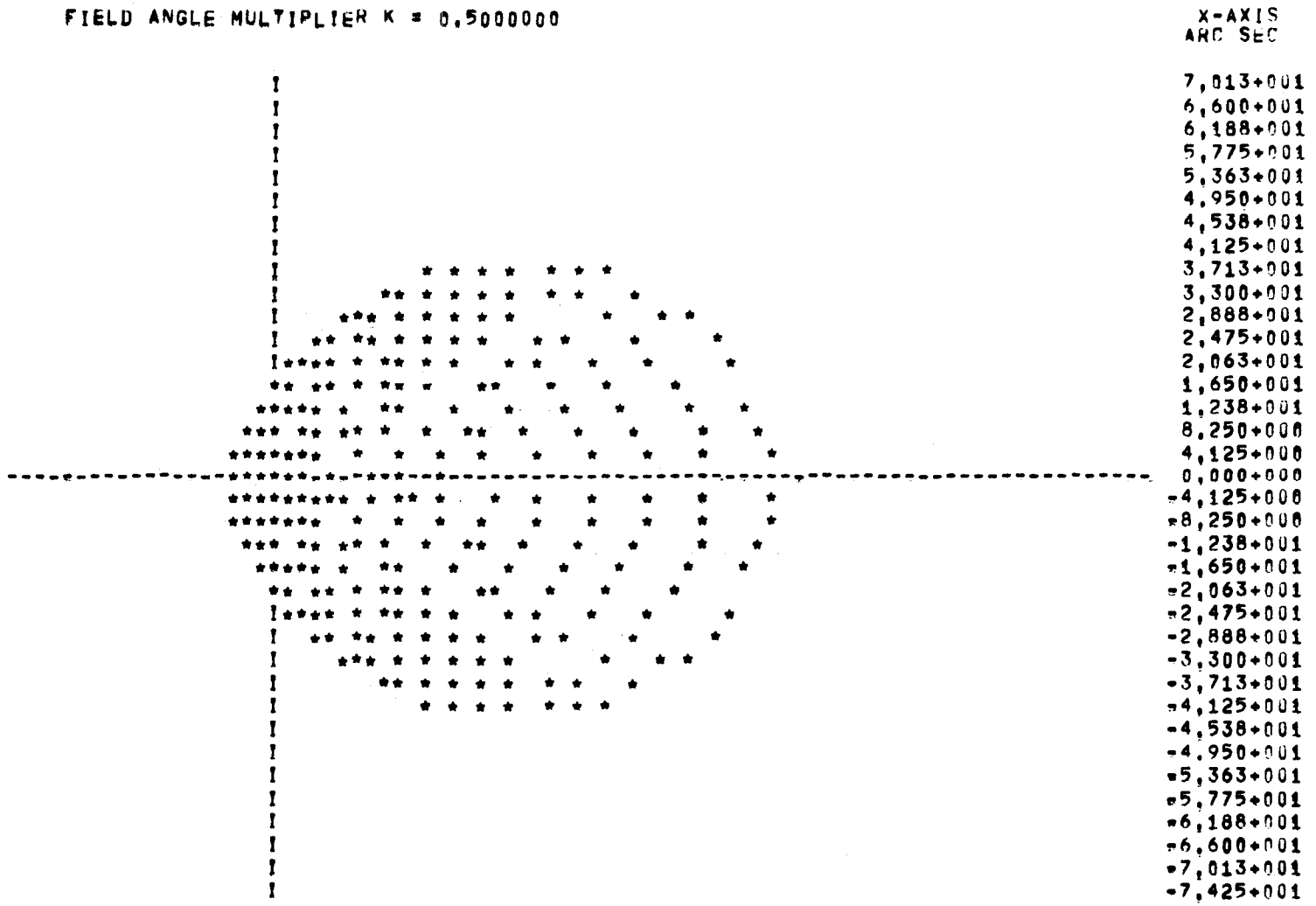

Figure 51: Spot Diagram for Scaled Super-Farron Lens; Field of View = 20^{o}; f/2.317; Incidence Angle = 5^{o}

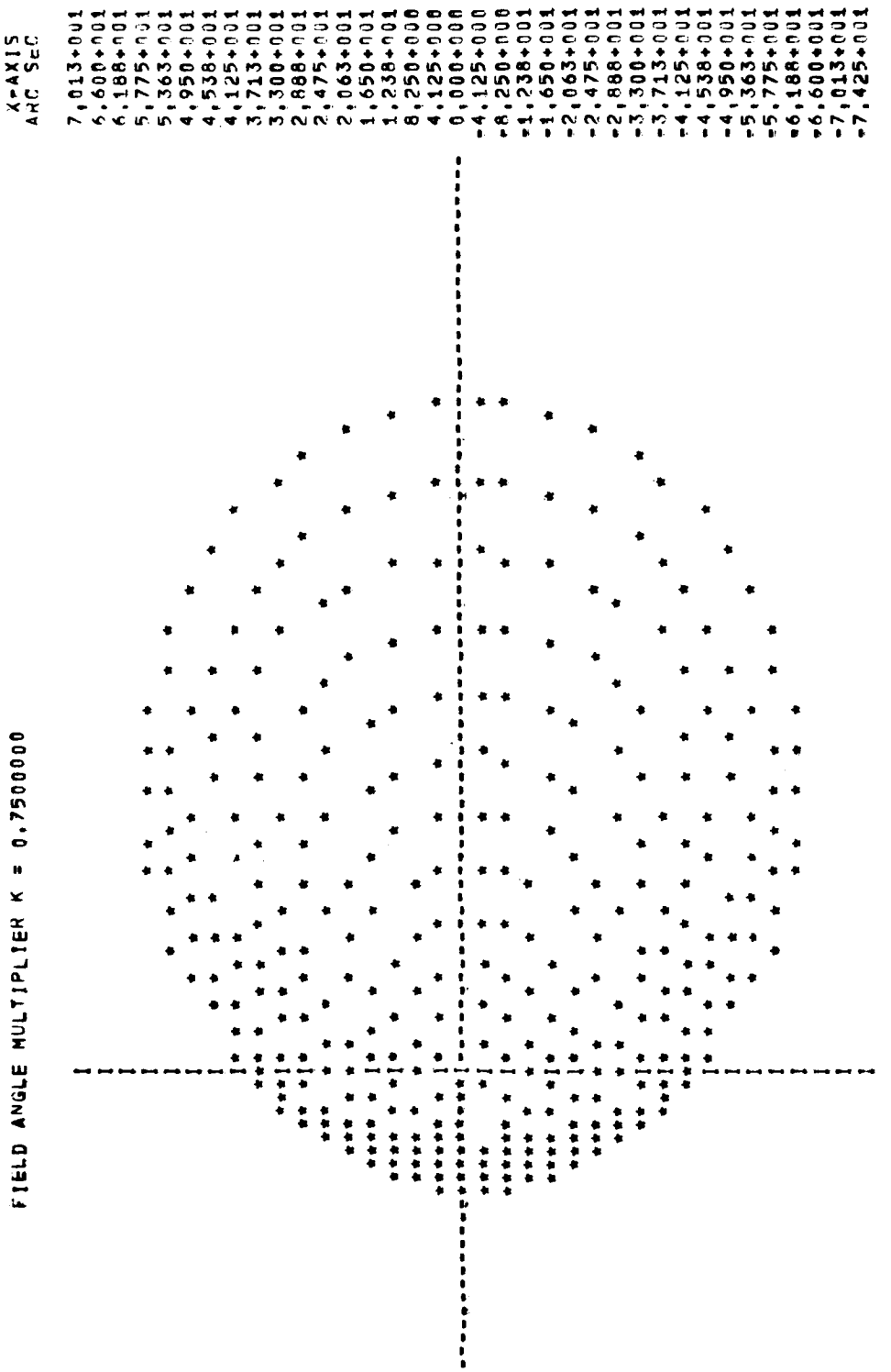

Figure 52: Spot Diagram for Scaled Super-Farron Lens; Field of View = 20^{o}; f/2.317; Incidence Angle = 7.5^{o}

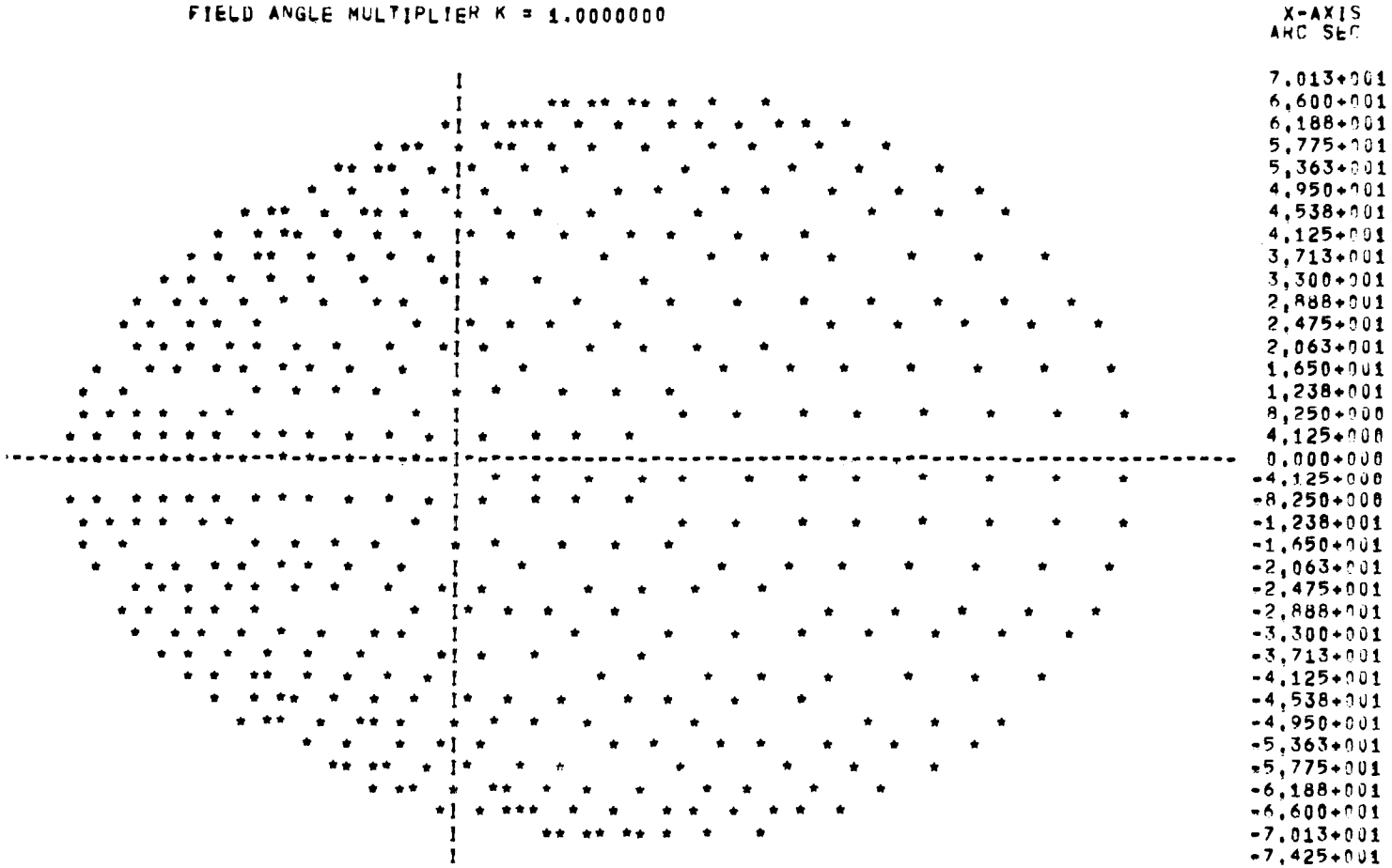

Figure 53: Spot Diagram for Scaled Super-Farron Lens; Field of View = 20^{o}; f/2.317; Incidence Angle = 10^{o}

2. Slit Design

The choice as to which slit design should be used is not an easy decision. It seems that there is no ideal design, for each design has its own advantages and disadvantages. Choosing a design thus amounts to deciding what disadvantages are tolerable or most tolerable to the total system.

Figure 54 illustrates what are considered the two best slit designs for the SCADS-IMP sensor. Of these, the single slit is favored.

First of all, the three slit and single slit designs are favored over other numbers of slits because of the problems of matching star transits. For example, if two slits are utilized, there is some difficulty in pairing the star transit times. That is, given a set of transit times, it is difficult to extract two and be sure they were produced by the same star. Such a pairing is necessary before the stars can be identified. Obviously, no pairing problem exists if a single slit is chosen.

Three slits greatly simplify the matching problem over that presented by other multiple slits. The slits can be so arranged that only triplicates of star transits are obtained such that the transit time difference between the third transit and second transit is equal to the difference between the second and first. When this test is satisfied, it is fairly certain that all three transit times were produced by the same star.

At this point, we have narrowed the choice of slit designs to the two illustrated in Figure 54. Let us now list the advantages and disadvantages of the single radial slit over the three slit design.

The advantages may be listed as follows:

1) No decision need be made as to which slit the star transits.
2) The background radiation problem is minimized. This is a strong

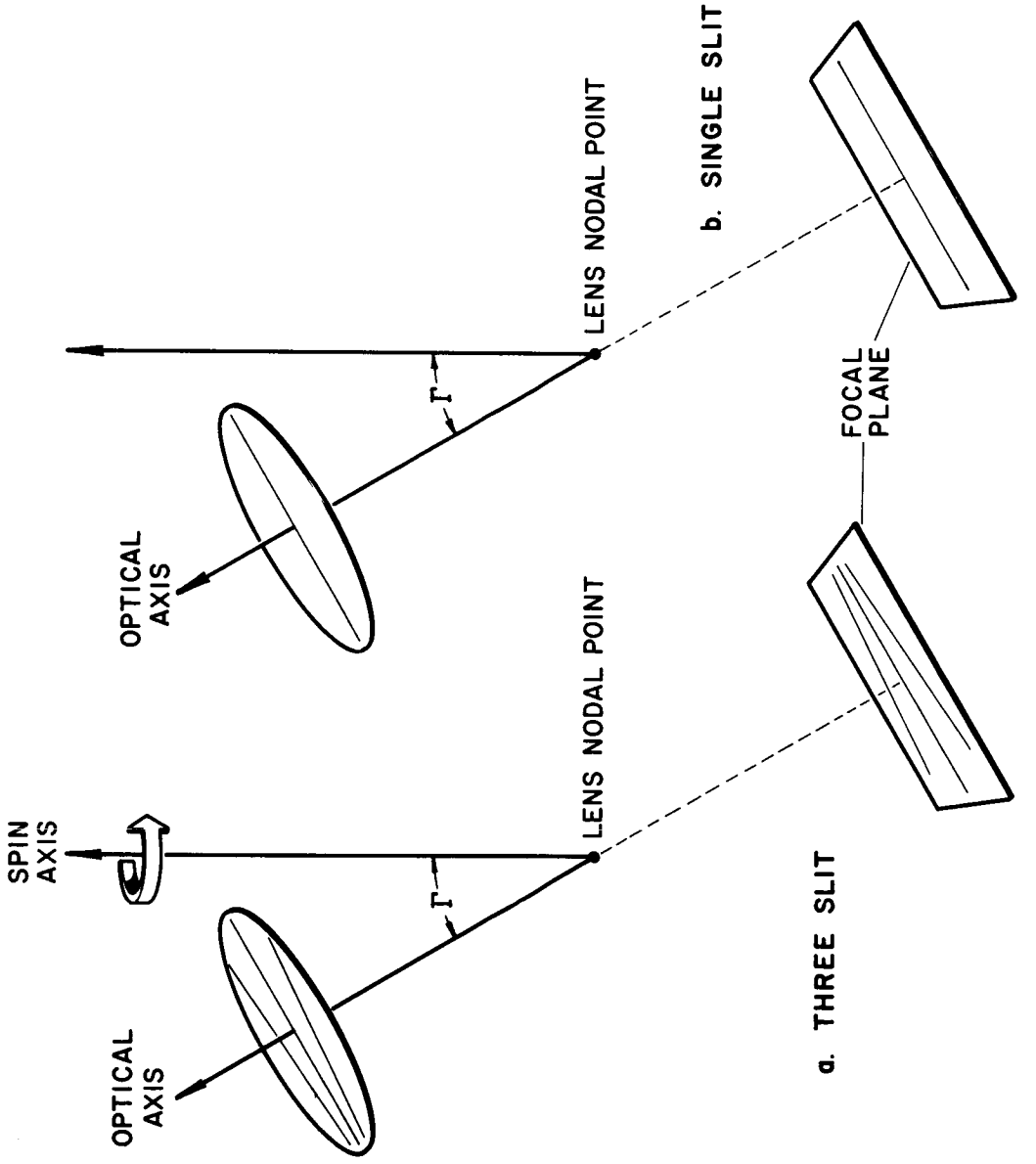

Figure 54: The Two Most Favorable Slit Designs for IMP

advantage in the case of SCADS-IMP since the sun is closer than 90^{o} to the spin axis for one-half of each scan period and the earth's limb is closer than 90^{o} to the optical axis for significant time intervals.

3) Coma, astigmatism, and other aberrations of optical systems tend to be symmetric about a radial line; thus greater accuracy can be achieved in estimating the center of the blur spot by employing a single radial slit.

4) A lens system may be chosen which minimizes sagittal (tangent to a radial line) distortions in favor of radial distortions. With a single radial slit, radial distortions cause virtually no error in determining the blur spot center.

5) Simple to fabricate.

6) The data gathering, data storage, and telemetry transmission requirements of the single slit system are less than for multiple slit systems.

The disadvantages of the single slit system are listed as follows:

1) Three stars constitute a minimum set if a single slit is used, while two stars are minimal if multiple slits are used.

2) Four or more stars are required for positive star identification (excluding magnitude data).

3) The star identification procedure is much more difficult to implement than with the three slit configuration. This is the strongest disadvantage of a single slit.

4) Errors in computed attitudes are slightly greater than with the three slit design. This statement, however, is true if both designs produce equal transit time errors; however, the transit time error would be somewhat smaller for the single slit since background noise is less for the single slit.

After considering the comparative advantages and disadvantages of the two designs, it appears that the single slit is preferable for the IMP system, particularly since small size and power are extremely important thus requiring a minimum amount of on-board data processing. The single slit is not a single line as pictured in Figure 54 , but should be wedge-shaped as explained in Reference [2], pages 28-31. The recommended slit width has been already determined as six arc minutes as projected onto the celestial sphere.

G. Electronic Design

1. Data Handling

The electronic complexity on board the SCADS-IMP vehicle depends largely upon the amount of required on-board data processing. However, the amount of on-board data processing required depends on the capacity and type of telemetry data channel(s) available for data transmission to a ground station. Since the telemetry data channels for the IMP vehicle are not explicitly specified as a part of this feasibility study, several alternative methods of data processing and transmission are mentioned. The following alternatives are included as possible methods of implementing data transmission:

(1) transmit filtered analog data only,

(2) transmit binary encoded star transit time data.

  (a) transmit all transit time data including data obtained from scanned region of celestial sphere nearest the sun,

  (b) only transmit transit time data obtained from scanned region away from sun,

  (c) selectively choose encoded transit data so only good geometry data is transmitted,

  (d) transmit transit data obtained for only the brightest stars detected during the acceptable half of the scan period away from the sun.

Of the alternatives listed above, the first alternative probably requires the least complex electronics. For this alternative, the star pulse signals would be filtered on-board the vehicle and the transit times between star transits would be encoded at the ground station. Consequently, this alternative is most susceptible to delay, distortion, and noise errors introduced by the telemetry channel. So for this alternative, the system accuracy is somewhat dependent upon the quality of any available analog telemetry channel, or conversely, the feasibility of alternative (1) depends upon telemetry channel characteristics.

Each variation of alternative two requires the binary encoding of the transit time data. Encoding transit time data on board the vehicle requires a stable oscillator, level detectors, storage registers, and control logic in addition to the analog signal filters. Since a single slit reticle is being employed, it is desirable to include encoding a crude indication of the star pulse amplitude as an aid in the star identification task.

Alternative (2a) would require a minimum amount of digital logic electronics since no selective data processing would be performed. However, this would require a relatively high bit rate PCM telemetry channel since all transit data would be transmitted.

Alternative (2b) would transmit transit data obtained from the acceptable half of the scan period only. This would require a crude sun-earth detector (solid state phototransistor detector) looking along a line 90 degrees to the spin axis in order to generate a gating signal which would inhibit data transmission for the scan period portion when the sun is closer than 90 degrees to the optical axis.

Alternative (2c) can be implemented by having a timer whose output prevents the transmission of star transit data for a certain interval after the previous star detection. The time out period for this timer would be set so 10^{o} or 15^{o} would be scanned during the interval. This alternative results in a lower required telemetry channel capacity and insures transmission of transit data for relatively good geometry stars.

Alternative (2d) would require the crude sun-earth detector described for alternative (2b) and would require a counter to count the number of star transits detected during the acceptable half of the scan period. The counter output would be required to drive a digital-to-analog converter which would raise or lower the detection threshold depending upon the number of stars detected on the previous scan.

2. Logic Design

Figure 55 shows a block diagram for the SCADS-IMP electronics which is an implementation of alternative (2a). Since no data storage is included, the number of star transits which may be transmitted per scan depends upon the continuous transmission rate of the telemetry channel. Star transits detected during the transmission interval of a transit data-word are ignored and are not transmitted; hence, alternative (2c) is also implemented by the logic functions in Figure 55. The azimuth angular separation between the closest adjacent stars whose transit data-words are transmitted depends upon the bit rate of the telemetry channel.

Only the logic blocks enclosed by the dotted lines in Figure 55 are required to implement data handling alternative (1). Note that this alternative permits a decided reduction in the complexity of on-board electronics. The only electronics required on board besides the photomultiplier are the analog signal filters and difference amplifier, the photomultiplier power supply with its automatic overload detection circuit and overload switch, and a low voltage power supply for the analog circuits.

As seen from Figure 55, the anode output of the photomultiplier (PMT) is connected to a load resistor, R_L, so that the anode current produces a negative anode signal voltage. The anode signal voltage drives a high input impedance amplifier which provides sufficient current gain to drive the relatively low input impedance to the parallel input connection of the two low pass filters labeled H and L.

The parallel connection of the two low pass filter inputs is important because by adjusting the cut-off frequencies and subtracting the respective outputs it is possible to remove the slowly varying (almost D.C.) background signal from the total signal, which includes the star signals. The slow variation in the background level is caused by the continuous scanning of portions of the celestial sphere having different background light intensities.

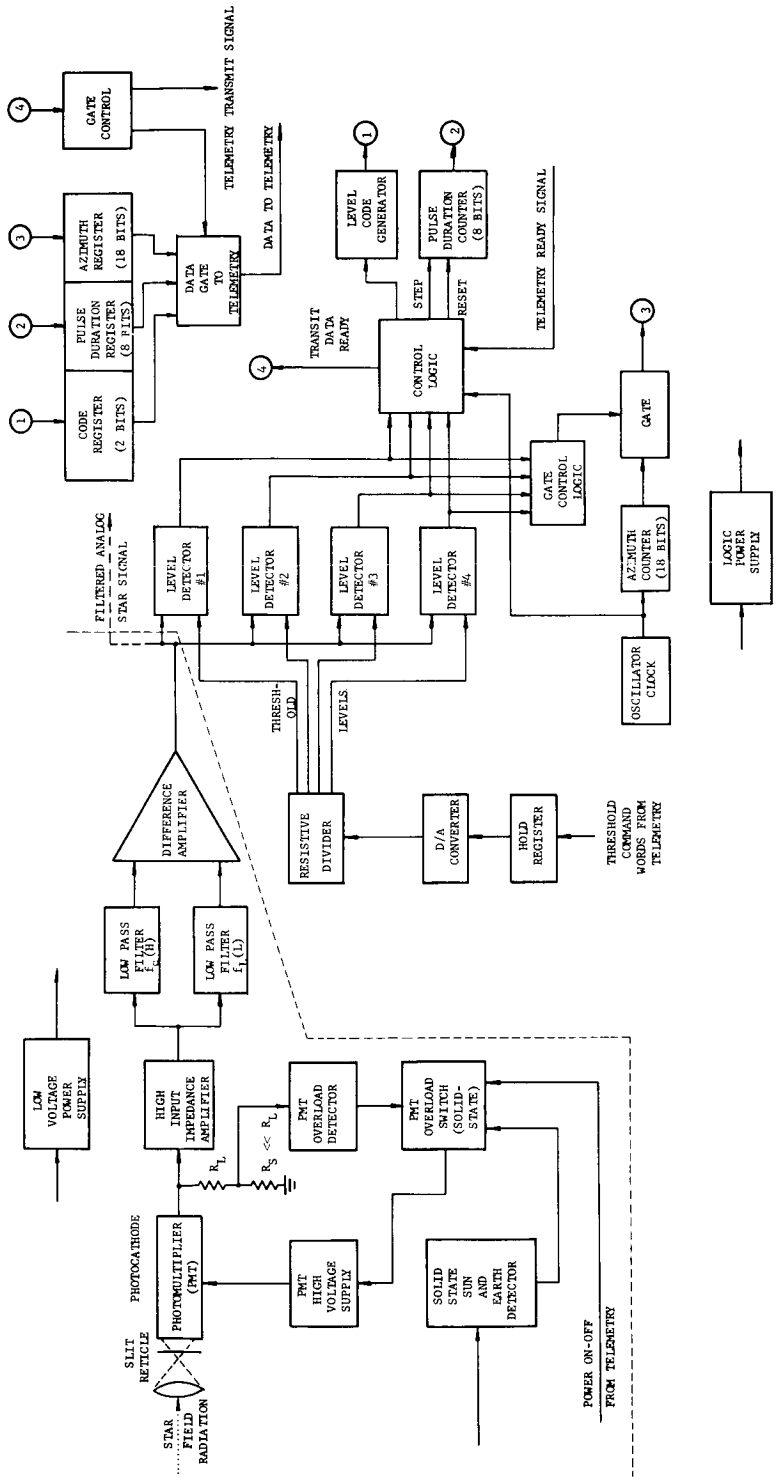

Figure 55: SCADS-IMP- On-Board Electronics Block Diagram

For example, the Milky Way background intensity is greater than for areas outside the Milky Way.

In Figure 56 waveformes illustrate why removal of the slowly varying background is desirable. The top waveform shows the output of the H (high cutoff frequency) low pass filter. The cutoff frequency of the H filter is set to attenuate the high frequency noise but still pass the star transit pulses. The middle waveform illustrates the output from the L (low cutoff frequency) low pass filter. The cutoff frequency of the L filter is set to attenuate all signals (including the star transit pulses) except the slowly varying background component. The bottom waveform is the inverted difference of the top two waveforms and illustrates the star transit pulses all rising above a common base level. Setting the threshold level as shown for the bottom waveform results in detection of all three star transit pulses shown for a single scan, whereas setting a similar threshold level for the top waveform having unfiltered background can result in missed star transit pulses, which can result in the failure to compute the attitude.

The cutoff frequency of the L filter is not particularly critical; however, certain broad restrictions must be imposed. First of all, the filter time constant (transient response time), T_f, must be much less than the rise time, T_r, of the change in background level. This restriction is necessary to insure that the L filter output will closely follow its input. So pick $T_f \leq T_r/10$. But $T_f \approx 1/\omega_c = 1/2\pi f_c$, so $f_c \geq 10/2\pi\ T_r$. Then if $T_r \cong 4$ seconds for an 8 second scan period, $f_c \geq 10/8\pi \approx .4$ cycles per second.

Another broad restriction is that the cutoff frequency of the L filter must be as low as possible to minimize the distortion to the star transit pulse after the background level has been removed. By subtracting the L filter output from the H filter output, the low frequency components of the star transit pulse are also removed along with the background level. Removing substantial low frequency components from a uni-polarity pulse has the

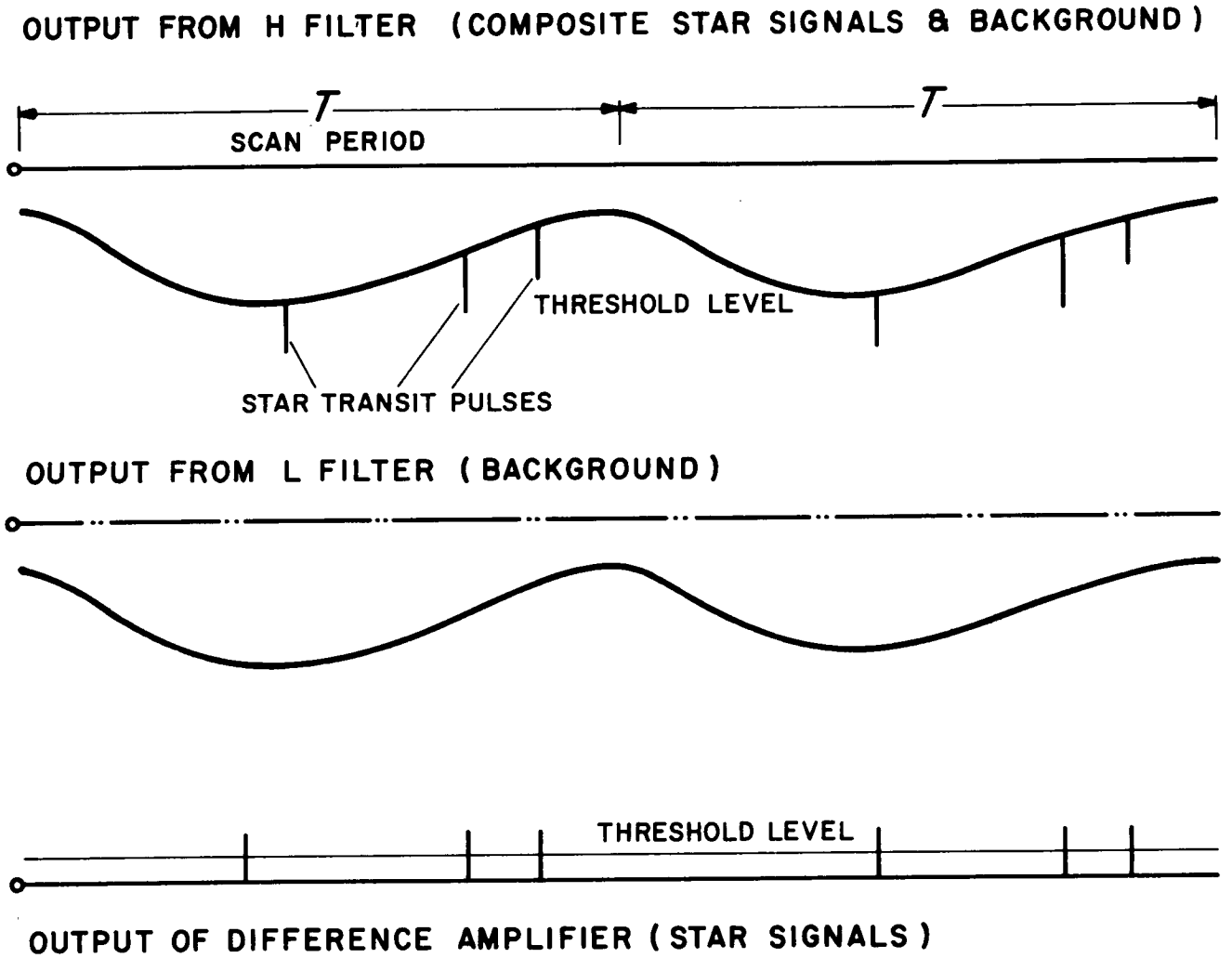

Figure 56: Waveforms Illustrating Background Filtering

effect of differentiating the pulse (Bennett [9]). Therefore, it is desirable that the L filter frequency response have a reasonably sharp roll-off. For the star transit pulse widths experienced for SCADS, the distortion caused by subtracting the low frequency components should be negligible.

The transfer function of the L filter should have a near linear phase shift versus frequency characteristic, so that the filter transient response is near critically damped.

The design parameters for the H filter of Figure 55 are considered to have a critical influence on the detection of weak star pulses and on the accuracy in locating the center of the star pulse. Consequently, a detailed discussion on star pulse signal filtering is given in Section III-G-3.

Figure 55 shows the filtered analog star signal from the difference amplifier driving the inputs to four parallel connected level detectors. The threshold for each detector is set at a different level. The purpose of this is to provide a method for crudely determining the amplitude of the star pulse and hence obtaining a crude estimate of star magnitude which serves as a very useful aid in star identification. When the filtered electrical signal has reached the lowest threshold, the corresponding level detector generates an output pulse which gates the binary representation of the star entry time from the azimuth counter into the azimuth data register and also starts the stepping of the pulse duration counter. Since the filtered star pulse has a finite slope, the next detection threshold will be reached at a somewhat later time instant provided the star pulse peak amplitude exceeds the second threshold level. As the second threshold is exceeded, the corresponding level detector generates an output pulse which also gates the output of the azimuth counter into the azimuth data register. Hence, if the oscillator clock has stepped the azimuth counter since the previous threshold was exceeded, the resulting contents of the

azimuth data register represents the azimuth count for the latest threshold crossing. The azimuth duration counter is also caused to be reset and then restarted stepping. This process for each star pulse continues until the highest threshold level below the star pulse peak has been exceeded. As the slit moves past the star and the filtered star pulse amplitude drops below the highest threshold, which is less than the pulse peak, the binary representation of the star transit duration is gated from the pulse duration counter into the pulse duration data register. Also, the highest detection threshold level less than the star pulse peak is encoded and stored in the code data register.

As soon as the complete set of data bits from a single transit pulse are stored in the data registers, a transmit signal informs the telemetry logic that a data word is ready for transmission. During transmission of the data word, no data is gated into the data registers. Hence, the logic functions of Figure 55 inherently implements data handling alternative (2c), and the spacing between star transits depends upon the data rate of the telemetry channel.

The thresholds of the level detectors may be controlled by ground station via telemetry command words. The telemetry command words are stored in a holding register which drives a digital-to-analog converter. The output level from the D/A converter is then resistively divided to form the threshold levels for the level detectors.

The frequency (or time period) of the oscillator clock must be chosen to be compatible with the sensor scan period and accuracy requirement. Since the star transit times are digitally encoded by averaging the threshold crossings of the star pulse, the clock frequency employed must provide adequate resolution so that the encoding error introduced does not excessively contribute to the total allowable error. The time encoding error must share the total allowable error with other sources

of error. The other major sources of error other than axis alignment errors have been recognized as star pulse asymmetries caused by:

(a) tangential asymmetry in the optical blur spot,

(b) asymmetry introduced by the electronic filter distortion,

(c) shot noise superimposed on the star signal.

For the SCADS-IMP sensor, it is estimated that items (a), (b), and (c) contribute approximately equally to the total error. These errors are discussed in Section V where the RMS uncertainty in the transit time introduced by shot noise is evaluated to be less than $T_s/7$ where T_s = time required for a point source to cross the slit. For a six arc minute slit width, this represents an angular uncertainty of 6/7 arc minute. So if all error sources excluding the encoding error contribution are considered independent, the combined angular uncertainty equals

$$6\sqrt{\frac{3}{49}} = 1.48 \text{ arc minute.}$$

It is reasonable to require that the transit time encoding error be comparable in comparison to the combined errors of the other major sources. Hence, a single period, T_c, of the clock frequency should correspond to an azimuth rotation of approximately 1.5 arc minute, so the clock frequency as a function of scan period may be expressed as

$$f = \frac{1}{T_c} = \frac{2.16 \times 10^4}{(1.5)\ T} \text{ cycles per second.}$$

The required clock frequencies for the scan periods of 2, 7, and 12 seconds are therefore 7.2 kc, 2.1 kc, and 1.2 kc, respectively.

Since transit time differences between stars are measured to determine star azimuth angular separations for a single scan period, only short term clock oscillator stability is required. Since the scan period is only of seconds duration, the required clock stability is readily achievable with a

conventional crystal or tuning fork oscillator.

Since a single clock period corresponds to an angular resolution of .15 arc minute, the azimuth counter must be capable of counting to

$$\frac{21600}{1.5} = 14.4 \times 10^3 < 2^{14}$$

which requires 14 binary bits.

It can be shown from the results of Section III-G-3 that the total time width at the base of the filtered star pulse corresponds to an azimuth angular rotation of approximately 25 arc minutes. Consequently, with a clock period resolution of 1.5 arc minute, the pulse duration counter must be capable of counting to 32 which requires five bits.

3. Filter Analysis and Design

The ability to detect star pulses from a photodetector in the presence of shot noise caused by background and star radiation is greatly influenced by the design parameters of the H filter shown in Figure 55. Analysis of the filtering problem is complicated by the fact that the RMS noise is dependent on the amplitude of the signal as described by the shot noise equation,

$$I_{RMS} = \left[2e \ (I_S + I_B + I_D) \ \Delta f \right]^{\frac{1}{2}} \qquad (27)$$

where

I_S = average current produced by star radiation striking the photodetector

I_B = average current produced by stellar background radiation striking the photodetector

I_D = average dark current of the photodetector

Δf = noise equivalent bandwidth of the electronic filter.

Because the noise is dependent upon the signal, the noise is non-stationary.

Consequently, to achieve optimum filtering it is apparent that the parameters of a linear filter must change with the amplitude of the signal; i.e. the filter parameters must be time variant and be capable of adapting with the magnitude of the pulse being filtered. It is impractical to implement a time variant linear filter, so to simplify matters, it will be assumed that the RMS noise is not dependent upon the signal level, in which case, the noise is considered stationary. Therefore, only linear time invariant filters will be considered.

The objective in filtering star pulses in the presence of shot noise is to minimize the attenuation of the signal while maximizing the attenuation to the RMS noise. This is equivalent to maximizing the ratio of peak signal to RMS noise. If the bandwidth of the filter passband is wide compared with that occupied by the signal energy, extraneous noise is introduced by the excess bandwidth and lowers the output signal-to-noise ratio. On the other hand, if the filter bandwidth is narrower than the bandwidth occupied by the signal, the noise energy is reduced along with a considerable part of the signal energy. The net result is again a lower signal-to-noise ratio. Thus for a given filter transfer function with a given input signal, there is an optimum bandwidth at which the signal-to-noise ratio is a maximum. For a given input signal, different filter transfer functions will yield differing maximum signal-to-noise ratios at the respective optimum bandwidths. The filter transfer function which yields the highest possible output signal-to-noise ratio is called a matched filter. It can be shown that the impulse response of the matched filter is the reverse image of the input signal; that is, it is the same as the input signal run backward in time.[10] Therefore, if the input signal is symmetrical in time, the impulse response of the matched filter must also be symmetrical. The output signal from any filter can be described by the convolution integral of the filter impulse response and the input signal,

$$y(t) = \int_{\tau_1}^{\tau_2} f(\tau) \cdot h(t - \tau)\, d\tau \qquad (28)$$

where

$f(t)$ = the input signal

$h(t)$ = the filter impulse response.

So if the input signal is symmetrical, then the output signal from a matched filter is also symmetrical.

A matched filter may not be physically realizable depending upon the form of the input signal it is required to match. If a matched filter is not physically realizable, then the desired filter is a physically realizable filter which has the highest output signal-to-noise ratio for the given input signal. If one filter transfer function has a higher maximum signal-to-noise ratio than another transfer function for a given input signal, then the filter with the higher signal-to-noise ratio is closest to matching the signal. So by calculating and comparing the maximum signal-to-noise ratios for two or more filter transfer functions and a given input signal, the filter most closely matching the input signal may be determined.

The form of the star pulse from the photodetector of a scanning optical system depends upon the energy density profile of the star image blur circle and the relative size of the rotating slit with respect to the blur circle. If the optical system produces a diffraction pattern that is two dimensional Gaussian, the energy density in the focal plane is given by[11]

$$I(x, y) = \frac{\epsilon_o \lambda_s}{2\pi \sigma^2} e^{\left[-\frac{1}{2\sigma^2}(x^2+y^2)\right]} \tag{29}$$

where

ϵ_o denotes the optical efficiency,

λ_s = average number of photons received from the star per unit time.

Let the slit width be chosen such that 80 percent of the star radiation passes the slit when the blur circle is centered in the slit. If T_s equals

the time it takes the center of the star image to cross the slit, then the average photon arrival rate at the photomultiplier is described by[11]

$$f_s(t) = \epsilon_o \lambda_s G(t) \tag{30}$$

where

$$G(t) = \Phi\left(\frac{t}{\sigma} + \frac{T_s}{2\sigma}\right) - \Phi\left(\frac{t}{\sigma} - \frac{T_s}{2\sigma}\right)$$

and

$$\Phi(t) = \frac{1}{\sqrt{2\pi}} \int_{-\infty}^{t} e^{-\frac{1}{2}x^2}\, dx.$$

Note that 80 percent of the star radiation passes through the slit when[11]

$$\frac{T_s}{2} = 1.28\,\sigma.$$

The function G(t) is graphed in Figure 57.

The average value of the photodetector output signal will be described by

$$f(t) = K\,G(t) \tag{31}$$

The impulse response in Equation (28) can be obtained analytically by finding the inverse Laplace transform of the filter transfer function, H(s). In general, H(s) will contain terms of the form

$$\frac{2\left[a\left(\frac{s}{\omega} + \alpha\right) + b\beta\right]}{\left(\frac{s}{\omega} + \alpha\right)^2 + \beta^2} \tag{32}$$

whose inverse transform is of the form

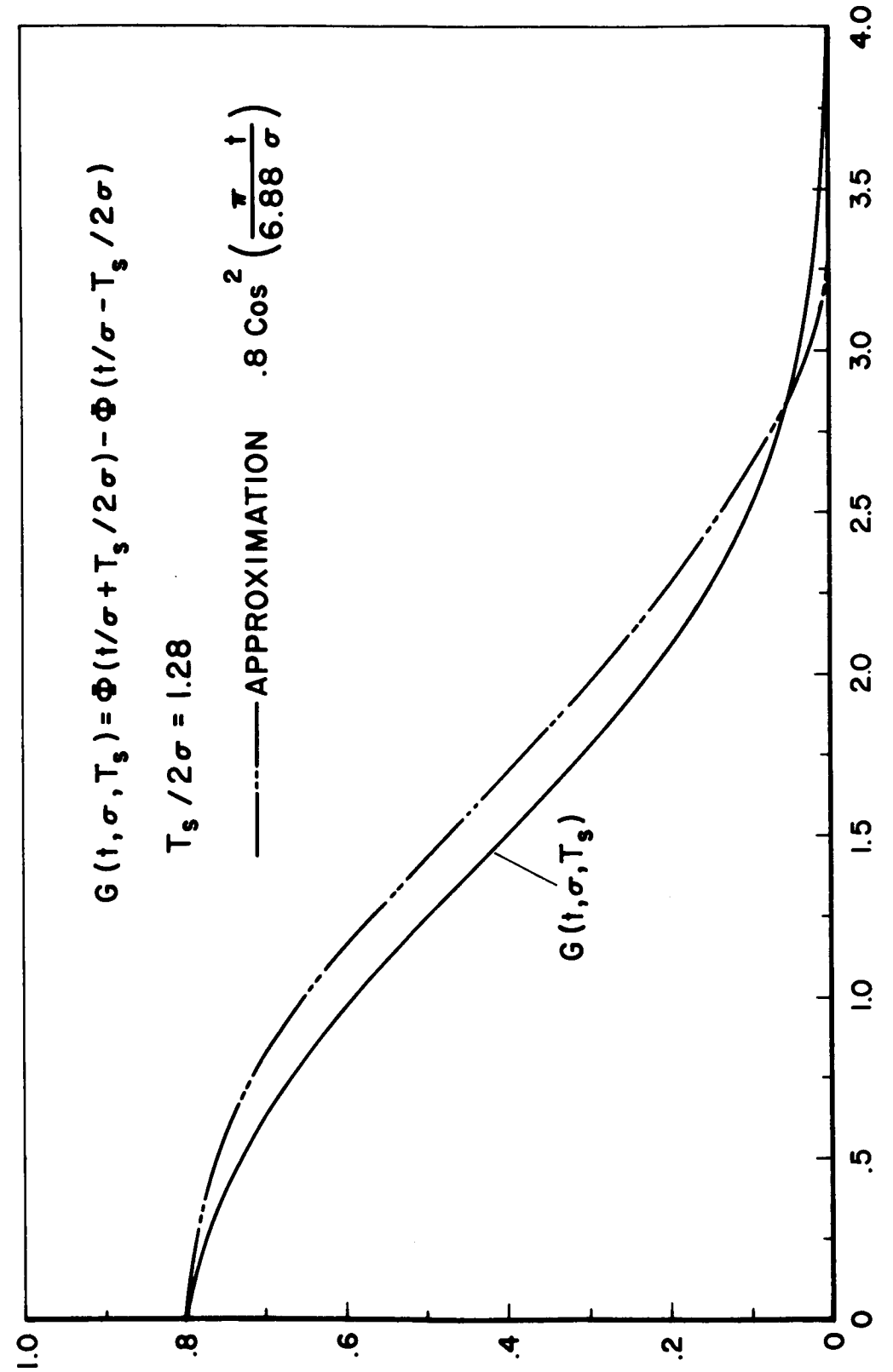

Figure 57: Percent of Star Radiation Passing Scanning Slit

$$h_i(t) = 2a_\omega e^{-\alpha\omega t} \cos(\beta\omega t) + 2b_\omega e^{-\alpha\omega t} \sin(\beta\omega t) \tag{33}$$

Equation (28) cannot be integrated in closed form after substitution of Equations (31) and (33). However, G(t) can be approximated by

$$f(t) = (.8) \cos^2\left(\frac{\pi}{2k}\frac{t}{\sigma}\right) \tag{34}$$

where k is selected to "minimize" the discrepancy between G(t) and f(t). It can be shown that[11]

$$\int_{-\infty}^{+\infty} G(t)\, dt = T_s \tag{35}$$

Also

$$\int_{-\infty}^{+\infty} f(t)\, dt = .8\, k\sigma \tag{36}$$

Now if $G(t)/T_s$ and $f(t)/.8\, k\sigma$ are considered as probability density functions, their second moments can be equated to determine k. It has been shown that the second moment[11]

$$\int_{-\infty}^{+\infty} t^2 \frac{G(t)}{T_s}\, dt = \sigma^2\left[1 + \frac{1}{3}\left(\frac{T_s}{2\sigma}\right)^2\right] \tag{37}$$

The second moment for $f(t)/(.8\, k\sigma)$ has been evaluated as

$$(.8)\int_{t=-k\sigma}^{t=+k\sigma} t^2 \frac{\cos^2\left(\frac{\pi}{2k}\frac{t}{\sigma}\right)}{(.8\, k\sigma)} = (k\sigma)^2 \frac{2}{\pi^2}\left[\frac{\pi^2}{6} - 1\right] = (k\sigma)^2\, (.130688)$$

For $T_s/2\sigma = 1.28$, $k = 3.44$. Hence,

$$f(t) = (.8) \cos^2 At \tag{38}$$

where

$$A = \frac{\pi}{6.88\,\sigma}$$

The function $f(t) = (.8) \cos^2 At$ is shown graphed in Figure 57. By shifting the time axis of Figure 57, G(t) can be approximated by

$$f(t) = (.8) \sin^2 At = (.8)/2\ (1 - \cos^2 At) \text{ for } 0 \leq t \leq \frac{\pi}{A} \qquad = 0 \text{ elsewhere.} \tag{39}$$

Now Equation (28) can be integrated analytically after substitution of Equations (33) and (39).

The optimum value for ω_c is that value which maximizes the ratio

$$\frac{S}{N} = \frac{y_{peak}(t, \omega_c)}{I_{RMS}} \tag{40}$$

where

$$I_{RMS}^2 = N_R^2 \int_0^\infty |H(f)|^2\, df = N_R^2 \frac{\omega_c}{2\pi} \frac{1}{2} \int_{-\infty}^{+\infty} |H(jx)|^2\, dx \tag{41}$$

= mean noise output power from the filter with white noise input.[12]

$$j(x) = j \frac{\omega}{\omega_c} = \frac{s}{\omega_c}$$

N_R = input RMS noise per unit bandwidth

$$= [2e(I_S + I_B + I_D)]^{\frac{1}{2}}$$

Comparing Equations (27) and (41) shows that the noise equivalent bandwidth is given by

$$\Delta f = \frac{\omega_c}{4\pi} \int_{-\infty}^{+\infty} |H(jx)|^2 \, dx \tag{42}$$

Since the integral in Equation (41) evaluates to a constant, the value of ω_c which maximizes Equation (40) may be determined from the ratio

$$\frac{y_{peak}(t, \omega_c)}{\sqrt{\omega_c}} \tag{43}$$

If two or more filter transfer functions are to be compared, Equation (41) must be evaluated and used to determine Equation (40) for each case. The transfer function which has the largest maximum value for Equation (40) has the impulse response which most closely matches the given input signal.

By comparing the maximum value of Equation (40) for the two pole transfer function with the maximum value of Equation (40) for the six pole case, it is possible to compare the effectiveness of each filter.

The two pole transfer function of a linear phase shift versus frequency filter is given by[13]

$$H(s) = \frac{1}{4\left(\frac{s}{\omega_c}\right)^2 + 3\left(\frac{s}{\omega_c}\right) + 1} = \frac{1}{4}\left\{\frac{2\,b\beta}{\left(\frac{s}{\omega_c} + \alpha\right)^2 + \beta^2}\right\} \tag{44}$$

where

$b = 1.51186$

$\alpha = .375$

$\beta = .331$

The numerator of Equation (40) will be evaluated by writing the analytic expression for y(t) and then numerically determining $y_{peak}(t, \omega_c)$ with a programmed digital computer. In order to determine y(t), the filter impulse response must be known. The filter impulse response is

$$h(t) = \frac{2}{4} \; b \; \omega \; e^{-\alpha\omega t} \sin(\beta\omega t) \tag{45}$$

The expression for y(t) is derived as follows:

$$y(t) = \int f(\tau) \cdot h(t - \tau) \, d\tau \tag{46}$$

where

$$f(\tau) = \sin^2 A\tau = \frac{1}{2} - \frac{\cos 2A\tau}{2} \quad \text{for } 0 \leq \tau \leq \frac{\pi}{A}$$
$$= 0 \quad \text{elsewhere} \tag{47}$$

and in general

$$\frac{h(t-\tau)}{k} = \sum_i \left[2 \, a_i \, \omega \, e^{-\alpha_i \omega (t-\tau)} \cos\left\{\beta_i \omega (t-\tau)\right\} + 2 b_i \omega \, e^{-\alpha_i \omega (t-\tau)} \sin\left\{\beta_i \omega (t-\tau)\right\} \right]$$

Since the terms of y(t) are similar for a given value of subscript i, the derivation will proceed for all terms having the same subscript. The terms of y(t) for the remaining subscripts are then summed to give the final result. For the remainder of the derivation let

$$a = a_i \, \omega \qquad b = b_i \, \omega$$
$$\alpha = \alpha_i \, \omega \qquad \beta = \beta_i \, \omega$$

$$\frac{y_i(t)}{k} = (2a \cos \beta t + 2b \sin \beta t) \frac{e}{2}^{-\alpha t} \int e^{\alpha \tau} \cos \beta \tau \, d\tau$$

$$+ (2a \sin \beta t - 2b \cos \beta t) \frac{e}{2}^{-\alpha t} \int e^{\alpha \tau} \sin \beta \tau \, d\tau$$

$$- (2a \cos \beta t + 2b \sin \beta t) \frac{e}{2}^{-\alpha t} \left\{ \begin{array}{l} \int \frac{e}{2}^{\alpha \tau} \cos[(2A + \beta) \tau] \, d\tau \\ + \int \frac{e}{2}^{\alpha \tau} \cos[(2A - \beta) \tau] \, d\tau \end{array} \right\}$$

$$+ (-2a \sin \beta t + 2b \cos \beta t) \frac{e}{2}^{-\alpha t} \int e^{\alpha \tau} \cos 2A\tau \sin \beta \tau \, d\tau \qquad (48)$$

For $0 \leq t \leq \frac{\pi}{A}$,

$$\frac{y_i(t)}{k} = -\frac{1}{2}(a \cos \beta t + b \sin \beta t)\left\{\begin{array}{l}\dfrac{\alpha \cos[(2A+\beta)t] + (2A+\beta)\sin[(2A+\beta)t]}{\alpha^2 + (2A+\beta)^2} \\ \\ + \dfrac{\alpha \cos[(2A-\beta)t] + (2A-\beta)\sin[(2A-\beta)t]}{\alpha^2 + (2A-\beta)^2}\end{array}\right\}$$

$$+\frac{1}{2}(a \cos \beta t + b \sin \beta t)\, e^{-\alpha t}\left\{\frac{\alpha}{\alpha^2 + (2A+\beta)^2} + \frac{\alpha}{\alpha^2 + (2A-\beta)^2}\right\}$$

$$+\frac{1}{2}(-a \sin \beta t + b \cos \beta t)\left\{\begin{array}{l}\dfrac{\alpha \sin[(\beta+2A)t] - (\beta+2A)\cos[(\beta+2A)t]}{\alpha^2 + (\beta+2A)^2} \\ \\ + \dfrac{\alpha \sin[(\beta-2A)t] - (\beta-2A)\cos[(\beta-2A)t]}{\alpha^2 + (\beta-2A)^2}\end{array}\right\}$$

$$+\frac{1}{2}(-a \sin \beta t + b \cos \beta t)\, e^{-\alpha t}\left\{\frac{(\beta+2A)}{\alpha^2 + (\beta+2A)^2} + \frac{(\beta-2A)}{\alpha^2 + (\beta-2A)^2}\right\}$$

$$+\frac{a\alpha + b\beta}{\alpha^2 + \beta^2} - \left[\frac{a\alpha + b\beta}{\alpha^2 + \beta^2}\right] e^{-\alpha t} \cos \beta t$$

$$+\left[\frac{a\beta - b\alpha}{\alpha^2 + \beta^2}\right] e^{-\alpha t} \sin \beta t \qquad (49)$$

For $t > \frac{\pi}{A} = 6.5 = R$

$$\frac{y_i(t)}{k} = (a \cos \beta t + b \sin \beta t)\, e^{-\alpha t} \left\{\frac{e^{\alpha R}(\alpha \cos \beta R + \beta \sin \beta R) - \alpha}{\alpha^2 + \beta^2}\right\}$$

$$+ (a \sin \beta t - b \cos \beta t)\, e^{-\alpha t} \left\{\frac{e^{\alpha R}(\alpha \sin \beta R - \beta \cos \beta R) + \beta}{\alpha^2 + \beta^2}\right\}$$

$$- \frac{1}{2}(a \cos \beta t + b \sin \beta t)\, e^{-\alpha t} \left\{\begin{array}{l} \dfrac{e^{\alpha R}[\alpha \cos[(2A + \beta)R] + (2A + \beta) \sin[(2A+\beta)R]]}{\alpha^2 + (2A + \beta)^2} \\ + \dfrac{e^{\alpha R}[\alpha \cos[(2A - \beta)R] + (2A - \beta) \sin[(2A-\beta)R]]}{\alpha^2 + (2A - \beta)^2} \\ - \dfrac{\alpha}{\alpha^2 + (2A + \beta)^2} - \dfrac{\alpha}{\alpha^2 + (2A - \beta)^2} \end{array}\right\}$$

$$+ \frac{1}{2}(- a \sin \beta t + b \cos \beta t) e^{-\alpha t} e^{\alpha R} \left\{\begin{array}{l} \dfrac{\alpha \sin[(\beta+2A)R] - (\beta+2A) \cos[(\beta+2A)R]}{\alpha^2 + (\beta + 2A)^2} \\ + \dfrac{\alpha \sin[(\beta-2A)R] - (\beta-2A) \cos[(\beta-2A)R]}{\alpha^2 + (\beta - 2A)^2} \end{array}\right\}$$

$$+ \frac{1}{2}(- a \sin \beta t + b \cos \beta t)\, e^{-\alpha t} \left\{\frac{(\beta + 2A)}{\alpha^2 + (\beta + 2A)^2} + \frac{(\beta - 2A)}{\alpha^2 + (\beta - 2A)^2}\right\}$$

Finally, $y(t) = \sum_i y_i(t)$ (50)

The denominator of Equation (40) may be evaluated by finding the partial fraction expansion of the integrand of Equation (41) and then applying the residue theorem for integrating about a closed contour.[14] The terms of the partial fraction expansion whose poles are in the upper half of the complex plane have been determined to be

$$\frac{(1.51186 - j\ 1.3333)}{(x + .3307 - j\ .375)}\ ,\ \frac{(-\ 1.51186 - j\ 1.3333)}{(x - .3307 - j\ .375)}$$

The complex number in each numerator is the residue of the integrand at the pole in the denominator. Now, by applying the residue theorem to evaluate the contour integral along a contour enclosing the upper half of the complex plane

$$\int_{-\infty}^{+\infty} |\ H(jx)\ |^2\ dx = (.25)^2\ 2\pi j\ [-2j(1.3333)] \tag{51}$$

So the noise equivalent bandwidth is

$$\Delta f = .5236\ f_c$$

and

$$N^2 = N_R{}^2\ \omega_c (.288675)^2$$

Equation (40) has been numerically determined versus ω_c for an arbitrarily chosen value of σ = .945 second in Equation (38). The results are tabulated in Table VII.

The results show that for σ = .945 second, the maximum output signal-to-noise ratio occurs for ω_c = 1.425. Hence, the product of $\sigma\ \omega_c$ at the highest signal-to-noise ratio is

$$\sigma\ \omega_c = (.945)(1.425) = 1.3466. \tag{52}$$

TABLE VII

PAYNTER (TWO POLE)

ω_c	$y_{peak} = P$	$\frac{I_{RMS}}{N_R} = (.28867512)\sqrt{\omega_c}$	$\frac{S}{N} = \frac{P\ N_R}{I_{RMS}}$
.85	.53836585	.26614530	2.022827
.875	.5502444	.27003084	2.037709
.9	.56183025	.27386126	2.051514
.925	.57312310	.27763883	2.064276
.95	.58412010	.28136570	2.076017
.975	.59485080	.28504384	2.086875
1.0	.60520320	.28867512	2.096485
1.025	.61555600	.29226128	2.106184
1.050	.62546210	.29580397	2.114448
1.075	.63505385	.29930473	2.12176349
1.1	.64457133	.30276501	2.12894921
1.125	.65371960	.30618620	2.13503939
1.15	.66253510	.30956957	2.14018160
1.175	.671353700	.31291637	2.14547324
1.2	.679744230	.31622774	2.14954017
1.225	.687771620	.31950480	2.15261748
1.250	.696012770	.32274859	2.15651684
1.275	.70384025	.32596010	2.15928345
1.30	.71140062	.32914027	2.16139040
1.325	.71878055	.33229001	2.16311212
1.350	.72595855	.33541017	2.16439039
1.375	.73296757	.33850158	2.16532983
1.40	.73976330	.34156500	2.16580533
1.425	.74637345	.34460119	2.16590502
1.45	.752804150	.34761087	2.16565192
1.475	.75906802	.35059471	2.16508691
1.50	.76515792	.35355337	2.16419354
1.525	.77107605	.35648747	2.16298219
1.55	.77682402	.35939762	2.16146122
1.575	.78245160	.36228439	2.15977177
1.60	.78790775	.36514835	2.15777436
1.625	.79321590	.36799001	2.15553650

This represents the condition for which the filter impulse response is most closely matched to the input signal

$$f(t) = \sin^2\left(\frac{\pi}{6.88}\frac{t}{\sigma}\right) \quad \text{for } 0 \leq t \leq 6.88\sigma$$
$$= 0 \quad \text{elsewhere.}$$

From Table VII, the maximum output signal-to-RMS noise ratio occurring for $\omega_c = 1.425$ is 2.1659. Evaluation of Equation (40) for a six pole linear phase versus frequency filter shows that there is only a loss of 1.8 percent in the ratio of peak signal-to-RMS noise for a two pole filter when compared to its six pole counterpart. This result tends to indicate that a two pole linear phase filter is adequate to smooth star pulses for applications where exceptional system accuracies are not required.

Further analysis shows that Equation (52) may be rewritten in terms of the slit transit time, T_s. Since $T_s = 2.56\sigma$

$$\omega_c = \frac{3.4473}{T_s} \text{ radians per second.} \tag{53}$$

But T_s is related to the scan period, T, and slit width, $\widehat{SW}$, by

$$T_s = \frac{\widehat{SW} \cdot T}{21,600} \text{ seconds}$$

where

$\widehat{SW}$ = slit width in arc minutes projected onto the celestial sphere, and

T = scan period in seconds, so

$$\omega_c = \frac{74.461.68}{\widehat{SW} \cdot T} \text{ radians per second.} \tag{54}$$

Figure 58 shows a plot of the noise-free input signal, f(t), and the noise-free output signal, y(t), for $\omega = 1.425$ and $\sigma = .945$. As shown in Table VII for $\omega = 1.425$, the noise-free input peak of unity is reduced by the filter to an output peak equal to .7464. The peak of the noise-free

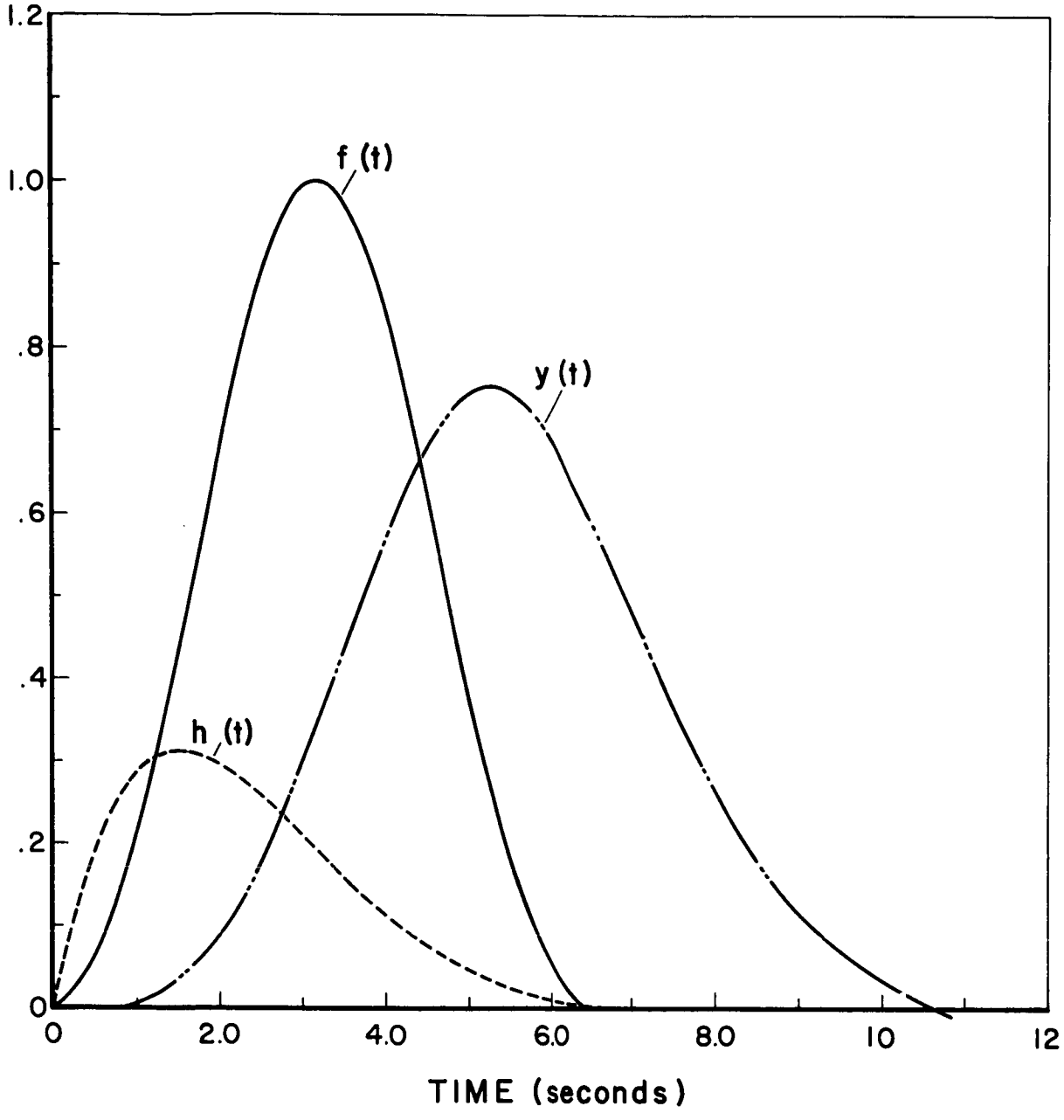

Figure 58: Star Pulse Input Signal to Filter, f(t); Filter Impulse Response, h(t); and Output Signal, y(t)

input signal corresponds to 80 percent of the star radiation striking the photocathode. Since I_S = the average current produced by 100 percent of the star radiation striking the photodetector, then the input signal peak corresponds to .8 I_S. Hence, the output signal peak corresponds to $(.7464)(.8)\ I_S = .597\ I_S$. Consequently, the peak output signal-to-RMS noise ratio is expressed by

$$\frac{S}{N} = \frac{(.597)\ I_S}{(1.26)\left[2e(.8\ I_S + I_B + I_D)\ \Delta f\right]^{\frac{1}{2}}} \tag{55}$$

where

$$\Delta f = \frac{(.524)(11851)}{\widehat{SW} \cdot T} = \frac{6210}{\widehat{SW} \cdot T}$$

and the denominator factor of 1.26 accounts for noise introduced by the photomultiplier dynode chain.[3]

Figure 58 also shows the filter impulse response, h(t), plotted for $\omega = 1.425$.

The second order transfer function of Equation (44) may be implemented by the circuit shown in Figure 59 . The design procedure for obtaining the values of R and C involves matching the poles of the desired filter transfer function with the poles of the circuit transfer function. If K = 1 in Figure 59 , then

$$C_1\ C_2\ R_1\ R_2 = \frac{4}{\omega_c^{\,2}}$$

and

$$C_2(R_2 + R_1) = \frac{3}{\omega_c}$$

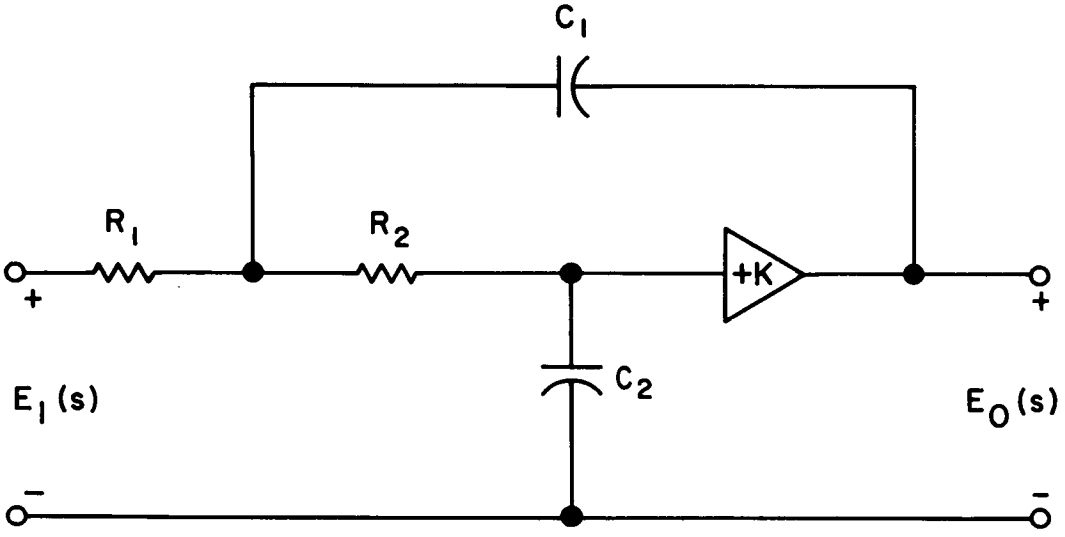

$$\frac{E_o(s)}{E_1(s)} = \frac{K}{s^2 C_1 C_2 R_1 R_2 + s\left\{C_2 R_2 + C_2 R_1 + (1-K) C_1 R_1\right\} + 1}$$

Figure 59: Practical Circuit Configuration Having Quadratic Transfer Function for Low Pass Active Filter

Now let $R_2 = R_1 = R$, so that

$$C_2 = \frac{3}{2R\,\omega_c} \quad \text{and} \quad C_1 = \frac{8}{3\,\omega_c R}$$

For $\widehat{SW}$ = 6 arc-minutes, and T = 2, 7, and 12 seconds, the values of ω_c may be tabulated from Equation (54) as follows:

T = 2 seconds	T = 7 seconds	T = 12 seconds
$\omega_c = 6205.1 \frac{\text{radians}}{\text{second}}$	$\omega_c = 1772.9 \frac{\text{radians}}{\text{second}}$	$\omega_c = 1034.2 \frac{\text{radians}}{\text{second}}$

4. Photomultiplier Overload Protection

In order to prevent degradation of the photomultiplier cathode and dynodes, it is necessary to limit the current emitted by these surfaces when bright sources such as the sun, earth, or moon get into the optical system field of view. Since current flow does not occur when high voltage is removed from the photomultiplier cathode and dynode chain, an obvious way of limiting the emission currents is to reduce or remove the electron acceleration voltages to the cathode-dynode chain whenever bright sources of radiation enter the field of view.

For the IMP vehicle, the sun should never get closer than 65 degrees to the optical axis, so with a simple shield direct sun radiation should never enter the optical system. However, locally reflected and scattered sun radiation will enter the optical system for 180 degrees of each scan period, but it is not expected that the magnitude of this scattered radiation will be great enough to cause excessively high degrading current levels in the photomultiplier. In Section III-A it was shown that the earth will get directly into the field of view during portions of each orbit for small values of the spin axis inclination with respect to the ecliptic plane. Since earth reflected sun radiation is almost as intense as direct sun radiation, it is certain that the photomultiplier emission current limits

will be exceeded if the photomultiplier voltage is not reduced or removed when the earth enters the field of view. The full moon intensity can also cause excessive emission currents, so it too must be considered as a bright source. However, Section III-A shows that the moon is less of a problem than the earth because the angle it subtends from the spacecraft is always small.

The logic block diagram in Figure 55 indicates ways of detecting an overload or a potential overload condition. Both of these conditions must provide logic signals which can temporarily reduce or remove the photomultiplier high voltage.

An actual overload condition can be detected at the photomultiplier output by sensing when the output signal across R_s exceeds a threshold level determined from the maximum average anode current rating. The output of a level detector will automatically switch OFF the photomultiplier high voltage. The photomultiplier high voltage must then be turned back ON by a telemetry command from the ground station, provided no bright source is in the field of view.

A potential overload condition can be sensed by placing a string of solid state photocells about the edge of the field of view. These detectors would be positioned so that as radiation from the earth or moon is about to enter the slit, at least one of the detectors would provide an output signal adequate to exceed a level detector threshold. Each photocell would drive a level detector and all the level detector outputs would be logically connected as an OR gate function. The OR gate output would automatically switch OFF the photomultiplier high voltage. The photomultiplier voltage would remain OFF until all photocell outputs fell below the threshold level at which time the photomultiplier voltage is automatically turned back ON.

5. Design of High Voltage Power Supply

It is required that the photomultiplier high voltage power supply be capable of turning OFF and ON within a small fraction of the scan period in order to prevent the formation of high current densities within the tube when bright radiation sources are scanned. The EMR photomultipliers can be purchased from the manufacturer with an integrated high voltage power supply wrapped around the tube envelope. However, the design of this supply does not permit rapid enough turn ON and turn OFF capability, especially for relatively short scan periods. Consequently, it is necessary to consider a specially designed high voltage supply which is capable of switching OFF and ON in tens of milliseconds.

A block diagram for a high voltage power supply design which permits fast switching is shown in Figure 60. The input voltage to a DC-AC inverter is regulated up or down inversely proportional to the voltage change at the high voltage output from the Cockroft-Walton voltage multiplier. A high gain feedback loop senses changes in the output voltage and causes the voltage regulator to provide correcting input voltage changes to the inverter. The following paragraphs discuss voltage multiplication and the achievable charging and decay time of the output voltage.

A common method of producing low current high voltage DC power from low voltage AC sources is the voltage doubler shown in Figure 61. One-half of the AC cycle is used to charge capacitor C_1 to the peak of the input and this capacitor charge in series with the other half cycle charges C_2 to twice the input peak voltage. This principle can be extended indefinitely at least theoretically to provide a very high voltage which is conveniently divided into equal steps. While this multi-step multiplier was originally developed for powering charged particle accelerators with requirements in the megavolt range; with the proper input viltage, it has voltage and current capabilities closely matching photomultiplier requirements. In Figure 61 it would be a simple matter to add a half wave rectifier to provide

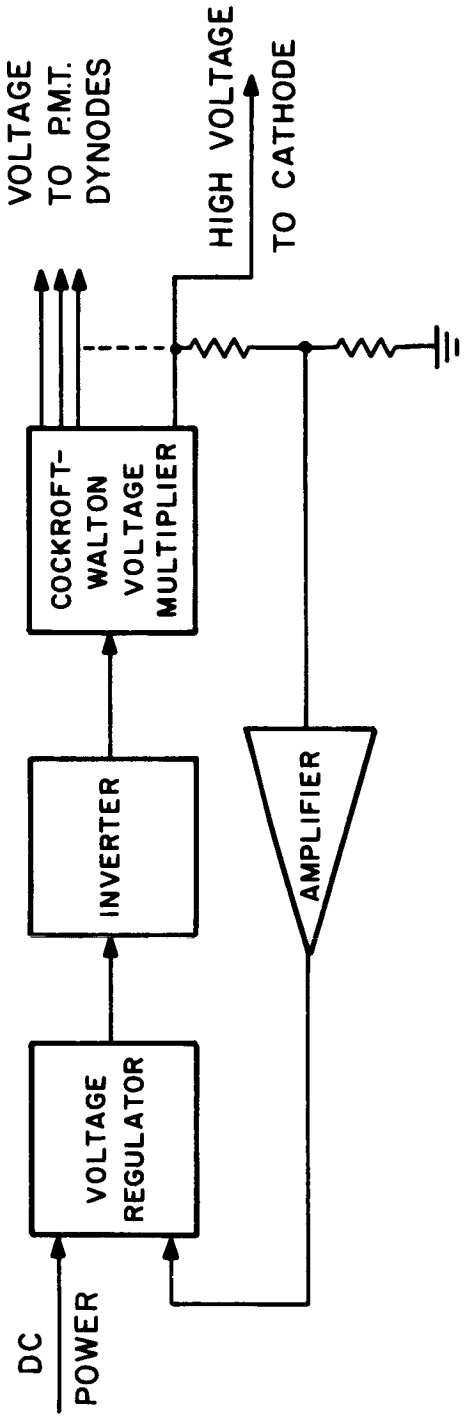

Figure 60 : Block Diagram for High Voltage Power Supply

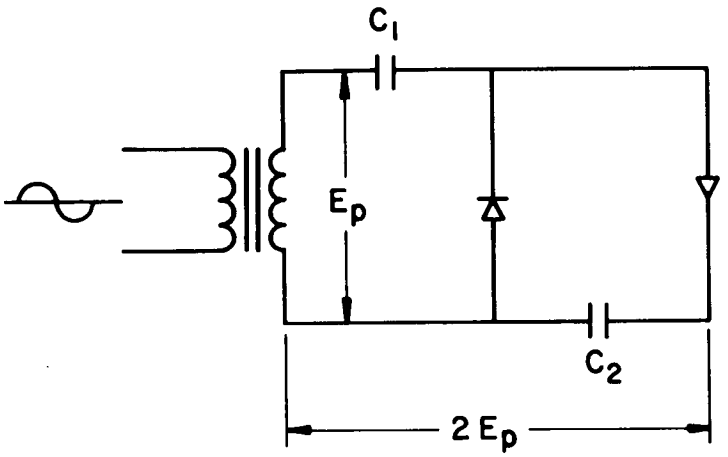

Figure 61: Voltage Doubler Circuit

the missing first step E_p, but then difficulty ensues when an arrangement for $3E_p$ is wanted. A system for tripling is shown in Figure 62. It is the same as Figure 61 with an added capacitor and diode and a different ground reference point. From the characteristics of these two circuits it is easy to deduce that a single multiplier will only produce odd or even multiples of the transformer voltage but not both. Of course, the transformer secondary could be designed for half the required voltage step but this does not produce the lowest possible supply output impedance, especially for the first two stages which ideally could be positive and negative half wave rectifiers. Multiple transformer windings produce unequal loading effects which are not desirable with high frequency saturable core inverters.

It would be possible to connect both of these networks, mutually extended to provide 14 voltage steps, to a single transformer for a photomultiplier tube power supply. A reduction in capacitor voltage requirement and thus size is achieved by an interlacing or series connection of the capacitor strings as shown in Figure 63. While the schematics in Figures 61 and 62 are for positive output the one in Figure 63 is reversed to show the actual negative output required for grounded photomultiplier output operation. A positive half wave rectifier is added to the lower end of the multiplier with the output grounded to provide two low impedance stages.

In a saturable transformer inverter, leakage reactance spikes of various amplitudes can exist depending on loading. With this multiplier where separate sections supply even and odd dynodes it is possible for a spike on one set to contribute enough voltage to seriously upset inter-dynode voltages under very light load conditions. It is thus necessary to load both sections to insure the voltage is determined by actual square wave amplitude. A voltage sensing divider across the supply for feedback regulator control will only load one section, and it is most economical to connect a load between the next highest even and odd voltages to load the other section.

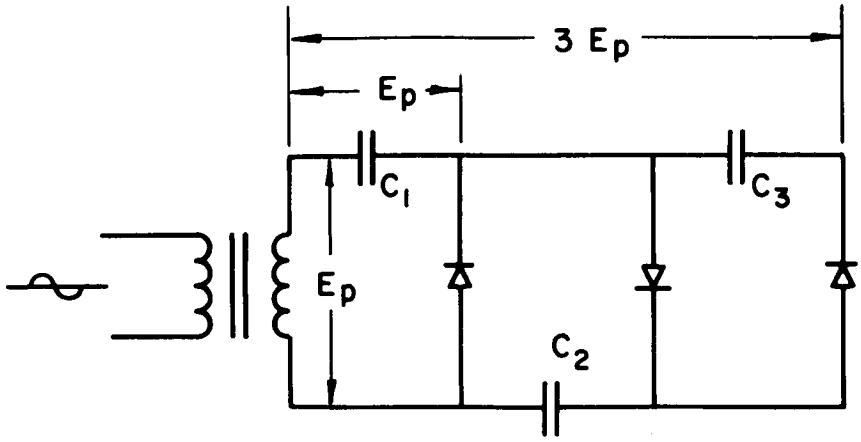

Figure 62: Voltage Tripler Circuit

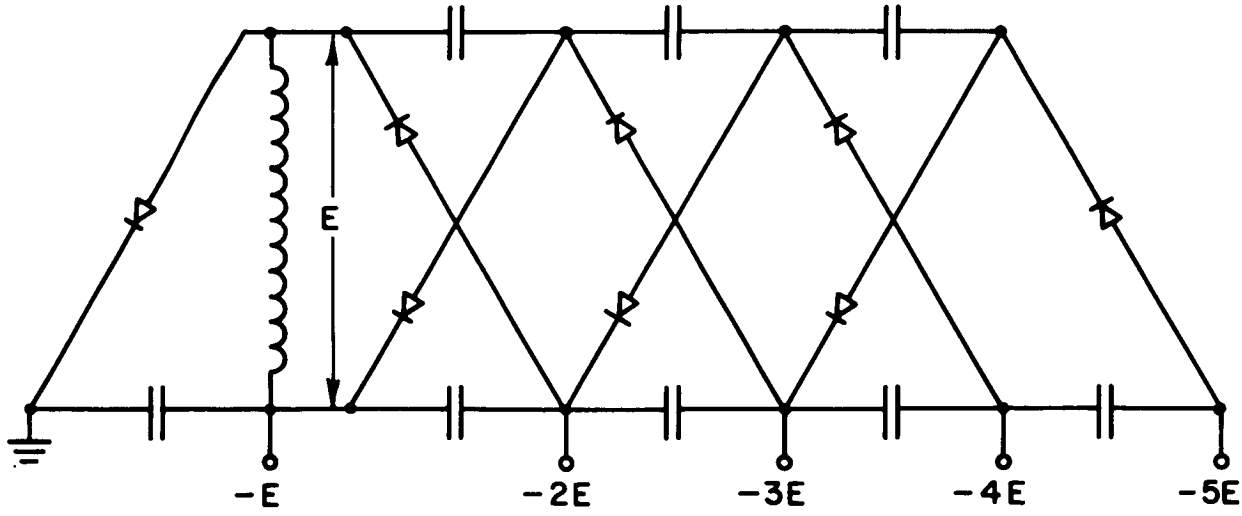

Figure 63: Interlaced Dual Even-Odd Multiplier

For a given load and ripple tolerance, supply frequency and capacitor size can be chosen. For a photomultiplier in a scanning system which must be turned OFF during earth or moon scan, charge and discharge times are also important. Discharge time is simply related to load and capacitor size by the equivalent exponential RC time constant. Charging time is more difficult to determine but has been obtained for a 14 stage multiplier (Figure 64) by computer simulation. For each half cycle it is possible to write equations for the voltage on each capacitor as a function of the voltage on the two capacitors at the end of the previous half cycle. The overall multiplication factor as a function of elapsed cycles is shown in Figure 65. With a 50 kilocycle input square wave, charging times are as follows:

99 percent full output requires 6.61 milliseconds,
99.9 percent full output requires 10.16 milliseconds.

6. Electrical Power Requirements

The power requirements for the SCADS-IMP sensor are of primary importance. These requirements have been estimated for the two electronic configurations discussed above. The first estimate will be for the configuration which requires transmission of the filtered analog star pulse signals to a ground station where all data processing is performed. For this configuration, the estimated power requirements have been tabulated in Table VIII. Approximately 0.9 watt total input power is required if the available telemetry channel will permit all data processing to be performed at the ground station.

The estimated power required to perform on-board data processing is tabulated in Table IX. The required switching time of the digital logic is relatively long since the maximum bit rate has been determined as 7.2 kilocycles; consequently, low power logic gates can be utilized. Logic gates are currently available which require only 1 milliwatt power

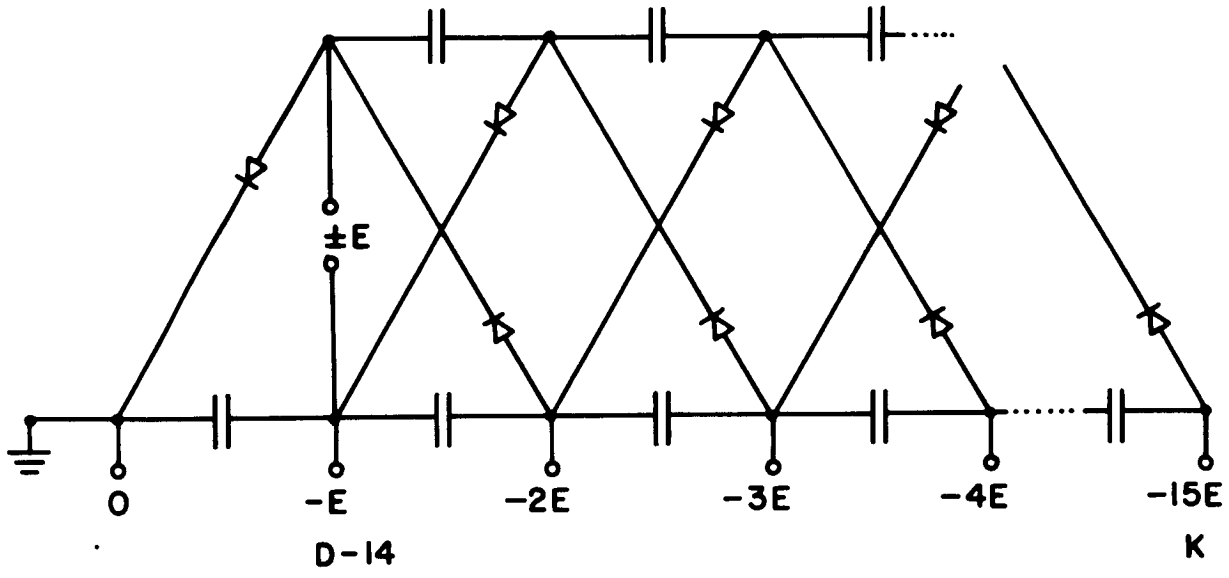

Figure 64: Cockroft-Walton Multiplier for EMR 14 Stage Photomultiplier Tube

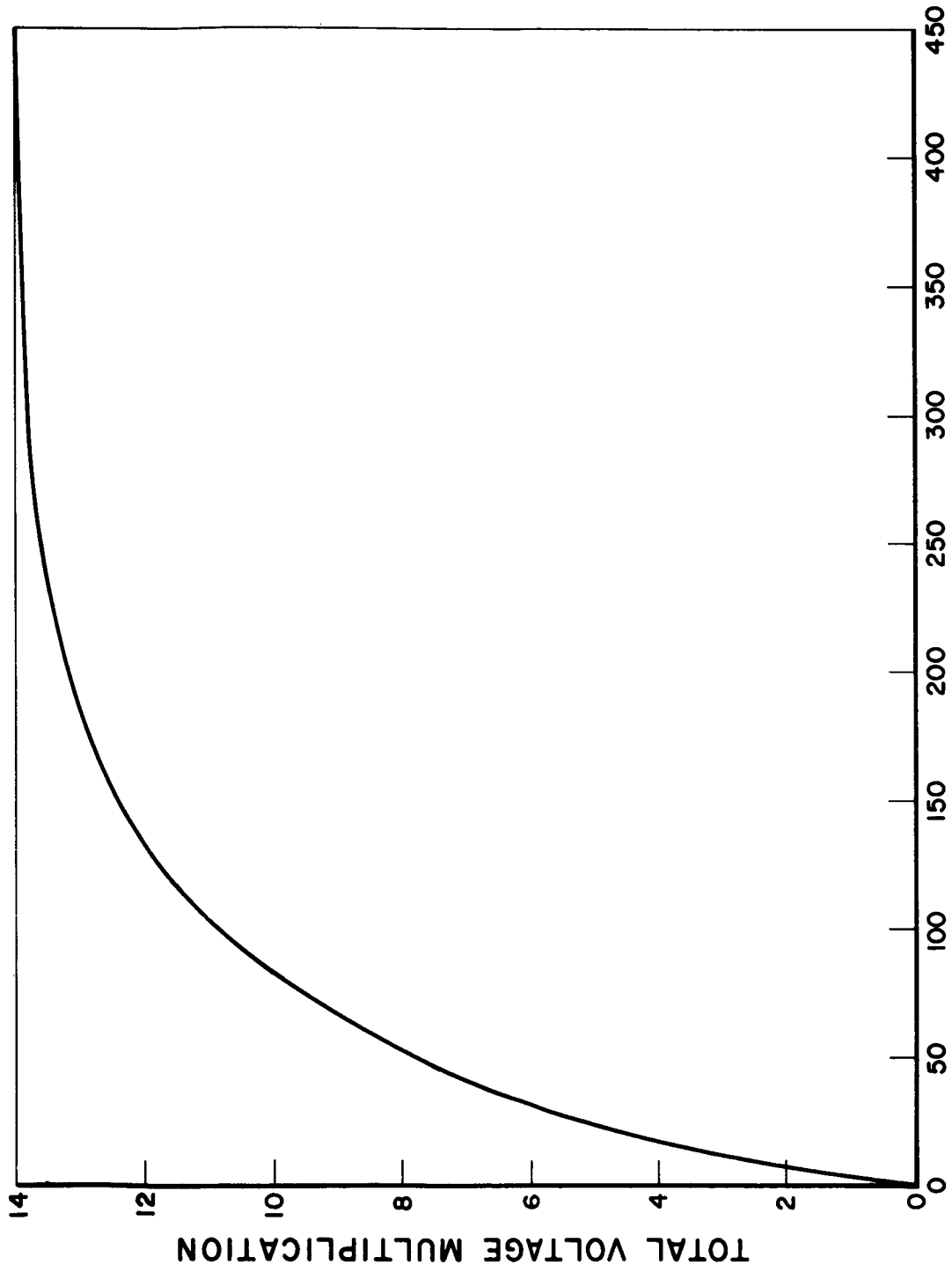

Figure 65: Charging Time of a 14 Stage Cockroft-Walton Multiplier

dissipation. The total input power required to include on-board data processing has been approximately estimated as 1.4 watts.

TABLE VIII

ESTIMATED POWER FOR SCADS-IMP SENSOR
(Ground Station Data Processing)

		Watts
PMT power supply		.30
analog circuits	.300	
PMT overload circuits	.150	
Subtotal	.450	
low voltage power supply (80% efficient)		.56
Total Input Power		.86

TABLE IX

ESTIMATED POWER REQUIREMENTS FOR SCADS-IMP SENSOR
(On-board Data Processing)

		Watts
PMT power supply		.30
oscillator plus azimuth counter	.3	
analog circuits	.3	
digital circuits	.2	
PMT overload circuits	.1	
	.9	
low voltage power supply (80% efficient)		1.1
Total Input Power		1.4

H. System Sensitivity to Extraneous Radiation

The SCADS-IMP sensor must operate in an environment containing two forms of extraneous radiation which interferes with system operation. One form of extraneous radiation is the direct or locally reflected radiation from the sun, earth, or the moon. The other form of radiation is the small particle radiation existing in radiation belts surrounding the earth. System sensitivity and interference from both radiation sources may be reduced by proper shielding. Particle radiation will be discussed first.

1. Particle Radiation

The IMP satellite orbit is inclined at 33 degrees to the earth's equator and comes to 2.6 earth radii at perigee receding to 15.6 earth radii at apogee. It thus passes through the outer Van Allen belt near perigee, and out of the magnetosphere near apogee. It is therefore exposed to Van Allen electrons and protons, the solar wind, and to cosmic rays. The effects of these radiations on the circuitry and the photomultiplier must be considered. The circuit effects will be considered first.

a. Circuit Damage, Van Allen Belts

Hard particle radiation changes the band structure of the usual semi-conductor devices by creating lattice defects and surface states, and thereby changing the device characteristics. The parameters most easily affected are the minority carrier lifetime or the diffusion length (which are related).

Experimental evidence indicates that in both silicon, Si, and Germanium, Ge, the energy necessary to displace a lattice atom is 13 ev*[15]. If a particle of mass m and energy E_o collides with an atom of mass M the maximum energy which can be transferred classically is

---

* ev = electron volts.

$$E_m = \frac{4\ Mm\ E_o}{(M + m)^2} \tag{56}$$

For protons incident on Si, Equation (56) states that displacements can occur for protons of energies 97.6 ev or greater. For electrons Equation (56) gives .167 M ev, so relativistic electrons are needed and Equation (56) is invalid. The relativistic equivalent of Equation (56) with the restriction that $E_o << MC^2$ (usually the case, for Si MC^2 = 26.13 B ev) is

$$E_m = 2 \frac{m}{M} E_o \left(\frac{E_o}{MC^2} + 2\right) \tag{57}$$

Equation (57) gives a damage threshold for Si as .145 M ev and for Ge, .326 M ev. If we confine ourselves to Si, it is thus unnecessary to consider electron energies much less than .145 M ev.

Vette[16,17] has given plots of the spectral distribution of electrons and protons in the Van Allen belts. These model the distribution existing in August 1964, and are displayed in Figures 66a and 66b. These are actually for the geomagnetic equatorial plane, (or an approximately equatorial orbit) but should approximate the worst conditions in the actual orbit.

Johnson[18] gives a plot of the range of radiation in solids, the thickness of material necessary to stop radiation of a given energy. This appears in Figure 67.

Weight and space considerations probably restrict us to integrated circuits. Unfortunately these are also more sensitive to radiation damage than discrete transistors. Gordon and Wannemacker[19] have studied the effects of particular radiation on MOS integrated circuits. They estimate that these will stand a total dose of 1.7×10^{11} electrons per square centimeter, plus 2×10^9 protons per square centimeter. If the circuitry is to

last a year this amounts to a flux of 5.39×10^3 electrons per second per square centimeter and 63.4 protons per second per square centimeter.

The IMP satellite will spend 18 percent of the time within about seven earth radii and 4 percent of the time with three earth radii (proton belt). Thus we estimate that a peak electron dose of about 2.9×10^4 per second square centimeter plus a peak proton dose of 1.57×10^3 per second square centimeter is tolerable. From Figures 66a and 66b we estimate that we should shield for about 2 M ev electrons and about 12 M ev protons. Figure 67 indicates that 1.50 grams per square centimeter of aluminum will do the job. This corresponds to a thickness of about .22 inch of aluminum, which does not seem unreasonable.

b. Cosmic Rays and the Solar Wind

The solar wind consists largely of low energy protons and electrons which will not penetrate this shielding. Cosmic ray intensities vary by about a factor two to three from quiet sun activity to times of high solar activity averaging about .88 per second per square centimeter, a value much smaller than the count rate in the Van Allen belts.

c. Photomultiplier Noise from Particulate Radiation

The peak count rate will occur at about 4.25 earth radii and amount to about 7×10^4 per second per square centimeter. This is an amount equal to the photon rate from a sixth magnitude star. Thus the background counts in the photomultiplier due to this flux of electrons on the photocathode should not be excessive.

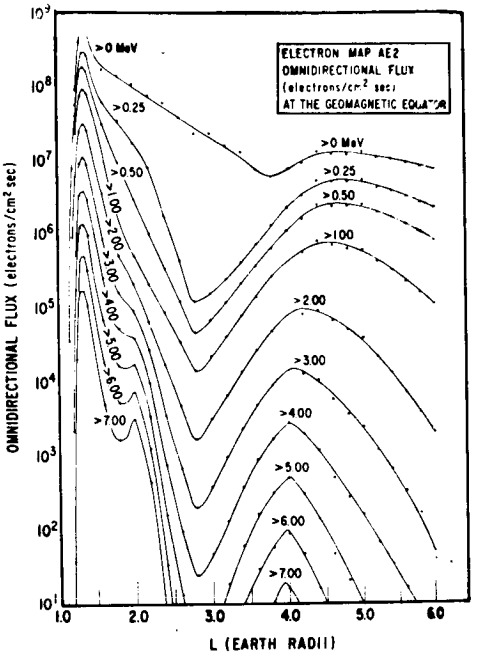

Figure 66a: Electron Fluxes at the Geomagnetic Equator

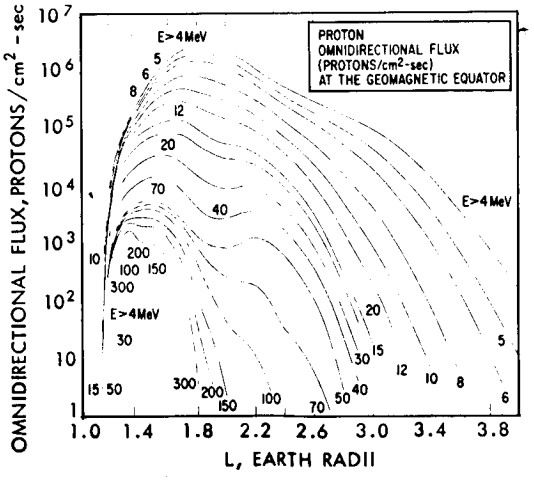

Figure 66b: The Omnidirectional Proton Flux at the Geomagnetic Equator

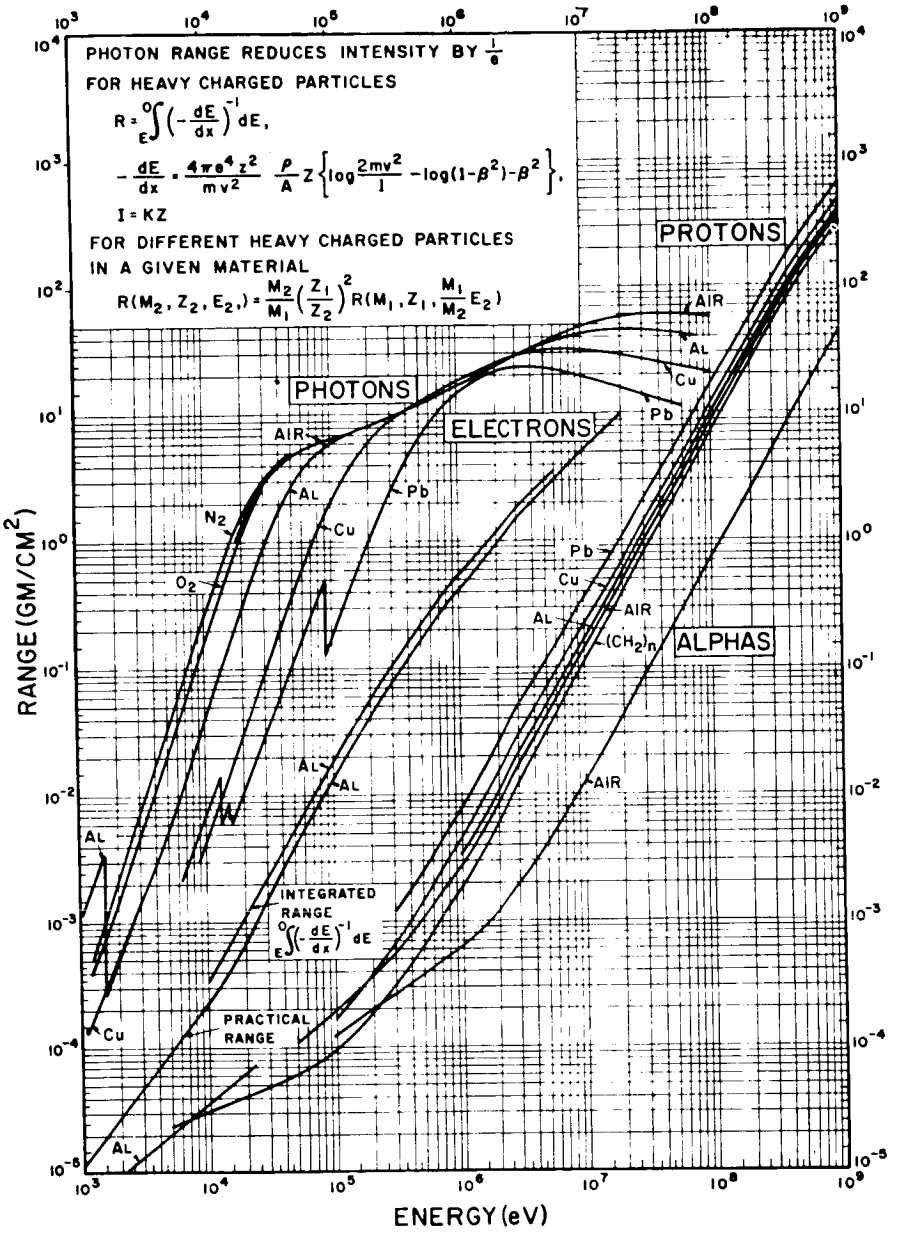

Figure 67: Range-energy Curves for Penetrating Radiations (after Fillius, 1963)

c. Photomultiplier Noise from Particulate Radiation

Here we may be guided by NASA Goddard experience with the OGO II air glow photometers. The main body photometer used an EMR 541 E-05M, a one-inch diameter end-on tube with a tri-alkali cathode on a sapphire window[20]. The orbit was polar with apogee near 1500 kilometers and perigee near 400 kilometers.

The photocathode current in this photometer was observed to vary from 5×10^{-16} to 3.3×10^{-9} amperes with the maximum occurring in low latitudes near 1500 kilometers (L = 1.23). "It was not a simple increase in dark current level, but consisted of a multitude of pulses, and tended to persist after the radiation levels had decreased."

Since L = 1.23 corresponds about to the maximum of the inner belt of fast electrons from the "starfish explosion" it is natural to attribute the effects to these fast electrons. We thus examine some of the possible ways in which these could cause noise in the photomultiplier.

Bremsstrahlung

Bremsstrahlung (X-rays) due to fast electrons cause photoemissions by the photoelectric effect (below .05 mc^2 in carbon, .1 mc^2 in aluminum), the Compton effect and by pair production (important at about 10 mc^2 in lead, 30 mc^2 in aluminum). This could be very serious in that the resulting X-rays are very penetrating and it could happen that attempts to shield against the fast electrons would only increase the X-ray production.

X-Ray Production by Bremsstrahlung in Aluminum.

We assume:

1) Normally incident monoenergetic electrons of energy, E_o, on an infinite slab of thickness X_1 centimeter;
2) We can neglect all energy loss mechanisms except ionization and excitation.

The number of photons which appear at $X = X_1$ is

$$n = N \int_0^a \int_{E_{min}}^{E(X)} e^{-\frac{X_1 - X}{\tau(k)}} \phi_k \frac{dk}{E_o - \mu} dX \quad , \tag{58}$$

where

$$\phi_k \frac{dk}{E_o - \mu} \quad , \quad (\mu = mc^2)$$

is the cross-section for emission of a photon in the range k, k + dk.

$\tau(k)$ is the range for photons in aluminum. $\tau(k)$ was actually taken from the graphs of range given by Johnson (Satellite Environment Handbook)[18] and was approximated by,

$$\begin{aligned} \log \tau(k) &= .440 \log k + 1.224 \\ &\qquad k > 5.5 \times 10^{-2} \text{ MeV} \\ &= 2.760 \log k + 4.126 \\ &\qquad k < 5.5 \times 10^{-2} \text{ MeV} . \end{aligned} \tag{59}$$

To find E(X) recourse was had to an empirical equation for range given in the American Institute of Physics Handbook[21]

$$\begin{aligned} &R = .412\ E^n \text{ gm/cm}^2 \\ &n = 1.265 - .0954 \ln E \\ &.01 \leq E \leq 2.5 \text{ MeV} \\ &R = .530E - .106 \text{ gm/cm}^2 \\ &2.5 \leq E \leq 20 \text{ MeV}. \end{aligned} \tag{60}$$

We take n = 1.181 in first approximation and define,

$$H(X) = \frac{X}{.412}^{\frac{1}{1.181}} \qquad X < 1.219 \text{ gm/cm}^2 \tag{61}$$

$$= \frac{X + .106}{.530} \qquad \geq 1.219 \text{ gm/cm}^2$$

Then,

$$E(X) = H(X_o - X), \tag{62}$$

where X_o is the range of electrons of incident energy E_o.

E_{min} was taken as .1 mc^2 reasoning that photons of energy much less than this would not escape.

Finally, X_2 was taken as the solution of

$$E(X_2) = E_{min} = .1\ mc^2$$

and a was defined as

$$a = \text{Min } (X_1, X_2), \tag{63}$$

which is just to say that an electron is followed until it either has energy less than .1 mc^2 or it passes through the slab.

$\phi_k \frac{dk}{E_o - \mu}$ was taken from Heitler[22]. The nonrelativistic approximation and the extreme relativistic approximation with complete screening (Thomas-Fermi model) were used with the changeover at $E = mc^2$.

The calculations were repeated for total photon energy radiated, putting $k\phi_k$ for ϕ_k.

The number, N, of bremsstrahlung photons coming through an aluminum shield of thickness X_1 = .25, .688, and 2.5 gms/cm^2 per incident fast electron is

plotted in Figures 68 to 70 , respectively, as is the energy radiated per incident fast electron, both as a function of incident energy.

The average photon energy as a function of incident energy appears in Figure 71. It may be noted that the shielding is not very effective against the X-rays, and the number of photons per incident electron as a function of shielding thickness with incident energy as a parameter is plotted in Figure 72.

The results indicate that photon energies of about an MeV are typical and that below 2.5 gms/cm^2 of aluminum less than one photon per incident electron is produced. There is a tendency for the number of photons to increase with shielding thickness up to a certain thickness for electrons of a given energy (i.e. thickness 1.6 gm/cm^2 at E_o = 2 MeV) and to decrease thereafter.

The nature of these results appears to rule out bremsstrahlung as a major contribution, particularly when we consider the results of the Van de Graaff simulation of the OGO II environment by Reed, et. al.[20]. On bombardment of the photometer by 2.6 MeV electrons the dark current is observed to decrease exponentially with the shielding thickness [their Figure 8]. If bremsstrahlung were the major contribution an initial dark current increase would occur according to Figure 72. Thus fast electrons and protons which penetrate the shielding are the likely cause of the observed noise.

Cerenkov Radiation

A. T. Young[23] has studied the noise due to Cerenkov pulses in an end-on photomultiplier caused by the muon component of cosmic rays traversing the face plate. He reports a minimum of about 50 photoelectrons for each Cerenkov pulse. Thus, the Cerenkov radiation caused by fast electrons in the face plate might have been a major factor in the photometer noise observed in the OGO photometer.

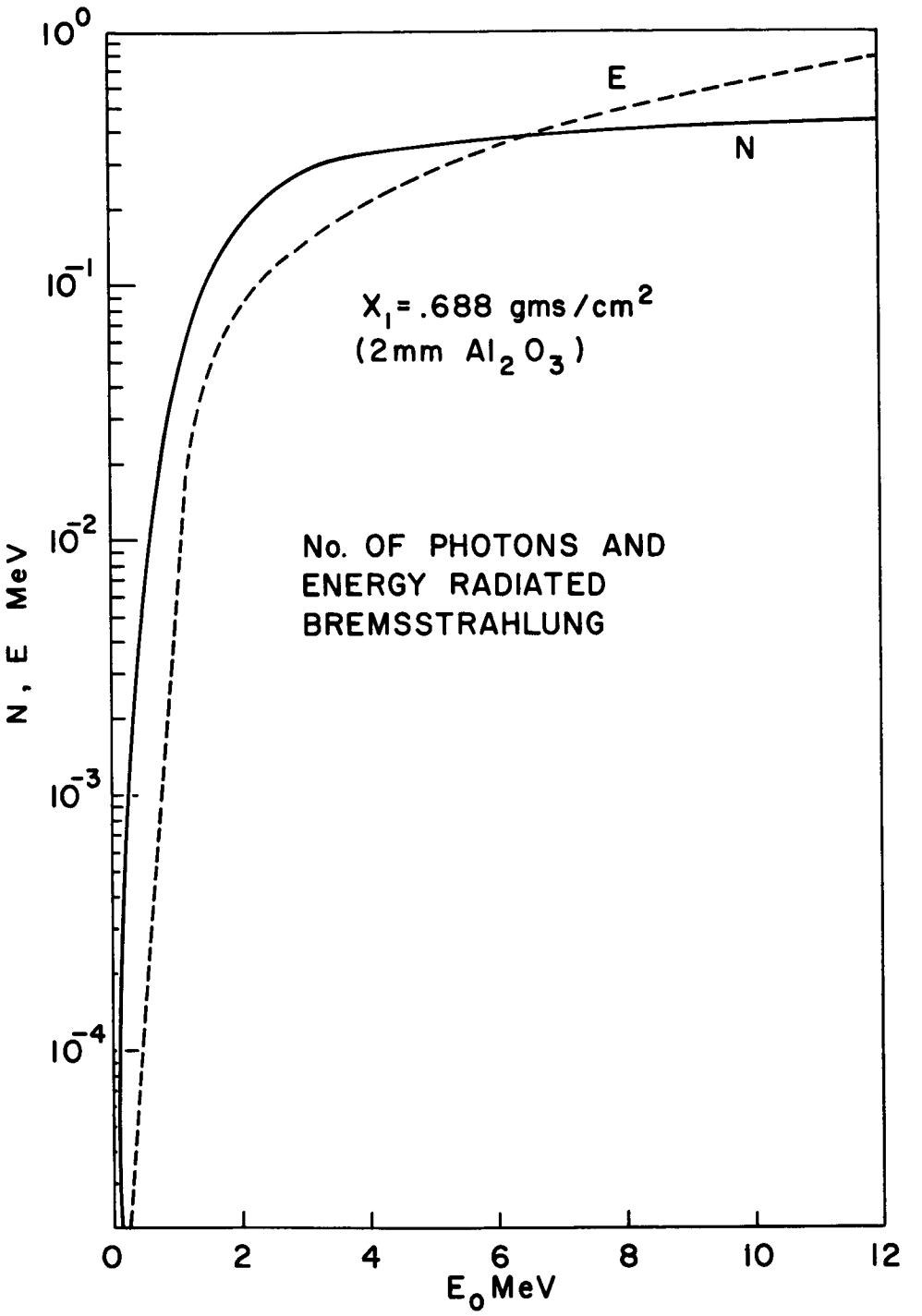
10^0
10^{-1}
10^{-2}
10^{-3}
10^{-4}
N , E MeV
E
N
X_1 = .688 gms/cm^2
(2mm Al_2O_3)
No. OF PHOTONS AND
ENERGY RADIATED
BREMSSTRAHLUNG
0
2
4
6
8
10
12
E_0 MeV

Figure 68

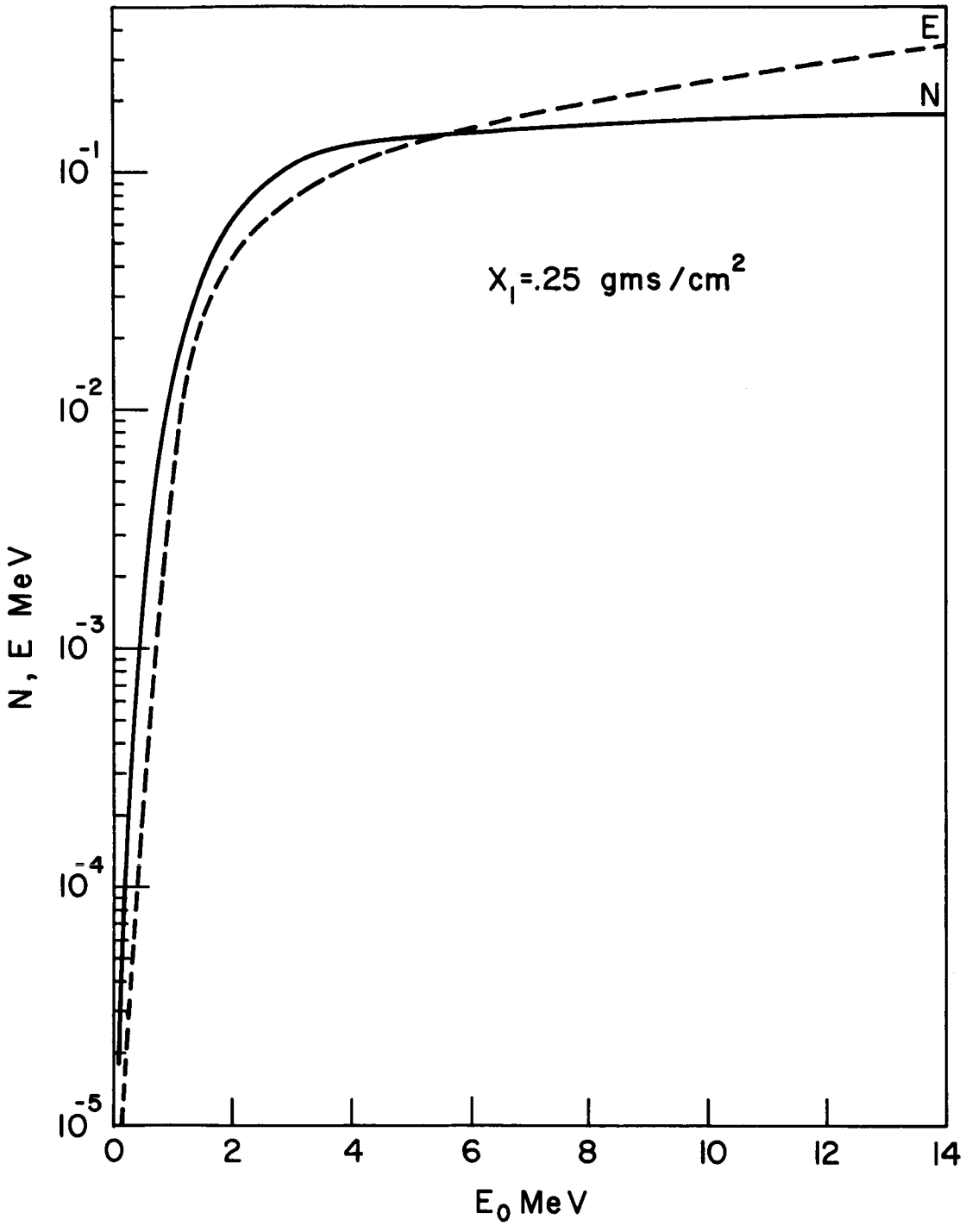

Figure 69: Number (N) of Photons and Energy (E) Radiated Bremsstrahlung. Data for X_1 = 0.25 gms/cm^2

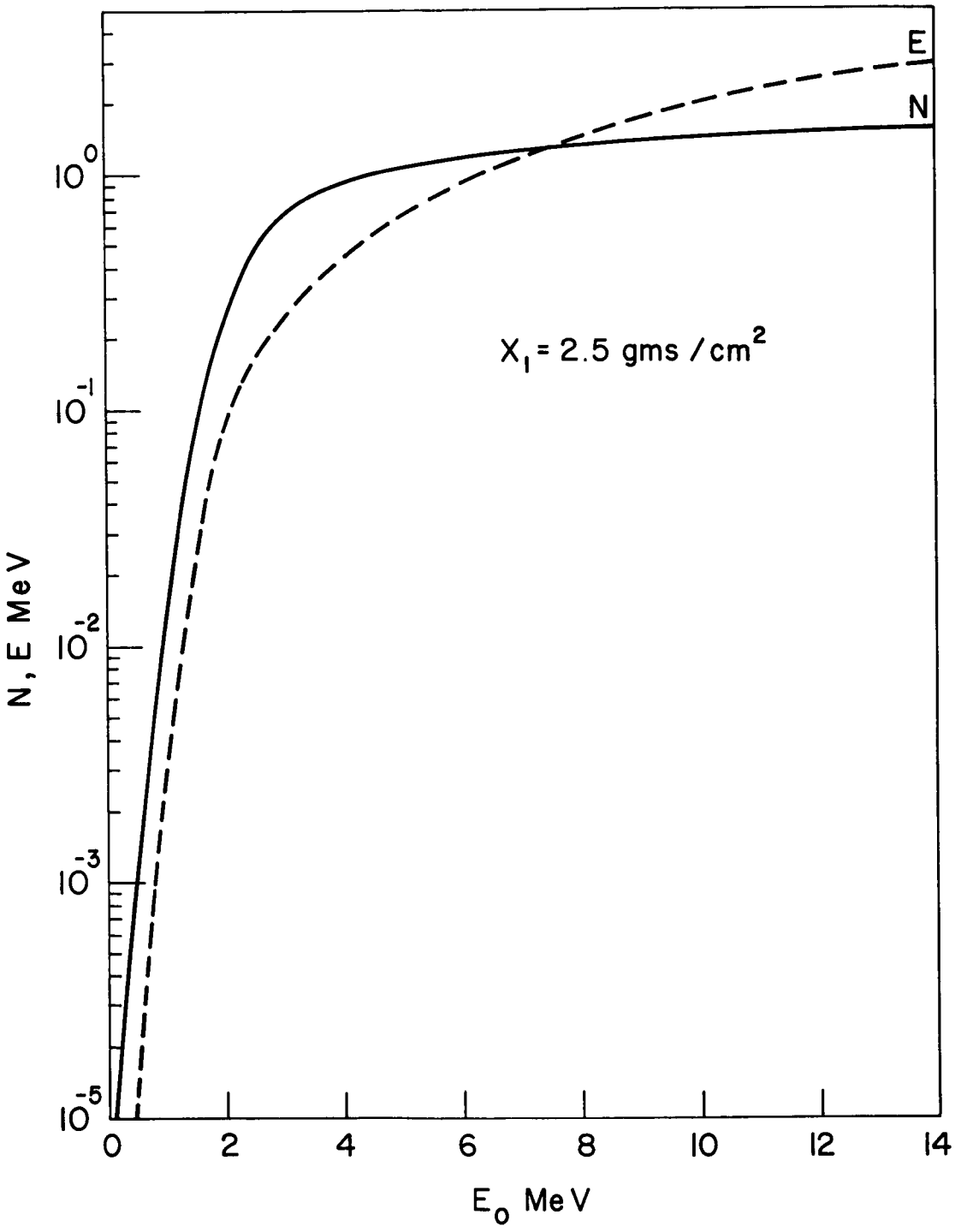

Figure 70: Number (N) of Photons and Energy (E) Radiated Bremsstrahlung. Data for X_1 = 2.5 gms/cm^2

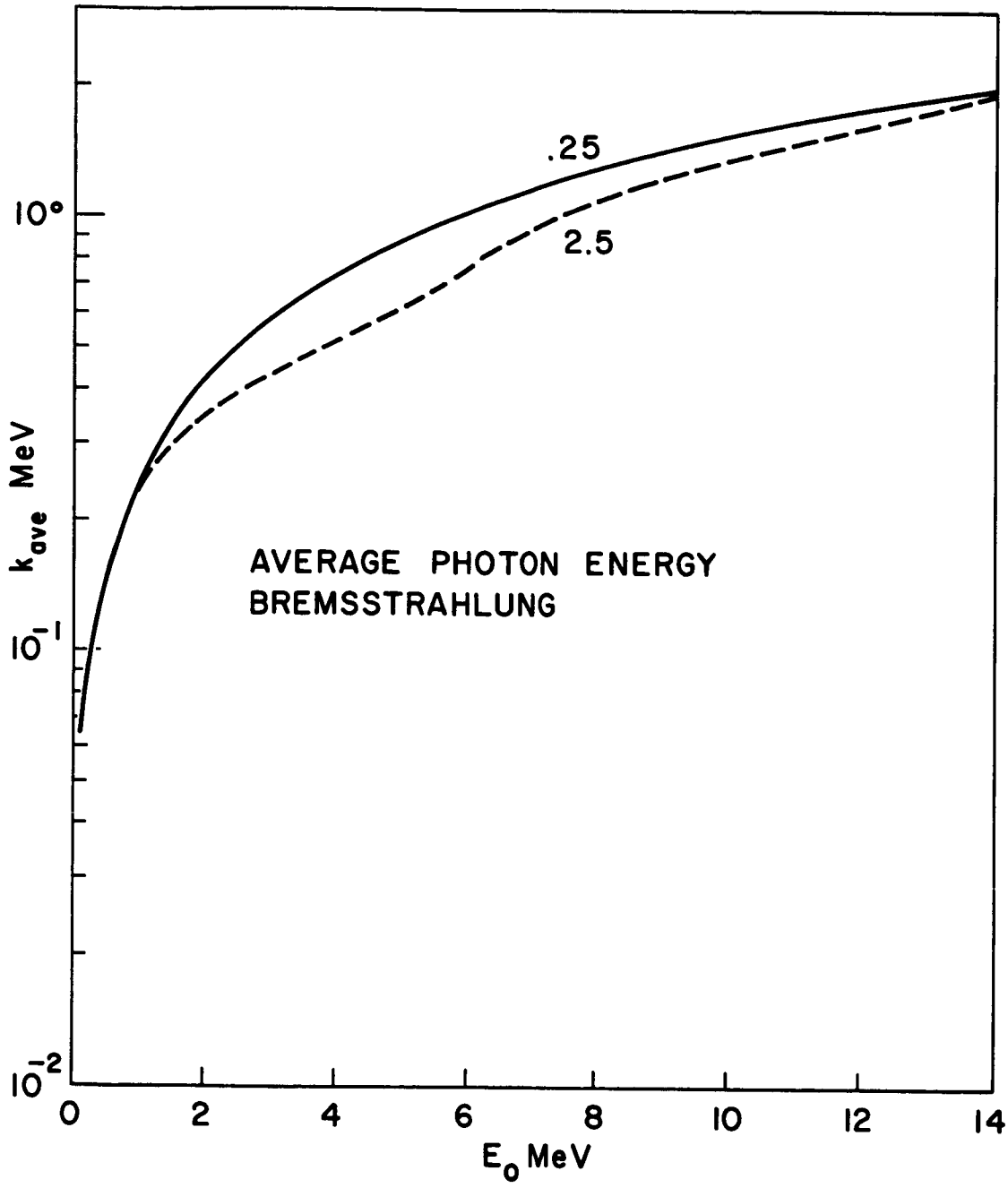
.25
2.5
AVERAGE PHOTON ENERGY
BREMSSTRAHLUNG
10^{0}
10^{-1}
10^{-2}
k_{ave} MeV
0
2
4
6
8
10
12
14
E_0 MeV

Figure 71

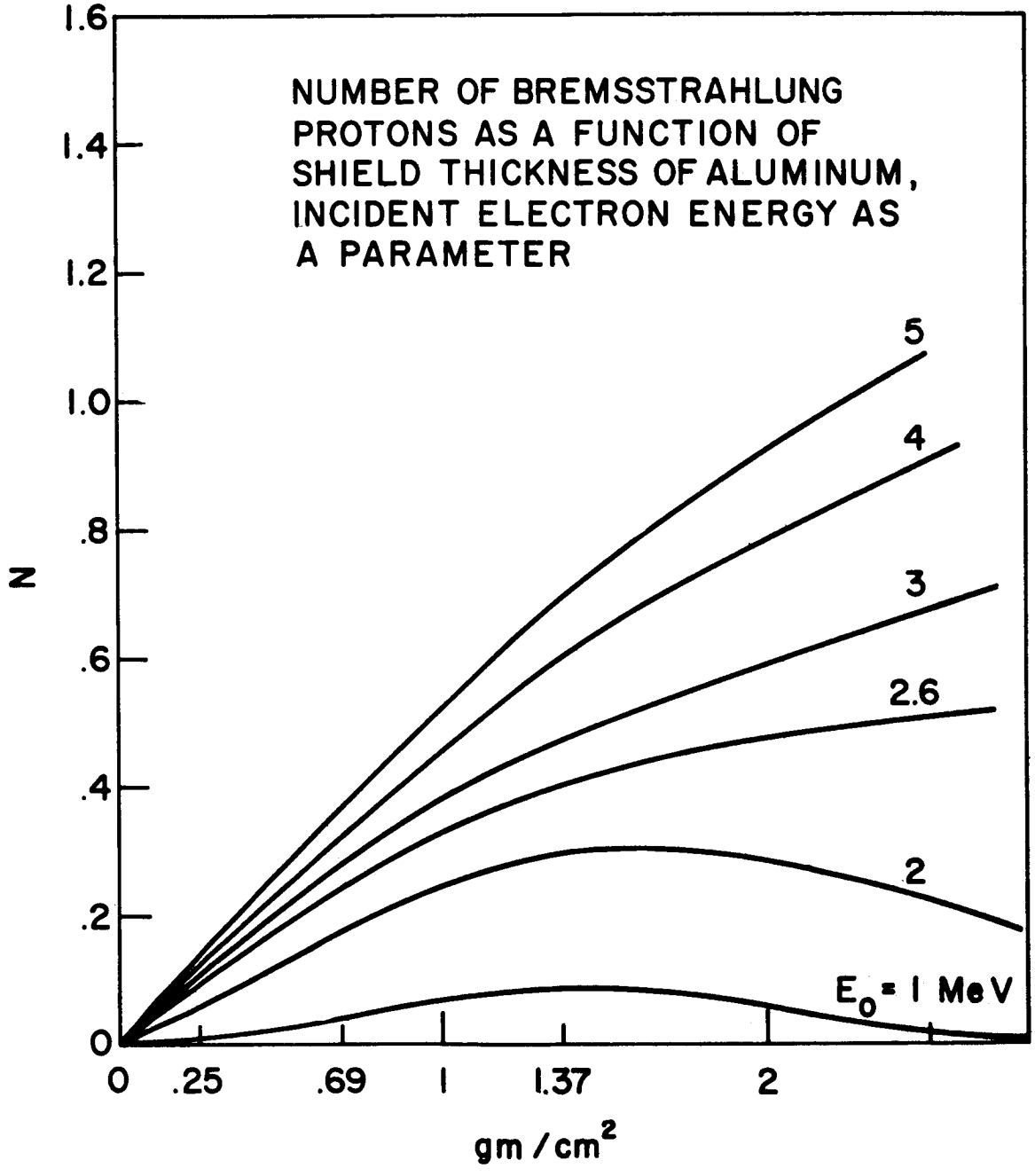
NUMBER OF BREMSSTRAHLUNG PROTONS AS A FUNCTION OF SHIELD THICKNESS OF ALUMINUM, INCIDENT ELECTRON ENERGY AS A PARAMETER
N
1.6
1.4
1.2
1.0
.8
.6
.4
.2
0
5
4
3
2.6
2
E_0 = 1 MeV
0
.25
.69
1
1.37
2
gm / cm^2

Figure 72

Moreover, the experiments of the NASA group clearly established that the photocathode and the first few dynodes were the sensitive element. C. Wolf [25] finds the radiation induced noise proportional to cathode area and concludes that either the lens elements or the photocathode was the sensitive element. NASA experiments failed to detect luminescence of the optics.

The rate of Cerenkov radiation per unit path length in the wavelength band $(\omega, \omega + d\omega)$ is given (e.g. Schiff[17] by

$$\frac{dE}{dx} = \frac{e^2}{c^2}\left(1 - \frac{1}{n_r^2 \beta^2}\right) \omega d\omega \tag{64}$$

where n_r = refraction index,
ω = angular frequency,
$\beta = v/c$,
v is electron velocity, and
c is light velocity.

If N is the average number of photons produced at frequency ω,

$$\frac{dN}{dx} = \frac{1}{h\omega}\ \frac{dE}{dx} \tag{65}$$

where $h = \frac{6.62 \times 10^{-27}}{2\pi}$ erg sec.

Equations (64) and (65) give

$$\frac{dN}{dx} = \frac{2\pi e^2}{hc}\left(1 - \frac{1}{n_r^2 \beta^2}\right) \Delta\nu_{12} \tag{66}$$

photons/incident electron,

where $\Delta\nu = \frac{1}{\lambda_1} - \frac{1}{\lambda_2}$

and $\lambda_{1,2}$ is the wavelength at angular frequency, $\omega_{1,2}$.

For a single electron incident on the photomultiplier window at energy E_o, the total number of photons generated would be

$$N = \frac{2\pi\,\Delta\nu_{12}}{137} \int_{E_{min}}^{E_o} \left(1 - \frac{1}{n_r^2\beta^2(E)}\right) \frac{dx(E)}{dE}\, dE \,. \tag{67}$$

Of course, $\frac{E_{min}}{mc^2} = \sqrt{1 + \frac{1}{n_r^2 - 1}} - 1,$

$$\beta^2 = \frac{t(t+2)}{(t+1)^2},$$

where $t = E/mc^2$, and we have put $e^2/hc = 1/137$.

In evaluating (67) the relation between x and energy E(x) would be the same as in the section on bremsstrahlung.

Then, to find the total number of Cerenkov photons produced in the Van Allen belts, it is necessary to average over the electron energy distribution and overall photocathode window orientations.

The computation can be simplified somewhat. In Figure 73 the factor $1 - 1/n_r^2\beta^2$ appearing in equation (67) is plotted for sapphire ($n_r = 1.796$ at 5000 Angstroms), and noted to rise rapidly from zero at $E_{min} \approx .204\ mc^2$, reaching almost its asSumptotic value at $E = mc^2$ (1 MeV). We therefore approximate this factor as zero below E_{min} and constant thereafter. Then, (67) becomes,

$$N \approx \frac{2\pi\Delta\nu_{12}}{137} \left(1 - \frac{1}{n_r^2}\right) L_{ave}, \tag{68}$$

where L_{ave} must now be suitably chosen.

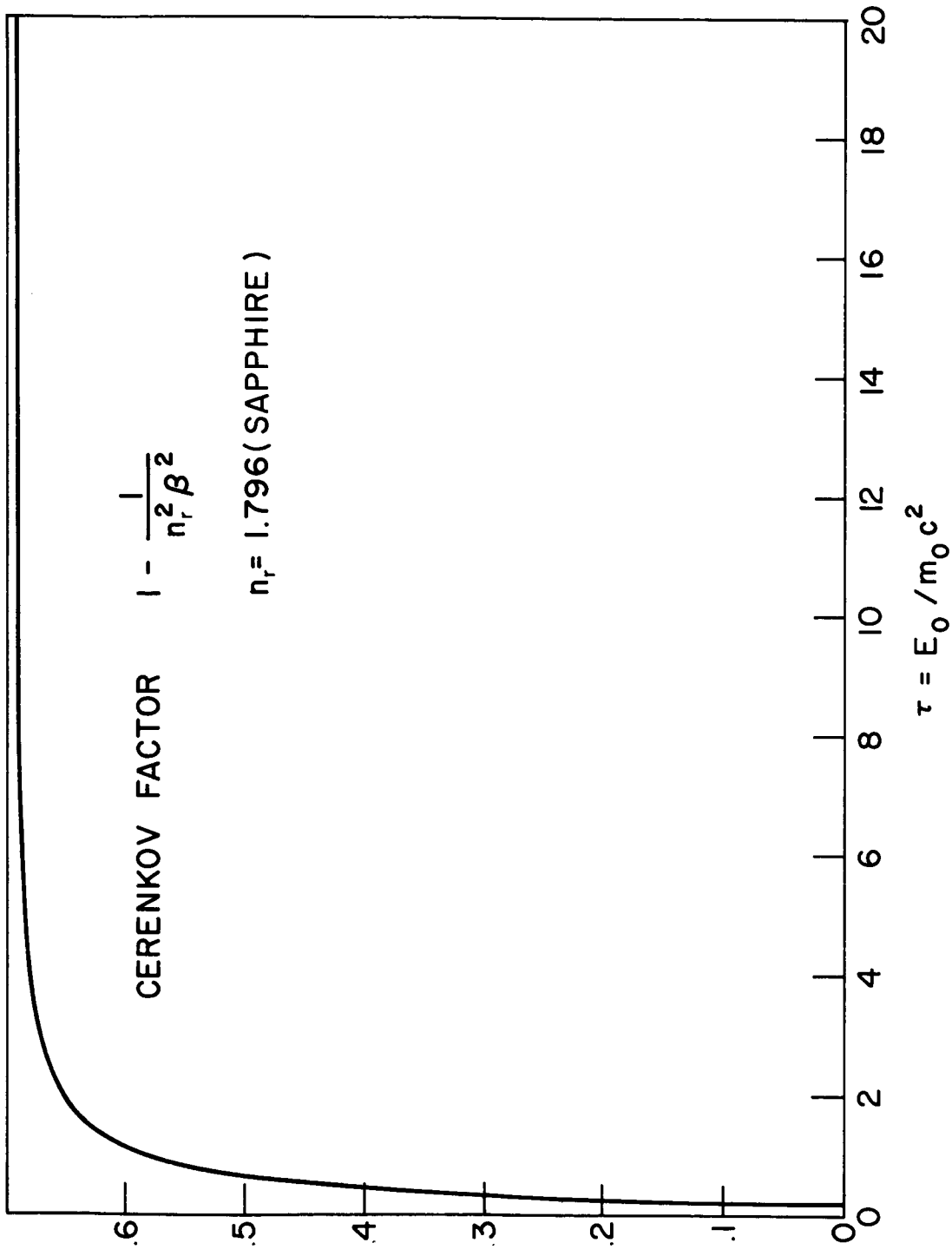
CERENKOV FACTOR $1 - \frac{1}{n_r^2 \beta^2}$
$n_r = 1.796$ (SAPPHIRE)
$\tau = E_0 / m_0 c^2$
0
2
4
6
8
10
12
14
16
18
20
0
.1
.2
.3
.4
.5
.6

Figure 73

If the photocathode window thickness is ℓ and its radius R_c, the thickness (path length) averaged overall orientations is found to be,

$$\ell_{ave} = \frac{2\ell}{\pi\sqrt{1+c^2}} \ln \frac{(\sqrt{1+c^2}+1-c)(\sqrt{1+c^2}+c)}{(\sqrt{1+c^2}-1+c)(\sqrt{1+c^2}-c)}, \tag{69}$$

where $c = \frac{2\ell}{\pi R_c}$.

If ℓ = 2 mm and $R_c = \frac{1}{2}$ inch, ℓ_{ave} = .392 cm = 1.73 gm/cm^2 (sapphire with density 3.50 gms/cm^3).

In the radiation belts electron energy distributions seem to fit a relation like

$$\frac{d\phi}{dE} = a\phi_o e^{-aE} \text{ electrons/cm}^2 \text{ sec MeV}. \tag{70}$$

We are thus lead to put for L_{ave} in equation (68) something like,

$$L_{ave} = \frac{\int_{E_{min}}^{\infty} e^{-aE} X(E)dE}{\int_{E_{min}}^{\infty} e^{-aE} dE}; \tag{71}$$

X(E) is taken as in equation (60) as,

$$\begin{aligned} X(E) &= .412\ E^{1.181} \text{ gm/cm}^2,\ E \leq 2.5 \text{ MeV} \\ &= .530\ E - .106 \text{ gm/cm}^2, \text{ otherwise.} \end{aligned} \tag{72}$$

To equation (72) we further add the restriction that,

$$X(E) \leq \ell_{ave}, \tag{73}$$

where ℓ_{ave} comes from equation (69).

Then equation (71) becomes

$$L_{ave} = \frac{\int_{E_{min}}^{E_{max}} e^{-aE} X(E)dE + \int_{E_{max}}^{\infty} e^{-aE}\, \ell_{ave}\, dE}{\int_{E_{min}}^{\infty} e^{-aE} dE} \qquad (74)$$

E_{max} is found using $\ell_{ave} = 1.73$ gm/cm^2 in (72) as, $E_{max} = 2.79$ MeV, a result which suggests that we can as well use only the first of equation (72) in (74) and obtain,

$$L_{ave} = \frac{a^{-\alpha} \left\{\gamma(\alpha,\ aE_{max}) - \gamma(\alpha,\ aE_{min})\right\}}{+\frac{\ell_{ave}}{a} e^{-aE_{max}}} \qquad (75)$$
$$\frac{1}{a} e^{-aE_{min}}$$

where $\alpha = 2.181$ and $\gamma(\alpha, X)$ is an incomplete gamma function.

Vette[17] has published a model for the inner and outer belt electrons. From his Figure 36 (page 20), which we reproduce as Figure 74, we find that at the peak of the inner belt the integral omnidirectional flux is,

$$\phi(> E) = 2.8 \times 10^8\ e^{-1.035E/cm^2}\ \text{sec} . \qquad (76)$$

Thus, a = 1.035 and we find after evaluating the gamma functions,

$$L_{ave} = 16.74 \times 10^{-2}\ \text{gm/cm}^2$$
$$= 4.784 \times 10^{-2}\ \text{cm},$$

and the average path length is less than one-half millimeter.

The minimum amount of shielding around OGO II main body photometer was about 60 mils or .4 gm/cm^2 (cf. their Figure 3). Thus, from Figure 75, range of electrons in aluminum, they are shielded for about one MeV electron. From Figure 74 (Vettes AE-2 environment) at L = 1.25, there are about $\phi = 10^8$

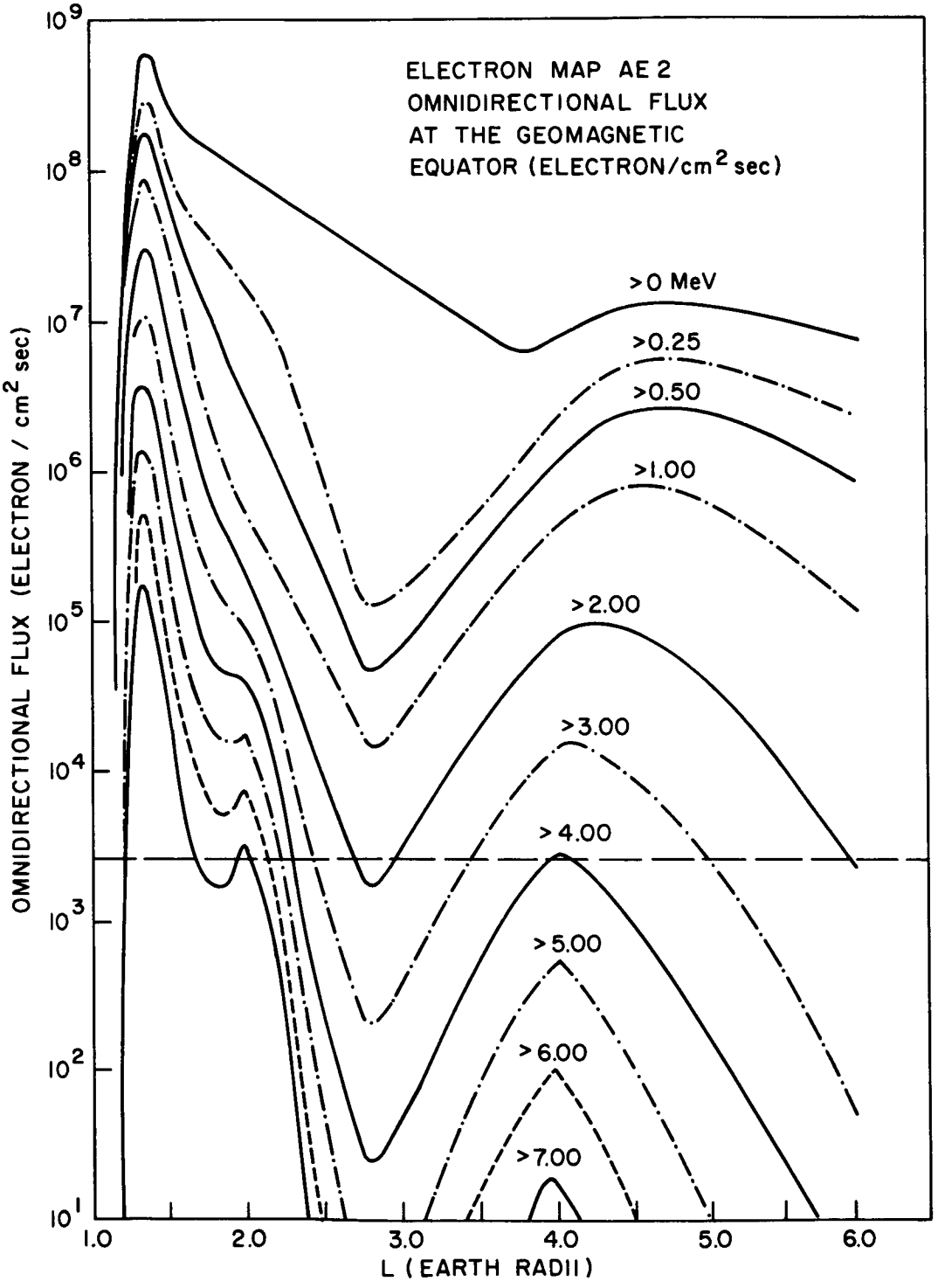
ELECTRON MAP AE 2
OMNIDIRECTIONAL FLUX
AT THE GEOMAGNETIC
EQUATOR (ELECTRON/cm² sec)
>0 MeV
>0.25
>0.50
>1.00
>2.00
>3.00
>4.00
>5.00
>6.00
>7.00
OMNIDIRECTIONAL FLUX (ELECTRON / cm² sec)
10⁹
10⁸
10⁷
10⁶
10⁵
10⁴
10³
10²
10¹
1.0
2.0
3.0
4.0
5.0
6.0
L (EARTH RADII)

Figure 74

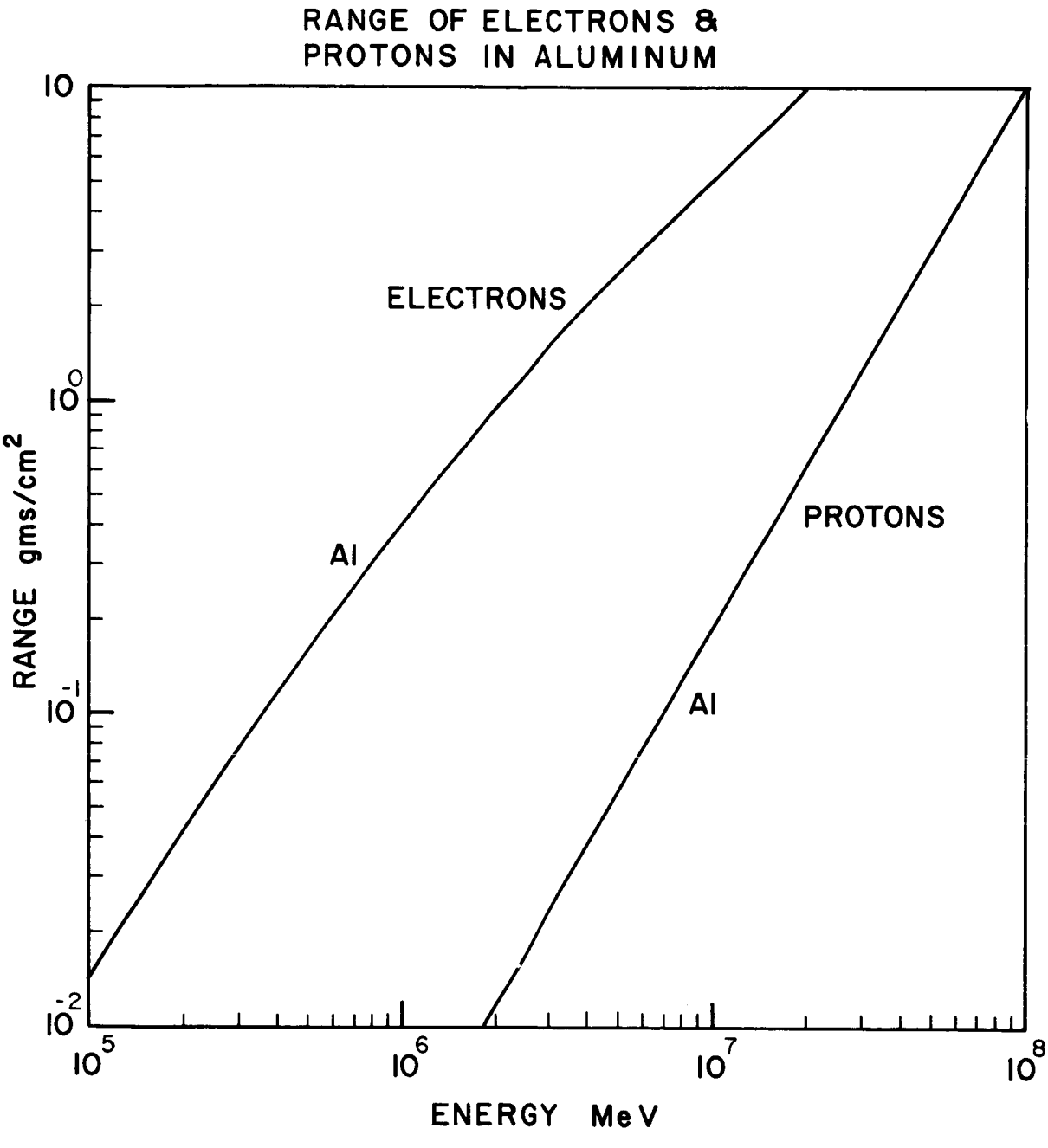
RANGE OF ELECTRONS &
PROTONS IN ALUMINUM
10
10^0
10^{-1}
10^{-2}
RANGE gms/cm^2
ELECTRONS
Al
PROTONS
Al
10^5
10^6
10^7
10^8
ENERGY MeV

Figure 75

electrons/cm^2 sec of energy greater than one MeV. If A is the projected cathode area,

$$A = \frac{\pi R_c^2}{2} \quad .$$

The Cerenkov wave fronts travel in the electron direction. Thus, only photons from electrons traveling toward the photocathode in the face plate cause photoevents.

The quantum efficiency, ϵ_q, of the 541E - 05M over the wavelength band 1500 to 5000 Angstroms is about 20% (Figure 76). Then the number of expected photoelectrons due to Cerenkov radiation in the inner belt would be,

$$N_c = \phi_o \frac{\pi R_c^2}{4} \epsilon_q \frac{2\pi \nu_{12}}{137} \left(1 - \frac{1}{n_r^2}\right) L_{ave} \quad . \tag{77}$$

Taking λ_1 = 1500 Å, λ_2= 5000 Å we have with $\phi_o = 10^8$, R_c = 1.27, ϵ_q = .2, n_r = 1.796, L_{ave} = .0478;

$$N_c = 1.78 \times 10^9/\text{sec}. \tag{78}$$

A photocathode current of 3.3×10^{-9} amp or 2.06×10^{10} electrons per second was observed. We conclude the Cerenkov radiation fails by about a factor 10 to explain the noise.

Shielding the Photocathode

If we are satisfied that the photomultiplier can be shielded from the radiation belts, and the work of the NASA group on OGO II indicates this to be true, the amount of shielding necessary to reduce the noise to a tolerable level can be straightforwardly estimated.

We shall wish to detect stars of magnitude $4^m.0$ against the background noise due to all sources.

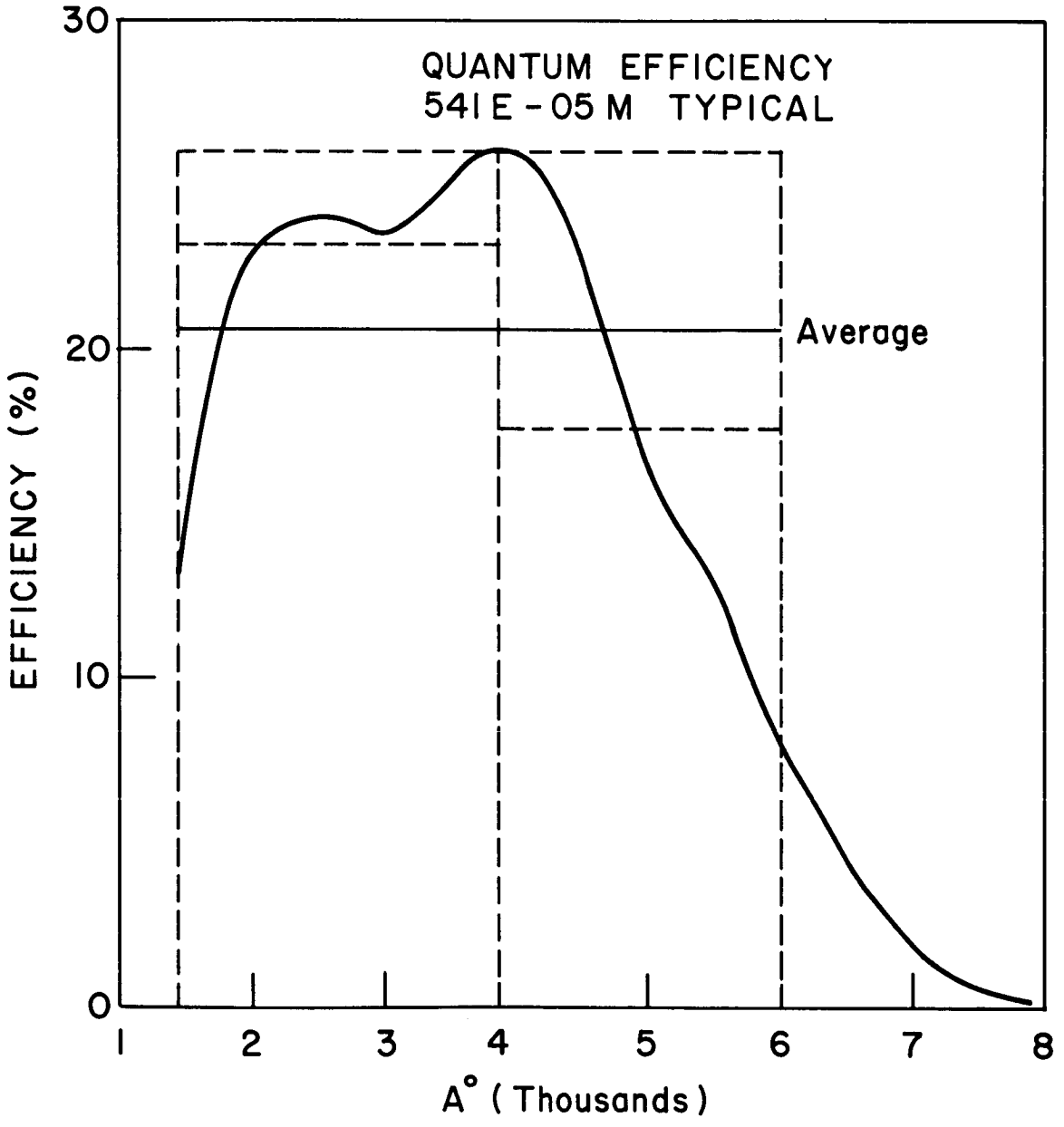
QUANTUM EFFICIENCY
541 E-05 M TYPICAL
Average
EFFICIENCY (%)
30
20
10
0
1
2
3
4
5
6
7
8
A° (Thousands)

Figure 76

From the work of Code[5] we can estimate the number, n_o, of photons per second per square centimeter incident on the earth's atmosphere from Vega. (Type A_o, $0^m.0$) This is,

$n_o = 1.66 \times 10^7/cm^2$ sec micron, at the center of the Johnson B filter (4300 Angstroms).

Then the number of resulting photoelectrons from a sensor with optical aperture, D, optical efficiency, ϵ_o, photomultiplier quantum efficiency ϵ_q, and bandpass $\Delta\lambda$, which views a star of magnitude M_B, is about

$$S = n_o \; 10^{-.4M_B} \frac{\pi}{4} D^2 \; \epsilon_o \; \epsilon_q \; \Delta\lambda. \tag{79}$$

If the faint star background is N tenth magnitude stars per square degree and A is the slit area in square degrees, the signal due to this source is

$$N_B = n_o \; N \; 10^{-4} \frac{\pi}{4} D^2 \; \epsilon_o \; \epsilon_q \; A\Delta\lambda. \tag{80}$$

A reasonable aperture is about two inches. Choose $\epsilon_o = .5$, $\epsilon_q = .2$, $\Delta\lambda = .3$ micron, $M_B = 3.5$, N = 320, A = .3 square degree. Then,

$$\begin{aligned} S &= 2.54 \times 10^5/sec, \\ N_B &= 1.53 \times 10^4/sec. \end{aligned} \tag{81}$$

In the absence of radiation noise the faint star background is the major source of noise, even so the d.c. signal due to it is less than the star signal by a factor 17. Therefore, we neglect it altogether.

The NASA group observed a dark current of 2.06×10^{10} electrons per second and were shielded for about an MeV. Above an MeV at the equator in the inner belt are about 10^8 electrons/sec cm^2. If each fast electron incident on the photocathode produced k photoevents,

$$2.06 \times 10^{10} \approx \frac{\pi}{2} R_c^2 \, k \times 10^8, \tag{82}$$

and since $R_c = 1.27$ cm, $k \approx 80$.

Allowable Noise.

Consider the situation of Figure 77. Some random process f(t) acting on the sensor causes an output,

$$I(t) = \sum_{k=-\infty}^{\infty} a_k \, p(t - t_k), \tag{83}$$

where p(t) describes the individual pulse shapes at the photomultiplier output and a_k their amplitude. Let a_k be a random variable.

I(t) is fed to the input of a filter with impulse response h(t). The filter output will be

$$I_o(t) = \sum_{k=-\infty}^{\infty} a_k \int_{-\infty}^{\infty} p(t - \tau - t_k) h(\tau) d\tau. \tag{84}$$

By Campbell's Theorem[25] the variance of I_o will be

$$\sigma^2 = \nu \, \overline{a^2} \int_{-\infty}^{\infty} \left[\int_{-\infty}^{\infty} p(\tau' - \tau) \, h(\tau) \, d\tau \right]^2 d\tau' \; ; \tag{85}$$

where ν is the rate at which photoevents occur and $\overline{a^2}$ is the second moment of a_k.

Since the filter response will be much slower than the photomultiplier we can as well take p(t) as the delta function. Then on integrating over τ,

$$\sigma^2 = \nu \, \overline{a^2} \int_{-\infty}^{\infty} h^2(\tau') d\tau' \tag{86}$$

$$= \nu \, \overline{a^2} \int_{-\infty}^{\infty} |H(f)|^2 df.$$

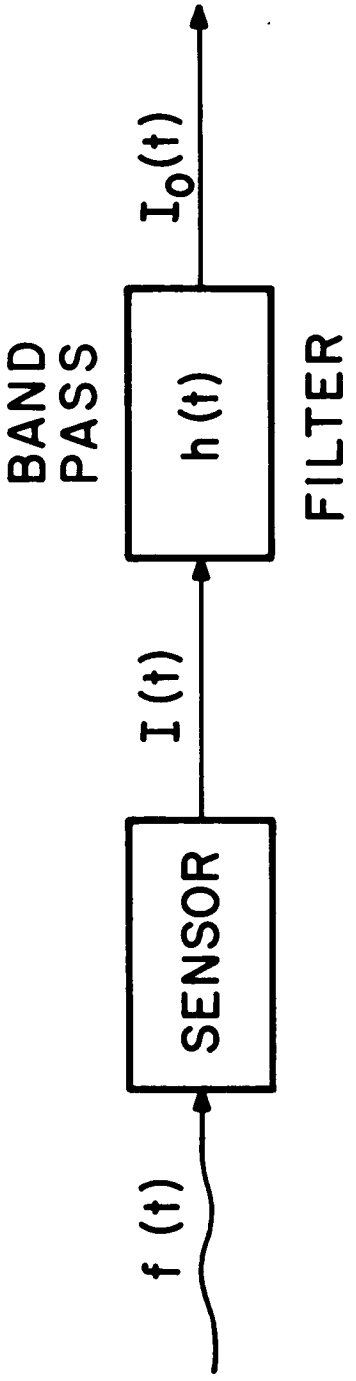

Figure 77: Star Signal Flow Diagram

Finally,

$$\sigma^2 = 2\nu\,\overline{a^2}\,\Delta f, \tag{87}$$

where,

$$\Delta f = \int_0^\infty |H(f)|^2\, df,$$

is the filter noise bandwidth.

To proceed further knowledge of the distribution of the a_k is needed. Lacking this knowledge, we assume a normal distribution with mean $\bar{a} = k$. Then,

$$\overline{a^2} = k + k^2 \approx k^2. \tag{88}$$

Then, if particle radiation noise dominates, photoevents due to this occurring at a rate N per second of mean magnitude k, the peak signal to RMS noise is

$$F = \frac{S}{\sqrt{2(S + k^2 N_p)\,\Delta f}}\ . \tag{89}$$

(Note that $\overline{a^2} = 1$ for signal photoelectrons.)

Accurate location of a star position at a signal to noise ratio of five is reasonable. Thus, take F = 5. A 0.1 degree slit rotating at 15 rpm transits a star in a time,

$$T_s = \frac{.1 \times 15}{360} \text{ sec.} \tag{90}$$

The optimum electrical bandwidth is about

$$\Delta f = \frac{1}{3T_s} = 80 \text{ cps.}$$

One can now solve for N from (89) with the result that

$$N_p = 6.25 \times 10^3 \frac{\text{fast electrons}}{\text{sec}} .$$

The average projected area of the photocathode being half its total area, the allowable Van Allen belt flux becomes,

$$\phi = 2.47 \times 10^3/\text{sec cm}^2. \qquad (91)$$

A dotted horizontal line which corresponds to this flux has been drawn in Figure 74. We see that unless we shield against at least three MeV, operation with an end-on tri-alkali photocathode is not possible through much of the belt. Since disturbed sun conditions may increase the outer belt radiation by factors of about 10^2, shielding the photocathode and first dynode stages for five MeV seems indicated. If the radiation environment were Vettes AE-2, this would require 2.5 gm/cm^2 about the neck of the sensor and amounts to about .9 centimeter thickness of aluminum.

Luminescence.

The NASA group[20] tested the luminescence of various window materials for irradiation with 50 KeV electrons from an electron microscope and by a millicure strontium 90 source. We will use the data from each experiment, in turn testing whether luminescence of the cathode window material caused by fast electrons can account for the OGO II results.

According to Heitler[26] in the region where the dominant loss mechanism for fast particles in matter is by collisions, the average energy loss is "very nearly proportional" to the number of primary ion pairs formed. The ratio of ionizations to excitations and the average energy transfer per ion pair are nearly independent of primary energy. About one primary ion pair is formed for each 32 KeV of energy loss practically independent of the particle type. Of course, primary ions (or electrons) subsequently produce secondaries.

Mott and Gurney[27] discuss the production of luminescence in solids. In speaking of irradiation with alpha and beta rays (presumably at moderate energies) they observe that most of the energy dissipation is by production of electron-hole pairs which subsequently recombine at impurity centers, Frenkel and Schottky defects, or at the surface where they either transfer their energy to the lattice atoms or radiate on recombining. A discussion of the mechanisms by which electrons and holes lose their excess energy is given.

The assumption,which the preceding few paragraphs are used here to justify, is that the radiance per incident particle is proportional to its energy loss.

Electron Microscope Data

On irradiation of sapphire with 10^8 - 50 KeV electrons one cm^2 sec., radiance of 10^{-4} ergs/sec cm^2 steradian was observed in the band 3500 - 4100Å. That is per 50 KeV electron an energy,

$$E \approx \frac{\pi}{2} \times 10^{-14} \text{ ergs/Å} \qquad (92)$$

was radiated into 2π steradians in the visible and ultraviolet.

We assume that the main body photometer was shielded for one MeV and that the energy distribution of electrons in the inner belt is given by equation (70) and the environment is Vettes' AE-2. This neglects belt decay as indeed we have previously done.

The average energy above an MeV is,

$$1 + \frac{1}{a} \text{ MeV} = 1 + \frac{1}{1.035} \text{ MeV}.$$

Of this on the average an MeV is lost in the shielding so that the average energy of electrons incident on the photometer cathode window was about

$$E_{ave} \approx 1/1.035 \text{ MeV}. \tag{93}$$

Over the wavelength band 1500 to 6000Å the 541E - 05M typically has a quantum efficiency ϵ_q of about 20%. Midband wavelength, λ_{ave}, is 3750Å, and bandwidth is 3500Å. The density of electrons above an MeV is again taken as 10^8/sec cm^2. Then the expected number of photoevents is,

$$n_{pe} = \frac{\pi}{2} R_c^2 \phi_o \left(E \frac{E_{ave}}{5 \times 10^{-2}} \right) \epsilon_q \frac{\lambda_{ave}}{hc} \Delta\lambda. \tag{94}$$

Using (92) and (93) in (94) with the data of the previous paragraph,

$$n_{pe} \approx 2/3 \times 10^{10}/\text{sec}. \tag{95}$$

This is within a factor three of the observed photocurrent.

Strontium 90 Irradiation.

Here NASA group[20] placed a millicure strontium 90 source one-quarter inch square in contact with various samples of window material. Within the wavelength band 1800 to 6300 Å the radiance from the sapphire sample was 3.8×10^{-10} watts/cm^2 steradian. Strontium 90 with a one-half life of 25 years has a daughter, yttrium 90, with a one-half life of 65 hours. Thus, the strontium 90 is in equilibrium with its daughter. The maximum beta energy of strontium 90 is .545 MeV, that of the yttrium 90 is 2.26 MeV. There is also 1.74 MeV gamma radiation at a rate of 6×10^2/sec cm^2 which will be neglected. There will be $2 \times 3.71 \times 10^7$ decay events/second, but only half of these would result in beta rays through the sapphire.

In his discussion of beta decay, Fermi[28] gives for the probability that the emitted electron has momentum in p, p + dp,

$$P(p)dp = \text{Const.} \left(\sqrt{1 + \eta_o^2} - \sqrt{1 + \eta^2} \right)^2 \eta^2 d\eta$$

$$\eta = \frac{p}{mc} = \sqrt{\frac{2E}{mc^2}} \quad ,$$

and

$$\eta_o = \frac{P_{max}}{mc} \quad .$$

The average energy carried away by a beta particle will be,

$$E_{ave} = \frac{\int_o^{P_{max}} P(p)\, \frac{p^2}{2m}\, dp}{\int_o^{P_{max}} P(p)\, dp} \quad . \tag{96}$$

The integral in the denominator of (96) is given by Fermi[28] in terms of a function $F(\eta_o)$.

$$F(\eta_o) = -\frac{\eta_o}{4} - \frac{\eta_o^3}{12} + \frac{\eta_o^5}{30} + \frac{\sqrt{1+\eta_o^2}}{4} \sin h^{-1}\eta_o \tag{97}$$

Defining,

$$\begin{aligned} E(\eta_o) &= \int_o^{\eta_o} \left(\sqrt{1+\eta_o^2} - \sqrt{1+\eta^2}\right)^2 \eta^4 d\eta \\ &= \frac{\eta_o}{8} + \frac{\eta_o^3}{24} - \frac{\eta_o^5}{60} + \frac{\eta_o^7}{105} - \frac{\sqrt{1+\eta_o^2}}{8} \sin h^{-1}\eta_o, \end{aligned} \tag{98}$$

$$E_{ave} = \frac{mc^2}{2} \frac{E(\eta_o)}{F(\eta_o)} \tag{99}$$

Using (97) to (99) we find

$$\begin{aligned} E_{ave}(.545 \text{ MeV}) &= .087 \text{ MeV} \\ E_{ave}(2.26 \text{ MeV}) &= .675 \text{ MeV}. \end{aligned} \tag{100}$$

There is a Cerenkov component in the radiance measured by the NASA group. Most of this is from the yttrium 90 decay. The amount of this will first be estimated assuming a monoenergetic beam of energy given by (100). This is equivalent to neglecting the energy dependence of beta in equation (64) and the contribution of the strontium 90.

The Cerenkov radiation per electron will be from (64)

$$E_c \approx 2\pi^2 e^2 \left(1 - \frac{1}{n_r^2}\right) \times \left(\frac{1}{\lambda_1^2} - \frac{1}{\lambda_2^2}\right) \ell_{ave} \quad . \tag{101}$$

Below .204 MeV the Cerenkov radiation in sapphire ceases. The range of .2 MeV electrons is about .04 gms/cm^2. That of .675 MeV electrons is about .250 gms/cm^2. Thus, we will use an average path length for Cerenkov radiation of .210 gm/cm^2 or (using a density of 3.5 gm/cm^3),

$$\ell_{ave} = .06 \text{ cm.} \tag{102}$$

Using (102), $n_r = 1.796$, $\lambda_1 = 1800$ Å, $\lambda_2 = 6300$ Å, $e = 4.803 \times 10^{-10}$ e.s.u.

$$E_c = 5.34 \times 10^{-10} \text{ erg/electron} \tag{103}$$

The number of electrons emitted per square centimeter per second per steradian is,

$$n_e = \frac{3.71 \times 10^7}{\left(\frac{2.54}{4}\right)^2 \times 4\pi} = 7.32 \times 10^6/\text{cm}^2 \text{ sec steradian} \tag{104}$$

The product of (103) and (104) is the estimate of the amount of observed light from the sapphire due to the Cerenkov component. This is,

$$I_c = 3.91 \times 10^{-3} \frac{\text{ergs}}{\text{sec cm}^2 \text{ steradian}} \quad , \tag{105}$$

an amount sufficient in itself to account for the NASA observation.

Nonetheless, some of the observed light must have been due to scintillation. Let us use the electron microscope data to estimate this component. There we had that an amount of energy,

$$E_{e\nu} = \frac{\pi}{1.5} \times 10^{-19} \frac{\text{ergs}}{\text{Å eV}} ,$$

was due to luminescence. Therefore, with .675 MeV electrons in the wavelength band 1800 to 6300 Å, we would have,

$$E_e = \frac{\pi}{1.5} \times 10^{-19} \times 3.5 \times 10^{3} \times .675 \times 10^{6} \qquad (106)$$

$$= 4.95 \times 10^{-10} \text{ ergs/electron.}$$

This is almost the same as the Cerenkov component of equation (103). Let us assume that the relative amounts of Cerenkov radiation and luminescence occurring in the strontium 90 experiment are given by (103) and (106). There we had that,

$$3.71 \times 10^{7}/(2.54/4)^2 \frac{\text{.675 MeV electrons}}{\text{cm}^2 \text{ sec}}$$

$$= 4\pi \times \frac{.675}{.675 + .087} \times \frac{.495}{4.95 + 5.34} \times 3.8 \times 10^{-3} \text{ ergs/cm}^2 \text{ sec.}$$

Where we use only the yttrium 90 beta particles in the computation, the energy radiated in luminescence is about,

$$E_e = 2.21 \times 10^{-10} \text{ ergs/.675 MeV electron.}$$

The expected number of photoevents due to luminescence of the NASA photometer cathode window in the AE-2 environment would be,

$$n_{pe} = \phi \frac{\pi R_c^2}{2} E_e \left(\frac{E_{ave}}{.675} \right) \epsilon_q \frac{\lambda_{ave}}{hc} .$$

Using $R_c = 1.27$ cm, $\epsilon_q = .2$, $\lambda_{ave} = 4050$ Å, $E_{ave} = 1/1.035$ MeV, and $\phi_o = 10^8/cm^2 sec$,

$$n_{pe} \approx 3.27 \times 10^9/sec. \quad (107)$$

This is within a factor six of the observed rate.

Using the electron microscope data we came within a factor three of the observed rate, and Cerenkov radiation came within a factor eleven. Considering the crudeness of the calculations, we perhaps have no right to expect better agreement. Nonetheless, none of these mechanisms has really accounted for all the observed noise. And since the belt decay was neglected, the discrepancy appears even greater.

It is likely that luminescence from the tube walls near the photocathode and scintillation of the tri-alkali itself are needed to fully explain all the noise, but it seems likely that fast electrons penetrating the shielding can account for most of the dark current increase observed on the OGO II main body air glow photometer.

The proton component has not been included. Shielding for MeV electrons also shields for 15 MeV protons (cf. Figure 75). Above 15 MeV Vette's HP 1-4[16] environment gives about 3×10^4 protons/cm^2 second at 1.3 - 1.4 earth radii. This is orders of magnitude less than the electron density at the same place.

Shielding Requirement S^3.

If an end-on photomultiplier of the 541E - 05M type is used 9/10 centimeter of aluminum seems needed to insure that $4^m.0$ magnitude stars are detected against the background of the radiation belt noise through the vehicle's orbit. This shield should cover the photocathode and first few dynodes extending well beyond the cathode in both directions along the tube axis.

A side window tube requires less shielding but must have a field lens to image the reticle onto the photocathode. A price must also be paid in quantum efficiency.

2. Bright Source Shielding

The primary purpose of the shield for the SCADS-IMP sensor is to prevent direct sunlight from falling on the lens surface. Several theoretical shield designs are discussed in this section which can accomplish this mission.

The designs presented here generally consist of two connected cones, of which the one next to the optics primarily delineates the field of view. The other larger cone serves to shield the inner one from all direct sunlight. Since direct sunlight does generally fall on the outer cone its angle is taken large enough so that it cannot be "seen" by any part of the optics.

This is shown schematically in Figure 78 where θ is the field of view and cone angle of the inner cone, α is the angle of the outer cone, β is the angle made by the sun's rays with the optical axis, and D is the diameter of the optics.

In general, the smallest possible cone is desired, which will occur when the distance $\overline{ab} = r$ is a minimum. It can be shown that this occurs for an angle α satisfying

$$\tan \alpha + \cot(\alpha - \theta/2) = \cot(\beta - \alpha) . \qquad (108)$$

Generally for angles of β such that the sun is close to the edge of the field of view, this type of baffle becomes very large in size, and it is desirable to look for ways to make it smaller.

One method is to truncate the top cone and replace the missing portion by a baffle with a knife edge stop around the field of view as shown in Figure 79, thus also providing some flexibility. With this design there is still no sun illuminated surface exposed directly to the lens.

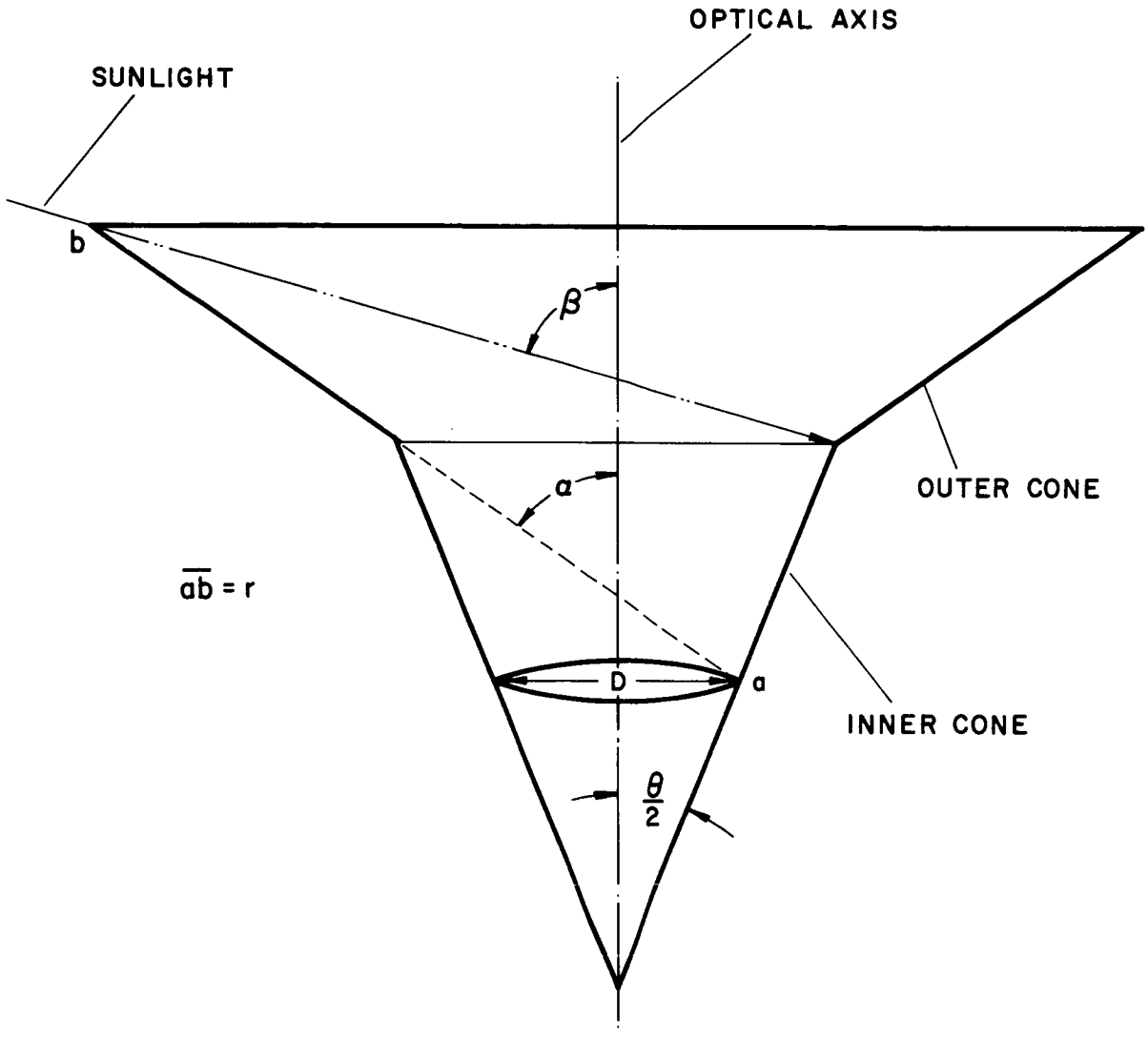

Figure 78: Connected Cones for Radiation Shielding

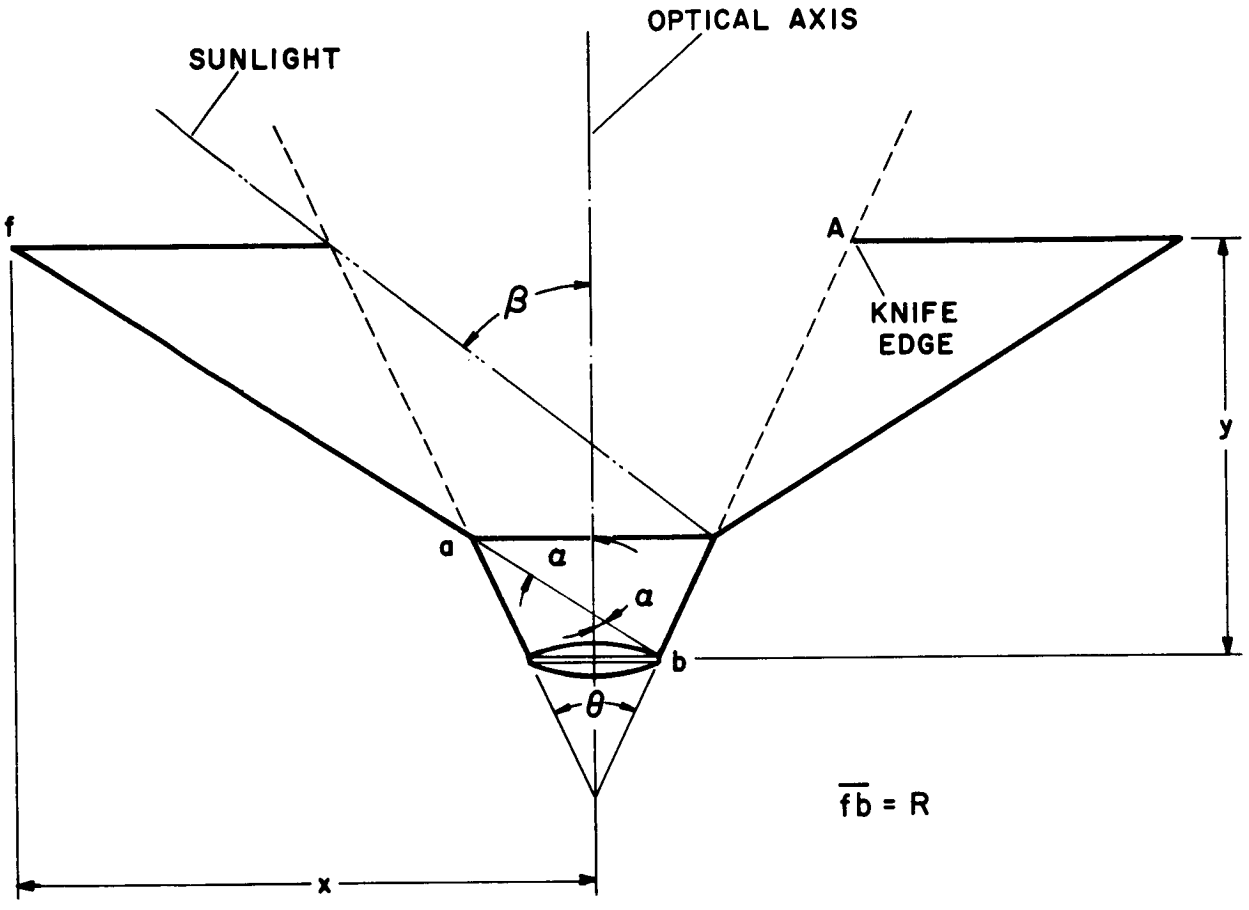

Figure 79 : Radiation Shield

The disadvantage of this design is that now the lens is exposed to light which has been scattered twice off the inner surfaces of the outer cone and baffle. The lens is also exposed to light diffracted and reflected off the knife edge of the baffle at A. Diffraction off the knife edge may be reduced by approximately a factor of ten by serrating the knife edge, producing a sawtooth edge in the manner of Purcell and Koomen[29]. The serrations, however, must be accurately made with sharp, smooth edges and are obviously harder to make than a nonserrated knife edge. It is necessary to mention also that the knife edge (or sawtooth) must be very sharp to minimize the specular reflection from it directly into the optics.

For this design the distance $\overline{bf}$ is minimized for α given by

$$\cot(\alpha + \beta) + \tan\alpha = \cot(\alpha - \theta/2). \tag{109}$$

Up to this point the cone interior has been regarded as a diffuse reflector. If we could obtain purely specular reflecting surfaces, the cone of Figure 80 is possible. It may be shown that in this case the cone ideally need be only

$$L = D/2 \csc\theta/2 \,(\csc(\beta - \theta/2) - 1) \tag{110}$$

in length.

Since scattering will occur to some extent from any specular reflector this design is really feasible only in so far as this scattering is kept within bounds. Lengthening the cone and/or increasing the cone angle may also be used to reduce light into the lens. Moreover, if the lens is antireflection coated for normal rays, rays at 60 degrees are totally reflected. This characteristic may be used to reduce scattered light into the photomultiplier. (It should be noted that the cone designs of Figures 78 and 79 may also advantageously make use of specular reflectors of low

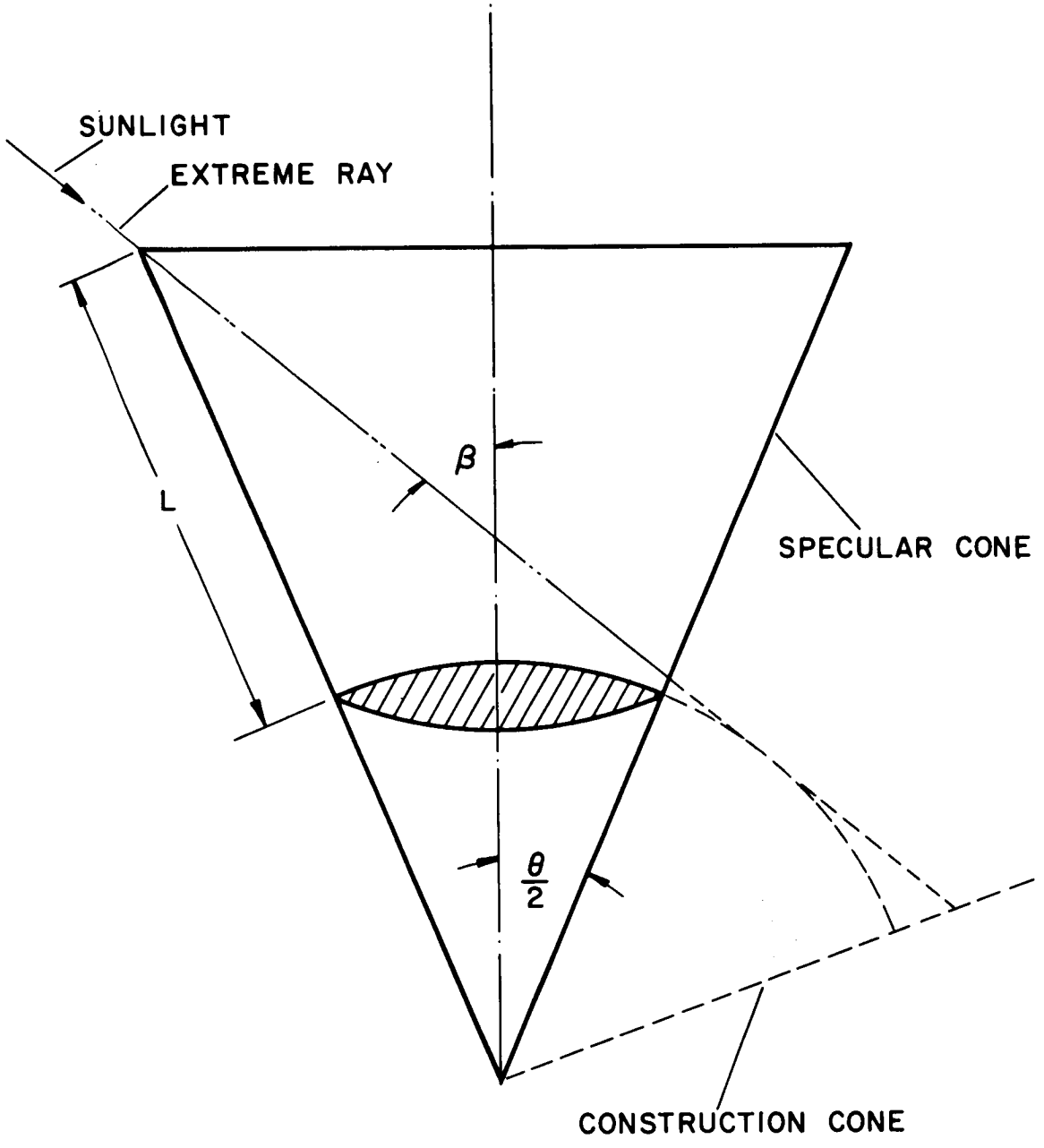

Figure 80 : Specular Reflecting Radiation Shield

optical efficiency.)

An antireflecting black paint with absorption of 99.9 percent ("Parson's Black") is available. Generally two reflections will occur before stray light in the designs of Figures 78 and 79 reaches the lens. This implies that in order to compete with these designs, diffuse reflection off the surface of the specular cone of Figure 80 must be held below one part in a million. This requirement means a high optical finish on a metallic surface and renders this solution somewhat speculative.

The edges of the lens elements will have to be coated with a light absorbing coating, or antihalation coating, to cut down scattering within the lens system. Scratches and dust on the lens elements, seeds, bubbles, and other inhomogeneities in the glass will also add to the scattering effects. Indeed, the problems regarding unwanted light resemble those encountered in solar coronographs.

For the "ideal" baffle (double cone without the knife edge) the length of a cone diagonal is given by

$$r = D \frac{\cos\alpha \sin(\beta + \theta/2)}{\sin(\alpha - \theta/2) \sin(\beta - \alpha)} \tag{111}$$

That same quantity for the cone with a knife edge baffle is given by

$$R = D \frac{\cos^2 \theta/2 \sin(\alpha + \beta)}{\cos(\beta - \theta/2) \cos\alpha \sin(\alpha - \theta/2)} \tag{112}$$

Given field of view, θ, and sun angle off the optical axis β, the outer cone angle α which minimizes r and R are given in Equations (109) and (110). Using these α, θ = 20 degrees, and various sun angles β the minimum cone sizes have been calculated and are given in Figure 81. It is

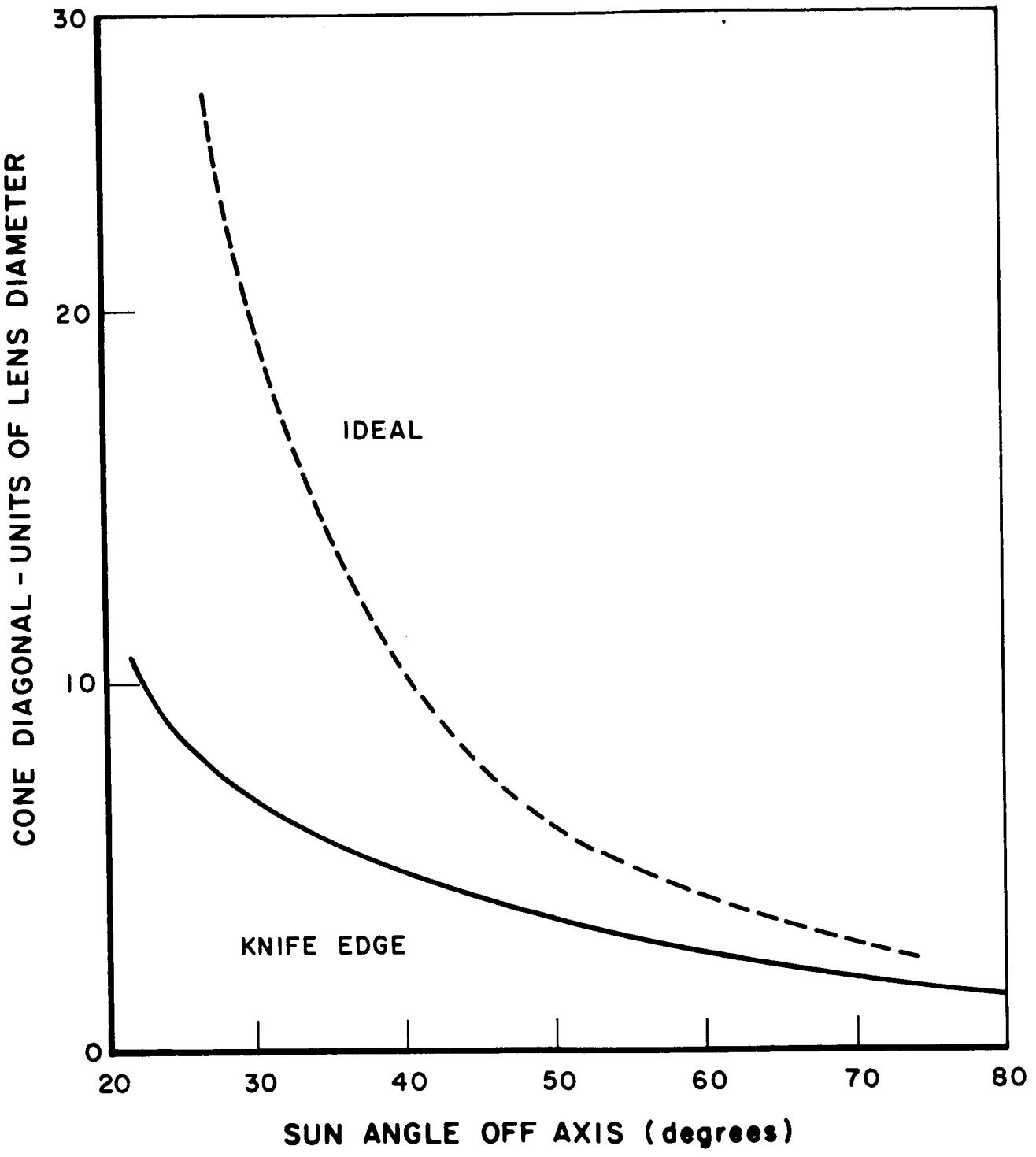

Figure 81: Minimum Cone Size as a Function of Sun Angle Off Optical Axis (Field of View, 20 Degrees)

interesting to note that, although at "small" sun angles (20 degrees to 30 degrees) a substantial size reduction results from the use of a knife edge baffle, the knife edge baffle rapidly loses its size advantage as the sun angle increases.

For the SCADS-IMP sensor the required shield dimensions have been determined for the knife edge shield of Figure 79 . The maximum radius and height of the shield are respectively given as

$$x = D\left\{\frac{\cos \theta/2}{\sin(\alpha - \theta/2)}\left[1 + \frac{\cos \beta \sin(\alpha + \theta/2)}{\cos \alpha \sin(\beta - \theta/2)}\right] \sin \alpha - \tfrac{1}{2}\right\} \qquad (113)$$

and

$$y = D \frac{\cos \theta/2}{\sin(\alpha - \theta/2)}\left[1 + \frac{\cos \beta \sin(\alpha + \theta/2)}{\cos \alpha \sin(\beta - \theta/2)}\right] \cos \alpha \qquad (114)$$

The field of view = $\theta = 20^{\circ}$ for a cant angle of 25°. The sun is nominally 90 degrees to the spin axis, but it will be assumed that it can get as close as 80 degrees to the spin axis. So the sun can get as close as $\beta = 55^{\circ}$ to the optical axis. Consequently, from the minimum cone relationship

$$\cos \beta = \cot(\alpha - \theta/2) \sin(\alpha + \beta) \cos \alpha, \qquad (115)$$

α must equal 54.07 degrees in order to prevent direct sun radiation from striking the lens face. Hence,

$$\begin{aligned} x &= D(2.072) \\ y &= D(1.864). \end{aligned} \qquad (116)$$

The required values of x and y for the optical aperture diameter determined in Section III-E have been tabulated in Table X.

TABLE X

SUN SHIELD DIMENSIONS

Scan Period Seconds	Optical Aperture Diameter--Inches	Maximum Shield Radius--Inches x	Maximum Shield Height--Inches y
$2 \leq T < 7$	2.648	5.486	4.935
$7 \leq T < 12$	1.506	3.120	2.807
$T \geq 12$	1.205	2.497	2.246

3. Susceptibility of Photomultiplier to Earth Reflected Sunlight

Since the SCADS sensor must scan through the earth, it is important to approximately determine the intensity of earth reflected sun radiation and to estimate what effect if any it will have on the photomultiplier.

The altitude of the IMP vehicle at perigee is given as 10^4 nautical miles or approximately 2.9 earth radii. Figure 82[30] shows that at an altitude of 2.9 earth radii, the maximum light intensity due to earth reflected sun radiation is approximately 250 foot-candles.

At this level of cathode illumination there is sufficient evidence available in the literature to indicate that cathode deterioration does not occur as long as the accelerating voltage is not applied to the cathode. Although emission of high photocurrent densities leads to a degradation of photocathode response, such emissions do not occur if an accelerating field is not applied to the cathode while it is subjected to a high illumination level. This is confirmed in a paper presented by CBS Laboratories in 1962[31]. Some of the results presented in this paper are shown in Figure 83. Figure 83 shows the results of measurements on two Cs-Sb cathodes each illuminated with an intensity of 4.64×10^{-6} watts per square centimeter and with high voltage applied to the photomultiplier. One cathode was deposited on an opaque nickel substrate and the other was semi-transparent and deposited on glass. The opaque cathode appeared to be superior because of its greater surface conductivity. Data was also presented on semi-transparent Cs-Sb cathodes deposited on a transparent conductive (TC) coating. Figure 83 shows a comparison of Cs-Sb on TC coatings with Cs-Sb on glass. The curves in Figure 83 labeled No. 0088Z and No. 0474Y had

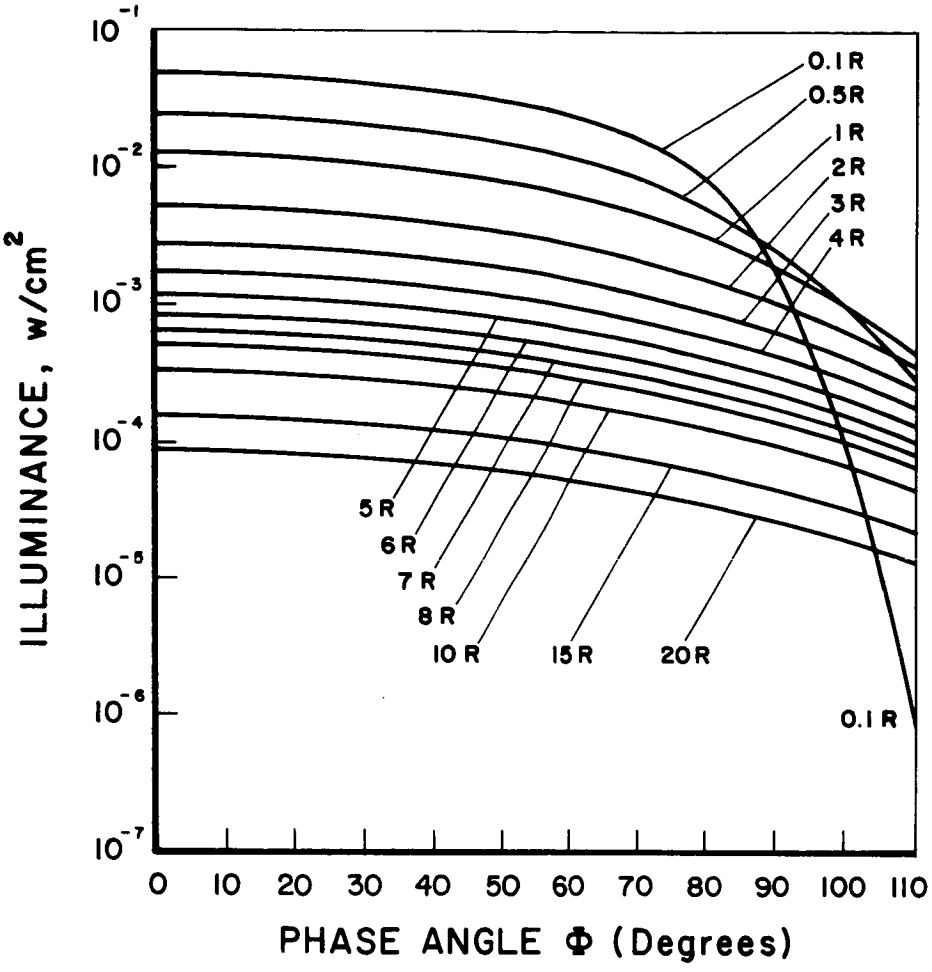

Figure 82 : Light Intensity Versus Phase Angle for Various Distances from the Surface of the Earth

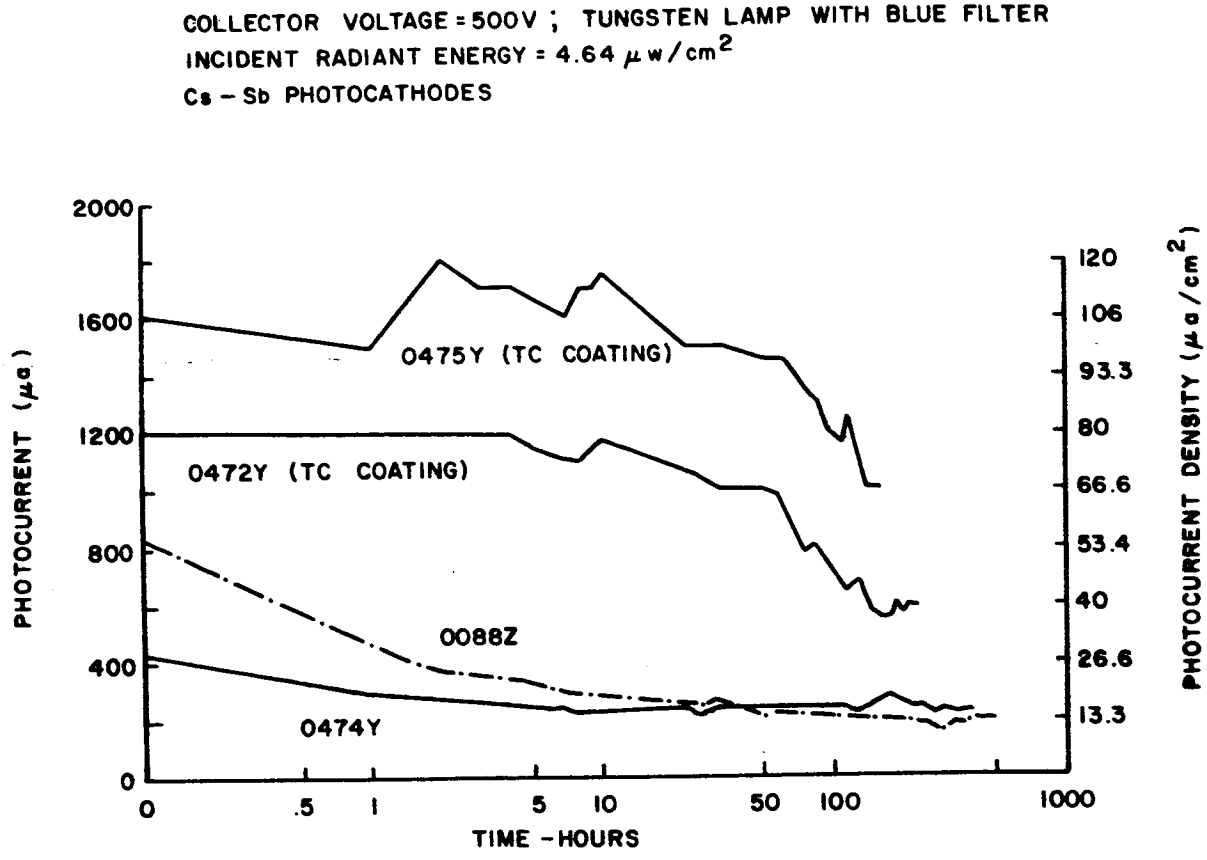

Figure 83: Fatigue Comparison of Cs-Sb Photocathodes Deposited on Glass Substrate Versus Deposition on Semitransparent Transconductive Coating When Voltage is Applied to the Photomultiplier

standard semi-transparent Cs-Sb cathodes deposited on soda-lime glass. The curves in Figure 83 labeled No. 0475Y and No. 0472Y had semi-transparent Cs-Sb cathodes deposited on a transparent conductive coating (TC) of tin oxide on soda-lime glass. The cathode with the transparent conductive coating appeared to degrade much more gradually. CBS then exposed a standard Cs-Sb cathode to an illumination of 4.64×10^{-6} watts per square centimeter with no voltage applied to the tube. No degradation of the cathode was observed over a period of eleven hours of continuous illumination. Then voltage was applied to the illuminated cathode and it was observed that the cathode sensitivity degraded similar to the lower curves in Figure 83 . This gives strong evidence that the cathode degradation is caused by the high photo-current rather than from the heat from the incident light. As further evidence, deterioration occurred as described even though the cathode was cooled. It is interesting to note that the main cause of deterioration appeared to be the loss of cesium from the Cs-Sb film. By replacing the cesium, the original sensitivity was restored.

In 1962 CBS Laboratories published [32] additional data on photocathodes operated with voltage applied to the photomultiplier while subjected to high illumination levels. Figure 84 shows results obtained with standard photocathodes when subjected to high illumination levels and voltage applied. Note that the illumination intensities in this case are much higher, 4500 foot-candles and 640 foot-candles. In this case, the possible cause of photocathode disintegration are positive ion bombardment, electrolytic action in the photocathode and photocathode poisoning from the substrate. CBS has verified by experiment that the Cs-Sb cathode when subjected to the high illumination as in Figure 84 does not degenerate if cathode voltage is not applied. In addition, CBS has also developed a low resistivity, transparent conductive tin oxide undercoating which is applied to the photocathode window.

Figure 85 shows fatigue of an undercoated photocathode operated while

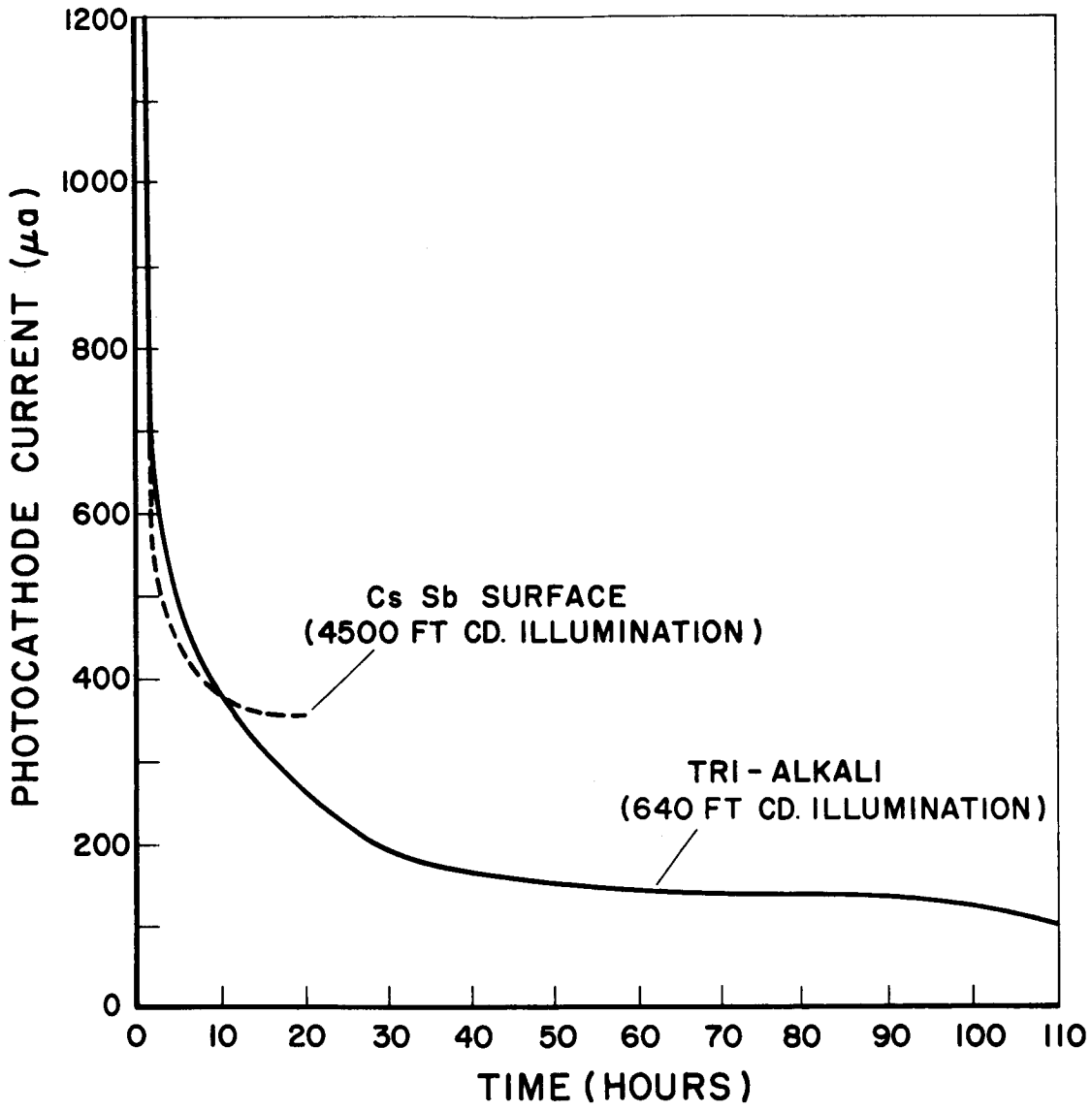

Figure 84: Photocathode Fatigue for Standard Photosensitive Surfaces When Photomultiplier Voltage is Applied

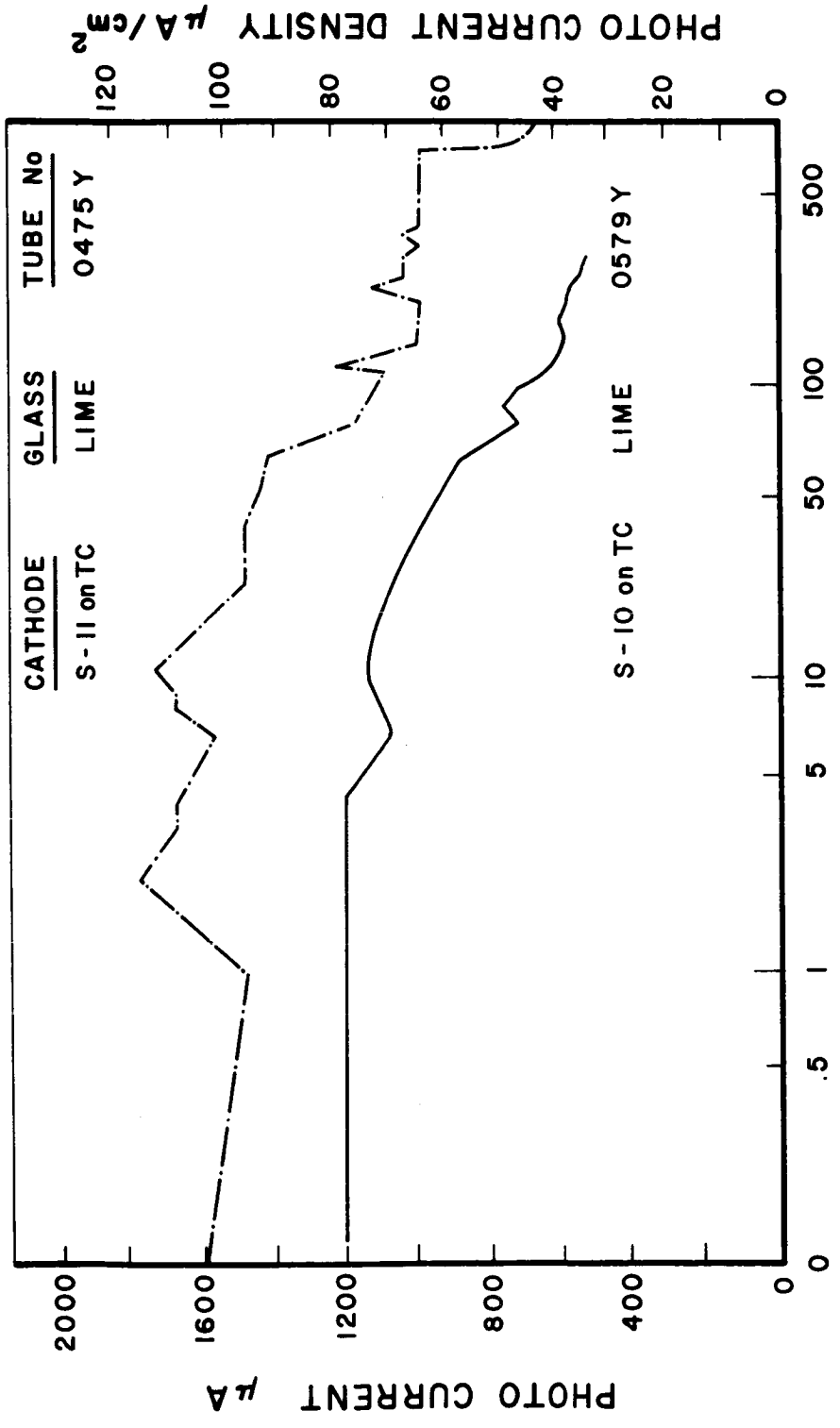

Figure 85 : Photocathode Fatigue for Specially Developed CBS Photosensitive Surfaces When Photomultiplier Voltage is Applied

subjected to an illumination intensity of 3.62×10^{-3} watts per square centimeter. Almost no fatiguing occurred for several hundred hours.

From the above discussion, it can be concluded that fatigue of the SCADS-IMP photomultiplier cathode will occur if voltage is applied to the tube while the sensor scans through the earth. However, fatigue will not occur if voltage to the tube is removed as the earth is scanned.

Although the cathode does not deteriorate while exposed to high illumination levels with no voltage applied, the cathode dark current is increased above normal if high voltage is applied immediately after the cathode has been exposed to high illumination. Information [33] is available on photomultiplier dark current after exposure to high light level; however, this does not apply directly since voltage was applied during cathode exposure. In this case with voltage applied it was found that dynode charging was the major contributor to the dark current increase. Adequate references are not currently available in the literature for a case when voltage is not applied to the tube during high cathode illumination.

I. Mechanical Packaging

A modular packaging technique should be employed which permits reliable operation, permits easy assembly and testing, is light weight and occupies a minimum volume. All electrical components and connectors used should be space-qualified items. Structural supports and framework should be fabricated of light weight metals such as aluminum.

The SCADS-IMP electronics will be comprised of discrete components and integrated circuits. These components should be mounted and soldered on multilayer printed circuit boards. The multilayer boards can be plugged together and then fastened to a support plate with screws that pass completely through the stacked boards as shown in Figure 86. Pluggable connectors can be used between circuit boards for easy fabrication and checkout. However, for increased reliability, there should be provision for permanent portable solder connections to be made after checkout is completed. As recommended in Section III-H-1, a 0.22 inch thick aluminum cover should be used to enclose the entire electronics subassembly and to shield the components from particle radiation as the IMP vehicle passes through the radiation belts.

Discrete components should be mounted by providing holes in the circuit boards through which the component leads can be inserted and then soldered on the reverse side. Integrated circuit chips should be mounted by soldering their leads directly to printed circuit pads. Wherever they are required for the integrated circuit chips, heat conductive mounting pads should be provided as a part of the circuit boards.

To insure optimum performance of the photomultiplier, it is essential that the tube be both magnetically and electrostatically shielded. It is recommended that the photomultiplier be shielded with two metal layers, each separated by a thin insulated layer. The inner metal layer should be a high mu metal while the outside layer should be a lower mu metal. The

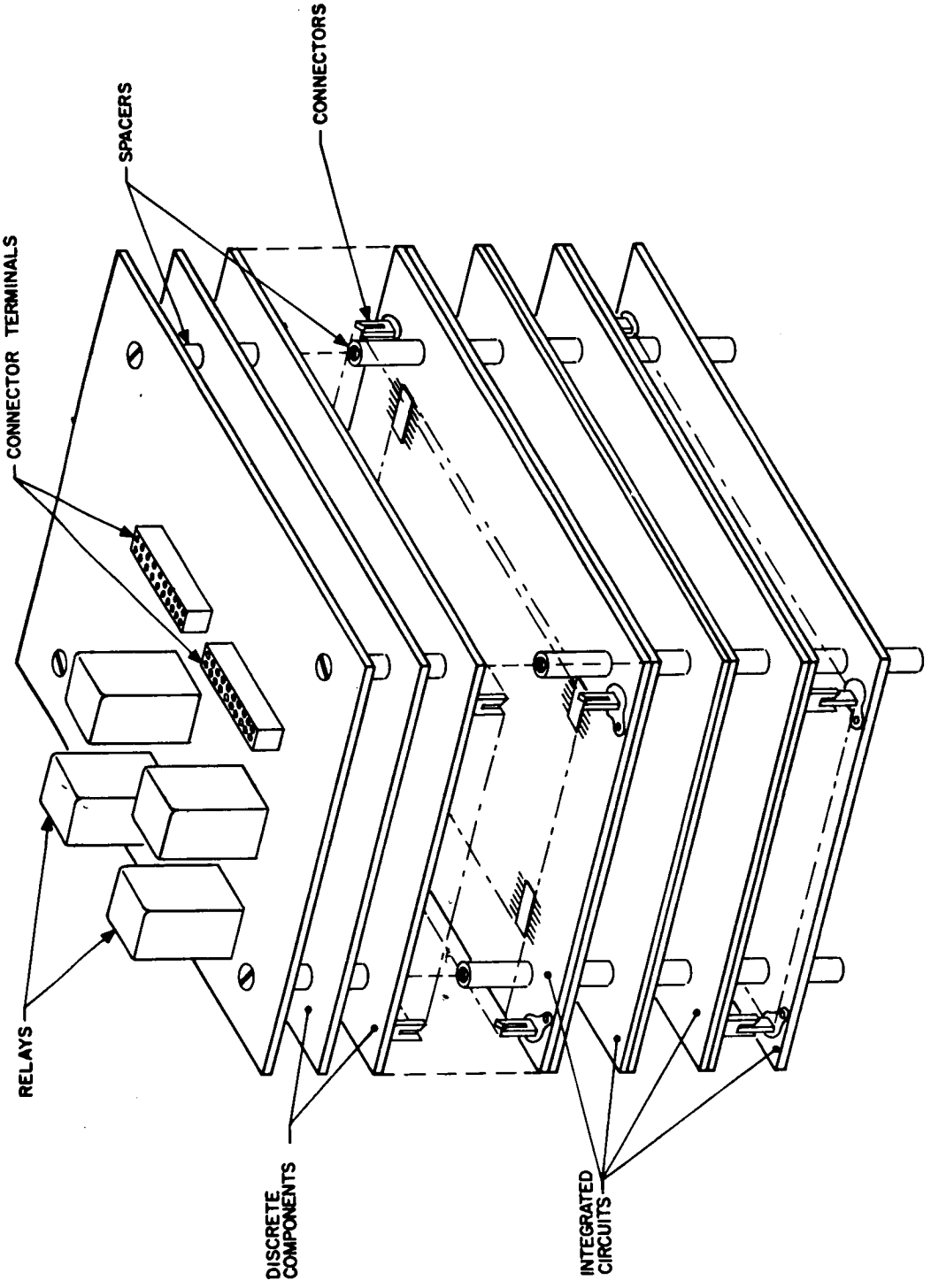

Figure 86: Mechanical Layout of the Electronics Unit

overall attenuation of two such insulated layers is known to be greater than the shielding possible with a single equivalent shield.

The preamplifier following the photomultiplier should be placed as close to the photomultiplier anode as is practical to reduce induced noise in the photomultiplier output signal lead. In addition, each low level amplifier and filter circuit module should be individually shielded to reduce induced noise due to radiation and coupling from high level circuits. Also, all low level signal interconnecting leads must be carefully isolated from high level and digital leads to reduce induced noise coupling into the low level signal leads.

Weight and Volume

Weight and volume are particularly important characteristics of the SCADS-IMP sensor. Both of these parameters have been estimated and tabulated for the various optical and electronic options. The sensor weight is tabulated in Table XI. It is estimated that on-board transit time encoding costs approximately .6 pounds of added weight.

The sensor volume is tabulated in Table XII. Note that a large percentage of the volume is required by the sun shield, especially for the shorter scan periods which have the larger optical apertures.

TABLE XI

ESTIMATED WEIGHT OF SCADS-IMP SENSOR
Pounds

Subassembly	Optical Options: $2 \leq T < 7$ sec. D = 2.65 inch f/1.05	$7 \leq T < 12$ sec. D = 1.51 inch f/1.85	$T \geq 12$ sec. D = 1.21 inch f/2.32
Lens	2.1	.7	.5
Photomultiplier (potted)	.38	.38	.38
Power Supplies	.13	.13	.13
Cathode Particle Shield	.3	.3	.3
Sun Shield	1.	.6	.5
Sensor Housing	.5	.5	.5
Subtotal	4.41	2.61	2.31
Electronics (No on-board transit time encoding)	.22	.22	.22
Total	4.63	2.83	2.53
Electronics (On-board transit time encoding)	.55	.55	.55
Total	4.96	3.16	2.86

TABLE XII

ESTIMATED VOLUME OF SCADS-IMP SENSOR
Cubic Inches

Subassembly	Optical Options: $2 \leq T < 7$ sec. D = 2.65 inch f/1.05	$7 \leq T < 12$ sec. D = 1.51 inch f/1.854	$T \geq 12$ sec. D = 1.21 inch f/2.32
Lens	15.3	5	3.2
Photomultiplier (EMR-541N)	6.5	6.5	6.5
Power Supplies	2.0	2.0	2.0
Cathode Particle Shield	3.2	3.2	3.2
Subtotal	27.0	16.7	14.9
Electronics (No on-board transit time encoding)	3.5	3.5	3.5
Total	30.5	20.2	18.4
Electronics (On-board transit time encoding)	7.5	7.5	7.5
Total	34.5	24.2	22.4
Sun Shield	470	85	43

PRECEDING PAGE BLANK NOT FILMED.

SECTION IV
MATHEMATICAL ANALYSIS

The purpose of this section is to provide a general discussion of the mathematical aspects of attitude determination by use of star transits across a slit. Details will not be provided here, for such details have been given in final reports of previously supported NASA programs.[2]

A. Physical Assumptions

As of this writing, it seems that we may assume the IMP satellite is a rigid body, torque-free, has two nearly equal moments of inertia, and is spinning nearly about the axis associated with the third moment.

We know that the torque-free assumption is not strictly true for the IMP satellite. The vehicle is torqued so that the spin axis is perpendicular to the sun's direction. Also, magnetic, gravity gradient, and radiation pressure torques will be present. The control torques will be small since the sun direction changes slowly. The natural torques will be small because of the satellite's large distance from the earth. Hence, the torque-free body assumption should be valid.

B. General Method of Attitude Determination

A slit is scribed on the focal plane of an optical system. Such a slit describes a curve when projected on the celestial sphere. If the slit is a straight line and the optical system is distortion free, then the curve is a great circle. Such may be considered the case here.

Since the slit is fixed with respect to the satellite, its great circle projection has a known equation if such an equation is written with a coordinate system fixed in the satellite. Now, the instant a star transits the slit we know the star lies on the slit's projection. Hence, at the instant of transit we may write

$$\hat{n} \cdot \hat{s} = 0 \tag{117}$$

where

$\hat{n}$ = unit vector normal to plane of the slit's projection,

$\hat{s}$ = unit vector to the star.

Since the slit is fixed with respect to the satellite, $\hat{n}$ is most easily written in a coordinate system fixed in the satellite. On the other hand $\hat{s}$ is most easily written in a celestial coordinate system. In order to write these vectors in the same coordinate system, parameters which specify the orientation of the coordinate system fixed in the body with respect to the celestial system must be introduced. However, these are the very parameters we are interested in determining.

In general then, each transit furnishes one equation in several unknowns. The number of unknowns is dependent on the physical assumptions. If we can assume the satellite is spinning uniformly about a fixed axis, then only three unknowns are present. However, for the IMP system as many as nine unknowns may be introduced. These unknowns may be listed as follows:

ϵ_1 and ϵ_2 -- misalignment angles of the instrument axis with respect to the principal body axis of the satellite,

ξ and τ -- angles which define the direction of the angular momentum vector of the satellite with respect to the celestial system,

θ -- half-cone angle or nutation angle of the satellite's motion*,

ϕ -- precession angle,

ψ -- spin angle,

$\dot{\phi}$ -- precession rate,

$\dot{\psi}$ -- spin rate.

So at least nine transits are necessary. More transits are desirable, for then a least squared solution may be utilized and the errors reduced.

To process in the neighborhood of 100 transits requires about 6 minutes of running time on a CDC 3200 computer. The running time is not greatly increased as the number of transits is increased. Moreover, it is independent of the time interval over which the measurements are taken.

A more complete discussion and analysis of the total problem may be found in Reference [2] , pages 161-190.

---

* For a nearly symmetric, torque-free, rigid body $\dot{\theta} \doteq 0$, the approximation being better as θ becomes smaller.

PRECEDING PAGE BLANK NOT FILMED.

SECTION V
ERROR ANALYSIS

A. Transit Time Errors Due to Asymmetric Filter Output

As can be seen in Figure 58 the noise-free output signal, y(t), is slightly nonsymmetrical as a result of driving a two pole linear phase filter with a symmetrical input signal. Consequently, a threshold level set for different output signal amplitudes of the output signal will result in slightly different averages of the threshold crossings. If the transit time is taken as the average of the leading edge and trailing edge threshold crossings, then for a single detection threshold, slightly different transit times will be obtained for stars of different magnitude. Therefore, it is of interest to determine the variations in the transit times due to an asymmetrical output signal of varying peak amplitude crossing a fixed threshold.

These variations in the transit times can be analyzed by fixing the output signal, y(t), in Figure 58 and varying the threshold as a percentage of the peak output signal. The results are tabulated in Table XIII. These results show that for a threshold set at 24 percent of the signal peak, the transit time was 5.529 seconds; whereas, for a threshold set at 95 percent of the peak signal, the transit time was 5.306 seconds. For these two cases, there is a transit time difference of .223 second. This difference can be compared to the slit transit time determined from Section III-G as

$$T_s = 2.56\sigma = 2.56(.945) = 2.419 \text{ seconds.}$$

The ratio of these two numbers is

$$\frac{2.419}{.223} = 10.85.$$

So with T_s corresponding to $\widehat{SW}$ = 6 arc-minutes, the .223 second time difference corresponds to a rotation angle difference of about 0.6 arc-minute.

It should be noted that for a detection threshold set at 58 percent of the

TABLE XIII

TRANSIT TIMES AS A FUNCTION OF DETECTION THRESHOLD

Output Peak = .74637

Threshold	Threshold Percent of Peak	Leading Edge t_1	Trailing Edge t_2	Transit Time $\frac{1}{2}(t_1 + t_2)$
.17988	24.1	2.5	8.558	5.529
.23710	31.8	2.75	8.212	5.481
.30046	40.3	3.00	7.881	5.440
.36795	49.3	3.25	7.554	5.400
.43709	58.6	3.50	7.243	5.371
.50517	67.7	3.75	6.948	5.349
.56934	76.3	4.00	6.660	5.330
.62683	84.0	4.25	6.386	5.318
.67511	90.5	4.50	6.125	5.312
.71204	95.4	4.75	5.855	5.302

peak signal, the transit time is 5.371 seconds. Taking the difference of this value and the value for the 95 percent threshold and then comparing to T_s, this ratio becomes

$$\frac{2.419}{.07} = 34.6.$$

Hence, for a single detection threshold, errors in the transit time increase as the range of star pulse amplitudes increases.

It is expected that the symmetry of the output pulse may be improved by employing a linear phase filter transfer function with a greater number of poles. Hence, there would be less variation in the transit times for a single threshold with a given range of star pulse amplitudes. However, for the SCADS-IMP sensor a two pole filter is adequate.

B. Transit Time Errors Due to Shot Noise

The random arrivals of radiant energy photons from the star and the random emmissions of electrons in the photomultiplier give rise to random amplitude fluctuations of the filtered star pulse. These random fluctuations cause variations in the leading edge and trailing edge threshold crossings of the star pulse which causes an uncertainty in the transit time obtained from averaging these threshold crossings. This section will describe a method for estimating the transit time uncertainty. The method basically consists of a computer simulation for which a model for threshold crossings of a noisy star pulse is established. The random noise is generated from computer generated random numbers for a large number of star pulses. The average of the threshold crossings is determined for each pulse and then the variance in this average is determined for all pulses.

Consider a noise free star pulse, $y(t)$, as shown in Figure 87. Assume that the pulse came from a star of limiting detectable magnitude, and that a threshold level, I_T, has been established as described in section III-E. The noise characteristics will be assumed stationary, although actually, the RMS noise increases as the average signal level increases. However, the actual RMS value of the noise at the threshold cannot be larger than the RMS value for an average noise level equal to I_T. Consequently, it is reasonable to expect that the resulting transit time variance will be slightly pessimistic.

The expression for the filter noise free output $y(t,\sigma)$ has been analytically determined in Section IIIG-3. Also, the peak value of $y(t)$ corresponds to .597 I_S, and $\sigma = \frac{T_s}{2.56}$, so the nominal leading edge threshold crossing, t_a, and the nominal trailing edge threshold crossing, t_b, can also be analytically determined. In sufficiently small time intervals about both t_a and t_b, the slope of $y(t)$ may be assumed constant. It may be further assumed that the star signal slope having superimposed noise must also be constant in small intervals about t_a and t_b since the filter holding time will not permit rapidly changing output excursions. However, because of the effect of the filter

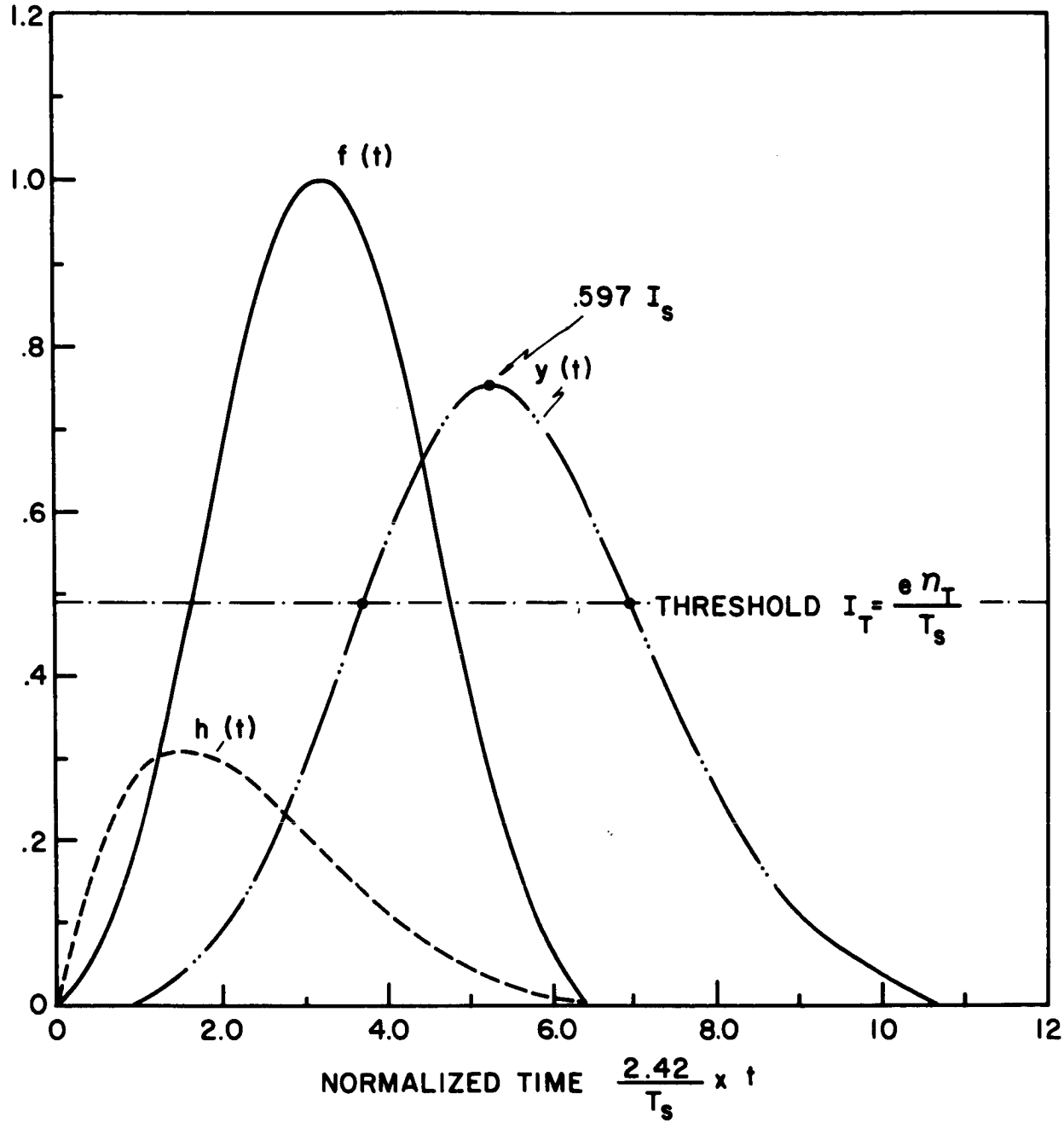

Figure 87 : Threshold Crossing of Noise-Free Star Pulse

holding time, the noise amplitudes at time $t_2 = t_a + \Delta t$ must be correlated to the noise amplitudes at time $t_1 = t_a - \Delta t$. Similarly, the noise amplitudes at times $t_3 = t_b - \Delta t$ and $t_4 = t_b + \Delta t$ are correlated to the amplitudes at t_1.

It has been shown that high density shot noise has a normal probability density function.[7] So at time t_1, the amplitude density function of the noise is given by

$$p(I_1) = \frac{1}{\sqrt{2\pi}\ \sigma_1} \exp\left[-\frac{1}{2} \left(\frac{I_1}{\sigma_1}\right)^2 \right]$$

where σ_1 = RMS value of I_1.

At time t_2, the amplitude density function is given by[34]

$$p(I_2 \mid I_1) = \frac{1}{\left[2\pi\, \sigma_1^{\,2} \left(1 - \rho_{12}^2 \right) \right]^{\frac{1}{2}}} \exp\left[-\frac{\left(I_2 - \rho_{12} I_1 \right)^2}{2\, \sigma_1^{\,2} \left(1 - \rho_{12}^{\,2} \right)} \right]$$

where ρ_{12} is the correlation coefficient between the random variable I_2 at t_2 and I_1 at t_1.

Similarly, at time t_3 the amplitude density function is

$$p(I_3 \mid I_1) = \frac{1}{\left[2\pi\, \sigma_1^{\,2} \left(1 - \rho_{13}^{\,2} \right) \right]^{\frac{1}{2}}} \exp\left[-\frac{\left(I_3 - \rho_{13} I_1 \right)^2}{2\, \sigma_1^{\,2} \left(1 - \rho_{13}^{\,2} \right)} \right]$$

and at time t_4 the density function is

$$p(I_4 \mid I_3) = \frac{1}{\left[2\pi\, \sigma_1^{\,2} \left(1 - \rho_3^{\,2} \right) \right]^{\frac{1}{2}}} \exp\left[-\frac{\left(I_4 - \rho_3 I_3 \right)^2}{2\, \sigma_1^{\,2} \left(1 - \rho_3^{\,2} \right)} \right]$$

Figure 88 shows the time interval close to the leading edge threshold crossing with the noise amplitudes I_1 and I_2 superimposed on $y(t)$ at times

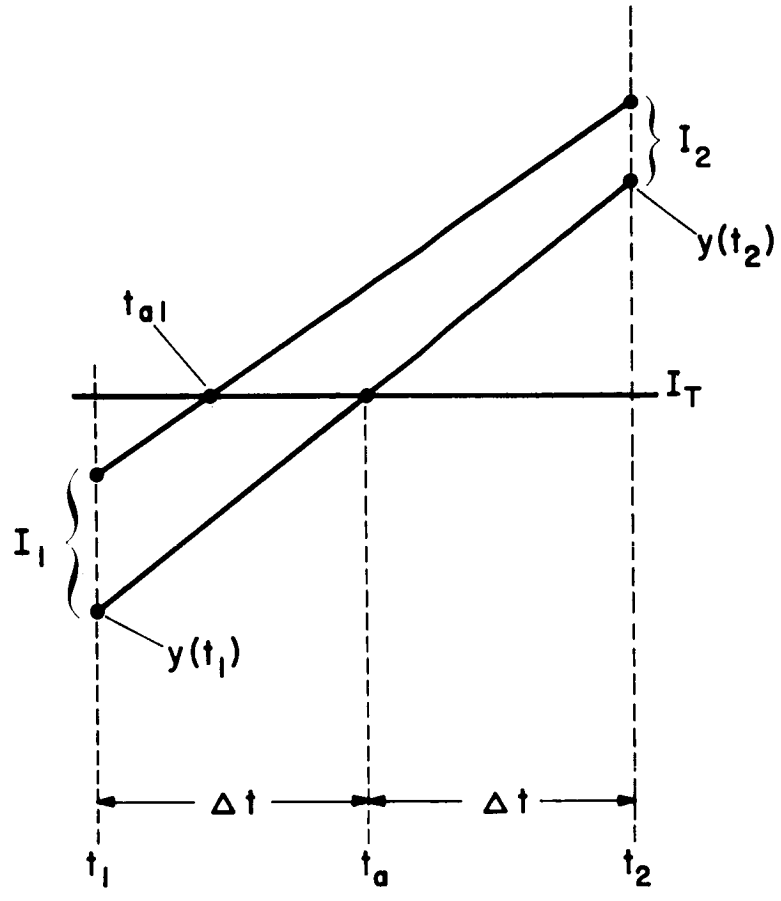

Figure 88 : Leading Edge Threshold Crossing

t_1 and t_2, respectively. With the noise superimposed, the threshold crossing is shifted from the noise free crossing time, t_a, to time t_{a1}. Since the slope of the noisy signal is assumed constant between t_2 and t_1, the shifted threshold crossing may be easily determined analytically for specific values of I_1 and I_2.

Specific values of I_1 and I_2 are determined from uniformly distributed random numbers generated by the computer random number generator. The random numbers, R_i, can take on any values between 0 and 1.0. Then the error function is evaluated so that

$$.5 + \frac{1}{\sqrt{2\pi}} \int_o^{x_1} e^{-y^2/2} dy = R_1$$

from which $I_1 = x_1 \sigma_1$. Similarly, I_2 is obtained by evaluating

$$= .5 + \frac{1}{\sqrt{2\pi}} \int_o^{x_2} e^{-y^2/2} \, dy = R_2$$

from which $I_2 = x_2 \, \sigma_1 (1-\rho_{12}^2)^{\frac{1}{2}} + \rho_{12} \, I_1$.

The shifted trailing edge threshold crossing may be similarly determined. Random numbers R_3 and R_4 are generated and the error functions

$$= .5 + \frac{1}{\sqrt{2\pi}} \int_o^{x_3} e^{-y^2/2} \, dy = R_3$$

$$= .5 + \frac{1}{\sqrt{2\pi}} \int_0^{x_4} e^{-y^2/2} \, dy = R_4$$

are evaluated. The noise amplitudes are determined from

$$I_3 = x_3 \sigma_1 (1 - \rho_{13}^2)^{\frac{1}{2}} + \rho_{13} I_1$$

$$I_4 = x_4 \sigma_4 (1 - \rho_{34}^2)^{\frac{1}{2}} + \rho_{34} I_3$$

After superimposing the noise amplitudes upon the noise-free signal, y(t), at times t_3 and t_4, respectively, the shifted trailing edge threshold crossing, t_{b1}, can easily be determined analytically.

The transit time for the noisy star pulse is computed as

$$t_{s1} = \frac{(t_{a1} + t_{b1})}{2} .$$

After this a new set of random numbers, R_1 through R_4, and their corresponding noise amplitudes are determined from which t_{s2} is determined. After repeating this procedure a large number of times to obtain t_{s3}, t_{s4}, etc., the variance of the transit times, $\sigma(t_s)$, is computed.

In order to compute the random noise amplitudes I_j, it is necessary to determine the correlation coefficients ρ_{1j} for j = 2, 3. The correlation coefficient, ρ_{12}, is defined as [35]

$$\rho_{12} = \frac{E[I(t_1), I(t_2)]}{(\mathrm{Var}[I(t)])^{\frac{1}{2}}}$$

where

$I(t_1)$ = the value of the shot noise current at time t_1
$I(t_2)$ = the value of the shot noise current at time t_2
$\sigma_1^2 = \mathrm{Var}[I(t)]$ = amplitude variance of the noise current.

It has been shown that[35]

$$E[I(t_1),\ I(t_2)] = \frac{I_T}{e}\int_0^{t=\infty} h(t)\cdot h(t+\tau)\ dt$$

where $h(t)$ = impulse response of the filter transfer function

$$\tau = t_2 - t_1$$

Also,[35]

$$Var[I(t)] = E[I^2(t)] = \frac{I_T}{e}\int_0^{\infty} h^2(t)\ dt$$

The impulse response for a two pole filter is given by

$$h(t) = K\, e^{-at} \sin bt$$

So

$$E[I(t_1),\ I(t_2)] = K^2\, e^{-a\tau} \cos b\tau \int_0^{\infty} e^{-2at} \sin^2 bt\ dt$$

$$+ \frac{K^2}{2}\, e^{-a\tau} \sin b\tau \int_0^{\infty} e^{-2at} \sin 2bt\ dt$$

$$= K^2\, e^{-a\tau}\left\{\frac{\cos b\tau}{a\left[\left(\frac{2a}{b}\right)^2 + 4\right]} + \frac{\sin b\tau}{4b\left[\left(\frac{a}{b}\right)^2 + 1\right]}\right\}$$

Also,

$$\sigma_1^2 = \mathrm{Var}[I(t)] = K^2 \int_0^\infty e^{-2at} \sin^2 bt \, dt$$

$$= \frac{K^2}{a\left[\left(\frac{2a}{b}\right)^2 + 4\right]}$$

So

$$\rho_{1j} = e^{-a\tau}\left\{\cos b\tau + \left(\frac{a}{b}\right) \sin b\tau\right\}$$

From Section III-G-3, the two pole linear phase versus frequency filter has

$$a = .375\ \omega_c$$

$$b = .3307\ \omega_c$$

For

ρ_{12}, $\tau = t_2 - t_1 = 2\,\Delta t$

ρ_{13}, $\tau = t_b - t_a$

ρ_{34}, $\tau = 2\Delta t$

Consequently, $\rho_{34} = \rho_{12}$.

Note that for $\tau = 0$, $\rho = 1$ as expected.

It is interesting to note that it is possible to express

$$\sigma_1^2 = \mathrm{Var}[I(t)] = \frac{n_T}{T_s} e^2 \int_0^\infty h^2(t)\, dt$$

$$= \frac{n_T}{T_s} e^2 \left(\frac{B\omega_c}{2}\right)^2 \frac{1}{\alpha\omega\left[\left(\frac{2\alpha}{\beta}\right)^2 + 4\right]}$$

$$= \frac{e^2 n_T}{T_s^2} (.574)$$

where from Section III-G-3

$$h(t) = \frac{B\omega_c}{2} e^{-\alpha\omega_c t} \sin(\beta\omega_c t)$$

$$B = 1.51$$

$$\alpha = .375$$

$$\beta = .331$$

$$\omega_c = \frac{3.45}{T_s}$$

Compare this result to Schottky's Theorem which gives

$$\sigma_1^2 = \mathrm{Var}[I(t)] = 2 e^2 \frac{n_T}{T_s^2} (.287)$$

where Δf = noise equivalent bandwidth of filter

$$= \frac{.287}{T_s}$$

In order to include the effects of noise introduced by the photomultiplier dynode chain, the value of σ_1 was increased by a factor of 1.3.[3]

The transit time variance was computed for two cases taken from Table II. One computation was for

$\widehat{SW}$ = 6 minutes of arc

$T_s = .556 \times 10^{-3}$ seconds (T = 2 seconds)

$n_s = 127.9$

$n_T = 200$

$n_{BD} = 150$

and the resulting RMS transit time variation was $.838 \times 10^{-4}$ seconds. The ratio of the slit transit time, T_s, to the transit time variation was

$$\frac{.556 \times 10^{-3}}{.838 \times 10^{-4}} = 6.65$$

The other computation was for

$\widehat{SW}$ - 24 minutes of arc

$T_s = .778 \times 10^{-2}$ (T = 7 seconds)

$n_s = 407$

$n_T = 2089$

$n_{BD} = 1924$

and the resulting RMS transit time variation was $.1125 \times 10^{-2}$ second. This compared to the slit transit time by the factor

$$\frac{.778 \times 10^{-2}}{.1125 \times 10^{-2}} = 6.91$$

For each computation, the computer was programmed to generate transit times for 500 star pulses.

Since the signal-to-noise ratio is approximately the same for all cases in Table II, it was concluded the same approximate transit time factor could be expected for all cases of the limiting detectable magnitude star where the false alarm rate and detection probability are fixed.

C. Orientation Errors Due to Transit Time Errors

In the previous sections, we have discussed the sources and magnitudes of the expected uncertainties in the transit times. It is these transit times which are the measured quantity from which the desired attitude may be computed. The purpose of this section is to evaluate the errors in the computed attitude which results from uncertainties in the measured transit times.

To gain some insight as to the error magnitudes which might be expected, a somewhat simplified error analysis was performed. For this error analysis, we assumed the sensor is spinning about a fixed axis. We then investigated the errors in right ascension and declination of the spin axis, and the error in the azimuth of the zero reference.

The field of view ($\Gamma = 25^{\circ}$ and $FOV = 20^{\circ}$) was chosen as per the recommendations in Section III-B. Note that star transits can be reliably measured over only one-half the scan period. Also a simple radial slit was utilized (see Figure 54) with a slit width projected onto the celestial sphere of 6 arc minutes.

The input error was the error in measurement of the transit time. However, we easily converted this error to an error in measurement of the angle from the zero reference to the slit at the instant of a star transit. Thus,

$$\sigma(\theta) = \frac{\sigma(t)}{T}$$

where

$\sigma(\theta)$ = standard deviation of rotation error,

$\sigma(t)$ = standard deviation of transit time error,

T = scan period.

We may assume $\sigma(\theta)$ = 1 minute of arc. This value was then used as the basic input error. The output error was then computed for various pointing directions.

The spin direction was maintained as roughly perpendicular to the sun's direction. So to specify the direction of the spin axis and the sun only two angles are required. These angles are the longitude of the sun measured in the ecliptic plane, and the angle the spin axis makes with the ecliptic plane.

The output errors were then computed as a function of the two angles which define the direction of the sun and spin axis. Results are shown in Figures 89, 90, and 91. In these figures the total error is plotted. We define total error as

$$\sqrt{\sigma^2(\alpha) + \sigma^2(\delta) + \sigma^2(\beta)}$$

where

$\sigma(\alpha)$ = standard deviation of error in the right ascension of the spin axis,

$\sigma(\delta)$ = standard deviation of the error in the declination of the spin axis,

$\sigma(\beta)$ = standard deviation of the azimuth error of the reference direction.

Figures 89 and 90 show regions in which the total error is in one of three contiguous intervals. These regions are plotted on a Mercator projection. For Figure 89 the three brightest stars in the field of view are utilized, while the four brightest are utilized in Figure 90. In both projections, three regions are shown: one in which the total error is greater than six minutes of arc, a second in which it is between three and six minutes of arc, and a third for which it is less than three minutes of arc.

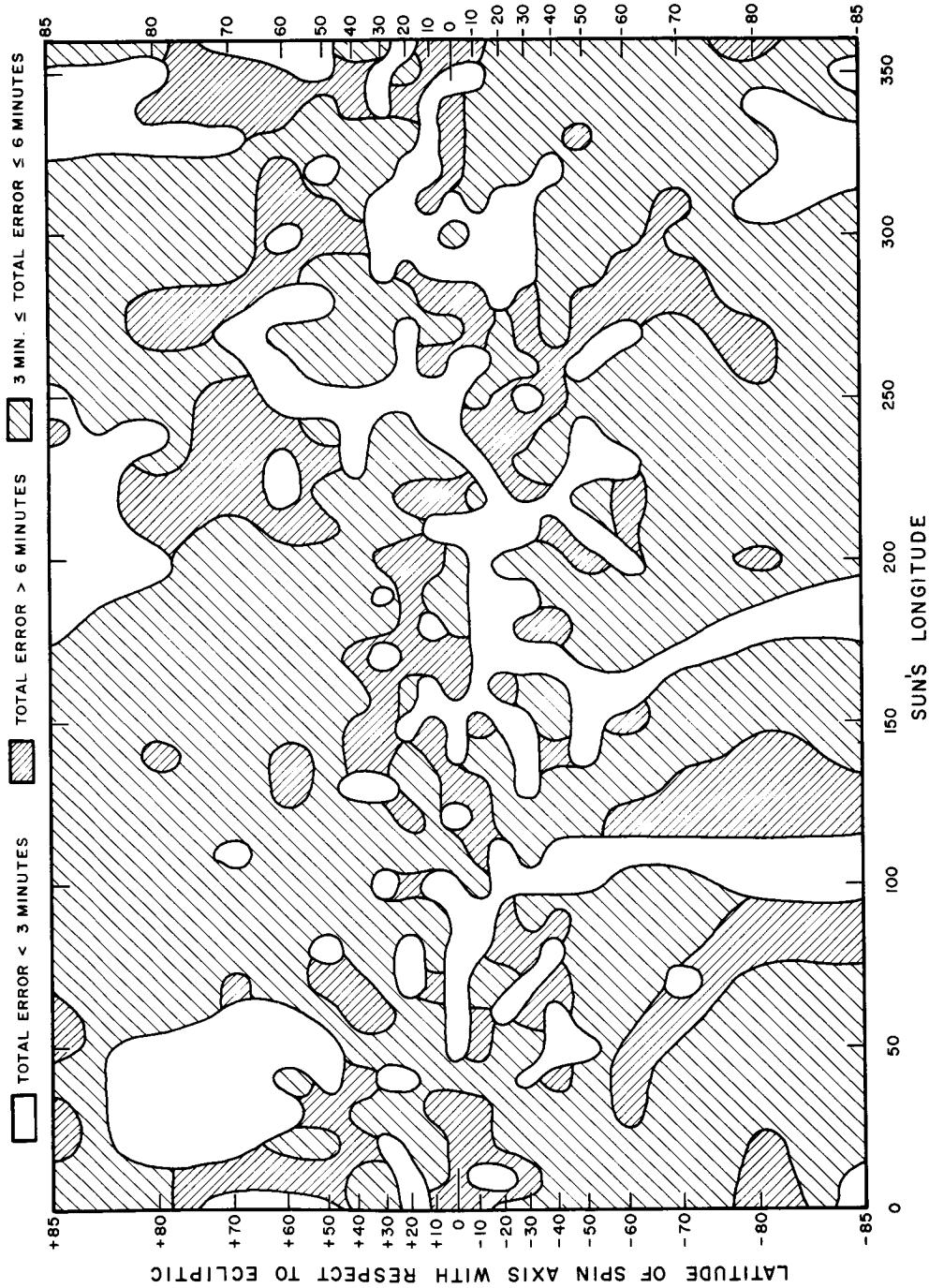

Figure 89: Total Error as a Function of Sun's Longitude and Latitude of Spin Axis for Three Stars in Field of View

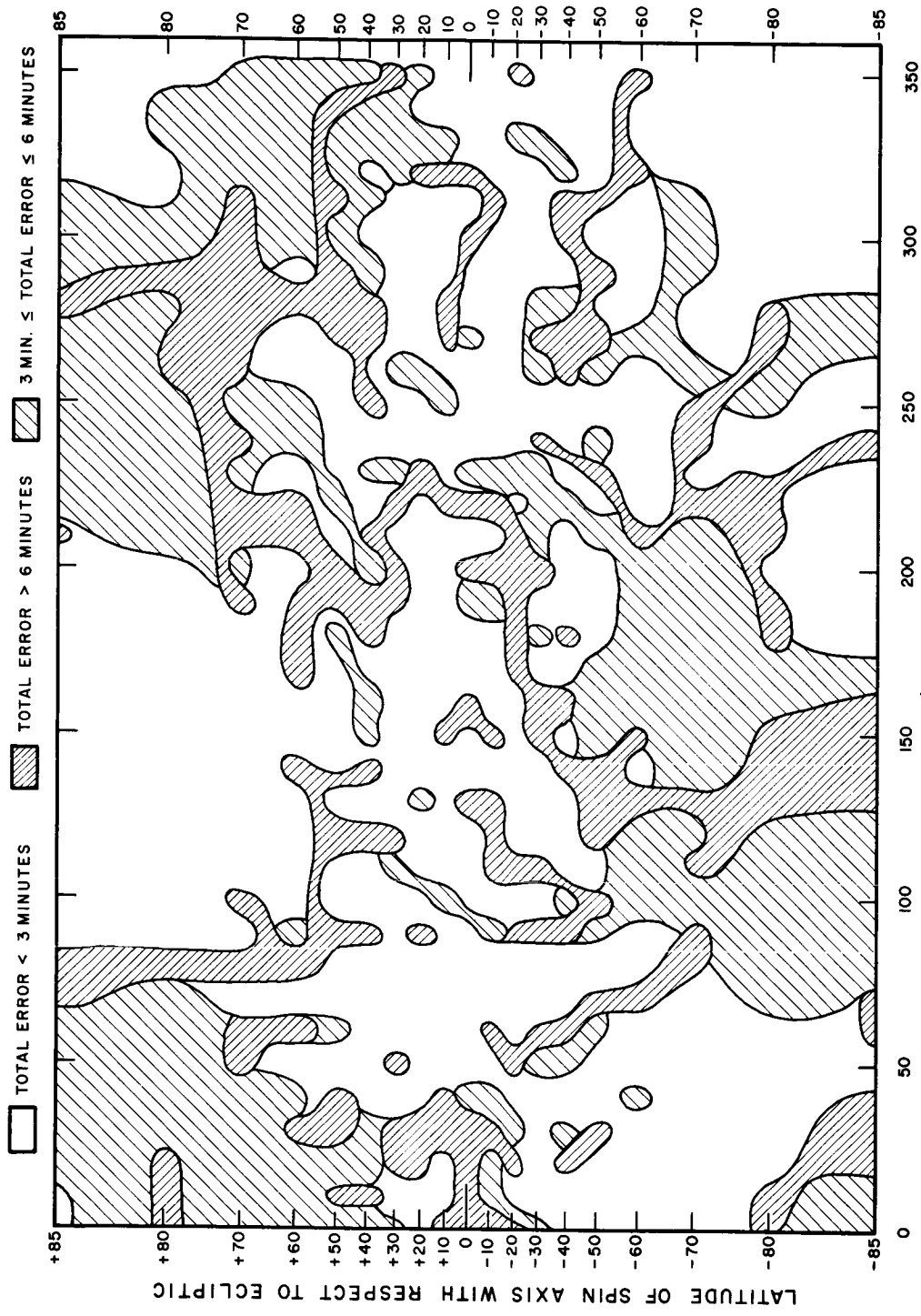

Figure 90: Total Error as a Function of Sun's Longitude and Latitude of Spin Axis for Four Stars in Field of View

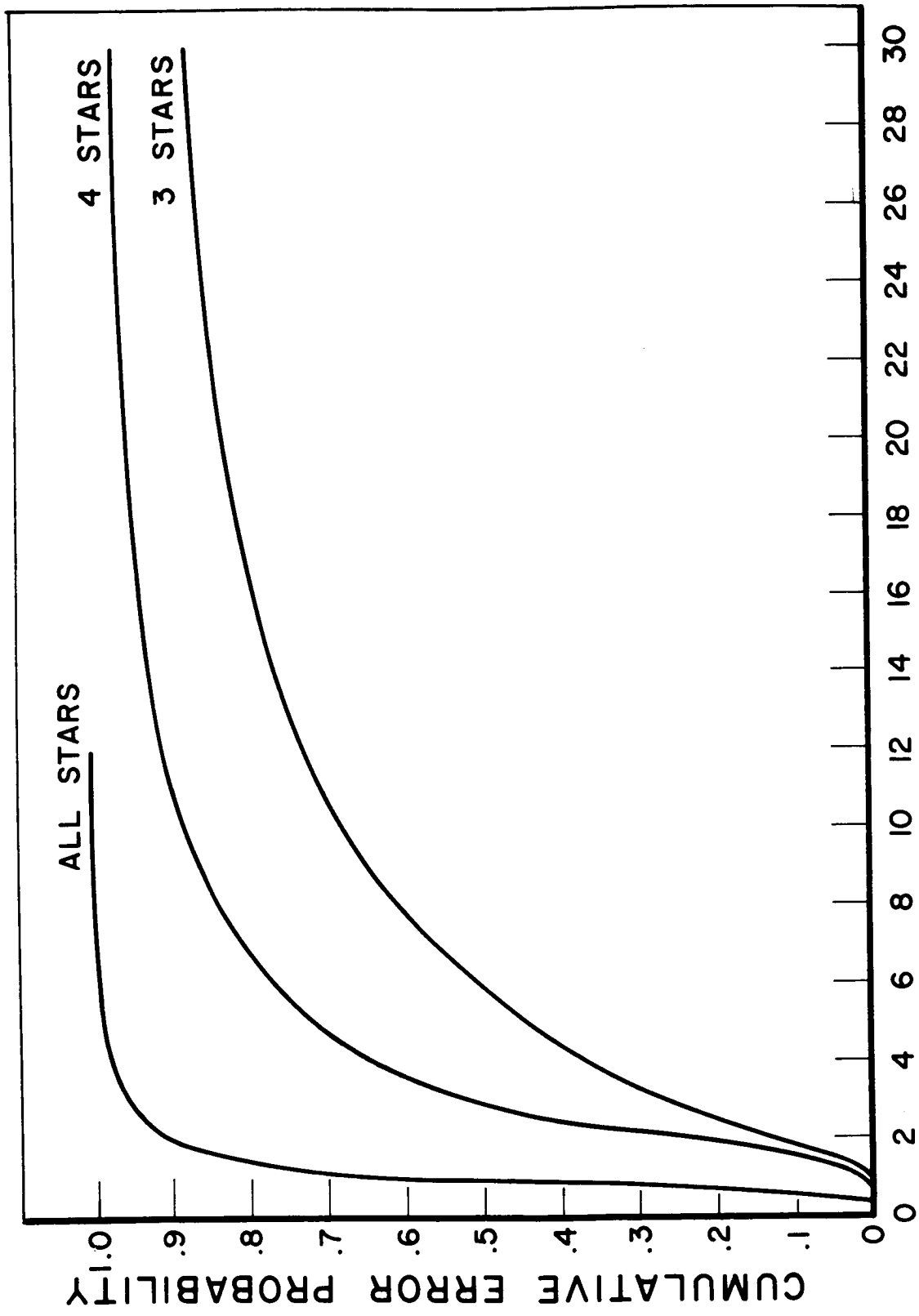

Figure 91: Cumulative Total Attitude Error for Three, Four, and All Stars of $m_v \leq 3.8$ in Field of View

Note that if only three stars are utilized, then there is an extensive area in which the error is excessive (greater than six minutes of arc) but if four stars are utilized this area becomes sufficiently smaller. For these plots no stars of visual magnitude greater than 3.8 were utilized.

Finally, in Figure 91 the cumulative total error probability is plotted as a function of the total error. This quantity is plotted for the following three cases:

(1) the three brightest stars in the field of view are utilized,

(2) the four brightest stars in the field of view are utilized,

(3) all stars in the field of view of visual magnitude 3.8 or less are utilized.

From this figure, it can be seen that the probability of the total error being six minutes or less is only .47 when three stars are utilized, .69 if four stars are utilized and .998 for all stars of magnitude 3.8 and brighter.

PRECEDING PAGE BLANK NOT FILMED.

SECTION VI
STAR IDENTIFICATION

The problem of determining attitude is discussed in Section IV and an equation is stated which must be satisfied whenever a known star is in the sensor slit. The key to the section which follows is the phrase "known star", for the problem of identifying stars from their transit times is discussed in the following paragraphs. The problem consists of establishing a one-for-one correspondence between transit times and star names (or catalog numbers). Absolute stellar magnitudes are not measured by the sensor; however, a method is described which does utilize relative magnitude measurements for the identification process.

Because of the multiple detection threshold capability of this sensor (see Section III-G-2), it is possible to order the detected stars according to their relative magnitudes and this capability will help us in some cases to resolve difficult identification situations.

The problem of identifying stars when only the relative azimuth of a set of targets is measured (angle as measured from some arbitrary reference about an unknown optical axis) is a very difficult one. Only if the approximate pointing direction of the instrument is known (to within a few degrees, say) can the method described here assure us of a relatively high probability of a successful identification.

A. Description of Problem

Before developing a method of identifying unknown targets from their transit times let us first consider some of the more important system parameters which directly influence the method of attacking the problem.

1. Field of View

The field of view of the optical system has been designed with a thirty degree diameter portion blocked off. There are two reasons for this central blocked portion.

(a) If a star were located directly along the spin axis, a constant signal output would be obtained instead of a series of pulses as desired.

(b) The azimuth matching nature of the identification technique could still produce false solutions for stars in close to the optical axis, since small changes in the assumed position of this axis cause large changes in the relative azimuth angles of such stars.

The outer diameter of the optical system is 35 degrees and completes the annular region in which the stars will be found. The center of this annulus is canted at an angle of 25 degrees from the spin axis.

2. Assumed Pointing Direction

One of the main reasons that the method of star identification described in this section is possible at all is because we have a reasonably good idea of where to look (on the celestial sphere) for a star pattern similar to the one detected by the sensor. The axes of the satellite are stabilized to an accuracy of $\pm$ 5 degrees and consequently because the orbital parameters will be known and the time of day of any observation will be recorded, a simple computation will determine the nominal direction of the optical axis to within $\pm$ five degrees in both right ascension and declination. From this very good starting point, it is not too difficult to find a star pattern (from a star catalog) similar to the detected pattern and hence to identify the transited stars.

3. Limiting Star Magnitude

Much of the star identification scheme depends on searching a list of possible stars for those having azimuth separations similar to the observed ones. Fortunately, we need only look at relatively small regions of the celestial sphere because of how well the pointing direction is already

known, but also we are further assisted by a knowledge of how faint a star the optical and electrical sensor can detect. We also will have information available to the identification program from the threshold detectors which will enable us to further restrict the list of all potential stars to be examined. One particular threshold detection scheme considered for SCADS-IMP has the following important features relevant here.

(a) Only stars of photographic magnitude $4^{m}.0$ and less (brighter) can be detected at all.

(b) Four fixed levels of detection are available to determine the relative magnitudes of the detected stars.

(c) All targets will be tagged with a magnitude indicator so that in many instances, a very bright object can immediately pin down one or more of the targets and enable the positive identification of that pulse-star pair.

This fortunate set of circumstances can happen when all but one or two of the targets have nearly the same magnitude (or at least all are detected at one threshold) and the other one or two are brighter and thus detected and tagged at a higher level, making them stand out from all the others.

B. Discussion of Method

The details of the azimuth only type pattern recognition technique to be used in the SCADS-IMP sensor are developed in the following paragraphs. In the discussion that follows, it cannot be over emphasized that the technique depends heavily on the presence of an approximate attitude. This "guess" is used by the computer program to search its star catalog (about 440 stars of magnitude $4^{m}.0$ and brighter) to find those which might lie in the scanned region of the celestial sphere. In this way a "computed azimuth pattern" (CAP) is generated. The measured azimuth pattern (MAP) provided by the sensor output is the one to be matched by varying the pointing direction.

The actual matching technique, i.e. the method of varying the parameters from which CAP is generated until CAP = MAP, can be illustrated by a manual analog. On a transparent sheet, lay out the measured azimuths as a set of radial lines (starting from an arbitrary zero azimuth). Overlay this sheet on a rectangular projection of the celestial sphere in the area of the assumed pointing direction. Translate the azimuth sheet on the star pattern and rotate it about the azimuth pattern center until coincidence of the patterns is achieved.

The above procedure is closely followed by the computer in achieving a CAP and MAP match. The computer solution is, however, more numerical, less sophisticated, and considerably more accurate. (The manual method cannot become much more accurate than a few minutes of arc without the aid of precision measuring machines. The computer--being in essence just a machine--could reduce the errors to a few seconds of arc if necessary.) Let us now examine more closely the sequence of functions performed by the computer program and the basic assumptions made in performing the star identification process.

1. Select Stars in the Field of View

Given the orbital parameters and the time and date, one can compute an assumed pointing direction and azimuth zero direction accurate to within a few degrees. The first task is to pick stars from the catalog which lie in an enlarged region about this direction and which, of course, are brighter than the limiting magnitude (see Figure 92). This region includes the nominal field of view plus five degrees of uncertainty plus one additional degree of cone angle. This will reduce the original list numbering some 440 candidates down by at least an order of magnitude. Furthermore, those stars actually detected by the sensor are guaranteed to be in this reduced list (unless a false target comes through) provided that the assumed position and the true position do not differ by more than, say five degrees.

2. Compute Azimuth Angle Differences

The reduced star list now contains the right ascension and declination of the candidate stars. For the pattern matching process we need to know the relative azimuth differences between the first and second stars, the second and third stars, etc. The star chosen to be the first star in the scan is the one with the smallest azimuth when measured from some arbitrary zero.

The computation of the azimuth angles is quite simple. Given the right ascension, α_i, and declination, δ_i, of the i^{th} star and the right ascension, α_o, and declination, δ_o, of the pointing direction, the azimuth, $\beta_o + \mu_i$, from north (measured counter clockwise) is given by the equation

$$\tan(\beta_o + \mu_i) = \frac{\sin(\alpha_o - \alpha_i)\cos\delta_i}{\sin\delta_i\cos\delta_o - \cos\delta_i\sin\delta_o\cos(\alpha_o - \alpha_i)}$$

where the signs of the numerator and denominator determine the proper quadrant. The angle, μ_i, is measured while β_o, α_o, and δ_o are to be determined.

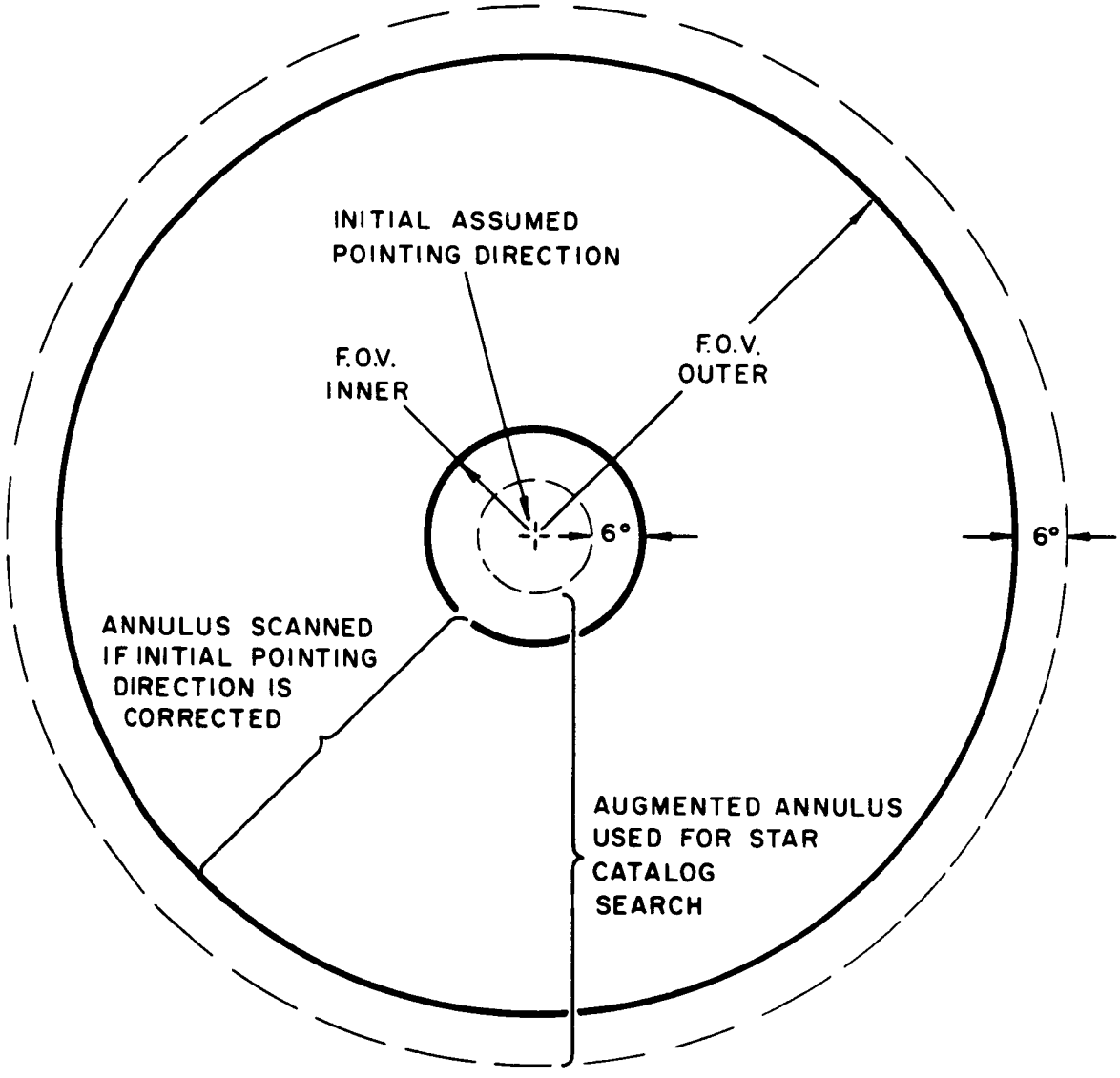

Figure 92: Augmented Annulus About Assumed Pointing Direction

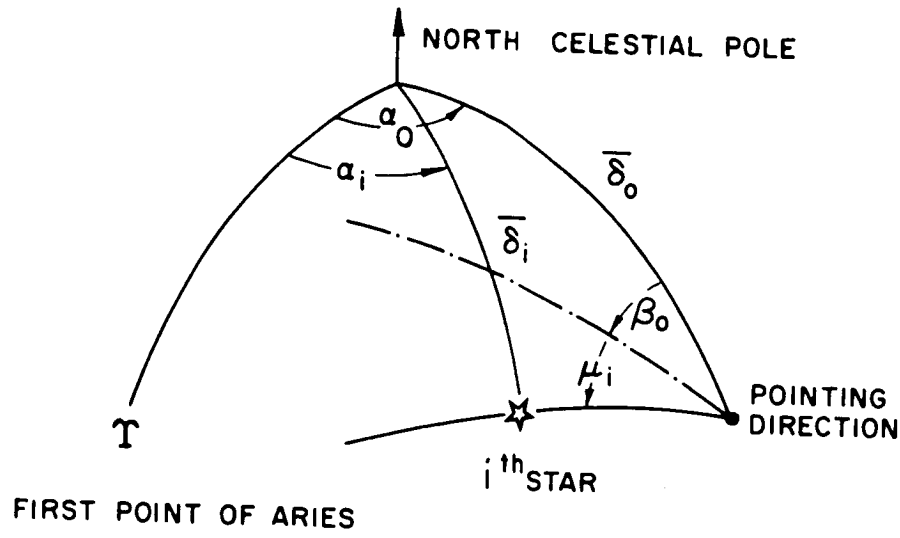

In this manner, an azimuth angle is calculated for all stars in the catalog within the field of view plus a safety margin of five degrees. An array is then constructed of the relative azimuths of these stars where the entries are formed by a simple subtraction,

$$\mu_{i,j} = \mu_i - \mu_j, \quad i > j.$$

j ↓ i →	1	2	3	4	5	...
1	0	5.6	14.7	39.2	101.0	
2		0	9.1	24.5	61.8	
3			0	13.4	37.3	
4				0	23.9	
5					0	
⋮						

Note that all entries below the first row are redundant. That is, having the azimuth differences between any star and the first star enables one to find all other separations. In order to save many arithmetic operations in the computer program, however, this array is set up once at the beginning of the program and just referenced thereafter. A second, and more important reason for filling in the complete array exists; namely the expected difficulty with undetected targets. That is, with any detection equipment of the type described in this report, a theoretical limiting magnitude for the dimmest star can be calculated and the instrument calibrated for this limit. However, there will always be some slightly brighter targets than this limiting magnitude which will go undetected on occasion, and some slightly dimmer objects which may occasionally be detected. To cope with the former (in the star identification process at least), we complete the array mentioned above so that it is possible, for example, to search for the separation of the fourth star and the second without insisting that the stars be detected in precisely the same order as the catalog indicates. Coping with the latter problem (dim stars) is easier; we simply extend our list of star candidates slightly beyond the limiting magnitude to insure including all possibilities (at the risk of making the task more difficult).

3. Comparing Measured with Computed Azimuths

The technique of matching stars with their measured azimuth angles is relatively simple. The scanning instrument measures the angles, μ_i, $i = 1, \ldots, N$. Since the azimuth zero direction is not known, we cannot depend on μ_i measured being equal to μ_i computed. However, the relative azimuths would be exact under those circumstances, and for this reason we do not need to rely on a knowledge of the azimuth zero reference. Suppose, however, that there are one or two stars in the field of view which are significantly brighter than the others--sufficiently bright to trigger at least one level above the base threshold. In this case, it should be relatively easy to find these same stars among the list of candidates and compare

their computed and measured azimuths. This will allow the computer program to take advantage of brighter stars in order to "nail down" a good reference to work from.

At this point, the computer program will consider each of the measured azimuth differences and search through the separation array seeking angles (and associated indices i, j) agreeing to within some generous tolerance angle μ_ϵ. A list of index numbers is kept for each measured pair of angles. When all target pairs have been processed, these lists may look like this.

Measured Azimuth Difference	μ_{21}	μ_{32}	μ_{43}	----	μ_{N1}
	4-3	6-4	7-6		5-1
Candidate Star Pairs	4-8	7-1			11-3
	5-4	7-2			11-4
					11-10

Note that the first target is used in both the first and last list to complete the scan. The actual identification process is now simply to scan across the lists looking for sets of indices of the form

b-a c-b d-c ---- N-a

The underlined indices exhibit such a form. We must conclude then that the identified stars are numbered a, b, c, ..., N, respectively. However, it may be possible to find other sets of N stars which also satisfy the above conditions, in this case each set must be further examined.

4. Using Residuals to Correct Assumed Position

For every azimuth difference, a residual exists. These residuals can be used to move the assumed pointing direction closer to the true position. Graphically, the scheme is as follows (the computer program will, of course, do the problem digitally, but in a similar manner).

Let the dotted lines (of Figure 93) refer to azimuths measured from the true pointing direction to each star, the solid lines are the azimuths from the assumed position (in this example, the true and assumed pointing directions differ by five degrees). Residuals are taken as the difference between measured and computed relative azimuths with careful attention paid to the sign. In Figure 93 a sample case is illustrated using three stars for clarity. The residuals are, respectively, +8, +19, -27, and the sum of squares is 1154. From the sign of each residual we can determine which direction to move in order to reduce the residual to zero. If the sign is positive, the computed angle is too small and we must move "toward" the pair of stars defining this angle. Toward as used here arbitrarily means along a line defined by bisecting the angle between the two stars. This motion can be justified since we have assumed that (1) stars will never be closer than fifteen degrees from the true pointing direction (central blocked region), and (2) the assumed pointing direction is never more than about five degrees from the true one. Therefore, positive residuals dictate moving toward the pair of stars along the bisector and negative residuals indicate motion away from the stars. A possible worst case geometry is shown in Figure 94 where both stars are only fifteen degrees off the pointing direction and the assumed direction is five degrees away. Even here it is clear that moving away from the stars (since the residual is negative) on the bisector will bring the assumed pointing direction closer to the true one. As we move the stars further from the optical axis the geometry gets better and the problem becomes simpler.

From the relative size of the residual an indication of how far to

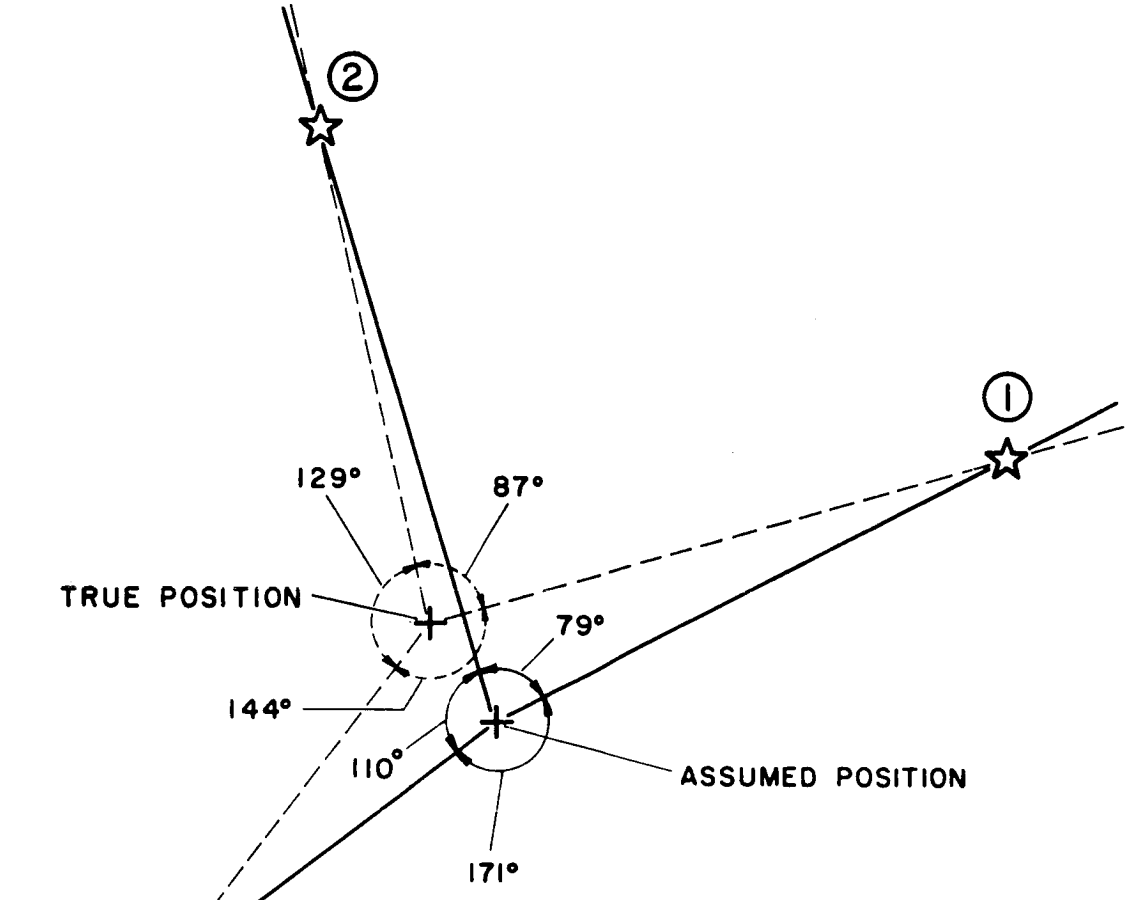

RELATIVE AZIMUTHS

MEASURED	COMPUTED	RESIDUAL
87	79	+8
129	110	+19
144	171	−27

SUM OF SQUARES 1154

Figure 93: Computed and Measured Relative Azimuths

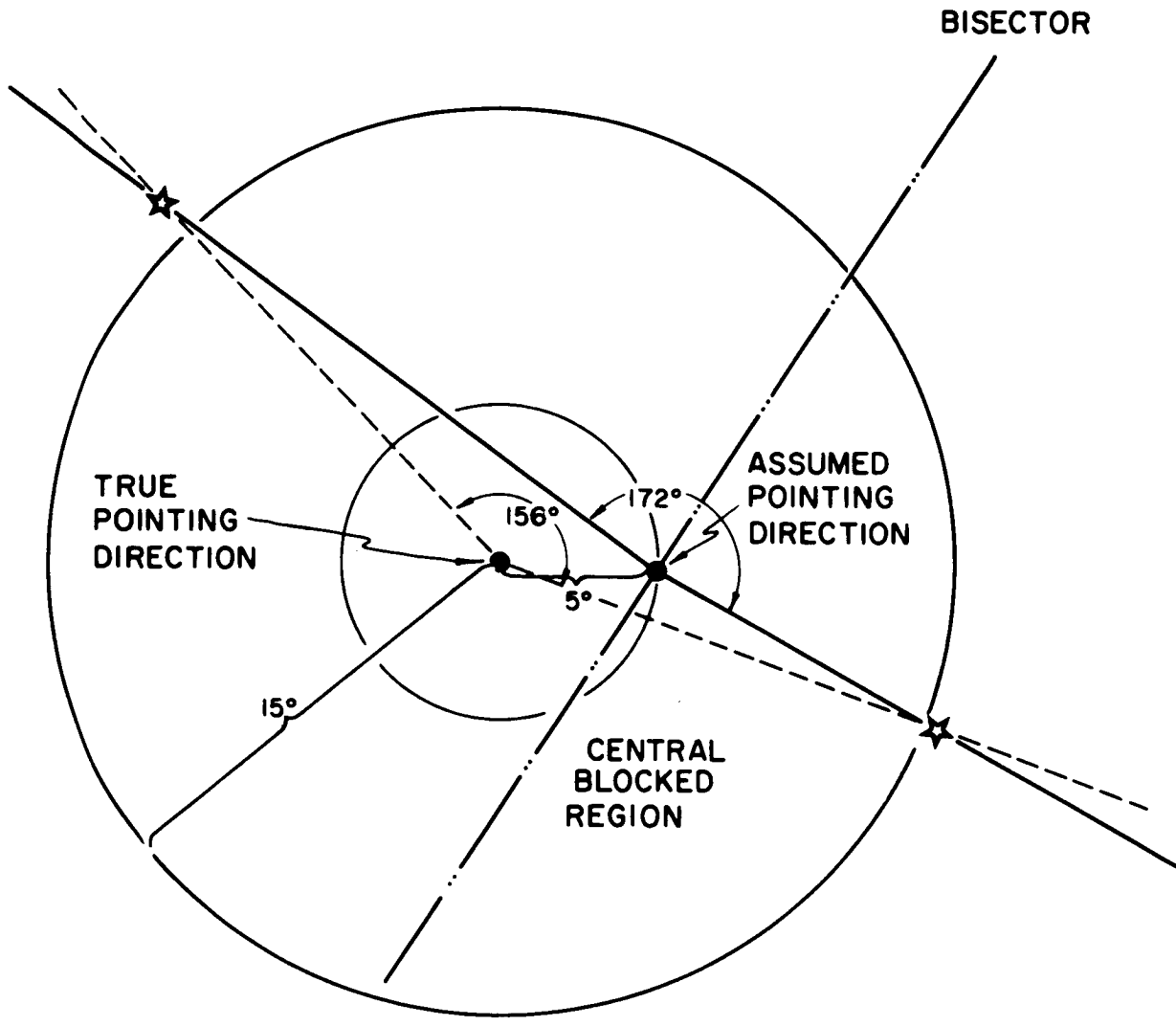

RESIDUAL = MEASURED − COMPUTED = 156° − 172° = −16°

Figure 94: Example of Difficult Geometry

move can be computed. The example above (Figure 93) seems to indicate that moving more along the bisector of stars 3 and 1 (in the negative sense) should be the dominant change since it has the largest residual (in absolute value). The fractional motions for the three pairs can be chosen then to be

$$\frac{8}{\sqrt{1154}} = .235 \qquad \frac{19}{\sqrt{1154}} = .558 \qquad \frac{27}{\sqrt{1154}} = .794$$

of some total motion. Since we cannot be more than five degrees from the true position, the total motion to correct our guess for three stars should be $2^{\circ}.566$* and each succeeding step should be half the previous one (if successive steps are necessary to resolve ambiguous star patterns). In Figure 95, the vector sum of the displacement of Figure 93 is shown and the resultant next assumed pointing direction is indicated. We have improved our position from an error of 5.0 degrees down to about 0.83 degree, a significant improvement.

After adjusting the assumed position for each of the possible star sets from above, a new array of relative azimuths is set up and the process is repeated (using a new tolerance, μ_{ϵ}, equal to half the old one) until a single set remains.

The only parameter which needs further study at this point is the tolerance angle, μ_{ϵ}. It is clear that for an assumed position within five degrees of the true one, the largest errors in relative azimuth occur when any two stars are just at the edge of the central blocked region. It is also true (although not so obvious) that the largest errors occur when

---

* From Table XI total motion factor for three stars is 66.2. Since the sum of squared residuals is 1154, the total motion is

$$5^{\circ} \times \frac{\sqrt{1154}}{66.2} = 2.566.$$

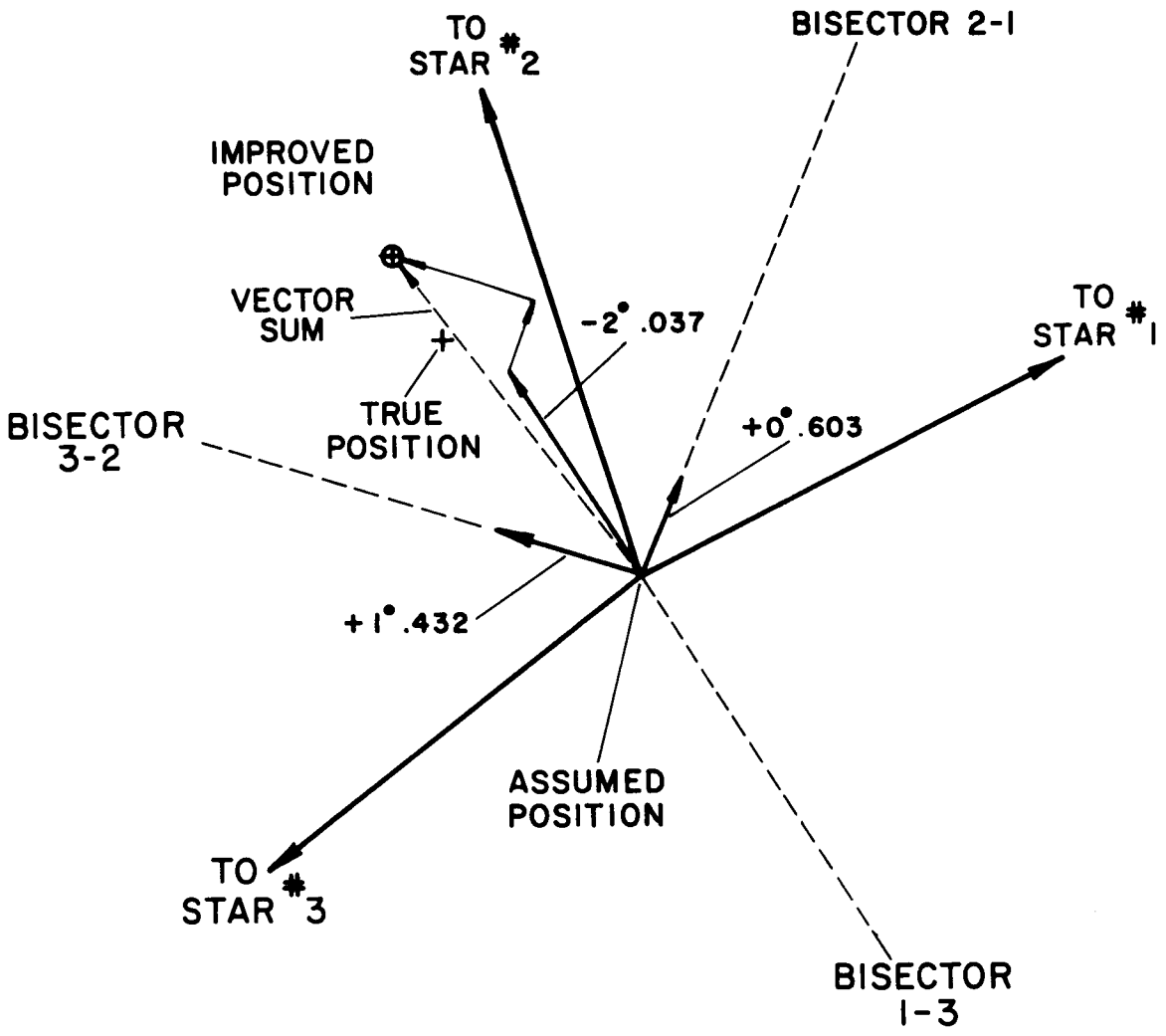

Figure 95: Moving Closer to the True Position

the relative azimuth is largest and that these errors occur when the assumed position is on the bisector of the relative azimuth between the two stars and interior to this angle.

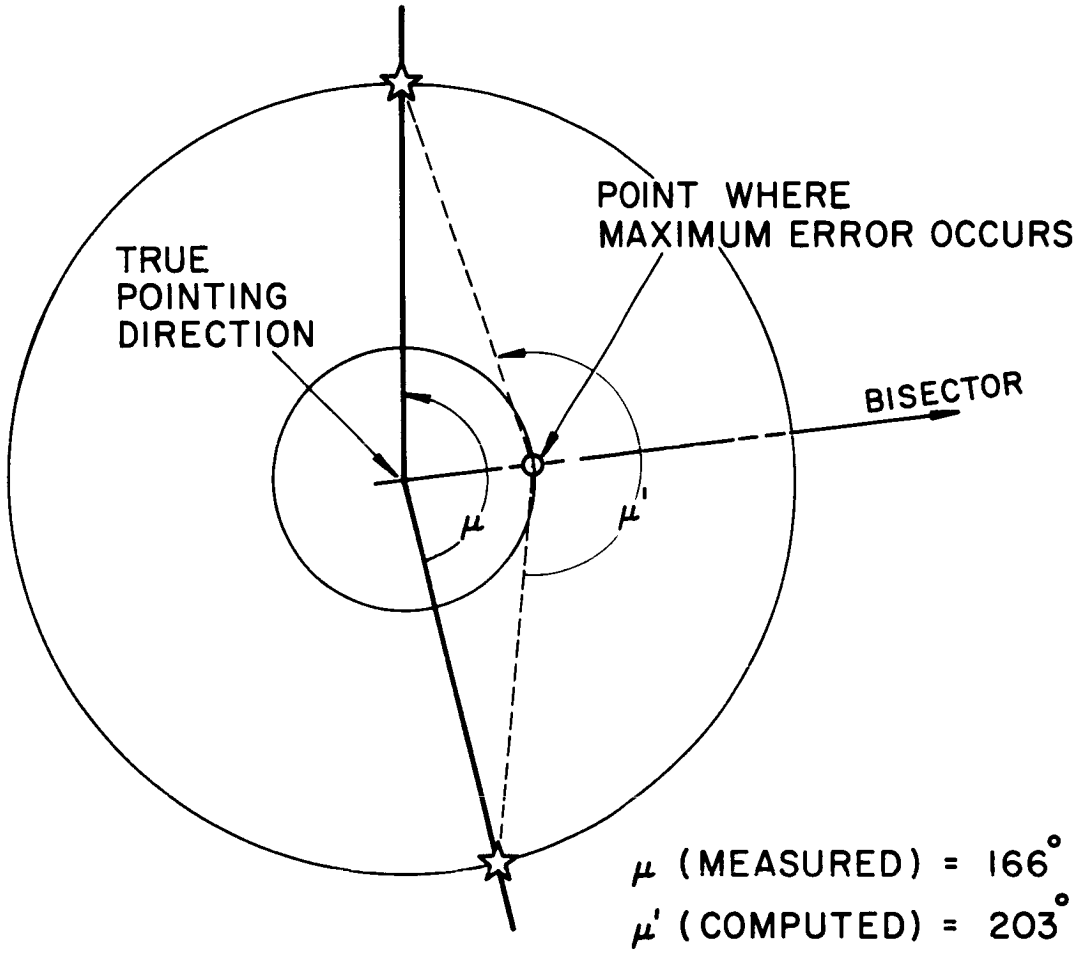

The largest expected residual can then be found when two stars are separated by an azimuth of 180 degrees. Fortunately, in all cases the star geometry is such that three or more stars will be detected and they will be separated on the average by about 120 degrees. At this angle the largest residual is about 38 degrees, and at 90 degrees, μ_ϵ = 34 degrees

(see Table XIV). The thing to do obviously when searching the separation array is to choose a tolerance, μ_ϵ, which depends on the measured separation and the number of detected targets and weight the smallest separation azimuth more heavily than the largest ones.

TABLE XIV

TOLERANCE TABLE

Number of Stars	Average Relative Azimuth	Tolerance (μ_ϵ)	Total* Motion Factor
3	120	38.2	66.2
4	90	34.3	68.6
5	72	30.0	67.2
6	60	26.4	64.6
7	51.4	23.4	61.8
8	45	20.9	59.1

* $$\text{Total Motion} = 5^o \times \frac{\sqrt{\sum_{i=1}^{N} (\text{residual})^2}}{\text{Total Motion Factor}}$$

REFERENCES

1. Battin, Richard H., Astronautical Guidance, McGraw-Hill Book Company, Inc., New York, 1964, 38-40.

2. Final Report: Feasibility Study for a Scanning Celestial Attitude Determination System, prepared by Control Data Corporation, Research Division, for NASA-Goddard Space Flight Center, Greenbelt, Maryland, Contract No. NAS5-9577, September 22, 1965.

3. Final Report: Breadboard Design of a Scanning Celestial Attitude Determination System (SCADS), prepared by Control Data Corporation, Research Division, for NASA-Goddard Space Flight Center, Greenbelt, Maryland, Contract No. NAS5-9661, November 1966.

4. Final Report: Special Techniques for Space Navigation, prepared by Control Data Corporation, Research Division, for NASA-Goddard Space Flight Center, Greenbelt, Maryland, Subcontract No. 247 of Prime Contract No. NAS9-153, Volume 2, July 1964, II-43.

5. Code, A. D., "Stellar Energy Distribution," in Stellar Atmospheres, J. L. Greenstein, editor, University of Chicago Press, Chicago, Illinois, 1960, Chapter 2, 50.

6. Norton, R. H., "The Absolute Spectral Energy Distribution of Canopus," in Technical Report No. 32-641, Jet Propulsion Laboratory, California Institute of Technology, California, August 15, 1964.

7. Rice, S. O., "Mathematical Analysis of Random Noise," in Bell System Technical Journal, Vols. 23 and 24, 1944-1945, 153. See also, "Selected Papers on Noise and Stochastic Processes," Nelson Wax, editor, Dover.

8. Smith, W. J., Modern Optical Engineering, McGraw-Hill Book Company, Inc., New York, 1966, 34.

9. Bennett, W. R., and J. R. Davey, Data Transmission, McGraw-Hill Book Company, Inc., New York, 1965, 60.

10. Skolnick, Merrill I., Introduction to Radar Systems, McGraw-Hill Book Company, Inc., 1962, 410.

11. Farrell, E. J., and C. D. Zimmerman, Optical and Electro-Optical Information Processing, MIT Press, Massachusetts, 1965, Chapter 35, 642, 646.

12. Schwartz, Mischa, Information Transmission, Modulation, and Noise, McGraw-Hill Book Company, Inc., New York, 1959, 507.

REFERENCES (continued)

13. Hansen, Peter D., "New Approaches to the Design of Active Filters," in The Lightning Empiricist, Vol. 13, No. 1-2, Philbrick Researches, Inc., Dedham, Massachusetts, 1965.

14. Churchill, R. V., Introduction to Complex Variables and Applications, McGraw-Hill Book Company, Inc., New York, 1948, 118.

15. Billington, Douglas S., and James H. Crawford, Jr., Radiation Damage in Solids, Princeton University Press, Princeton, New Jersey, 1961.

16. Vette, J. I., "Models of the Trapped Radiation Environment," in Volume I: Inner Zone, Protons and Electrons, NASA SP-3024.

17. Vette, J. I., "Models of the Trapped Radiation Environment," in Volume II: Inner and Outer Zone Electrons, NASA SP-3024.

18. Johnson, F. S., Satellite Environment Handbook, Second Edition, Stanford University Press, Stanford, California, 1965.

19. Gordon, F., Jr., and H. E. Wannemacker, IEEE Transactions on Nuclear Science, NS-13, No. 6, December 1966.

20. Reed, E. I., W. B. Fowler, C. W. Atkin, and J. F. Brun, "Some Effects of MeV Electrons on the OGO II Air Glow Photometers," Goddard Space Flight Center, Greenbelt, Maryland, X-616-67-132.

21. Billings, Bruce, H., American Institute of Physics Handbook, Second Edition, McGraw-Hill Book Company, Inc., New York, 1963, 8-43.

22. Heitler, W., The Quantum Theory of Radiation, Third Edition, Oxford, New York, 1954, 246-249.

23. Young, A. T., "Cosmic Ray Induced Dark Current in Photomultipliers," in Review of Science Instruments, Vol. 37, No. 11, November 1966, 1472.

24. Schliff, L. I., Quantum Mechanics, McGraw-Hill Book Company, Inc., New York, 1949, 262 ff.

25. Wolf, C., "The Effect of the Earth's Radiation Belts on an Optical System," in Applied Optics, Vol. 5, No. 11, November 1966, 1838.

26. Heitler, W., The Quantum Theory of Radiation, Third Edition, Oxford, New York, 1954, 368.

27. Mott, N. F., and R. W. Gurney, Electronic Processes in Ionic Crystals, Second Edition, Oxford, New York, 1940.

REFERENCES (concluded)

28. Fermi, E., Nuclear Physics, Revised Edition, University of Chicago Press, Chicago, Illinois, 1950.

29. Newkirk, Gordon, and David Bohlin, "Reduction of Scattered Light in the Coronagraph," in Applied Optics, Vol. 2, No. 2, February 1963, 131-140.

30. Meisenholder, G. W., "Planet Illuminance," in JPL Technical Report No. 32-361, California Institute of Technology, Pasadena, California, November 10, 1962.

31. Wilder, W. P., and B. R. Linden, "The Characteristics of Photocathodes Under High Light Levels," CBS Laboratories, presented at Image Intensifier Symposium sponsored by NASA-U. S. Army, Fort Belvoir, Virginia, October 24-26, 1961.

32. Schenkel, R. W., "New Developments in Photoemissive Tubes," in IRE Transactions on Nuclear Science, NS-9, June 1962, 83-87.

33. Final Report for Investigation of Dark Current in Ascop 541F Multiplier Phototubes After Exposure to High Light Level, prepared by Electro-Mechanical Research, Inc., for NASA-Goddard Space Flight Center, Greenbelt, Maryland, Contract No. NAS5-9089, December 1964.

34. Davenport, W. B., Jr., and W. L. Root, Random Signals and Noise, McGraw-Hill Book Company, Inc., New York, 1958, 149.

35. Parzen, E., Stochastic Processes, Holden-Day, Inc., San Francisco, California, 1962, 53, 150.

APPENDIX A

DATA SHEETS FOR EMR-541N AND EMR-543N PHOTOMULTIPLIERS

MODEL 541N-01-14
PRELIMINARY SPEC
MARCH, 1966

I PHYSICAL CHARACTERISTICS

Number and type of dynodes:	14; venetian-blind; Ag-Mg
Maximum overall length (unpotted):	3.94 inch (100 mm)
Typical weight (unpotted):	71 grams
Window material:	7056 glass
Cathode sensitive area:	1 in. (25 mm) diameter, area = .786 in^2
Cathode type:	Semitransparent: bi-alkali

	Note	Minimum	Typical	Maximum	Units
II. PHOTOCATHODE CHARACTERISTICS	1				
Quantum efficiency (Q) at 4100 Å		18	21.5		%
Cathode luminous sensitivity (S_k)		55	72.0		μA/lm
Cathode peak radiant sensitivity (σ_k)		.059	.071		A/W
Typical quantum efficiency					See Fig. 1
III. MULTIPLIER PHOTOTUBE CHARACTERISTICS, DC	1				
Voltage required for current amplification (G) of:					See Fig. 2
10^4			1690		V
10^5			2280		V
10^6			2950	3400	V
Dark current (i_D) at a current amplification of:					
10^5	1, 2		2.6×10^{-12}		A
10^6			2.5×10^{-11}	1×10^{-10}	A
10^7			2.5×10^{-10}		A
Anode luminous sensitivity (S) at a current amplification of 10^6		55	72.0		A/lm
Anode peak radiant sensitivity (σ) at a current amplification of 10^6		59,000	71,000		A/W
Equivalent anode dark current input at current amplification of 10^6	1				
Luminous, (E_D)			3.5×10^{-13}	1.8×10^{-12}	lm
Radiant at 4200 Å ($\mathcal{E}_D$)			3.5×10^{-16}	1.7×10^{-15}	W

EMR PHOTOELECTRIC DIVISION
ELECTRO-MECHANICAL RESEARCH, INC.
BOX 44 • PRINCETON, NEW JERSEY 08540

	Note	Minimum	Typical	Maximum	Units
Equivalent noise input at current amplification of 10^6	1				
Luminous, (E_N)			3.9×10^{-14}	1.0×10^{-13}	lm
Radiant at 4100 Å, ($\mathcal{E}_D$)			4.0×10^{-17}	1.0×10^{-16}	W
IV. MULTIPLIER PHOTOTUBE CHARACTERISTICS, PULSE	1				
Dark current counts at a current amplification of 10^6 at 20°C	2, 3		125		Pulses /sec
Pulse height resolution (FWHM) for Cs^{137}, NaI (Tl)	4		8.0		%
MAXIMUM RATINGS	5				
Supply voltage				3600	V
Anode current				.3	mA
Ambient temperature				150	°C

I. ENVIRONMENTAL

Shock	100 g, 11 millisecond duration
Vibration	30 g, 20 to 3,000 cps
Temperature	-55°C to 150°C

II. PACKAGING

Potted weight (typical)	170 grams Normally packaged in a 1-3/8" O.D. x 4-1/4" length fiberglass housing.

NOTES:
1. All data at room temperature = 20°C.
2. Measured after dark current stabilization.
3. Discriminator bias at 1/4 of the average single electron pulse height.
4. Harshaw scintillation crystal, NaI (Tl) Type D, size: 1 in. x 1 in., S/N BY 591
5. Absolute maximum ratings, prolonged exposure at maximum ratings may result in permanent deterioration of tube performance.

EMR PHOTOELECTRIC DIVISION
ELECTRO-MECHANICAL RESEARCH, INC.
BOX 44 • PRINCETON, NEW JERSEY 08540

MODEL 541N-01-14
PRELIMINARY SPEC
MARCH, 1966

TYPICAL SPECTRAL RESPONSE CHARACTERISTICS

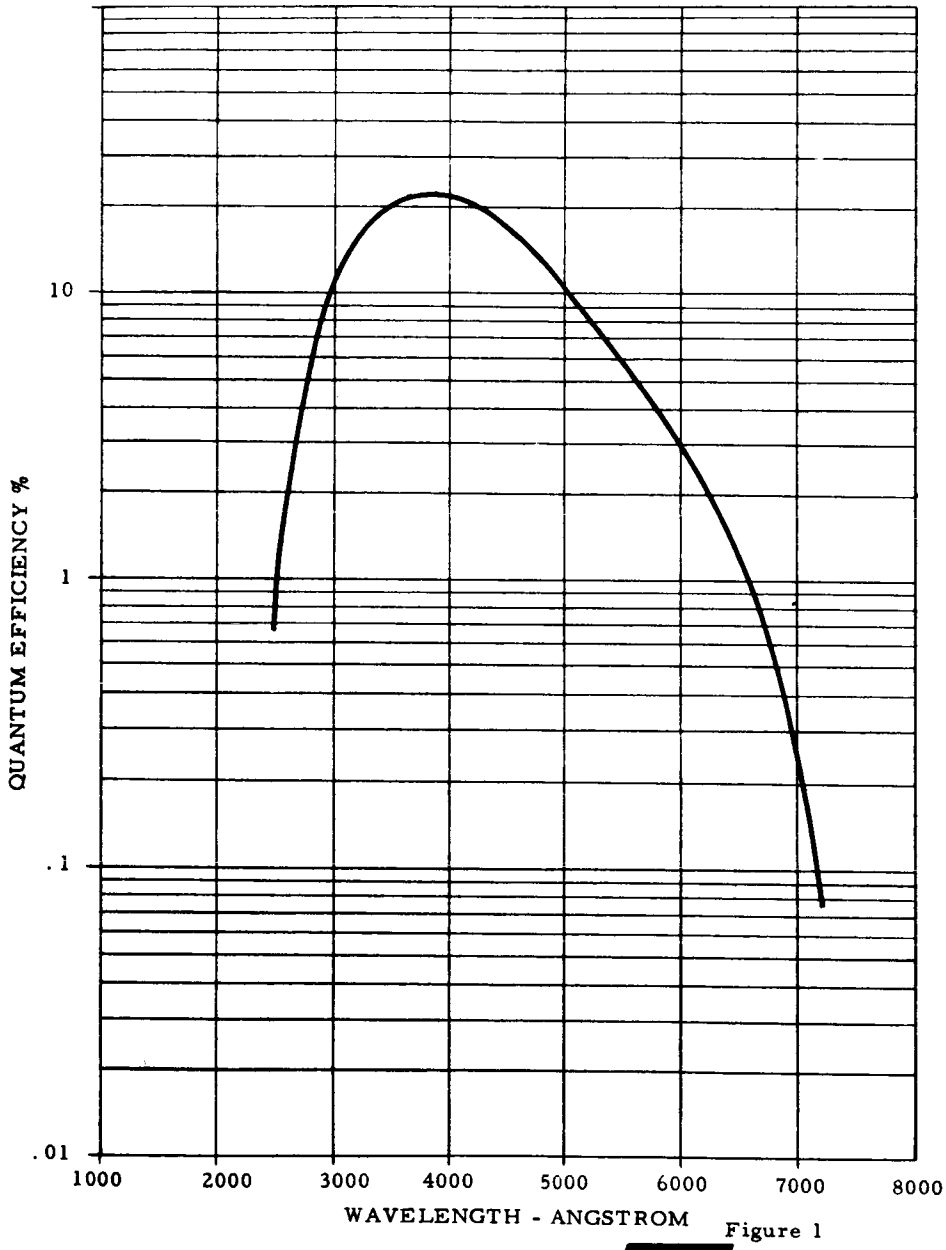

Figure 1

EMR PHOTOELECTRIC DIVISION

ELECTRO-MECHANICAL RESEARCH, INC.
BOX 44 • PRINCETON, NEW JERSEY 08540

MODEL 541N-01-14
PRELIMINARY SPEC
MARCH, 1966

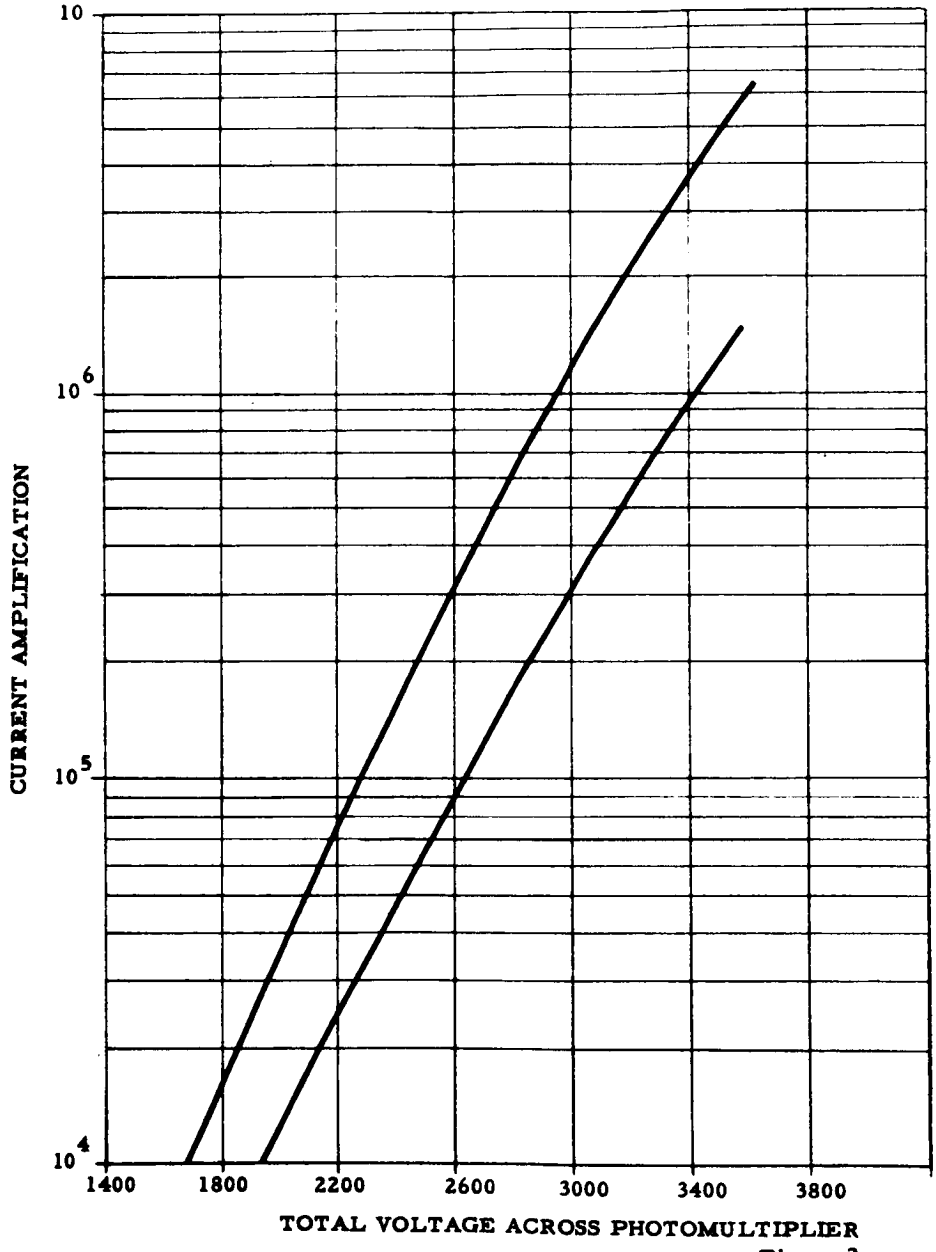

Figure 2

EMR PHOTOELECTRIC DIVISION

ELECTRO-MECHANICAL RESEARCH, INC.
BOX 44 • PRINCETON, NEW JERSEY 08540

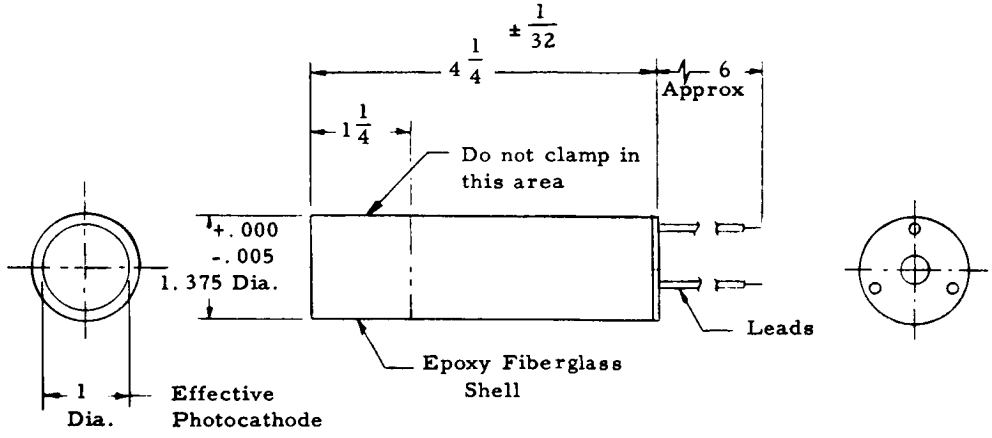

NOTES:
1. Resistor values equal thru-out unit

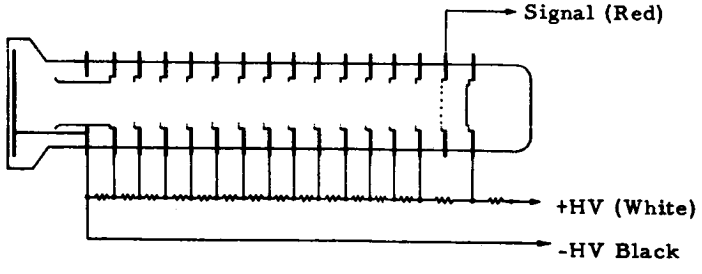

Figure 3

EMR PHOTOELECTRIC DIVISION

ELECTRO-MECHANICAL RESEARCH, INC.
BOX 44 • PRINCETON, NEW JERSEY 08540

PRELIMINARY SPECIFICATION DATA

MODEL 543N-01-14 MULTIPLIER PHOTOTUBE

I. PHYSICAL CHARACTERISTICS

Number and type of dynodes:	14; venetian-blind; Ag-Mg
Maximum overall length (unpotted):	6.50 inch
Typical weight (unpotted):	188 grams
Window material:	7056 glass
Cathode sensitive area:	1.7 in. diameter (area = 2.5 sp. in.)
Cathode type:	Semitransparent: bi-alkali

II. PHOTOCATHODE CHARACTERISTICS

	Note	Minimum	Typical	Maximum	Units
Quantum efficiency (Q) at 4100 Angstroms	1		18.0		%
Quantum efficiency at 6300 Angstroms			.89		%
Cathode luminous sensitivity (S_k)			55.2		μA/lm
Cathode peak radiant sensitivity (σ_k)			.060		A/W
Typical Multiplier Phototube Response and Quantum Efficiency					See Fig. 1

III. MULTIPLIER PHOTOTUBE CHARACTERISTICS, DC

		Note	Minimum	Typical	Maximum	Units
		1				See Fig. 2
Voltage required for current amplification (G) of:	10^4			1418		V
	10^5			1951		V
	10^6			2657		V
	10^7			3313		V
Dark current (i_D) at a current amplification of:	10^5	1, 2		2.4×10^{-12}		A
	10^6			2.1×10^{-11}		A
	10^7			2.6×10^{-10}		A

		Note	Minimum	Typical	Maximum	Units
	Anode luminous sensitivity (S) at a current amplification of 10^6			55.2		A/1m
	Anode peak radiant sensitivity (σ) at a current amplification of 10^6				60,000	A/S
	Equivalent anode dark current input at current amplification of 10^6	1				
	Luminous, (E_D)			3.8×10^{-13}		1m
	Radiant at 4100 Angstroms (ϵ_D)			3.5×10^{-16}		W
	Equivalent noise input at current amplification of 10^6					
	Luminous, (E_N)			4.6×10^{-14}		1m
	Radiant at 4100 Angstroms, (ϵ_D)			4.25×10^{-17}		W
IV.	MULTIPLIER PHOTOTUBE CHARACTERISTICS, PULSE	1				
	Dark current count at a current amplification of 10^6 at 20°C	2, 3		200		Pulses per sec.
	Pulse height resolution (FWHM) for Os^{137}, NaI(Tl)	4		7.80		%
V.	MAXIMUM RATINGS	5				
	Supply voltage					V
	Anode current					mA
	Ambient temperature					°C

		Note	Minimum	Typical	Maximum	Units
VI.	ENVIRONMENTAL					
	Shock			50 g, 11 millisecond duration		
	Vibration			20 g, up to 3,000 cps		
	Temperature			$-55^{\circ}C$ to $150^{\circ}C$		
VII.	PACKAGING			Normally packed in a 2" O.D. x 7-3/16 length Fiberglass housing		
	Potted weight (typical):			385 grams		

NOTES:
1. All data at room temperature = $20^{\circ}C$.
2. Measured after dark current stabilization.
3. Discriminator bias at 1/4 of the average single electron.
4. Harshaw scintillation crystal, NaI (Tl)
   Type D, size: 2 in. x 2 in.x S/N 7PA6.
5. Absolute maximum ratings, prolonged exposure at maximum ratings may result in permanent deterioration of tube performance.

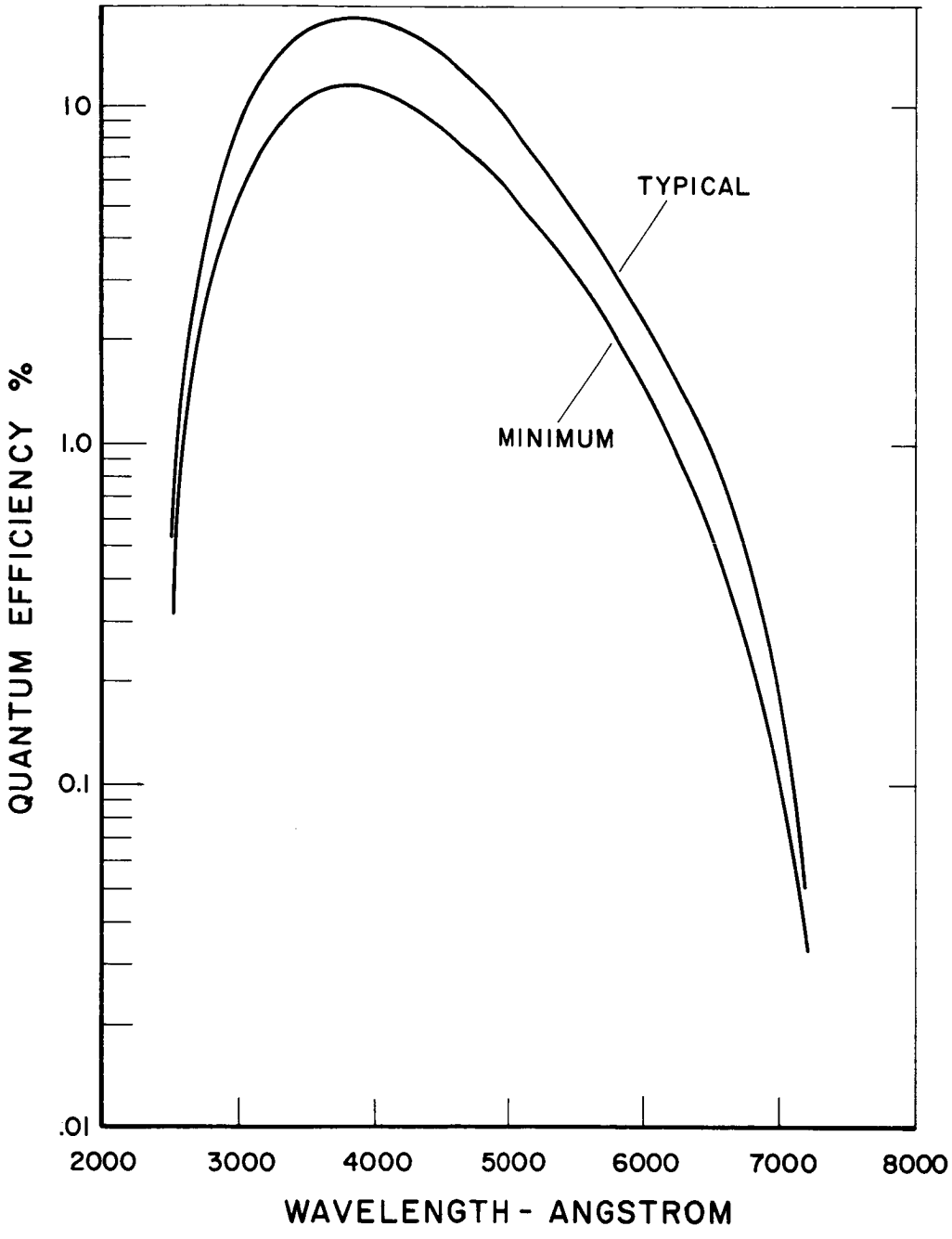

Figure 4: Quantum Efficiency
Model: 543N-01-14

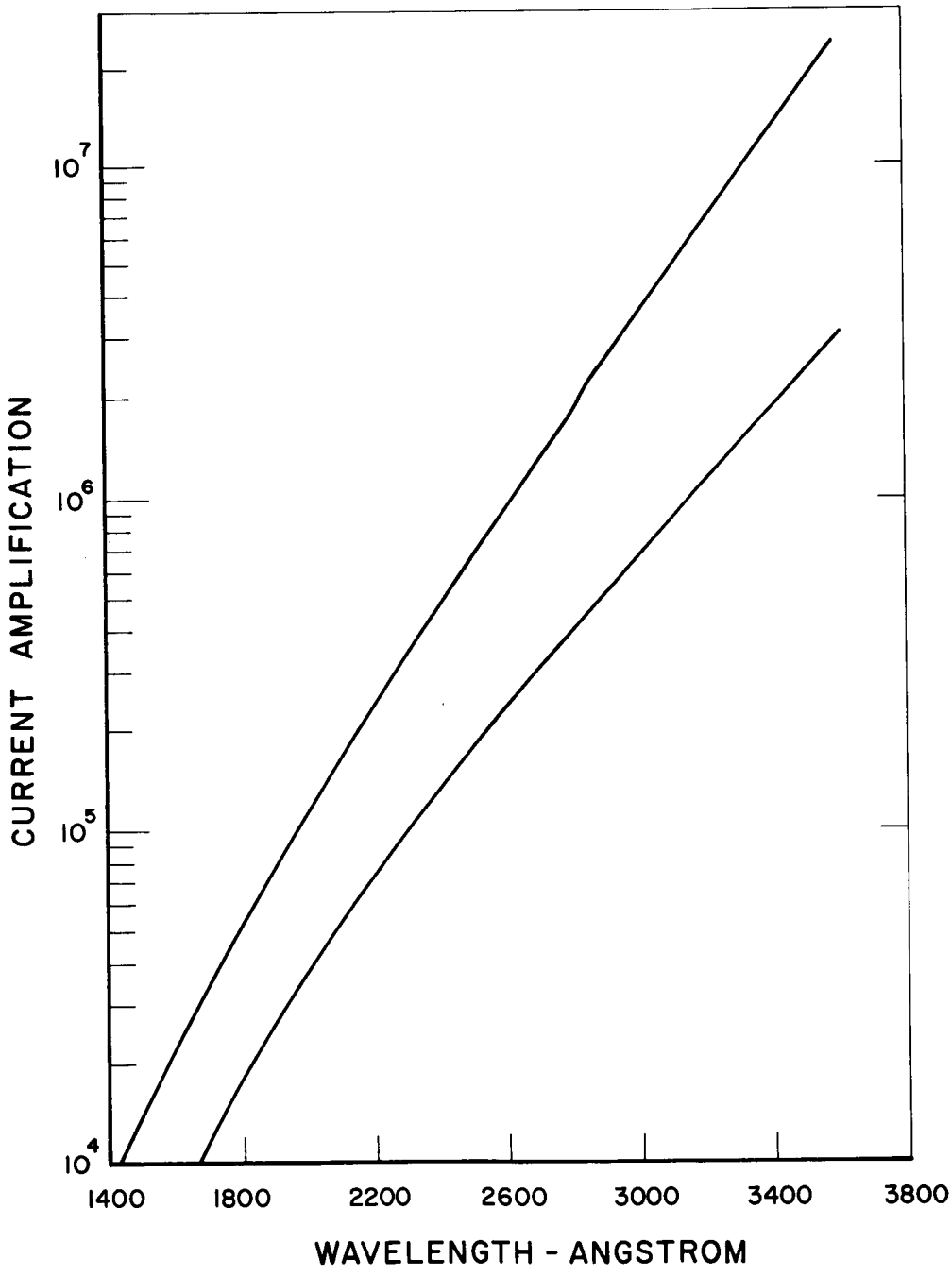

Figure 5: Current Amplification
Model: 543N-01-14